Collective effects in RF-dressed 39 potassium ultra-cold gases

Alfred Hammond

▶ **To cite this version:**

Alfred Hammond. Collective effects in RF-dressed 39 potassium ultra-cold gases. Other [cond-mat.other]. Université Paris-Saclay, 2023. English. NNT : 2023UPASP128 . tel-04446638

HAL Id: tel-04446638
https://theses.hal.science/tel-04446638v1

Submitted on 8 Feb 2024

HAL is a multi-disciplinary open access archive for the deposit and dissemination of scientific research documents, whether they are published or not. The documents may come from teaching and research institutions in France or abroad, or from public or private research centers.

L'archive ouverte pluridisciplinaire **HAL**, est destinée au dépôt et à la diffusion de documents scientifiques de niveau recherche, publiés ou non, émanant des établissements d'enseignement et de recherche français ou étrangers, des laboratoires publics ou privés.

THESE DE DOCTORAT

NNT : 2023UPASP128

Collective effects in RF-dressed ^{39}K ultra-cold gases

Effets collectifs dans les gaz ultra-froids de potassium ^{39}K habillé par radio-fréquence

Thèse de doctorat de l'université Paris-Saclay

École doctorale n°572 : ondes et matière (EDOM)
Spécialité de doctorat : physique
Graduate School : Physique
Référent : Institut d'optique

Thèse préparée dans les unités de recherche : Université Paris-Saclay, Institut d'Optique Graduate School, CNRS, Laboratoire Charles Fabry, 91127, Palaiseau, France, sous la direction de **Thomas BOURDEL**, chargé de recherche CNRS

Thèse soutenue à Paris-Saclay, le 27 septembre 2023, par

Alfred HAMMOND

Composition du Jury

Membres du jury avec voix délibérative

Pascal SIMON Professeur des université, LPS - Université Paris-Saclay	Président
Romain DUBESSY Maître de conférence, LPL – Université Paris Sorbonne Nord	Rapporteur & Examinateur
Baptiste BATTELIER Ingénieur de recherche, LP2N - Université de Bordeaux	Rapporteur & Examinateur
Laurence PRUVOST Directrice de recherche, LCPMR – Sorbonne université	Examinatrice

Membres du jury sans voix délibérative

Thomas BOURDEL Chargé de recherche CNRS, LCF – Université Paris-Saclay	Directeur de thèse

Contents

Introduction

Version française :

Selon les historiens occidentaux, la théorie des quatres éléments d'Aristote - la terre, l'eau, l'air et le feu - fût la première tentative d'expliquer la nature et la complexité de toute la matière en terme de substances simples et sans mythes ou animisme. Ce modèle devint obsolète seulement à la fin du $18^{\text{ème}}$ siècle avec le développement de la chimie analytique. Durant les deux siècles qui suivirent, toutes nos théories actuelles sur le monde microscopique furent découvertes. Pourtant, la quête vers la compréhension de la complexité du monde continue, maintenant dans de nombreuses spécialités qui reflètent la fragmentation de la physique, de la chimie et de la biologie, en domaines spécialisés.

Remarquablement, les physicients sont forcés de faire de nombreuses hypothèses simplificatrices lorsqu'ils encadrent l'étude d'un système. La plupart de ces hypothèses sont justifiées par le sens commun, en accord avec ce qui a déjà été vérifié expérimentalement. Ce cadre narratif va de pair avec un contexte technologique, dans lequel nous cherchons des phénomènes nouveaux et intéressants. La recherche présentée dans ce manuscrit n'aurait pas pu être réalisée avant l'invention du LASER, des caméras CMOS, des pompes ioniques, des ordinateurs... Et son sujet est aussi proche de perspectives appliquées comme les matériaux quantiques et les technologies quantiques.

D'un autre côté, les questions fondamentales explorées durant ces trois années portaient sur la compétition entre différents processus physiques dans le système : un gaz ultra-froid de potassium ^{39}K. Nous nous sommes souvent demandé si nous comprenions vraiment ce qu'il se passe à différentes échelles du système et nous avons souhaité élaborer une description simple des phénomènes observés. Dans la suite de cette introduction, nous allons présenter les principaux concepts physiques entrant en jeu.

La mécanique quantique

De la découverte fortuite de $\hbar$ par Max Planck en 1900, à l'introduction de l'équation de Schrödinger en 1925, le développement de la mécanique quantique fût un processus laborieux. Cette théorie du mouvement des atomes et des électrons fait appel à une description mathématique qui n'a aucun équivalent dans nos vies quotidiennes. premièrement, elle s'applique uniquement aux systèmes physiques qui ont une action ($\mathcal{A} \simeq \Delta x \Delta p$, produit des variations typiques des coordonées et des impulsions associées durant le mouvement) de l'ordre de $\hbar$. La constante de Planck réduite est égale à $\hbar = 1.05 \times 10^{-34}\,\mathrm{kg\,m^2 s^{-1}}$, ce qui est incroyablement petit comparé à l'action de systèmes courants. Par exemple, une balle de tennis de 60 g servie à 200 km/h a une action de $61\,\mathrm{kg\,m^2 s^{-1}}$. Seules les particules microscopiques, comme les atomes, les photons ou les électrons peuvent avoir une action de l'ordre de $\hbar$.

Quand elle s'applique à un système, la théorie de la mécanique quantique stipule que le mouvement ne peux plus être décrit par une simple trajectoire $x(t)$ (ou (x, p) dans l'espace des phases) mais plutôt par une somme pondérée d'orbites discrètes (appellées états propres quantiques). Ces orbites discrètes sont calculables théoriquement à partir de l'équation de Schrödinger, une équation différentielle linéaire. Les coefficients de pondération caractérisent entièrement l'état physique du système mais ne peuvent généralement pas être interprété comme des poids de probabilité car ce sont des nombres complexes. En conséquence, des orbites différentes peuvent interférer les unes avec les autres comme des vagues le feraient. Ce phénomène abstrait, appelé la dualité onde-particule, a été vérifié expérimentallement et n'admet aucune explication par la mécanique classique. D'autres expériences confortant le formalisme de la mécanique quantique ont été réalisées. Parmi elles, la célèbre expérience d'Alain aspect (1982) utilisant les inégalité de Bell pour prouver la nature non-classique de certains états quantiques dit "intriqués". Il a été récompensé par le prix Nobel de physique 2022 pour son travail.

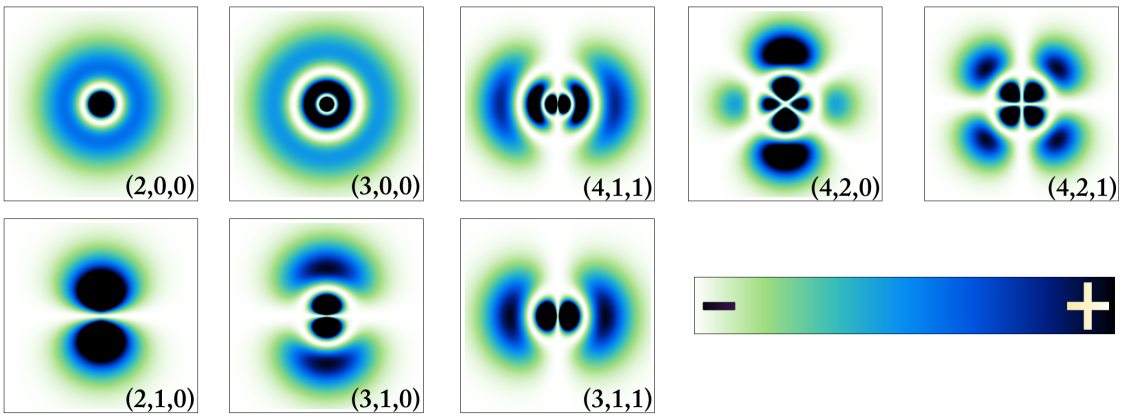

Figure 1: Tracé de la densité de probabilité pour certains états propres quantiques de l'atome d'hydrogène. Ceci illustre la délocalisation quantique et la dualité onde-particule. Les nombres (n, ℓ, m_ℓ) dans les coins sont utilisé pour étiqueter chaque état quantique. Une couleur blanche représente une probabilité de présence de l'électron nulle et une couleur bleu sombre une probabilité de présence de l'électron élevée. Seuls des coupes verticales du profil de probabilité sont affichés puisqu'il n'y a pas de dépendance avec la longitude.

Les gaz ultra-froids et la condensation de Bose-Einstein

Bien que la mécanique quantique doit certainement être utilisée pour le mouvement d'un simple atome, elle n'est en général pas nécessaire pour un gaz de $N \gg 1$ particules. Les propriétés macroscopiques du gaz sont le résultat d'un moyennage thermique qui vient cacher tout comportement quantique des atomes. De fait, les physiciens comme Boyle, Marriott, Joule, Kelvin, Gay-Lussac, Van der Waals... n'ont jamais observé aucun comportement non-classique (quantique) quand ils ont étudié toutes sortes de gaz. Par exemple, à la fin du 17$^{\text{ème}}$ siècle, Boyle et Marriott ont comfirmé expérimentallement qu'à suffisament basse pression, tous les gaz se comportent comme un gaz parfait.

L'histoire des gaz quantiques commença deux siècles et demi plus tard, en 1935, alors qu'Einstein aidé par les travaux de Bose, compris que le modèle du gaz parfait est mis en défaut aux très basses températures à cause de la nature indiscernable des particules du gaz. En effet, la physique quantique prédit que la probabilité que M particules avec un spin entier (bosons) se rassemblent dans un même état quantique est amplifiée d'un facteur gigantesque $M!$ en comparaison avec le résultat si elles étaient discernables. Ce phénomène est connu sous le nom d'amplification bosonique. Les atomes de potassium ^{39}K, et tous les autres alcalins avec un nombre impair de nucléons, sont des bosons.

A basse température T, Le poids d'occupation de Boltzmann $\frac{1}{Z}\exp\left(-E/k_BT\right)$ pour un état quantique d'énergie E implique que le particules ont plus de chances d'être dans l'état d'énergie minimale (avec donc une énergie cinétique nulle, $\vec{k} = 0$). Si les particules étaient discernables dans une boite de taille L, cet état quantique contiendrait la moitié des particules seulement à des températures extrèmement basses de l'ordre de $T_d \simeq \frac{4\pi^2\hbar^2}{2mL^2k_B}$, numériquement égale à 0.6 nK pour le potassium ^{39}K avec $L = 20\,\mu$m. heureusement, avec l'amplification bosonique, l'accumulation dans l'état fondamental est amplifiée et la température critique est multipliée par un facteur $0.16 \times N^{2/3}$. Numériquement, pour $N = 10^5$ atomes de potassium, cette température, dite de condensation, est $T_c = 350$ nK. L'accumulation macroscopique dans l'état de plus basse énergie est appellée la condensation de Bose-Einstein. Cette dernière est restée une préduction théorique jusqu'à la fin des années 90, date à laquelle Cornell & Wieman et Ketterle l'ont observé dans des gaz dilués d'alcalins. Ils reçurent le prix Nobel de physique en 2001 pour leur travaux. Finalement, aux températures en dessous d'un dixième de T_c, le gaz est presque complètement condensé et il aquiert ainsi des propriétés macroscopiques de nature quantique.

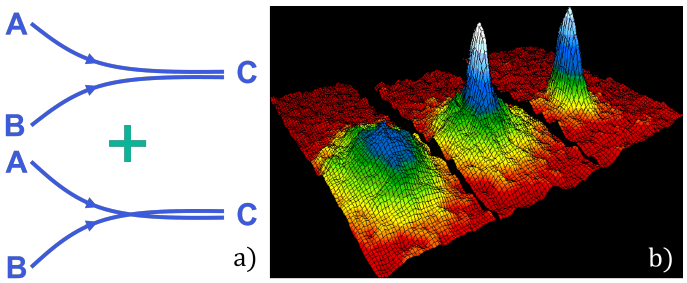

Figure 2: a) Equivalence des deux processus pour deux particules indiscernables allant des états A et B vers toutes les deux dans l'état C. Ceci explique l'amplification bosonique d'un facteur $2! = 2$ for 2 particles. b) Distribution d'impulsion en fausses couleurs : la célèbre preuve expérimentale de la condensation de Bose-Einstein publiée en 1995 par l'équipe de Cornell à JILA.

Interactions dans les gaz neutres dilués

Le rôle des intéractions a été volontairement omis dans la discussion précédente, bien qu'elles soient d'importance capitale pour la thermalisation du gaz durant son refroidissement. Heureusement, les intéractions ne changent pas radicallement la discussion physique sur la condensation de Bose-Einstein d'un gaz neutre dilué. La raison est que le potentiel d'intéraction entre atomes neutres décroit très vite avec la distance $E_{int}(r) \propto r^{-6}$ et que les atomes sont loins les uns des autres la pluspart du temps. En d'autre termes, le libre parcours moyen est de l'ordre de la taille macroscopique du gaz. En conséquence, les collisions impliquant plus de deux particules sont très improbables et elles n'affectent pas les propriétés macroscopiques du gaz. Les intéractions à deux particules sont isotropes, faibles et de courte portée, tous leurs effets macroscopiques sont contenus dans la donnée d'un simple nombre en $\mathrm{J} \cdot \mathrm{m}^3$, habituellement noté g pour un gaz quantique. La contribution de telles interactions à l'énergie libre d'un gaz condensé de N particules dans une boite large de volume V est simplement $g\frac{N^2}{2V}$ qui est, comme attendu une quantité extensive, et proportionnelle au nombre de paires de particules dans le gaz : $N(N-1)/2 \sim N^2/2$.

L'approximation en champ moyen (MF) et au-delà (BMF)

Les effets des interactions peuvent aussi être compris avec l'aide de l'approximation en champ moyen : tous les atomes sont pris dans le même état quantique qui est décrit par une fonction d'onde quantique φ. Celle-ci obéit à une équation de Schrödinger modifiée, l'équation de Gross-Pitaevskii, avec un terme non-linéaire $g|\varphi|^2\varphi$ qui représente les intéractions de contact à deux particules. Dans de nombreux cas et du fait de l'amplification bosonique, cette approximation est plus que suffisante pour expliquer tous les péhnomènes physiques se déroulant dans un gaz quantique. Cependant, dans ce manuscrit, nous devrons faire appel à une description théorique plus complexe : l'approximation au-delà du champ moyen, équivalente à autoriser des corrélations par paires de particules. (figure 7).

Sous l'approximation de champ moyen, les propriétés de gaz ultra-froids purs sont très simples du fait de l'unique paramètre g. Elles sont loin de présenter aucun agencement fantastiquement complexe, symétries cachées, fractales, invariances d'échelle ou dynamique chaotique... alors que cela pourait en théorie apparaître dans un système avec de nombreux degrés de liberté (problème à N-corps). Cela est le prix à payer pour des intéractions faibles. Ces intéractions ne peuvent pas être amplifiées avec une augmentation de la densité car les gaz quantiques d'alcalins ne sont que méta-stable. Ils forment rapidement un solide si la densité devient suppérieure à tipiquement $10^{21}\,\mathrm{m}^{-3}$. Dans le domaine des gaz quantiques, de nombreuses perspectives sont actuellement explorées pour atteidre des régimes avec une dinamique plus riche ou une équation d'état inédite : intéractions dipôlaires, réseaux optiques, systèmes en dimension réduites, influence d'un forçage, mélanges, ordre topologique, potentiels désordonés...

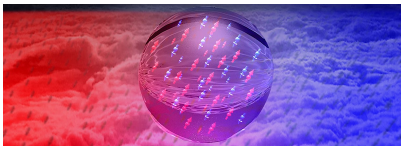

Figure 3: Vue artistique d'une gouttelette quantique, un mélange de spin dans lequel les effets au-delà du champ moyen jouent un rôle prédominant dans l'équation d'état. credit: ICFO Barcelona

Habillage radio fréquence (RF) et mélanges de spin

Le concept de l'atome habillé par un champ électromagnétique fut introduit pour la première fois en 1969 par Cohen Tannoudji et Serge Haroche [1]. Ils furent tous deux séparément nominé au prix Nobel de physique (1997, 2012) pour leurs découvertes ultérieures, bien plus sensationelles, sur les intéractions entre la lumière et la matière.

Un atome est dit "habillé par un champ électromagnétique" quand l'ensemble des deux peux être considéré comme un unique objet quantique. Dans ce manuscrit, le champ habillant est un champ magnétique oscillant à une fréquence ω de l'ordre de 40 MHz appartenant au domaine des radio fréquences. Il couple de manière résonante et cohérente deux états internes $|1\rangle$ et $|2\rangle$ de l'atome isolé. l'atome habillé a aussi deux niveaux quantiques notés $|+\rangle$ et $|-\rangle$. Ce sont tous deux des supperpositions quantiques des états $|1\rangle$ et $|2\rangle$. Leur différence en énergie ne dépend plus des énergies des deux états isolés E_1, E_2 bmais plutôt de la force Ω du champ couplant et de son désaccord en fréquence $\delta = \omega - (E_2 - E_1)/\hbar$. Un atome dans l'état $|-\rangle$ est à la fois dans l'état $|1\rangle$ et l'état $|2\rangle$.

Tant que le champ RF est présent et si les atomes sont dand l'état habillé $|-\rangle$, le gaz est un mélange de spin cohérent. En comparaison, dans un mélange incohérent, les atomes sont ou dans l'état $|1\rangle$ ou bien dans l'état $|2\rangle$ et ils ne peuvent pas changer d'état interne. Nous appellons ceci un mélange de spin par analogie entre tout système à deux niveaux et le spin 1/2. Dans ce manuscrit, nous montrerons que les mélanges cohérent ont des propriétés ont des propriétés nouvelles en comparaison avec les mélanges incohérent.

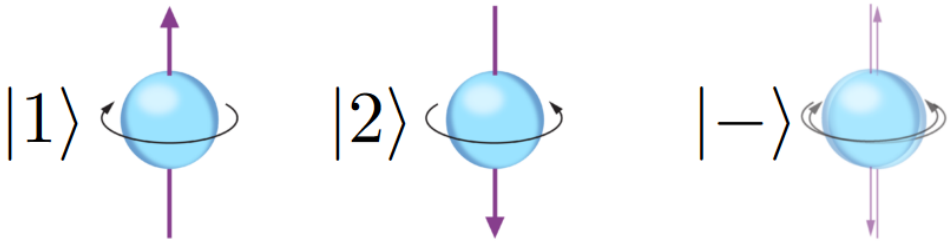

Figure 4: Vue d'artiste de la supperposition quantique se déroulant dans l'état quantique $|-\rangle$

Structure de ce manuscrit

Mon travail doctoral, dans l'équipe du potassium^{39}K, rentre dans le sujet général des gaz quantiques à intéractions ajustables. J'ai rejoint l'équipe en septembre 2020, directement en tant que doctorant, et après avoir passé l'agrégation de physique en 2020. Durant ma première année, l'équipe voulait étudier les mélanges de spin incohérent mais a été suprise par les propriétés intéressantes des mélanges cohérents. Cela nous a incité à nous focaliser sur les effets au-delà du champ moyen dans un mélange cohérent [2]. Suivi, une année plus tard, par l'étude expérimentale des interactions attractives à trois corps en champ moyen [3], toujours dans les mélanges cohérent. ma troisième année de thèse fut dévouée à l'implémentation de nouvelles fonctionalités sur l'expérience et à un travail théorique sur les perspectives à étudier.

Ce manuscrit est organisé en six chapitres, que je suggère de lire dans l'ordre, sauf pour le chapitre 2 qui peut être lu indépendament.

Chapitre 1: physique à un et deux corps des gaz ultra froids

Je donne ici le contecte général du manuscrit. Après avoir présenté le traitement des intéractions imposé par la méchanique quantique, nous retrouvons les conditions de stabilité d'un condensat et d'un mélange de condensats. Nous revenons ensuite à de la physique atomique et présentons comment l'habillage radiofréquence est réalisé en pratique. La derniere sous-partie se focalises sur la description des intérations élastiques et inélastiques entre deux atomes dans des états habillés.

Chapitre 2: l'expérience de potassium ^{39}K : maintenance et améliorations

Ce chapitre est dédié au dispositif expérimental. Nous présentons brièvement la séquence de refroidissement utilisée pour fabriquer des condensats de potassium ^{39}K. La seconde partie est dédiée à l'observation des transferts RF imparfaits durant la séquence et à une rapide présentation de deux paramètres expériementaux influant ce phénomène. Troisièmement, nous expliquons comment un nouveau dispositif expérimental de piegeage par boite a été ajouté à l'expérience et ensuite caractérisé. Il fonctionne grâce à un "digital micro-mirror device" (DMD) et un laser vert (blue detuned). Finalement, le principe et les premiers résultats d'un nouveau dispositif imparfait d'imagerie par absorption sont donnés.

Chapitre 3: effets au-delà du champ moyen dans les mélanges cohérents de condensats de potassium ^{39}K

Ce troisième chapitre présente notre étude, en colaboration avec D.S. Petrov et A. Recati, sur les effets au-delà du champ moyen dans les condensats habillés par radio-fréquence [2]. Les formules théoriques issues de la théorie de Bogoliubov sont présentées. Elles mènent à une expression mathématique pour l'énergie au-delà du champ moyen E_{BMF}. L'expérience a consisté en la mesure de la taille du condensat après une longue expansion unidimensionnelle. Les résultats sont en accord avec une importance dominante de l'énergie BMF, dépendant de Ω sur la dynamique.

Chapitre 4: intéractions à trois corps en champ moyen dans les condensats habillés de potassium ^{39}K

Le chapitre 4 présente un effet de champ moyen plutôt intuiti, et donnant naissance à un effet effectif d'attraction à trois corps en champ moyen, qui vient coexister avec l'effet à deux corps conventionnel. Après une interprétation physique du phénomène, nous calculons la formule pour la force d'intéraction à trois corps. Nous avons ensuite été capable de comfirmé cette formule avec deux séries d'expériences. Une sur des mesures de fréquences d'oscillations de respirations du condensats et l'autre sur le seuil de stabilité sur l'effondrement radial du condensat habillé. Un résultat important est l'ajustabilité indépendante de la force d'intéraction à deux particules et à trois particules.

Chapitre 5: comportement du consensat habillé aux faibles couplages de Rabi

Le chapitre 5 étudie la validité des résultats précédents (chapitres 3 et 4) aux fréquences de Rabi Ω plus faibles. Nous commençons par une étude numérique exacte pour l'état interne d'un condensat habillé dans un régime ou les intéractions sont plus fortes que le couplage Rabi. Notre préoccupation est la validité de l'approche en champ moyen. Les résultats numérique suggèrent de calculer l'état interne du condensat après avoir introduit une dimension artificielle et une equation de Schrödinger efficace. Nous continuons ensuite avec l'expression de l'énergie en champ moyen à toutes les valeurs de Ω. La dernière partie se concentre sur les modifications de l'énergie E_{BMF} avec Ω, spécifiquement dans le contexte des gouttellettes quantiques. We then pursue on the expressions of the MF energy at all values of Ω. Après avoir rappellé les conditions d'existences de ces gouttellettes, nous étudions numériquement la dépendance de leur densité de saturaton avec la fréquence de Rabi Ω.

Chapitre 6: dynamique à une dimension et excitation de densité

Le chapitre 6 est prospectif. Nous commençons avec une expérience de pensée sur l'expérience, qui sert de prétexe pour introduire une approche en terme de théorie des perturbations. Cela nous permet de légitimer la nature réelle de l'intéraction de champs moyen à trois corps et sa coexistence avec la renormalization au-delà du champ moyen. Dans un second temps, nous utilisons cette approche unificatrice pour prédire ce que doit être le comportement hydrodynamique de condensat habillé dans un cas âriculier intéressant. Si les intéractions à deux corps sont au total nulles et en géométrie unidimensionnelle, la dynamique est gouvernée par les intérations attractives à trois corps. Les équatiions du mouvement sont invariantes d'échelle et une surprenante instabilité de modulation devraît être observable en commençant avec un profil de densité uniforme.

English version:

Western historians believe that Aristote's theory of the four classical elements - earth, water, air, fire - was the first ever attempt to explain the nature and complexity of all matter in terms of simpler substances and without relying on myths or animism. This model became obsolete only at the end of the 18^{th} century with the development of analytical chemistry. In the following two and half centuries, all our current physical theories on the microscopic world were discovered. Yet the quest to understand the complexity of the world continues, now at many different levels reflecting the fragmentation of physics, chemistry and biology in further specialized branches.

Remarkably, physicists have to make a lot of assumptions or relevant hypothesis when framing the study of a system. Most of these hypothesis are justified by common sense in agreement with what has already been verified experimentally. This narrative framework comes in pair with a technological context, in which we look for interesting novel phenomena. The research presented in this manuscript could not have been realised before the inventions of LASER, CMOS cameras, ionic pumps, computers... And its subject is also close to applied perspectives like quantum materials and quantum technology.

On the other hand, the fundamental questions encountered during these three years were on the interplay between different physical processes in the system : an ultra-cold gas of ^{39}K potassium. We often wondered "do we really understand what is happening at the different length-scales in the system ?" and we wanted to achieve a simple description of the observed phenomena. We will now list in this introduction the main physical concepts involved.

Quantum mechanics

From the fortuitous experimental discovery of $\hbar$ by Max Planck in 1900, to the introduction of Schrödinger equation in 1925, the development of quantum mechanics was a rather difficult process. This theory on the motion of atoms and electrons involves a mathematical description which has no counterpart in our everyday life. Firstly, it applies only to physical systems which have an action ($\mathcal{A} \simeq \Delta x \Delta p$, product of the typical variations of coordinates and momenta during the motion) of the order of $\hbar$. Planck reduced constant is equal to $\hbar = 1.05 \times 10^{-34}\,\mathrm{kg\,m^2 s^{-1}}$ which is incredibly small compared to action of standard systems. For example, a 0.06 kg tennis ball served at 200 km/h has an action of 61 $\mathrm{kg\,m^2 s^{-1}}$. Only microscopic particles like atoms, protons or electrons can have an action of the order of $\hbar$.

When it applies to a system, quantum mechanics states that the motion can no longer be described by a trajectory $x(t)$ (or (x, p) in the phase space) but instead by a pondered sum of discrete orbits (called quantum eigen-states). These discrete orbits can in theory be found by solving Schrödinger equation, a linear partial differential equation. The pondering coefficients, describing the physical state of the system, cannot be interpreted as probability weights because they are complex numbers. In other words, different orbits can interfere with each other as classical waves would. This abstract phenomenon, sometimes called the wave-particle duality, has been verified experimentally, and cannot be explained by classical mechanics. Other experiments proving the formalism of quantum mechanics have been realised. Among them is the famous experiment of Alain Aspect (1982) using Bell inequalities to prove the non-classical nature of some entangled quantum states. He was awarded the Nobel prize in Physics 2022 for his work.

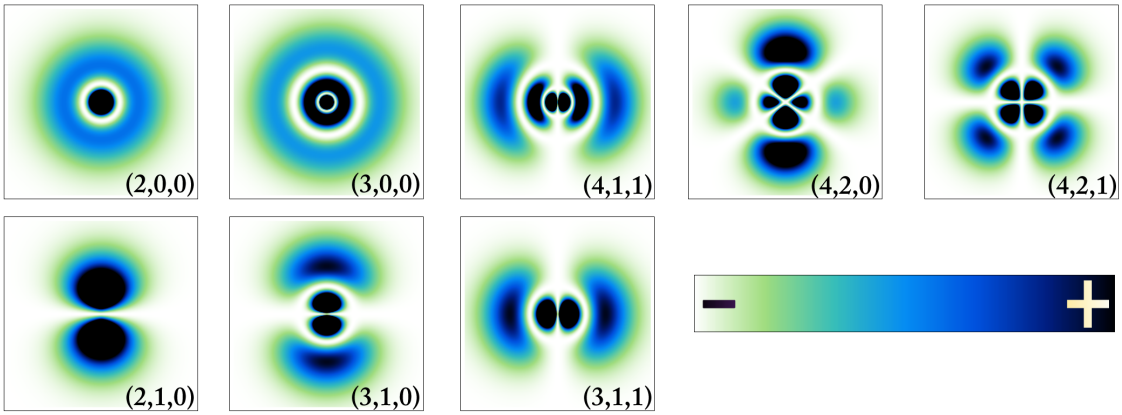

Figure 5: Probability density plots for some eigen-states of the hydrogen atom. This illustrates quantum delocalization and the wave-particle duality. The numbers (n, ℓ, m_ℓ) in the corners are used to label quantum states. A white color represents a null probability of presence and a dark blue color a high probability of presence. Only vertical plane cuts are shown since there is no dependence on longitude angle.

Ultra-cold gases and Bose-Einstein condensation

While quantum mechanics must be used for the motion of a single atom, it is not generally needed for a gas of $N \gg 1$ particles. The macroscopic properties of the gas are the result of a thermal averaging hiding any quantum behavior of atoms. Hence, physicists like Boyle, Marriott, Joule, Kelvin, Gay-Lussac, Van der Waals... never observed any non-classical (quantum) properties when they studied all kind of gases. For example, at the end of the 17^{th} century, Boyle and Marriott confirmed experimentally that at low enough pressure, all gases behave like ideal gases.

The story of quantum gases started two and half centuries later in 1925, as Einstein, helped by the work of Bose, understood that the ideal gas model fails at low temperatures because of the indistinguishable nature of particles. Indeed, quantum physics predicts that the probability of M identical particles with an integer spin (bosons) to gather in the same quantum state is amplified by a tremendous factor $M!$ compared to the results if they were distinguishable. This phenomenon is known as bosonic amplification. Atoms of ^{39}K and all other alkali with an odd number of nucleons are bosons.

At low temperature T, Boltzmann occupation probability $\frac{1}{Z}\exp\left(-E/k_BT\right)$ for a quantum state of energy E stipulates that particles are more likely in the state of minimal energy (with zero kinetic energy, $\vec{k} = 0$). If the particles were distinguishable in a cube box of size L, this ground state would contain half of the N particles only at extremely low temperatures $T_d \simeq \frac{4\pi^2\hbar^2}{2mL^2k_B}$, numerically equal to 0.6 nK for ^{39}K with $L = 20\,\mu$m. Hopefully, with bosonic amplification, the accumulation in the ground state is boosted and the critical temperature is multiplied by a factor $0.16 \times N^{2/3}$. Numerically, for $N = 10^5$ potassium atoms, this so-called condensation temperature is $T_c = 350$ nK. The accumulation of particle in the same quantum state is called Bose-Einstein condensation. It remained a theoretical prediction until the 90s when Cornell & Wieman and Ketterle observed it in dilute gases of alkali atoms. They received the Nobel prize of Physics in 2001 for their work. Finally, at temperature below a tenth of T_c, the gas is almost fully condensed and it acquires macroscopic quantum properties.

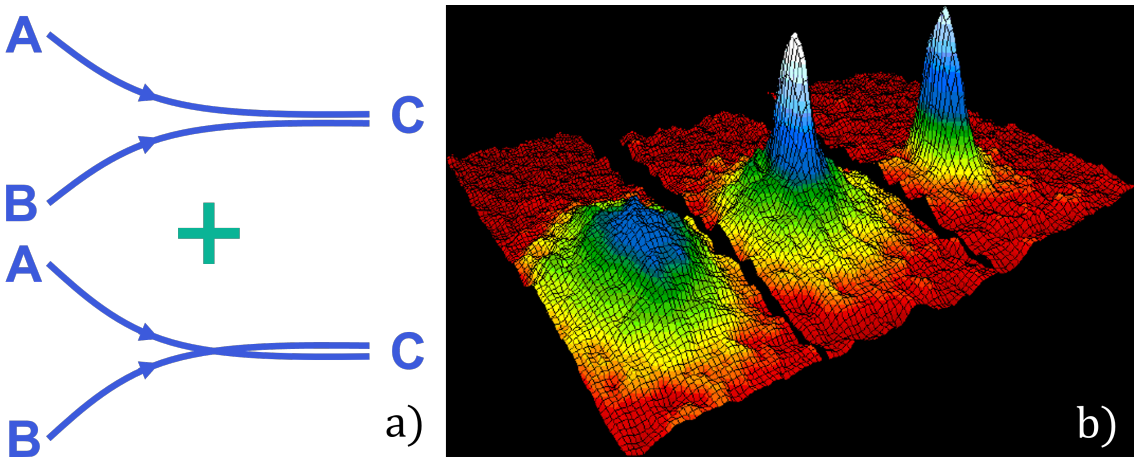

Figure 6: a) Equivalence of two processes for two identical particles going from quantum states A and B to both in quantum state C. This explains the bosonic amplification of $2! = 2$ for 2 particles. b) Momentum distribution in false colors. The famous experimental proof of Bose-Einstein condensation published in 1995 by Cornell's team at JILA.

Interactions in neutral dilute gases

The role of interaction was omitted in the above discussion even though they are very important for thermalization of the gas during the cooling. Hopefully, interactions do not change radically the physical discussion on Bose-Einstein condensation for neutral dilute gases. The reason is because the interaction potential between neutral atoms decreases very fast with the distance $E_{int}(r) \propto r^{-6}$ and atoms are very far from each other most of the time. In other words, the mean free path is of the order of the macroscopic size of the gas. As a consequence, collisions involving more than two particles are very unlikely and they don't affect the properties of the gas. The macroscopic effects of any isotropic, weak, short-range, two-body interactions depend on a single number in $\mathrm{J} \cdot \mathrm{m}^3$, usually noted g for a quantum gas (and noted a for a Van der Waals gas). The contribution of such interactions to the free energy of a condensed gas of N particle in a large box of volume V is simply $g\frac{N^2}{2V}$ which is as expected an extensive quantity and is proportional to the number of pairs of particles in the gas $N(N-1)/2 \sim N^2/2$.

Mean-field approximation and beyond

The effects of interaction can also be understood with the mean-field approximation. All atoms are assumed to be in the same quantum state which is described by a quantum wave-function φ. This wave-function obeys a modified Schrödinger equation, Gross-Pitaevskii equation, with a non-linear term $g|\varphi|^2\varphi$ representing two-body contact interactions. In many cases and thanks to bosonic amplification, this approximation is more than enough to explain all physical phenomena happening in a quantum gas. However, in this manuscript, we will have to use a more complex theoretical description: the beyond-mean-field approximation which is equivalent to allowing correlations between pairs of particles (figure 7).

Under the mean-field approximation, the properties of ultra-cold pure gases are very simple because of the single parameter g. They are far from displaying any fantastic complex order, hidden symmetries, fractals, scale invariance, chaotic dynamics... as could in theory happen in systems with a lot of degree of freedom (N-body problem). This is the price to pay for weak interactions. The interactions cannot be strengthened with an increase of the density because ultra-cold alkali gases are only meta-stable. They will quickly form a solid if the density becomes larger than typically $10^{21}\,\mathrm{m}^{-3}$. In the field of quantum gases, many different perspectives are currently being explored to reach regimes with more complex dynamics or equation of state, for example: dipole interactions, latices, reduced dimensions, topological order, mixtures, external driving, disordered potentials...

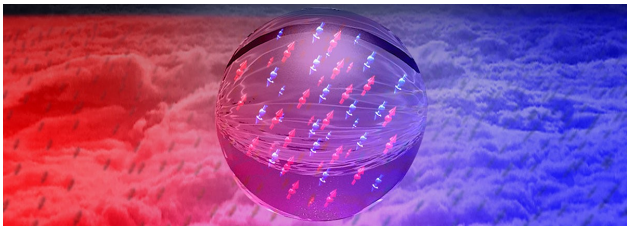

Figure 7: Artistic view of a quantum droplet, a spin mixture in which beyond-mean-field effects play a dominant role in the equation of state. credit: ICFO Barcelona

Radio frequency (RF) dressing of atoms and spin mixtures

The concept of an atom dressed by an electromagnetic field was first introduced in 1969 by Cohen Tannoudji and his student Serge Haroche [1]. They were separately awarded the Nobel prize in physics (1997, 2012) for their later discoveries, a lot more sensational, on interactions between light and matter.

An atom is said to be dressed by an electromagnetic field when the system of the two can be considered as a single quantum object. In this manuscript, the dressing field is a magnetic field oscillating at a frequency ω of the order of 40 MHz belonging to the radio-frequency domain. It couples resonantly and coherently two internal states $|1\rangle$ and $|2\rangle$ of the bare atom. The dressed atom has also two quantum levels noted $|+\rangle$ and $|-\rangle$. They are both quantum superpositions of the states $|1\rangle$ and $|2\rangle$. Their difference in energy no longer depends on the energies of the two bare state E_1, E_2 but rather on the strength of the coupling field Ω and on its frequency detuning $\delta = \omega - (E_2 - E_1)/\hbar$. An atom in state $|-\rangle$ is at the same time in state $|1\rangle$ and state $|2\rangle$.

As long as the RF field is present and if atoms of the gas are in the $|-\rangle$ dressed state, the gas is said to be a coherent spin mixture. In comparison, in an incoherent mixture atoms are either in state $|1\rangle$ or in state $|2\rangle$ and they cannot change state. We call it a spin mixture by analogy between two-level systems and spin 1/2. In this manuscript, we show that coherent mixtures have novel properties compared to incoherent mixtures.

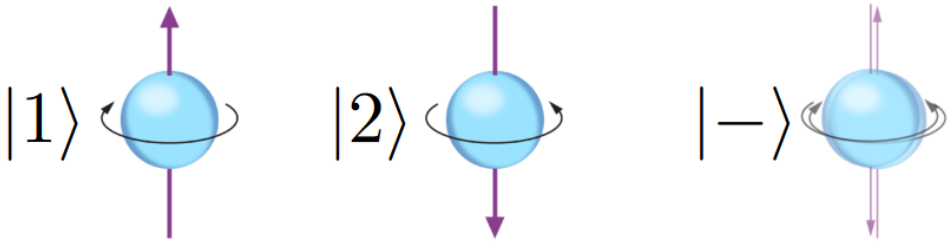

Figure 8: Artistic view of the quantum superposition happening in state $|-\rangle$

Outline of this manuscript

My doctoral work, in the potassium ^{39}K team, fits in the general topic of quantum gases with tunable interactions. I joined the team in September 2020, directly as a phD student, and after passing the agrégation de physique exam in July 2020. During my first year, the team planned to study incoherent spin mixtures but was surprised by the novel properties of coherent mixtures. This lead us to a focus on beyond-mean-field effects in coherent mixtures [2]. Followed a year later by the experimental study of mean-field three-body effect [3], still in coherent mixtures. My third doctoral year was devoted to the implementation of new features on the experiment and to a theoretical work on perspectives.
The manuscript is organized in six chapters that I suggest to read in order, except for chapter 2 which can be read independently.

Chapter 1: one-body and two-body physics of ultra-cold gases

The general framework of the manuscript is given in this chapter. After presenting the treatment of interactions imposed by quantum mechanics, we derive the condition of stability of condensates and mixture of condensates. We then go back to single atom physics and present how the RF-dressing is effectively realised. The last section begins the study of elastic and inelastic interactions between two dressed atoms.

Chapter 2: The ^{39}K experiment : maintenance and improvements

This chapter is dedicated to the experimental setup. We briefly present the cooling sequence used to make condensates of potassium ^{39}K. The second part is on the observation of imperfect RF transfers during the sequence and a quick presentation of two experimental parameters influencing this phenomenon. Thirdly, we explain how a new box-trapping device was added to the experiment and characterised. It works with a digital micromirror device (DMD) and a green LASER (blue detuned). Finally, the principle and the first imperfect results of a new absorption imaging setup are given.

Chapter 3: Beyond-mean-field energy in ideal RF-dressed ^{39}K BEC

The third chapter presents our study in collaboration with D.S. Petrov and A. Recati on beyond-mean-field effects in RF-dressed condensates [2]. The theoretical formulas for the Bogoliubov spectrum are presented. They lead to a mathematical expression for the BMF energy. The experiment consisted in the measurement of the size of the condensate after a long one-dimensional time of flight. The results quantitatively agree with an expansion driven by the repulsive BMF energy and depending on the Rabi frequency Ω.

Chapter 4: Mean-field three-body interactions in RF-dressed ^{39}K BEC

Chapter 4 presents an intuitive mean-field effect giving rise to an effective three body attractive interaction, coexisting with a conventional two-body interaction. After a physical interpretation of the phenomenon, we derive the formula for the strength of the effective three-body interaction. We were able to confirm this formula with two sets of experiments.

One on frequency measurements of breathing mode and the other on three-body induced collapses of the RF-dressed condensate. A major results is the independent tunability of two-body and three-body interaction strengths.

Chapter 5: Behavior of the RF-dressed BEC at small Rabi coupling

Chapter 5 study the validity of previous results - chapters 3 and 4 - at small Rabi coupling. We start with a numerical exact solution for the internal state of the condensate in a regime where interactions are stronger than the Rabi coupling. The main concerns is the validity of the mean-field coherent state ansatz. Numerical results suggest to introduce an artificial dimension and find the internal state of the condensate with an effective Schrödinger equation. We then pursue on the expressions of the MF energy at all values of Ω. The last section focuses on the modification of BMF energy with Ω, specifically in the context of quantum droplets. After explaining the physical origin of such droplets, we study the dependence of their density with Ω.

Chapter 6: One-dimensional dynamics and density excitations

Chapter 6 is prospective. We begin with a thought experiment, which serves as a pretext to introduce a quantum perturbation approach. It legitimates the real nature of the three-body MF interaction and its coexistence with the BMF renormalization of two-body interaction. In the second part, we use this unified result to predict what should be the hydrodynamic behavior of the RF-dressed condensate in a specific case. If the total two-body interaction strength is zero and in one-dimensional geometry, the dynamics is driven by three-body attractive interactions. The equations are scale invariant and a peculiar modulation instability should appear from a uniform density profile.

Chapter 1

1. Framework : one-body and two-body physics of ultra-cold gases

The goal of this chapter is to present elementary processes framing our study. We will not discuss the phenomenon of Bose-Einstein condensation (BEC), a collective effect, since it is done in introduction and in many textbooks [4][5]. Instead, we focus on the one-body or two-body physics of quantum gases, either at the atomic scale or at the macroscopic mean-field scale. Firstly, a broad picture on the nature and origin of interactions in a neutral gas will be given. Then we will remind the reader the suitable formalism to describe an atom coherently driven by a radio-frequency (RF) electromagnetic field. In a third part, we will review the conditions of stability of a pure BEC and of binary mixtures of BEC. Finally, we derive the expression of the elastic and inelastic two-body interaction strength between two RF-dressed atoms colliding at low energy.

1.1 Interactions between atoms in ultra-cold ^{39}K gas

1.1.1 Interaction between neutral atoms

The properties of a non-ionised dilute fluid can be understood from the concept of elementary entities - atoms or molecules - far from each others most of the time and that weakly interact at long range. This allows us to give a theoretical meaning to an "isolated particle of the gas" and define internal/external degrees of freedom of the so-called particle. For an atom, external degrees of freedom are the coordinates of the center of mass and internal degrees of freedom are the quantum states of the electrons and of the nucleus. At ambient temperature and below, nuclear physics can be forgotten so the nucleus total spin norm is fixed. Likewise, core electrons are frozen in their respective quantum states (orbital and spin). Finally, the internal state of an atom simply consists in the assignment of shell electrons on discrete quantum levels. For a ^{39}K potassium atom, there is only one shell electron and the nuclear spin is $I = 3/2$. Energy levels of this electron gives the fine and hyperfine structure of the atom. Each of them is defined by the usual five quantum numbers (n, l, j, F, m_F) (in analogy with Hydrogen see [6] chap. XII). Figure 1.1 shows the

first available energy levels of the single shell electron of potassium ^{39}K and the splitting of degeneracy by Zeeman effect in the presence of an external magnetic field.

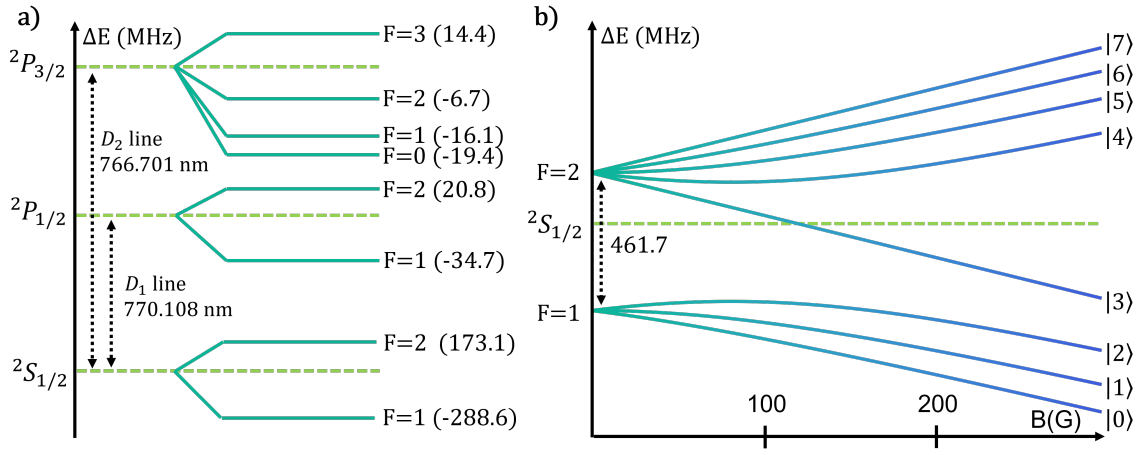

Figure 1.1: a) Fine and hyperfine structure of potassium ^{39}K b) splitting of degeneracy of lowest hyperfine manifolds in presence of an external magnetic field due to Zeeman effect. (adapted from [7])

For practical purposes, in all this manuscript, we will give short names to all 8 levels of the two lowest hyperfine manifold for which the three first quantum numbers are given by $(n, l, j) = (4, 0, 1/2)$. State $|0\rangle$ will refer to the state tending to $|F = 1, m_F = 1\rangle$ at low magnetic fields, respectively $|1\rangle$ tends to to $|F = 1, m_F = 0\rangle$ and $|2\rangle$ tends to $|F = 1, m_F = -1\rangle$. $|4\rangle$ to $|7\rangle$ are defined likewise by figure 1.1. We can also use Clebsch-Gordon coefficients to specify these states in terms of the nuclear spin and electron spin projection $|m_I, m_S\rangle$:

$$\begin{array}{lcl} |0\rangle \underset{B\to 0}{\longrightarrow} |F=1, m_F=+1\rangle &=& \frac{\sqrt{3}}{2}\left|+\frac{3}{2},-\frac{1}{2}\right\rangle - \frac{1}{2}\left|+\frac{1}{2},+\frac{1}{2}\right\rangle \\ |1\rangle \underset{B\to 0}{\longrightarrow} |F=1, m_F=\ 0\rangle &=& \frac{1}{\sqrt{2}}\left|+\frac{1}{2},-\frac{1}{2}\right\rangle - \frac{1}{\sqrt{2}}\left|-\frac{1}{2},+\frac{1}{2}\right\rangle \\ |2\rangle \underset{B\to 0}{\longrightarrow} |F=1, m_F=-1\rangle &=& \frac{1}{2}\left|-\frac{1}{2},-\frac{1}{2}\right\rangle - \frac{\sqrt{3}}{2}\left|-\frac{3}{2},+\frac{1}{2}\right\rangle \end{array} \quad (1.1)$$

At non-zero magnetic fields, quantum number F is no longer a good quantum number and this is why we define states $|i\rangle_{0\leq i\leq 7}$ by continuity. We shall discuss Zeeman effect more precisely in section 1.3.

Let's now recall the form of interactions between two atoms in any given internal states among the 8 hyperfine levels in $^2S_{1/2}$ displayed in figure 1.1 b).

Van der Waals interactions:

At large distance, the dominant effect is a dipole-dipole interaction. The electric dipole of an atom is zero on average, because the shell electron is in a spherical s orbital. Yet two nearby atoms are still able to mutually polarize electrically each other through quantum dispersion. The resulting attractive interaction potential is the well-known Van der Waals potential of London dispersion type :

$$U_{vdW} = -\frac{C_6}{r^6} \tag{1.2}$$

Where the coefficient C_6 is proportional to the square of the static electric polarizability α of the atom. For potassium ^{39}K, it is equal to $C_6 = 3925 E_h\, a_0^6$, with E_h being 1 Hartree and a_0 the Bohr radius. As the distance between atoms gets smaller, one needs to take into account higher orders of the multipolar electric interaction between atoms. They manifest by the addition of terms, still explained by quantum dispersion, $-\frac{C_8}{r^8}$ (dipole-quadrupole) and $-\frac{C_{10}}{r^{10}}$ (quadrupole-quadrupole).

Magnetic interactions:

In an external magnetic field, the magnetic dipole moment of an atom in an external magnetic field is never zero. We must therefore also add a magnetic dipole-dipole interaction potential between the two atoms (labelled by A and B) :

$$U_{mag} = \frac{\mu_0}{4\pi} \frac{\vec{m}_A \cdot \vec{m}_B}{r_{AB}^3} \tag{1.3}$$

However, in the case of potassium, we can neglect this weak magnetic interaction. For two atoms at a distance of the order of the chemical bond length, $r_1(K_2) = 406\,\text{pm}$, the magnetic dipole-dipole potential is of the order of $3\,\mu$eV while the electric interaction energy is typically a few electron-Volts as for chemical bonds. On the other hand, the magnetic interaction is a short-range potential (defined in the next subsection). Its range b_{mag} is a few times smaller than the range of the Van der Waals interactions b_{vdW}. Therefore, we can neglect magnetic interactions with respect to electric ones at all distances.

$$\begin{cases} b_{mag} &= \frac{m\mu_0\mu_B^2}{\pi\hbar^2} &= 0.2\,\text{nm} \\ b_{vdW} &= \left(\frac{mC_6}{\hbar^2}\right)^{1/4} &= 7\,\text{nm} \end{cases} \tag{1.4}$$

.

Chemical bonding electric potentials:

At small inter-particle distances, the nature of the electric interaction changes. There is no reason for the two shell electrons to remain only around their original nucleus. Therefore, they delocalize over the two atoms. This process is best described by the theory of linear combination of atomic orbital (LCAO) introduced by Heitler and London in 1927 and later summarized by Slater in 1968 [8] and Demtroder in 2010 [9]. In good approximation, two atomic s orbitals are combined to give the standard σ and σ^* molecular orbitals. Under the

Born-Oppenheimer approximation, during the collision of two atoms, the effective electric potential between them is simply the energy of the orbital configuration with respect to the distance between nuclei.
This orbital configuration depends of the spin state of the pair of shell electron because of Pauli exclusion principle. In an anti-symmetric spin state (singlet), both electrons have to be in the σ orbital (chemical bond). In a symmetric spin state (triplet), the two electrons have to be in the anti-bonding orbital configuration (one in the σ orbital and the other in the σ^* orbital). The effective potential on the atoms can be computed analytically with the LCAO theory (figure 1.2).

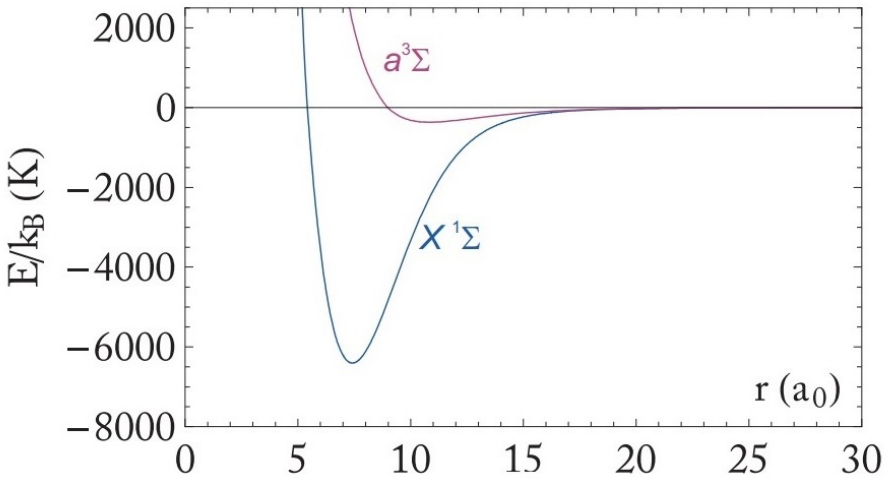

Figure 1.2: Born-Oppenheimer potentials for the singlet ($X^1\Sigma$) and triplet ($a^3\Sigma$) spin channel in Potassium ^{39}K. At large distances the two potentials both coincide with Van der Waals interactions of equation 1.2. Plot taken from [7] based on theoretical fit and computation performed by [10][11].

However, because of entanglement with nuclear spins, the spin state of the pair of electrons does not have a well defined parity (see Clebsch-Gordon coefficients in equation 1.1). This complicates the resolution of the scattering problem on the technical point of view. It can still be achieved straightforwardly by solving a Schrödinger equation with multiple coupled channels. Each channel having a well defined parity of the electron pair spins, with either a triplet or singlet effective potential on the atoms, and the coupling between these channels being simply the hyperfine Hamiltonians of both atoms. We shall come back to this subtlety in subsection 1.2 when discussing inelastic processes.

If the scattering is elastic, the two atoms get out of the interaction zone with the same internal state they came in and **we can model the collision with an effective spherically symetric scattering potential $V(r)$ that would give the same scattering properties**.

1.1.2 Quantum universality of two-body short-range interactions at low energies

In the classical mechanics collision of two atoms with a spherically symmetric, or Newtonian, interaction potential $V(r)$, it is well-known that the angular momentum with respect to their center of mass is conserved [12]. The quantum mechanical treatment adds the constant $\hbar$ which quantifies the possible values of angular momentum norm and projection. Thus, the effective potential barrier on the radial motion becomes $\hbar^2 l(l+1)/(mr^2)$ with $l \in \mathbb{N}$. Writing the radial part of the relative wave-function as $\phi(r) = u(r)/r$, the effective uni-dimensional Schrödinger equation on $u(r)$ takes the form :

$$-\frac{\hbar^2}{m}\frac{d^2u}{dr^2}(r) + \left(\frac{\hbar^2 l(l+1)}{mr^2} + V(r)\right) u(r) = E\,u(r) = \frac{\hbar^2 k^2}{m}\,u(r) \tag{1.5}$$

With the additional condition $u(0) = 0$ [1]. Scaling analysis tells us that the first left term, which comes from the radial part of the Laplacian, varies as the inverse square of a length. Because the Van der Waals potential, and thereby $V(r)$, decreases faster than $1/r^2$ at large distances, it is called a short-range potential. For large r, the radial equation then becomes equivalent to the free particle one with $V(r) = 0$. The distance above which this approximation is true can be found by dimensional analysis. Equalizing $\hbar^2/(mb^2)$ and C_6/b^6, we find the range b_{vdW} of the Van der Waals potential.

$$b_{vdW} = \left(\frac{mC_6}{\hbar^2}\right)^{1/4} = 7\,\text{nm} \tag{1.6}$$

The interaction potential $V(r)$ has an effect only in the sphere of radius b_{vdW}. This volume is definitely not accessible for $l \geq 1$ and small energies $E = \hbar^2 k^2/m$ because of the effective repulsive potential well $\hbar^2 l(l+1)/(mr^2)$. More physically, if the two colliding particles have a non zero relative angular momentum and a small incoming kinetic energy, in their center of mass frame, it means that the lever arm of their incoming velocities is large.Thus, classically, their trajectories pass very far from each others and they don't interact with each other. Consequently, any low energy collision manifests itself only in an s-wave scattering channel for which $l = 0$. The low-energy criterion is, for $l = 1$, $E \ll 2\hbar^2/mb_{vdW}^2$ which is numerically equal to to $h \times 10\,\text{MHz}$ or to $k_B \times 500\,\mu\text{K}$. We shall assume it is verified from now on.

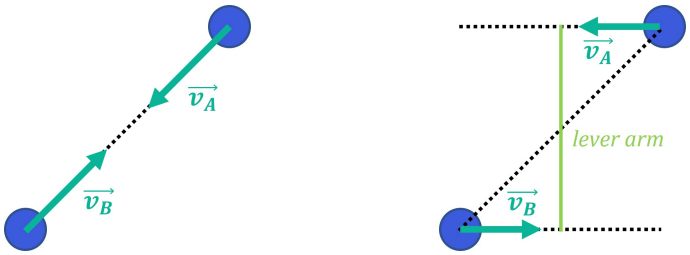

Figure 1.3: Semi-classical picture of two colliding atoms in their center of mass frame. *left*: the angular momentum is zero. *right*: the angular momentum is a non-zero multiple of $\hbar$ and the lever arm is large because the velocities are small, consequently the two atoms will pass far from each other.

[1] This condition is needed to recover the Schrödinger equation on $\phi(r) = u(r)/r$ in the whole space since a singularity could happen at the origin $\Delta\left(\frac{u(r)}{r}\right) = \frac{\Delta u(r)}{r} - 4\pi\delta(\vec{r})u(r)$

We can deduce more from the finite range nature of the potential $V(r)$. Considering from now on, only the physically relevant $l = 0$ scattering channel, equation 1.5 on the radial wave-function $u(r)$, becomes at large r :

$$-\frac{d^2u}{dr^2}(r) = k^2\, u(r) \tag{1.7}$$

It has free-wave solutions of the form (up to a global phase and arbitrary normalisation):

$$u(r) = \sin\left(kr + \delta\right) = \frac{e^{ikr+i\delta} - e^{-ikr-i\delta}}{2i} \tag{1.8}$$

This corresponds to the sum of a spherically symmetric incoming wave towards the interaction zone ($r \leq b_{vdW}$) and of a spherically symmetric outgoing wave with the same energy but with a phase shift of 2δ. The conservation of probability imposes the coefficients in front of these two contributions to be equal, therefore leaving only the phase δ as a physically interesting quantity. The minus sign in front of the incoming wave is a matter of convention so that in the absence of any scattering potential, $V(r) \equiv 0$, the phase δ would be zero. Indeed, in this case the solution given by equation 1.8 remains true as $r \to 0$ and the minus sign comes from the condition $u(0) = 0$. The phase δ can be restricted to $\left[-\frac{\pi}{2}, \frac{\pi}{2}\right]$ and it depends both on the form of $V(r)$ and on the energy E of the pair of particles.

If the energy $E = \hbar^2k^2/m$ is small, we can divide the space in three depending on the value of r. The interaction zone ($r < b_{vdW}$), the linear zone ($b_{vdW} < r < 1/k$); and the free oscillations zone ($r > 1/k$). In the linear zone, the solution 1.8 is equivalent to :

$$\begin{aligned} u(r) &\simeq \sin(\delta) + kr\cos(\delta) \\ u(r) &\underset{\sim}{\propto} \tan(\delta)/k + r \end{aligned} \tag{1.9}$$

The linear zone exists only if the energy E is smaller than $\hbar^2/mb^2$ which is the s-wave criterion we already assumed to be true.

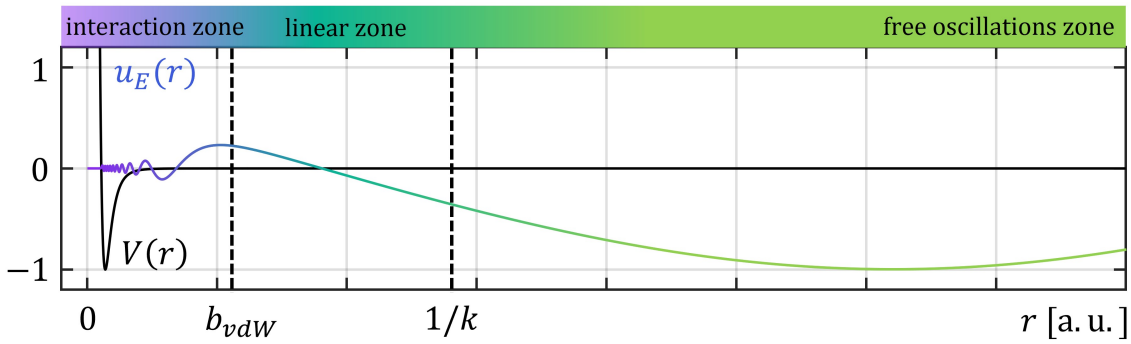

Figure 1.4: Numerical solution of a typical low-energy solution of equation 1.5 for $l = 0$ and a simple toy-model for potential $V(r)$ with a Van der Waals tail C_6/r^6, a Coulomb repulsive core and a substantial depth. See text for the definition of $u_E(r)$. For realistic experimental parameters, the energy E will be much smaller than in this simulation. tipically, $kb_{vdW} \leq 10^{-3}$ thus enlarging tremendously the linear zone.

On the other hand, in the interaction zone, the effect of potential $V(r)$ is strong, the characteristic energy scale is the electron-Volt as shown on figure 1.2. At low energies $E \ll V(r)$, the radial dynamical equation 1.5 becomes :

$$-\frac{\hbar^2}{m}\frac{d^2u}{dr^2}(r) + V(r)\,u(r) = 0 \tag{1.10}$$

Let $u_E(r)$ be the solution of equation 1.5 with energy $E = \hbar^2k^2/m$, tending to zero at the origin and normalized to be asymptotically equal to 1.8 with a yet unknown δ. According to equation 1.10, the shape of $u_E(r)$ (up to the normalisation factor) is independent of E in the interaction zone. In particular, at the edge with the linear zone, u_E and $\frac{du_E}{dr}$ are also independent of E. Matching these two numbers with equation 1.9, we conclude that $\tan(\delta)/k$ is independent of E in the limit of low energies ($k \to 0$). This discussion is only approximately rigorous because the transition between the interaction zone and the linear zone is progressive. The exact value of $\tan(\delta)/k$ may be found with a very mathematical approach, as presented by Messiah [13]. He proved that for reasonably well-behaving short-range $V(r)$:

$$\frac{\tan(\delta)}{k} \sim \int_0^\infty -\sin(kr)\frac{V(r)}{E}u_E(r)dr \underset{\substack{k\to0\\E\to0}}{\longrightarrow} -a \tag{1.11}$$

This limit, regardless of how theoreticians are able to compute it, defines the scattering length a which can be either positive, negative, null or infinite. The properties of a low-energy two-body collision with a short range potential $V(r)$ may be fully encased in the value of the scattering length if the next order correction to the phase shift δ with k is negligible [13][14]:

$$\frac{\tan(\delta)}{k} \underset{k\to0}{\sim} -a - k^2\frac{a^2b_{eff}}{2} \tag{1.12}$$

The effective range $|b_{eff}|$ is of the order of b_{vdW}[15], which is the only length-scale given by dimensional analysis. It is a relevant parameter only if $1/a$ is very small compared to k^2b_{eff}. This will not be the case for our potassium ^{39}K experiment so we will focus on the scattering length a and replace the true potential $V(r)$ with a zero-range, or contact, pseudo-potential V_{pp} yielding the same scattering length at low energy :

$$V_{pp}(\phi)(r) = g\,\delta(\vec{r})\,\partial_r\left(r\phi(r)\right) = g\,\delta(\vec{r})\,u'(r) \tag{1.13}$$

With $\delta(\vec{r})$ the Dirac distribution and $g = 4\pi\hbar^2a/m$ the interaction strength. For this pseudo-potential, the relation $\tan\delta/k = -a$ is actually true for any wavevector k. But a momentum cutoff Λ must be imposed on the maximum authorised value of k to be in accordance with equation 1.12, definitely false at high energies. With this pseudo-potential, the size of the interaction zone effectively vanish $b_{eff} = 0$ and the radial wave-function of any pair of particle must behave with the following asymptotic behavior, also called Bethe-Peierls boundary conditions [16][13]:

$$\phi(r) = \frac{u(r)}{r} \underset{r\to0}{\propto} 1 - \frac{a}{r} \tag{1.14}$$

When studying the macroscopic dynamics of a BEC with a wave-function $\psi(r)$, smoothly varying at the macroscopic scale, the pseudo-potential V_{pp} can be replaced by simpler contact potential $g\delta(\vec{r})$ thanks to the regularity of ψ. The effective Hamiltonian describing two-body contact interactions then writes:

$$H_{2b} = \frac{g}{2}\iint \hat{\psi}^\dagger(\vec{r}_1)\hat{\psi}^\dagger(\vec{r}_2)\hat{\psi}(\vec{r}_2)\hat{\psi}(\vec{r}_1)\ \delta(\vec{r}_2-\vec{r}_1)\, d^3\vec{r}_1 d^3\vec{r}_2 \tag{1.15}$$

Finally, it is also common to define the s-wave scattering amplitude $f_0(k)$ linked to the irreversible quantum scattering (in the sense of the Fermi golden rule) of two low-energy atoms from a state of well defined relative momentum $\vec{k}_i = 2k_i\vec{u}_z$ to all the states with a relative momentum $\vec{k}_f$ on a sphere of radius $2k_i = ||\vec{k}_f||$.

$$f_0(k) = \frac{e^{2i\delta}-1}{2ik} \qquad \Leftrightarrow \qquad \frac{1}{f_0(k)} = k\cot(\delta) - ik \tag{1.16}$$

The scattering cross section of such irreversible process is $\frac{\sigma_0}{4\pi} = |f_0(k)|^2 = \frac{1}{k^2\cot(\delta)^2+k^2}$.

1.1.3 Feshbach resonances

In the above discussion, it remains unclear what is going to be the value of the scattering length a in our experiments with Potassium ^{39}K. Logically, a must depend on the shape potential $V(r)$. One can indeed show that if the depth of potential $V(r)$ is continuously varied, by multiplying it by $\lambda > 0$ to get $V(r) \to \lambda V(r)$, the scattering length will also vary continuously - except at some discrete values λ_c , at which a new bound state of energy $E = 0$ appears in the potential $\lambda_c V(r)$. At these points, the scattering diverges to $-\infty$ and reappears for $\lambda > \lambda_c$ around $+\infty$. This phenomenon causes no problem in the physics of the two-body collision because the phase-shift δ remains well defined for every λ according to formula 1.12.

In our case, we should remember that the potential $V(r)$ is not well defined because the scattering process actually involves multiple coupled channels with different parity for the electron spin pair. Yet, when we vary the external magnetic field, we change the interplay between these different channels and the energy difference between them. Thus modifying the effective potential $V(r)$. At some critical values B_c of magnetic field, the scattering length will also diverge according to a process called Feshbach resonance. For magnetic field close to the resonance, the scaling is :

$$a = a_{bg}\left(1 - \frac{\Delta B}{B - B_c}\right) \tag{1.17}$$

The parameter ΔB is the width of the resonance, it can be either positive or negative, and a_{bg} is the background value of scattering length. It is negative, for all known resonances, in the case of potassium ^{39}K as can be seen on figure 1.5. The location of resonances depends on the considered states of the two atoms in the lowest hyperfine manifold, although they obey some universal behavior linked to the Feshbach resonance process. These resonances can be measured experimentally which allows theoreticians to precisely find the triplet and singlet potentials and finally compute a prediction for the scattering lengths at any magnetic field and for all internal states. In this thesis, we used numerical data from [10] and [11] which was the most precise predictions available. The scattering length between two atoms in states $|i\rangle$ and $|j\rangle$ is labeled $a_{ij} = a_{ji}$.

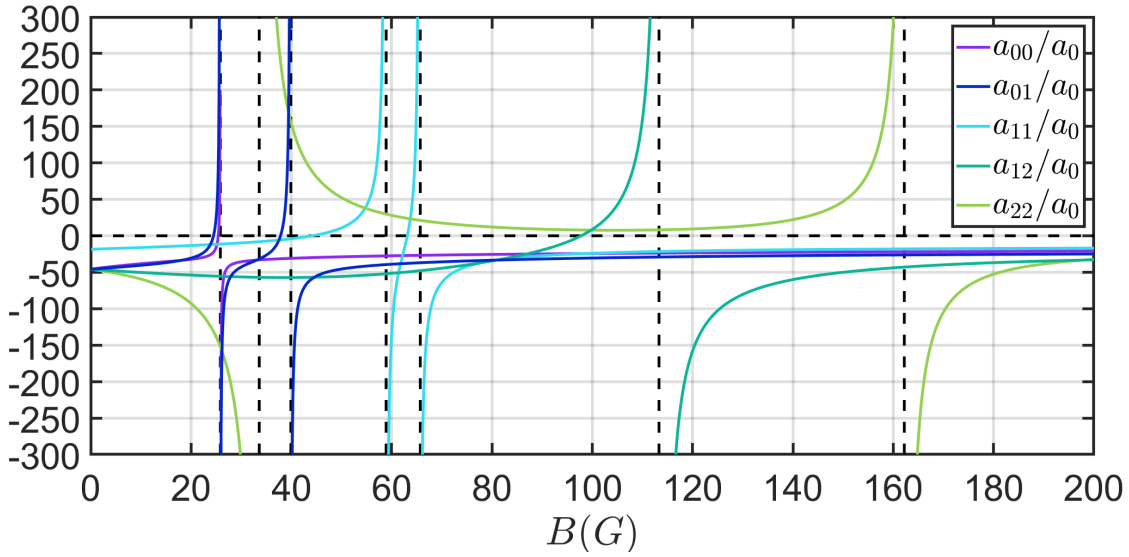

Figure 1.5: Intra-species a_{ii} and inter-species a_{ij} scattering lengths for two atoms with states in $|0\rangle$, $|1\rangle$ and $|2\rangle$ of ^{39}K with respect to magnetic field between 0 and 200 G.

1.2 Stability of a BEC and of a mixture of BEC

In this section, we recall a few results on the interplay between particle interactions in a BEC and its self-stability. Then we discuss the case of an uncoherent mixture of two BEC. Such mixture cannot exist for any values of the inter-species and intra-species scattering lengths.

1.2.1 Inelastic 2-body collisions

A collision is said to be elastic if the colliding atoms get out of the interaction zone in the same internal states they came in. Using common conservation laws, it is possible to prove that two body collision in some specific states are elastic. Oppositely, if we can find at least one state-changing scattering process fulfilling all conservation laws, then the collision is inelastic.
Let's consider a collision between two particles in some states $|i\rangle$ and $|j\rangle$ among the 8 states of the two lowest hyperfine manifold (shell electron in the $4s$ atomic orbital). Following notations of figure 1.1, we have i, j in $[\![0, 7]\!]$ and the internal state energy of state $|i\rangle$ which depends on the magnetic field, will be labeled ε_i.

Conservation laws:

- *Parity :*
  At low energy, the collision is a s-wave process. The space wave-function of the pair is symmetric with respect to their exchange. According to the spin-statistic theorem, the internal state of the pair must also be symmetric. In the other case, the two particle simply do not interact with each other. Therefore, the initial state of the effectively colliding pair can only be $|i,i\rangle$ if $i=j$ or $(|i,j\rangle + |j,i\rangle)/\sqrt{2}$ if $i \neq j$. We note these symmetrical state (i,j) to enclose both cases. There are 28 different pairs (i,j).
- *Pair of total angular momentum projections :*
  As we will explain in the next section 1.3, the total angular momentum projection m_F of any state $|i\rangle$ is independent of the external magnetic field and are simply given by:
  - $m_F = \ \ 2 : |7\rangle$
  - $m_F = \ \ 1 : |6\rangle$ and $|0\rangle$
  - $m_F = \ \ 0 : |5\rangle$ and $|1\rangle$
  - $m_F = -1 : |4\rangle$ and $|2\rangle$
  - $m_F = -2 : |3\rangle$

  The interaction potential does not act on nuclear and electron spins. So the final value of the pair of m_F must be conserved. For example, if the initial states is $(6,4)$, then the pair of m_F of the two atoms is equal to $\{1,-1\}$, and the final state can only be among in $(6,4),(6,2),(0,4),(0,2)$.
- *Energy :*
  The global conservation of energy, written between the initial states (i,j) and final states (m,n), reads :

$$\varepsilon_i + \varepsilon_j + \frac{\hbar^2 k_i^2}{m} = \varepsilon_m + \varepsilon_n + \frac{\hbar^2 k_f^2}{m} \tag{1.18}$$

  The initial kinetic energy $\hbar^2 k_i^2/m$ is negligible compared to any difference of internal state energies.

Selection rules and inelastic processes:

From these three conservation laws, we can assert the elasticity of low-energy collisions between two atoms in the lowest hyperfine manifold ($i,j \in [\![0,3]\!]$). The conservation of energy forbid the final state to be in the upper hyperfine manifold ($i,j \in [\![4,7]\!]$). Adding the conservation of the pair of angular momentum projections is enough to prove elasticity.

Inelastic collision may happen if at least one of the two atom is in the upper hyperfine manifold ($j \in [\![3,7]\!]$) and is not a stretched state ($|m_F| \neq 2$). It represents 18 of the 28 possible collisions, when at least i or j is in $\{4,5,6\}$. It is interesting to investigate the change of internal state during such inelastic collision because it will also manifest for collisions between two atoms in some RF-dressed states (1.4.2).

For example, let's consider the case of an initial state $(5,5)$. The selection rules forces the final state to be in $(5,5),(5,1),(1,1)$. Strictly speaking, the final state after the collision is a quantum sum of three entangled states where the radial wave-function of the pair depends on the internal state of the pair because of conservation of energy (equation 1.18). Let's give a qualitative picture on the physics at play by reasoning only on the internal state. At any magnetic field B, states $|1\rangle$ and $|5\rangle$ both have $m_F = 0$ as we will prove in section 1.3. Therefore, they are simply expressed as quantum sums of the two states $|m_I, m_s\rangle = \left|+\frac{1}{2}, -\frac{1}{2}\right\rangle$ and $|m_I, m_s\rangle = \left|-\frac{1}{2}, +\frac{1}{2}\right\rangle$. They are also normalised and orthogonal. The interaction potential is unable to flip a nuclear or electron spin because it only acts on the radial wave-function. But it may induce some relative phase shift between the two coefficients in front of $\left|+\frac{1}{2}, -\frac{1}{2}\right\rangle$ and $\left|-\frac{1}{2}, +\frac{1}{2}\right\rangle$. thus changing the state of the atom from $|5\rangle$ to a quantum sum of $|5\rangle$ and $|1\rangle$.

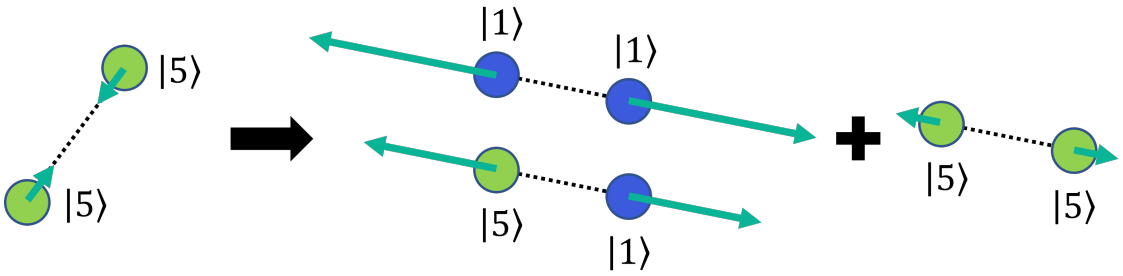

Figure 1.6: Schematic view of available final states in a two-body inelastic collision. The resolution of Schrödinger equation actually shows that the final state is a quantum superposition of all available outcomes in the s-wave approximation.

Finally, any inelastic collision detailed above release a large kinetic energy of the order of the hyperfine constant 460 MHz. The pair of atoms will then simply leave the external trap which typically has a depth under a few kHz. In other words, two-body inelastic collisions are synonym of two-body losses. In this thesis, we shall work on quantum gases of atoms in states $|0\rangle, |1\rangle$ or $|2\rangle$ for which two-body inelastic collisions are forbidden.

1.2.2 Inelastic 2+1-body recombinations

Until now, we left aside the possibility for three atoms to be together in a volume of b_{vdW}^3. In this case, the interaction potential between them is not the sum of three pair interactions. The presence of a third atom indeed modifies the static electric polarisability of the two others which in turn changes the strength of Van der Waals interactions. Nevertheless, the dilute nature of the gas implies that this scenario is very unlikely and should not rule the low energy dynamics of the gas (out of a Feschbach resonance). In other words, the modification of the macroscopic energy of the gas due to genuine three body effects is negligible compared to the one induced by two-body collisions.

This reasoning would be flawless if the two-body potential was itself not too strong. That is to say if we could compute the two-body scattering properties with the Born approximation. However, at short range, the two-body potential has a depth of a few electron-volts with several possible bound states corresponding to some diatomic molecular states. Some of them even have non-zero angular momentum l, allowing the molecule to turn around its center of mass. Consequently, a three-body interaction process can also

lead to the formation of a two-body molecule and a single particle, also called three-body recombination. The conservation of energy and momentum states that the molecule and the particle obtain an significant kinetic energy in the process with opposed momentum in the center of mass frame.

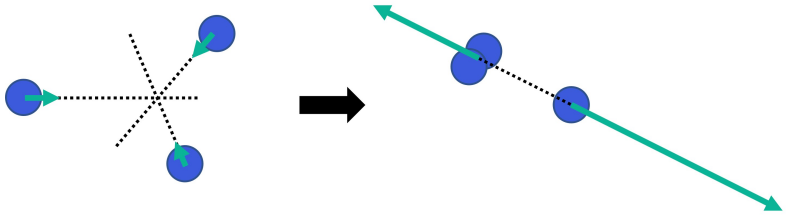

Figure 1.7: Schematic view of a three-body recombination

Once again, this process leads to the loss of the two-body molecule and of the third particle. When we use the contact potential $V_{contact}$, the existence of deep bound states is masked, but the loss process is effectively restored on the macroscopic dynamics by introducing an imaginary term in the many-body Hamiltonian of the gas :

$$\hat{H}_{3b\,rec} = -i\hbar\frac{K_3}{3}\int \hat{n}(r)^3 d^3r \tag{1.19}$$

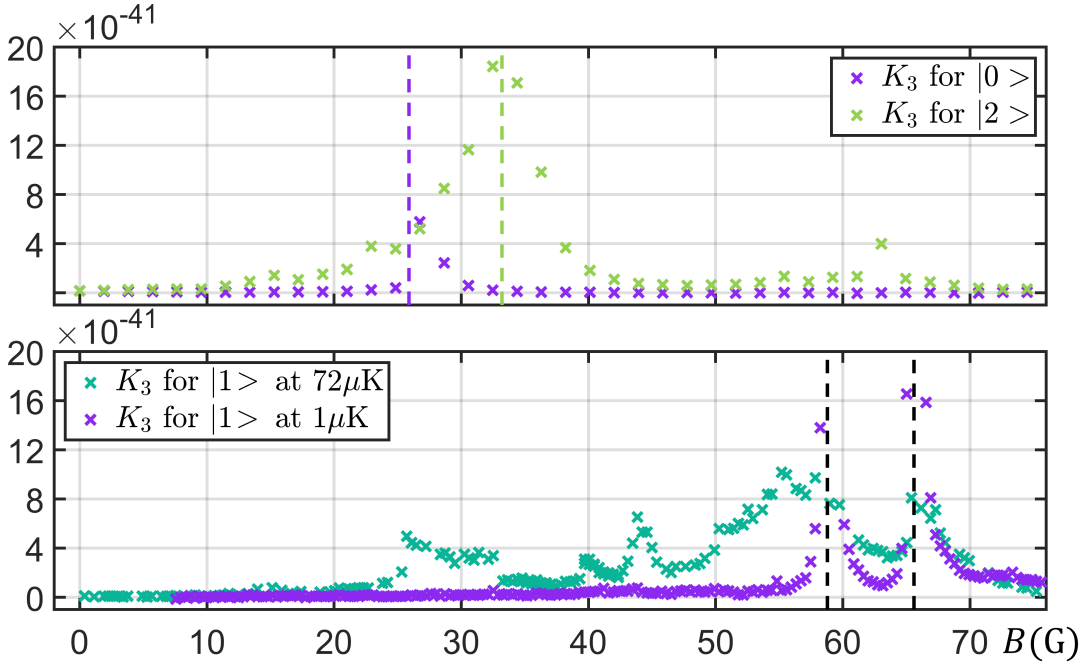

Figure 1.8: Experimental estimations of the K_3 loss coefficient for a thermal potassium gas in state $|2\rangle$ in an optical dipole trap with radial frequency 7.4 kHz and axial frequency 130 Hz. The initial number of atom was 6×10^6 and the temperature 72 μK. The number of atom was measured again after 300 ms to get an estimation of the loss coefficient K_3. Losses are increased around the Feshbach resonances. For state $|1\rangle$ at 72 μK we also observe losses far from resonances, not explained by s-wave physics.

The coefficient K_3 is expressed in $\mathrm{m}^6\,\mathrm{s}^{-1}$. Its typical value for potassium ^{39}K is around $10^{-40}\,\mathrm{m}^6\,\mathrm{s}^{-1}$ depending on internal state and magnetic field. It is commonly assumed, although experimentally verified[17], that coefficient K_3 can be expressed in term of the two-body scattering length a, thus suggesting that the underlying physical process is dominantly ruled by the sum of three two-body interactions. Dimensional analysis therefore imposes the scaling $K_3 \propto \hbar a^4/m$, also verified theoretically [18][19]. Three body losses become overwhelming around Feshbach resonances because $a \to \pm\infty$. According to the Ehrenfest theorem, the effective 3-body recombination hamiltonian leads to a decrease of the total number N of atoms in the BEC given by :

$$\left.\frac{dN}{dt}\right|_{3b\,rec} = -K_3 \int n^3(r)\, d^3r \tag{1.20}$$

Because this loss process is highly non-linear, it may be completely negligible or dynamically dominant depending on the density of the gas and on the timescale of observation, which is given by the typical energy of the other macroscopic process we study. In this thesis, we try to limit as much as possible the losses by working either on very dilute gases, not too close to Feshbach resonances or by looking at the behavior of the gas on relatively short timescales.

1.2.3 Macroscopic stability of a pure BEC

Now that we have pinpointed at and managed to fulfill the conditions of elasticity for two-body collision and meta-stability for 2+1 body processes, we may discuss the macroscopic stability of a pure quantum gas with contact interactions $g\delta(r)$. Under the standard mean-field approximation, all the particle of the gas are in the Bose-Einstein condensate with normalised wavefunction $\phi(r)$, trapped by a macroscopic external potential $U_{ext}(r)$, the energy of the system reads :

$$E = \int \frac{N\hbar^2}{2m}|\nabla\phi(r)|^2 + NU_{ext}(r)|\phi(r)|^2 + g\frac{N(N-1)}{2}|\phi(r)|^4\, d^3r \tag{1.21}$$

At equilibrium, the condensate wave-function $\phi(r)$ is given by the minimization of this energy functional. The external potential U_{ext} plays no role in the compression stability because we expect atoms to simply gather around its minima where it is approximately constant on a macroscopic scale. Meanwhile, the quantum kinetic energy - first term of the integral in equation 1.21 - tends to delocalize or spread the BEC wave-function $\phi(r)$ according to Heisenberg principle. It gives a positive quantum kinetic pressure. Finally, the last term in equation 1.21 - two-body mean-field interaction energy - will tend to focalize $\phi(r)$ in order to minimize the energy E if and only if g is negative.

Let's assume $g < 0$ and that the three-dimensional cloud has a typical size L. In order of magnitude $\phi \sim \frac{1}{\sqrt{L^3}}$ and $\nabla\phi \sim \frac{1}{L\sqrt{L^3}}$. After integration over the volume L^3, the quantum kinetic energy scales as $\frac{N\hbar^2}{2mL^2}$ and the interaction energy as $g\frac{N^2}{2L^3}$. Consequently, for small size L, the two-body interaction energy always dominates the quantum kinetic energy and the minimisation of energy E states that the size of the BEC must tend to 0. Such a process is called a **collapse** because as the density of the cloud increases, inelastic 2+1-body losses will eventually dominate and destroy the system.

The condition of compression stability can also be derived from thermodynamic properties of an homogeneous BEC of density $n = N/V$ in a box of volume V. In this case, the energy is $E = \frac{gNn}{2}$. From the thermodynamic identity at zero temperature, we find the pressure $P = -\frac{\partial E}{\partial V} = \frac{gn^2}{2}$ and the compressibility β :

$$\beta = \frac{1}{n}\frac{\partial n}{\partial P}\bigg|_N = \frac{1}{gn^2} \tag{1.22}$$

The compressibility must be positive for the system to be at pressure equilibrium with itself. Finally, a quantum gas at zero temperature and with two-body contact interactions has compression stability if and only if the interaction strength g is positive.

Internal states	B_c(G)	ΔB(G)	$a_{bg}(a_0)$
$\|0\rangle\|0\rangle$	25.9	-0.47	-33
	402.4	-52	-29
$\|1\rangle\|1\rangle$	58.8	-9.6	-18
	65.6	-7.9	-18
$\|2\rangle\|2\rangle$	33.6	55	-19
	162.3	-37	-19

Figure 1.9: First intra-species Feshbach resonances of potassium ^{39}K, taken from [10]

For potassium ^{39}K, this condition ($g > 0$) restricts severely the external magnetic fields and the internal states $|i\rangle$ of the atoms for which the gas is macroscopically (meta)stable. Indeed, the scattering lengths are, for potassium ^{39}K, mostly negative except around Feshbach resonances (see figure 1.5). But close to a resonance, the dominant effect of interactions is 2+1-body losses. The width of each resonance $|\Delta B|$ is a crucial parameter allowing (or not) the survival of a metastable BEC in some given internal state around the resonance. Using data from [10] summarized in table 1.9, we see that the first resonance around 25.9 G is very sharp, it cannot be used experimentally. The next one at 402.4 G is usable to condense in state $|0\rangle$ but it is not practical in the context of RF coherent coupling because of the relatively high magnetic field needed.

Finally, **we will always work with BEC in states $|1\rangle$ or $|2\rangle$. The widest and most practical window of stability for pure condensates in these states ($g_{ii} > 0$) is between** 33.6 G **(resonance of** g_{11}**) and** 58.8 G **(resonance of** g_{22}**)** as can be verified on figure 1.5.

1.2.4 Stability of an incoherent mixture of two BEC

An incoherent mixture of two BEC is simply described by the two wave-functions of the two condensates : ϕ_1 and ϕ_2 . In other word, each condensate has its own density of particle n_j and phase φ_j with $\phi_j = \sqrt{n_j}e^{i\varphi_j}$. Assuming again that the whole system is homogeneous in a box of volume V, the two-body interaction energy now involves three different interaction strengths. g_{ij} is the interaction strength between an atom of the fluid i and an atom of the fluid j. As for a pure BEC, we only need to count the number of available pair of each type in the sytem to compute the interaction energy :

$$E = V\left(g_{11}\frac{n_1^2}{2} + g_{22}\frac{n_2^2}{2} + g_{12}n_1n_2\right) \tag{1.23}$$

At equilibrium, the pressure is again $P = E/V$. But the condition of self-stability in this case is better expressed by the requirement that the function $E(n_1, n_2, V)$ is a minimum under the condition of constant volume V (thermodynamic potential). It leads to the three inequalities :

$$\begin{cases} g_{11} & > & 0 \\ g_{22} & > & 0 \\ g_{11}g_{22} - g_{12}^2 & > & 0 \end{cases} \tag{1.24}$$

The third inequality delimits the stability domain with respect to the value of g_{12}.

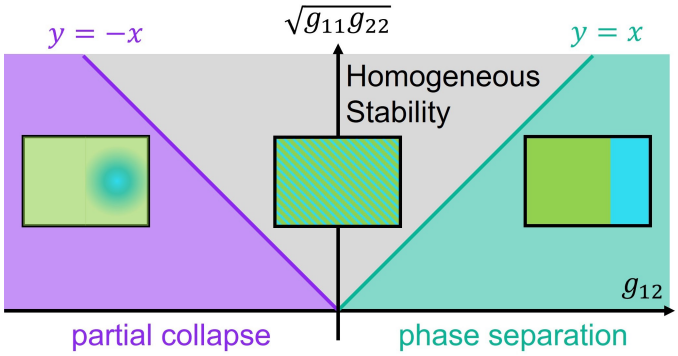

Figure 1.10: Phase diagram of the incoherent mixture of BEC assuming $a_{11} > 0$ and $a_{22} > 0$.

The right edge is given by $g_{ij} = \sqrt{g_{11}g_{22}}$. Above this value, it is energetically favorable for the fluid to phase separate in two pure BEC, thus increasing both densities n_j, but suppressing repulsive inter-species interactions. The second edge is given by equation $g_{ij} = -\sqrt{g_{11}g_{22}}$. Under this value, partial collapses happen because of attractive inter-species interactions. For a given initial mixture proportion (n_1, n_2) one of the two fluid will remain in excess while a mixture of the two in the most unstable proportions will collapse. The so-called most unstable proportion minimizes the interaction energy E in the collapse zone. One can easily prove that it happens at :

$$\frac{n_1}{n_2} = \frac{g_{22} - g_{12}}{g_{11} - g_{12}} \quad \Leftrightarrow \quad \frac{n_1 - n_2}{n_1 + n_2} = \frac{g_{22} - g_{11}}{g_{11} + g_{22} - 2g_{12}} \tag{1.25}$$

These formulas also give the mixture proportion that minimize the energy E in the stable region although there is no collapse there.

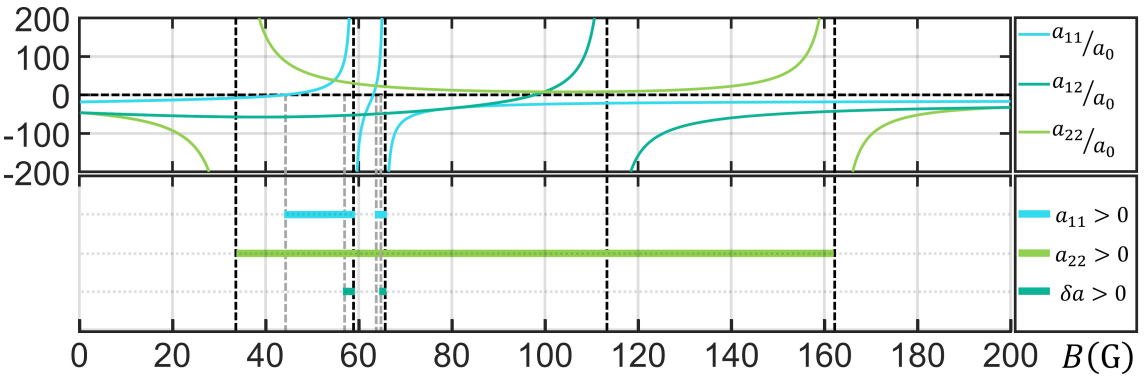

Figure 1.11: Domain of stability for incoherent mixtures of BEC in states $|1\rangle$ and $|2\rangle$. Because the scattering length are mostly negative, the phase separation case never happen. Outside the region of positive $\delta a = \sqrt{a_{11}a_{22}} + a_{12}$, any incoherent mixture partially collapses.

1.3 Radio frequency (RF) dressing of atoms

In this section, we recall the formalism of a single atom dressed by a near-resonant oscillating electromagnetic field. We treat the field classically for two reason : Firstly, its quantum state is a coherent state with an enormous number of photons ($\sim 10^{14}$). Secondly, we will only consider single-photon resonant transition. One can find a complete description of multi-photons resonances in references [20][21][22]. We also focus here on the transition between state $|1\rangle$ and $|2\rangle$ although the same method is used for other transfers during the cooling sequence (see section 2.1).

1.3.1 Zeeman effect and RF magnetic coherent coupling

Under a steady magnetic field $\vec{B}_0$ of around 50 G, the energy degeneracy between internal states $|1\rangle$ and $|2\rangle$ is lifted by Zeeman effect. The difference in energy between these two states becomes of the order of 35MHz, thus enabling resonant transitions in the radio-frequency domain. Apart from energy matching, there are other selection rules involved for such a transition to be possible but they ultimately depend on the structure of the two states. Thus, let's first recall the modification of internal states $|1\rangle$ and $|2\rangle$ due to Zeeman effect. If we limit ourselves to the two lowest hyperfine manifolds for which $l = 0$, the hyperfine and Zeeman Hamiltonian that totally lifts the initial degeneracy of $4s$ levels is :

$$\hat{H}_0 = \hbar \mathcal{A} \vec{I} \cdot \vec{S} \quad + \left(g_S \mu_B \vec{S} + g_I \mu_N \vec{I} \right) \cdot \vec{B}_0 / \hbar \tag{1.26}$$

The quantification axis (Oz) is taken along the direction of $\vec{B}_0$, which enable us to use spin ladder operators $I_\pm = I_x \pm i I_y$ and $S_\pm = S_x \pm i S_y$ [2]:

$$\hat{H}_0 = \hbar \mathcal{A} \left(I_z S_z + \frac{1}{2} I_+ S_- + \frac{1}{2} I_- S_+ \right) \quad + \left(g_S \mu_B S_z + g_I \mu_N I_z \right) B_0 / \hbar \tag{1.27}$$

From this writing, it becomes clear that operator $I_z + S_z$ commutes with $\hat{H}_0$. Consequently, the projection m_F of the total angular momentum of the atom remains a good

[2] Ladder operators have the property $L_\pm |l, m_L\rangle = \sqrt{(l \mp m_L)(l \pm m_L + 1)}\, |l, m_L \pm 1\rangle$ if $|m_L| \leq L$

quantum number and the Hamiltonian only couples states by pairs with equal m_F. For example in the case $m_F = -1$, state $|m_I, m_S\rangle = \left|-\frac{3}{2}, \frac{1}{2}\right\rangle$ is only coupled with state $|m_I, m_S\rangle = \left|-\frac{1}{2}, -\frac{1}{2}\right\rangle$. The diagonalization of several sets of two-levels quantum system is then easily performed. Matching the behavior at zero magnetic field with the Clebsch-Gordon coefficients 1.1 gives us the exact expressions of states $|1\rangle$ and $|2\rangle$ at any magnetic field in the $|m_I, m_S\rangle$ basis :

$$\begin{cases} |1\rangle &= \cos\left(\frac{\alpha}{2}\right) \left|+\frac{1}{2}, -\frac{1}{2}\right\rangle - \sin\left(\frac{\alpha}{2}\right) \left|-\frac{1}{2}, +\frac{1}{2}\right\rangle \\ |2\rangle &= \cos\left(\frac{\beta}{2}\right) \left|-\frac{1}{2}, -\frac{1}{2}\right\rangle - \sin\left(\frac{\beta}{2}\right) \left|-\frac{3}{2}, +\frac{1}{2}\right\rangle \end{cases}$$
$$\begin{cases} \cot(\alpha) &= \frac{x}{2} \\ \cot(\beta) &= \frac{x-1}{\sqrt{3}} \end{cases} \quad \text{with} \quad \alpha, \beta \in [0, \pi] \qquad x = \frac{(g_S\mu_B - g_I\mu_N)B_0}{\hbar\mathcal{A}} \tag{1.28}$$

Of course, the structure of these two states at high and low magnetic fields could have been found by neglecting respectively the hyperfine coupling or the Zeeman interaction with respect to the other. But around 50G, the magnetic field is intermediate ($x \approx 0.6$) and the exact diagonalization is needed.
The energies of states $|1\rangle$ and $|2\rangle$ are given by :

$$\begin{cases} \varepsilon_1 &= \langle 1|\hat{H}_0|1\rangle &= -\frac{\hbar\mathcal{A}}{2}\left(\frac{1}{2} + \sqrt{4 + x^2}\right) \\ \varepsilon_2 &= \langle 2|\hat{H}_0|2\rangle &= -\frac{\hbar\mathcal{A}}{2}\left(\frac{1}{2} + \sqrt{4 - 2x + x^2}\right) - g_I\mu_N B_0 \end{cases} \tag{1.29}$$

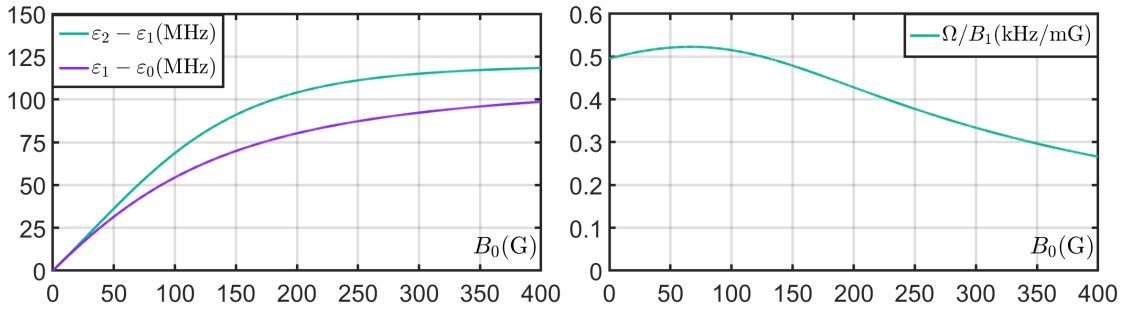

Figure 1.12: Natural frequencies of RF transitions $|1\rangle \leftrightarrow |2\rangle, |1\rangle \leftrightarrow |0\rangle$ and coupling strength of the transition $|1\rangle \leftrightarrow |2\rangle$

Their difference $\varepsilon_2 - \varepsilon_1 = \hbar\omega_0$ is of the order of 35MHz at 50G as announced in the beginning of 1.3.1. To induce a transition between states $|1\rangle$ and $|2\rangle$, we apply a weak radio frequency electromagnetic field $\vec{B}_1(t)$ at a frequency ω close to ω_0. Even though we omitted writing it for clarity, the shell electron is in the $4s$ orbital in these two states so there is no electric coupling of any kind between them. On the other hand, the magnetic dipole moment between these two state is non zero. Writing for any angular momentum operator, $\vec{L} = L_z\vec{u}_z + \frac{L_+ + L_-}{2}\vec{u}_x + \frac{L_+ - L_-}{2i}\vec{u}_y$, we find :

$$\begin{aligned} \vec{\mu}_{12} = \langle 2|\, g_S\mu_B\vec{S} + g_I\mu_N\vec{I}\,|1\rangle &= \langle 2|\, g_S\mu_B S_- + g_I\mu_N I_-\,|1\rangle \,\frac{\vec{u}_x + i\vec{u}_y}{2} \\ &\approx -g_S\mu_B \sin\left(\frac{\alpha}{2}\right)\cos\left(\frac{\beta}{2}\right)\frac{\vec{u}_x + i\vec{u}_y}{2} \end{aligned} \tag{1.30}$$

Where on the last line, we neglected the nuclear part of the magnetic dipole because $g_I\mu_N$ is ten thousand times smaller than $g_S\mu_B$ for potassium ^{39}K. Only the component of $\vec{B}_1(t)$

that has a -1 helicity around axis (Oz) can resonantly induce a transition of the atom between the states $|1\rangle$ and $|2\rangle$. Indeed, an atom in state $|1\rangle$ can absorb a photon of energy $\hbar\omega_0$ and angular momentum $-\hbar$ around axis (Oz) to end up in state $|2\rangle$. This process is reversible because the quasi-classical field $\vec{B}_1$ plays the role of a photon reservoir.

In our experiment, the RF magnetic field is created by a coil with an axis pointing horizontally towards atoms. We take this axis to be (Ox). The RF magnetic field has a linear polarisation along (Ox) which means that we can write it as $\vec{B}_1(t) = \frac{B_1}{2}(\cos(\omega t)\vec{u}_x + \sin(\omega t)\vec{u}_y) + \frac{B_1}{2}(\cos(\omega t)\vec{u}_x - \sin(\omega t)\vec{u}_y)$. This shows that the field is the sum of a $+1$ helicity part around (Oz) and a -1 helicity part. Fortunately, the $+1$ helicity part is non resonant for the transition between states $|1\rangle$ and $|0\rangle$ because around 50G, this other resonance is approximately 5MHz below the one we are interested in, as can be seen on figure 1.12. Finally, the Hamiltonian governing the internal dynamic on the $(|1\rangle, |2\rangle)$ basis in presence of the RF field can be rewritten under the rotating wave approximation (RWA) to take only into account the resonant process.

$$\hat{H}_{Rabi} = \frac{\hbar}{2}\begin{pmatrix} \delta & -\Omega \\ -\Omega & -\delta \end{pmatrix} \qquad \text{where} \qquad \begin{cases} \delta &= \omega - \omega_0 \\ \Omega &= |\vec{\mu}_{12}\cdot\vec{u}_x|B_1/\hbar \end{cases} \tag{1.31}$$

1.3.2 Rabi dressed states

Parameters δ, Ω are called detuning and Rabi frequency. They can be tuned experimentally by respectively changing the frequency ω of the RF and the output power of the RF generator. Following the standard diagonalization of a 2×2 Hamiltonian [23], the two eigenstates of the Rabi Hamiltonian are found to be, up to an arbitrary phase :

$$\begin{cases} |-\rangle &= \sin\left(\frac{\theta_d}{2}\right)|1\rangle + \cos\left(\frac{\theta_d}{2}\right)|2\rangle \\ |+\rangle &= \sin\left(\frac{\theta_d}{2}\right)|2\rangle - \cos\left(\frac{\theta_d}{2}\right)|1\rangle \end{cases} \qquad \theta_d \in [0,\pi] \text{ with } \cot(\theta_d) = \frac{\delta}{\Omega} \tag{1.32}$$

Their eigen-energies are :

$$\varepsilon_\pm = \pm\frac{\hbar}{2}\sqrt{\delta^2+\Omega^2} = \pm\frac{\hbar\Omega}{2\sin(\theta_d)} \tag{1.33}$$

In order to better describe the internal dynamics and for the clarity of following discussions, we use the Bloch sphere representation with $|2\rangle \leftrightarrow \vec{u}_z$ and $|1\rangle \leftrightarrow -\vec{u}_z$. A general state[3] $|\vec{u}\rangle$ on the $(|1\rangle, |2\rangle)$ basis is identified with a unit vector $\vec{u}$ on the sphere according to :

$$\begin{aligned} |\vec{u}\rangle &= e^{i\varphi/2}\sin(\theta/2)|1\rangle + e^{-i\varphi/2}\cos(\theta/2)|2\rangle \\ \vec{u} &= \sin(\theta)(\cos(\varphi)\vec{u}_x + \sin(\varphi)\vec{u}_y) + \cos(\theta)\vec{u}_z. \\ &\text{with} \qquad \theta\in[0,\pi] \quad , \quad \varphi\in[0,2\pi[\end{aligned} \tag{1.34}$$

It is then straightforward to see that state $|-\rangle$ correspond to a vector with azimuth $\varphi = 0$ and colatitude $\theta = \theta_d$. Meanwhile, state $|+\rangle$ has an azimuth $\varphi = \pi$ and a colatitude $\theta = \pi - \theta_d$. We will call θ the polarisation angle because $z = \cos(\theta)$ is the difference in probability of finding the atom in state $|2\rangle$ and probability of finding the atom in state

[3] up to a global phase which is irrelevant except in some path-splitting interference experiments

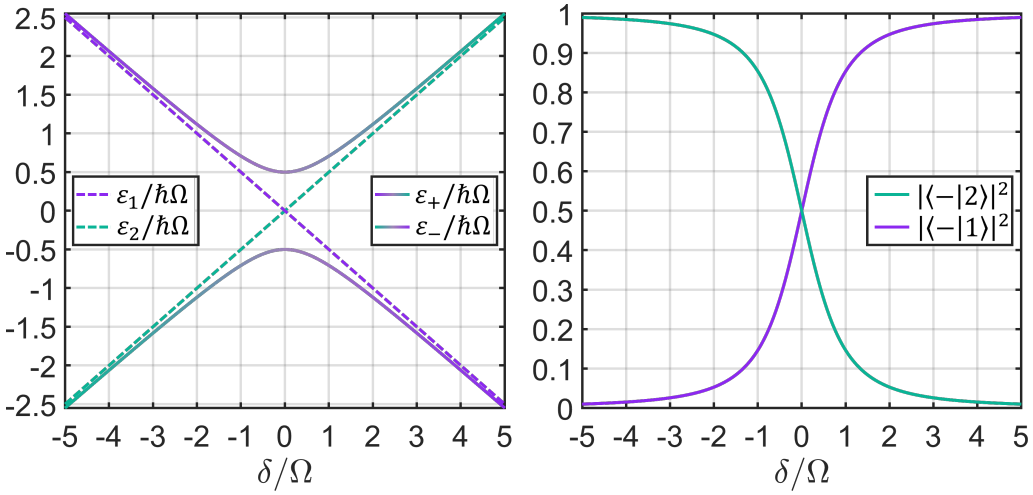

Figure 1.13: Energies and structure of the Rabi dressed-states with respect to detuning δ

$|1\rangle$. Finally, the dynamics of the two level system given by $\hat{H}_{Rabi}$, is equivalent to the one of vector $\vec{u}$ with the following dynamical equation given by Ehrenfest theorem.

$$\frac{d\vec{u}(t)}{dt} = -(\delta\vec{u}_z + \Omega\vec{u}_x) \wedge \vec{u}(t) \tag{1.35}$$

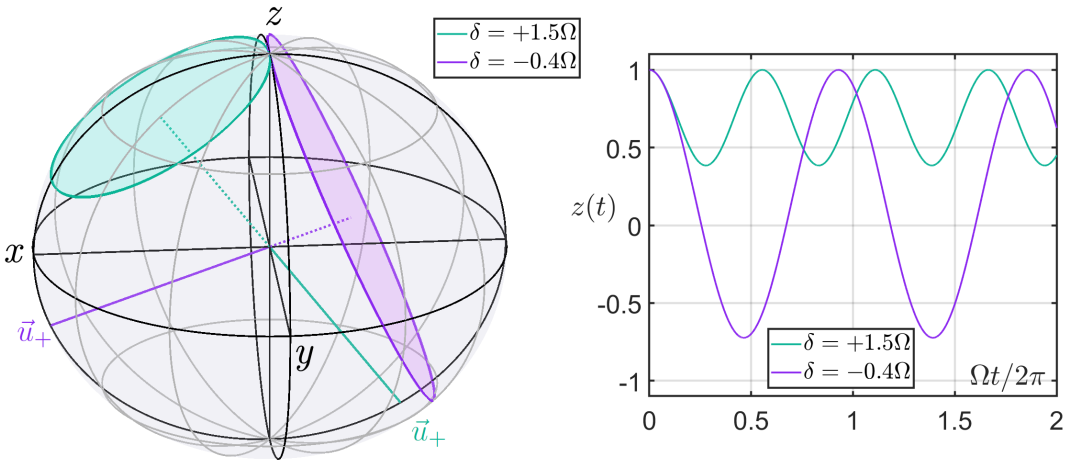

Figure 1.14: Rabi oscillations for two different value of detuning δ

It is simply the equation of precession of $\vec{u}$ around $\vec{u}_+ = -\vec{u}_-$ at a frequency $\sqrt{\Omega^2 + \delta^2}$. In the case of constant (δ, Ω), and starting initially from state $|2\rangle$, we recover the well-known result of Rabi oscillations : $z(t) = \cos(\theta(t)) = 1 - \frac{\Omega^2}{\Omega^2+\delta^2}\left(1 - \cos\left(t\sqrt{\Omega^2 + \delta^2}\right)\right)$

1.3.3 Adiabatic sweeps

At resonance, $\delta = 0$, one can use Rabi oscillations to change the internal state of the atom by applying a pulse of chosen duration. For example, a $\pi/2$-pulse lasts $\pi/(2\Omega)$ and transfers the atom from state $|2\rangle$ to state $\frac{i}{\sqrt{2}}|1\rangle - \frac{i}{\sqrt{2}}|2\rangle$. A pulse corresponds to two quenches of the Rabi frequency, or equivalently of the power of the RF source, from zero

to a constant value then back to zero. However, parameters δ and Ω may also be varied smoothly and slowly. If their time derivative is very small compared to the square of the effective Rabi frequency $\delta^2 + \Omega^2$ (**adiabatic condition**) :

$$\left|\frac{d\Omega}{dt}\right| \ll \delta^2 + \Omega^2 \quad \text{and} \quad \left|\frac{d\delta}{dt}\right| \ll \delta^2 + \Omega^2 \tag{1.36}$$

then we expect an atom initially in one of the two initial eigenstate, let's say state $|-\rangle_{\delta_0,\Omega_0}$ to remain at all times in the time dependant $|-\rangle_{\delta(t),\Omega(t)}$ state. The given dynamics is called an "adiabatic sweep". As for a thermodynamic transformation, the adiabatic case refers to an infinitely slow change of parameters which is never realised in practice. There is always a small transfer to the incorrect eigenstate (here $|+\rangle_{\delta(t),\Omega(t)}$) but by an amount that should be physically too small if the adiabatic condition is well verified. The advantage of the sweep method appears if we stop at some chosen value of δ_f and Ω_f and let the RF field turned on. The state of the atom then remains forever $|-\rangle_{\delta_f,\Omega_f}$ which is both a quantum superposition of the two initial states $|1\rangle, |2\rangle$ and a stationary state of the Hamiltonian of the atom. These interesting properties will remain true for interacting atoms in a BEC, although the Hamiltonian will be modified by the presence of inter-particle interactions.

$$\begin{array}{ccccccc} \delta(t) & : & \delta_0 & \longrightarrow & \delta_0 = 9\Omega_0 & \longrightarrow & \delta_f \\ \Omega(t) & : & 0 & \longrightarrow & \Omega_0 = \Omega_f & \longrightarrow & \Omega_f \\ |\vec{u}(t)\rangle & : & |2\rangle & \longrightarrow & |-\rangle_{\delta_0,\Omega_0} & \longrightarrow & |-\rangle_{\delta_f,\Omega_f} \end{array} \tag{1.37}$$

Experimentally the suitable range of RF power is very limited. Firstly, high powers induce electromagnetic noise on all electronic devices in the experiment room (magnetic field source, laser frequency locks...). On the other hand, at small RF power, the Rabi frequency becomes negligible compared to time-fluctuations of the natural frequency ω_0 - which are themselves caused by magnetic field noise. Consequently, the adiabatic condition on δ cannot be verified simultaneously at resonance and at low Rabi frequencies. Around 50 G, we shall limit ourselves to final Rabi frequencies Ω_f in $[2, 40]$ kHz. Note that the RF field can be slowly turned-on/off when the RF is out of resonance because in this case, the effective Rabi frequency $\sqrt{\delta^2 + \Omega^2}$ remains large at all times compared to time-fluctuations of ω_0.

There is another experimental limitation on the range of accessible detunings δ. Indeed, to tune precisely the frequency ω (and thereby δ) when around the resonance, it is better to have a frequency modulation range (FM) not too large compared to Ω_f. Otherwise the relative detuning δ/Ω would be very sensitive to fluctuations of the FM voltage command. Thus, we will always start adiabatic sweeps on δ with an "out of resonance" configuration corresponding to a detuning δ_0 of only $\pm\, 9\,\Omega$ and stay in this range for δ_f.

$$\Omega_f \in [2, 40] \text{ kHz} \qquad \text{and} \qquad \delta_f \in [-9, 9] \times \Omega_f \tag{1.38}$$

Let's focus on adiabatic sweeps in the $|-\rangle$ state. Starting with a gas of atoms in state $|2\rangle$ and at a given "out of resonance" detuning $\delta_0 = +\,9\,\Omega_f$, the RF power is turned on very slowly in a few ms from zero to its final value Ω_f. This limits the electromagnetic RF perturbation induced on electronic devices in the room and also ensure that the initial state of atom is changed into the state $|-\rangle_0 = \sin\left(\frac{\theta_0}{2}\right)|1\rangle + \cos\left(\frac{\theta_0}{2}\right)|2\rangle$ where actually $\theta_0 = \text{acot}(9) = 0.1107$ so that $|-\rangle_0 = 0.055\,|1\rangle + 0.998\,|2\rangle$. The state has been slightly moved out of the North pole in the Bloch sphere. The detuning is then changed from

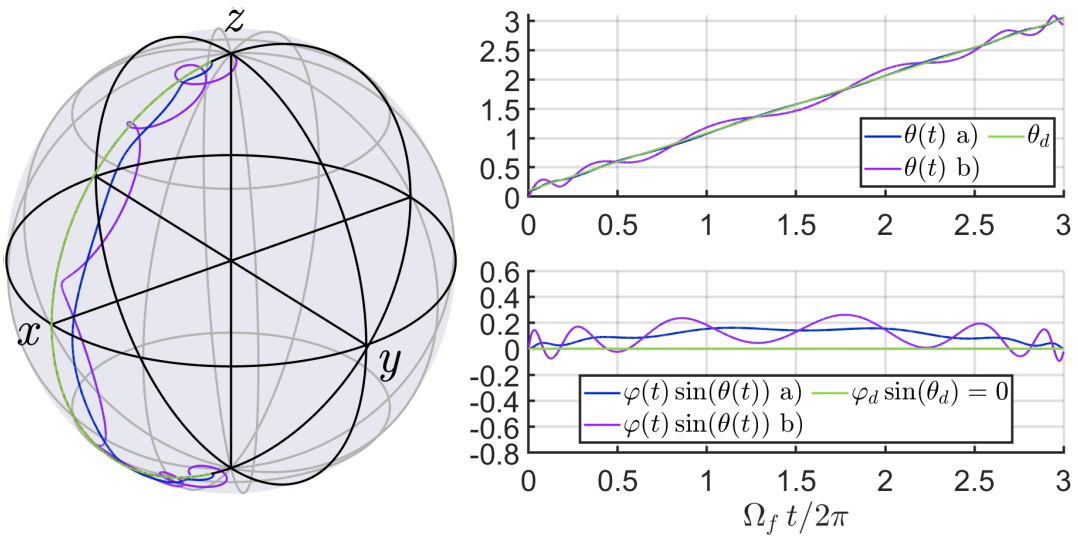

Figure 1.15: Results of the adiabatic sweep on δ given by equation 1.41 for a sweep duration of $\tau = 3 \times 2\pi/\Omega_f$ in case a) with a slow switch-on of the RF power, in case b) with a sudden switch-on of the RF power. The only difference is that in case b) the initial state is at the North pole while in case a), the initial state is slightly out of the North pole (see text). In case b), we can see a precession around the time dependant $\vec{u}_+$ in addition to the adiabatic following along $\vec{u}_-$

δ_0 to δ_f in a way that fulfill as best as possible the adiabatic condition 1.36. In order to justify the time dependence of $\delta(t)$ that we use, it is instructive to write the two level Schrödinger equation in the time-dependant basis $(|+\rangle_t, |-\rangle_t)$. Writing the state of the atom as $|\vec{u}(t)\rangle = a(t)\,|+\rangle_t + b(t)\,|-\rangle_t$, we get :

$$i\hbar \frac{d}{dt}\begin{pmatrix} a \\ b \end{pmatrix} = \left[\frac{\hbar\Omega_f}{2\sin\theta_d}\begin{pmatrix} 1 & 0 \\ 0 & -1 \end{pmatrix} + \frac{\hbar\dot{\theta}_d}{2}\begin{pmatrix} 0 & -i \\ i & 0 \end{pmatrix} \right]\begin{pmatrix} a \\ b \end{pmatrix} \quad \text{with } \cot\theta_d = \frac{\delta(t)}{\Omega_f} \tag{1.39}$$

The first matrix on the right side simply gives the eigen-energies of the two states $|\pm\rangle_t$ in accordance with equation 1.33. The second matrix on the right side may induce transfers between states $|+\rangle_t$ and $|-\rangle_t$ but only if $\left|\dot{\theta}_d\right|$ is of the order of $\Omega_f/\sin(\theta_d)$. Note that it is not possible to apply the time-dependant quantum perturbation theory because the eigen-energies depend on time. However, around resonance, the factor $\sin(\theta_d)$ will be in good approximation close to one and it is where we should worry about possible breaking of adiabadicity. Imposing the condition $\left|\dot{\theta}_d\right| \ll \Omega_f$ is strong enough to ensure that the sweep is adiabatic at any time and it actually gives back the adiabatic condition (1.36) :

$$\left|\frac{d\delta}{dt}\right| = \Omega_f \left|\frac{d\cot(\theta_d)}{dt}\right| = \frac{\delta^2+\Omega_f^2}{\Omega_f}\left|\dot{\theta}_d\right| \ll \delta^2+\Omega_f^2 \tag{1.40}$$

The simplest sweep on the detuning $\delta(t)$ verifying this condition is given by a constant slope $\dot{\theta}_d = \lambda \ll \Omega_f$. Thus $\theta_d = \theta_0 + \lambda t$ and the time dependence of δ is:

$$\delta(t) = \Omega_f \cot(\theta_0 + \lambda t) = \Omega_f \cot\left(\theta_0 + (\pi - 2\theta_0)\frac{t}{\tau}\right) \tag{1.41}$$

Where we also introduced the time $\tau = \frac{\pi-2\theta_0}{\lambda}$ of a full sweep going from δ_0 to $-\delta_0$. The above function $\delta(t)$ has a meaning only for times in $[0, \tau]$, which gives δ in $[-\delta_0, \delta_0]$. To

get any desired value of final detuning δ_f, one just has to stop at the corresponding time in $[0, \tau]$. We can also give a physical interpretation to λ, the slope of detuning around the crossing of the resonance, at $t = \tau/2$, is $\frac{d\delta}{dt} = \lambda\Omega_f$.

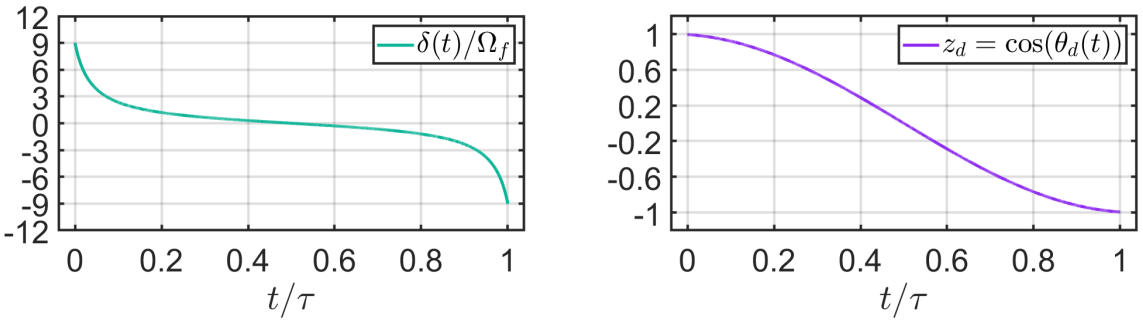

Figure 1.16: shape of the ideal sweep on detuning δ given by equation 1.41. Note how the target polarisation z_d follow a cosine curve and is almost linear time-dependant in the quantum mixture region around resonance

To conclude this section, we should give more details on the protocol that interests us the most. We want to create a gas with of atoms each in a steady quantum state which is a superposition of $|1\rangle$ and $|2\rangle$. To achieve this goal, we simply have to stop the sweep before its end and maintain a constant detuning. The RF coherent coupling should of course stay on to ensure that states $|\pm\rangle$ remain stationary states. By choosing the time at which we stop the sweep we can build any state with azimuth $\phi = 0$ and colatitude $\theta \in [\theta_0, \pi - \theta_0]$.

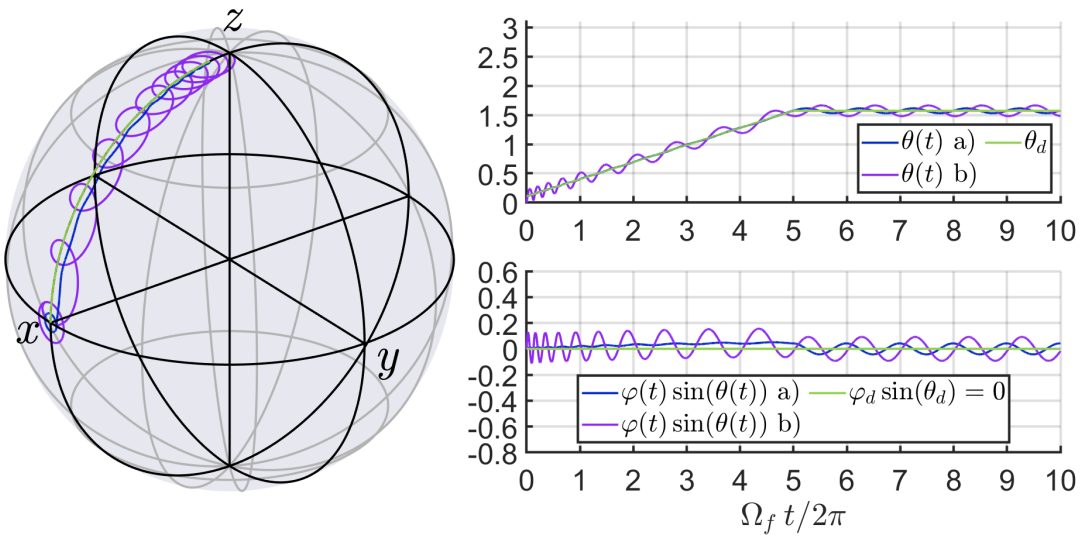

Figure 1.17: Results of an adiabatic half-sweep on δ given by equation 1.41 lasting a time $\tau/2 = 5 \times 2\pi/\Omega_f$ then a constant zero detuning for the same amount of time. Case a) corresponds to an anterior slow switch-on of the RF power and case b) to a sudden switch-on of the RF power.

Around the middle of the sweep, the relation between time and detuning or time and mixture proportion is linear which is an interesting feature. It is also possible to perform a sweep in the $|+\rangle$ state, by changing the sign of the detuning in formula 1.41 but such

state will not be stable with respect to two body collisions [24]. Finally, note that for a sweep stopped halfway the condition $\Omega\tau \ll 2\pi$ becomes more critical than for a full sweep (see figure 1.17). Indeed it is important to have very little precession around the fixed point after the end of the sweep.
On figures 1.16 and 1.17, we have included the time evolution of the internal state if the RF power is turned-on instantly (purple) and if the power RF power is turned on very slowly before the sweep. The latter enables the initial state to be the stationary state $|-\rangle$ at $\theta = \theta_0 = 0.1107$, otherwise the initial state is $|2\rangle$ ($\theta = 0$) which adds an unwanted precession motion (purple) on top of the optimized sweep dynamics (blue).

To conclude this section, we insist on what should be kept in mind : in the following, we will study RF-dressed gases and describe the internal state of atoms in the natural $\{|+\rangle, |-\rangle\}$ basis. These states depend only on the ratio δ/Ω which is imposed externally. One should always come back to equation 1.32 when in need of their exact form. Finally, note that even if the RF magnetic field is a quasi-classical coherent state with average photon number $N = 10^{14}$ photons, the states $|\pm\rangle$ are in a sense quantum sums of states $|1\rangle \otimes |(N+1)\text{photons}\rangle$ and $|2\rangle \otimes |N\text{photons}\rangle$.

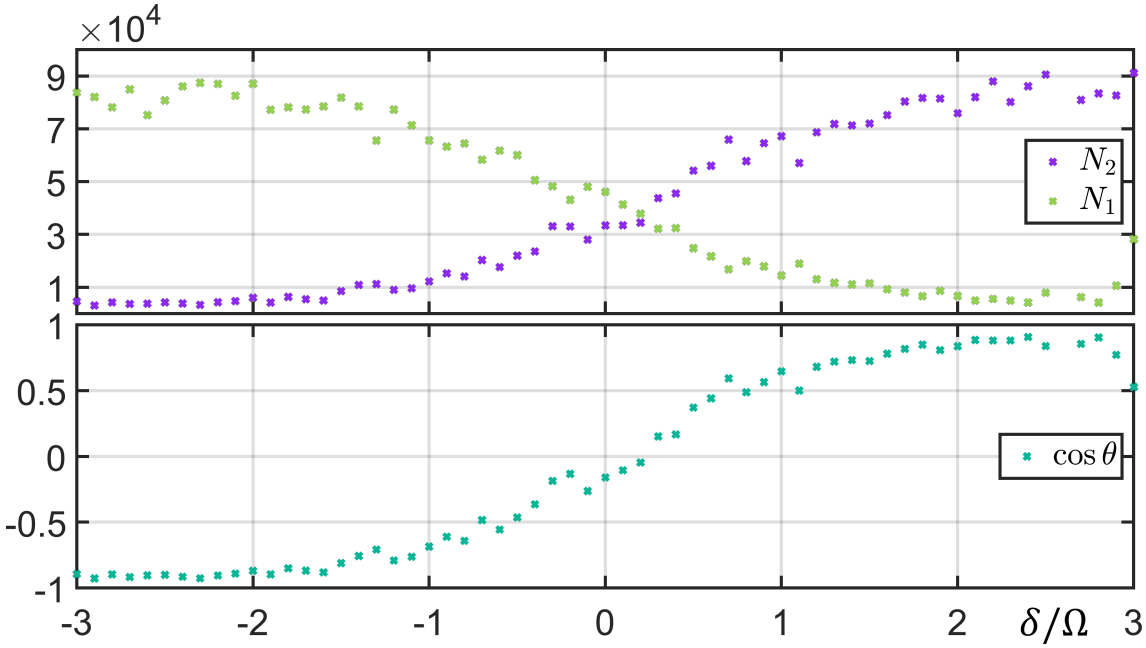

Figure 1.18: Experimental number of atoms in each states $|1\rangle$ and $|2\rangle$ after an adiabatic sweep from $\delta_0 = 9\Omega$ to δ (x axis) at a Rabi frequency of $\Omega/2\pi = 11$ kHz and with a duration of the full sweep of 0.8 ms.

1.4 Interactions between two atoms in RF-dressed states

In this section, we show that the elastic two-body interaction strengths between two atoms in a RF-dressed state can be derived from their values in absence of RF coupling. We shall insist on the physical origin of this result which is not granted at any value of the RF power. We then consider also the case of inelastic two-body collisions between RF dressed atoms, using second quantization formalism, we derive the strengths of such inelastic transitions. We pursue with an analysis of the behavior of the elastic interaction strength with the external driving parameters. Finally, we rewrite all two-body interaction strengths in function of three new parameters. In further chapters, we shall see why they are more relevant than the g_{ij} to investigate dynamical properties of the RF-dressed BEC.

1.4.1 Two-body elastic collisions

In presence of the RF coherent coupling, the two possible states of an isolated atom are the $|\pm\rangle$ states given by equation 1.28 with respect to δ/Ω. In order to investigate the macroscopic behavior of the RF-dressed gas, we must first study the collision between two atoms in these dressed states. A low energy collision will be elastic only if the two atoms are in the $|-\rangle$ state - internal state with minimal energy - and if in addition the effective Rabi frequency $\tilde{\Omega} = \sqrt{\delta^2 + \Omega^2}$ is larger than the kinetic energy of the pair $\hbar^2 k^2/m$. Indeed, any transition from $|--\rangle$ to either $(|+-\rangle + |-+\rangle)/\sqrt{(2)}$ or $|+,+\rangle$ is then energetically forbidden.
Note that Ω and δ are also bounded from above, for experimental and theoretical reasons: - experimentally, we can only explore $\Omega/2\pi$ up to 40 kHz which in turn limits $|\delta|/2\pi$ up to 360 kHz - theoretically, we want to remain under the two-level approximation, which requires to be far from the other resonant transition between states $|0\rangle$ and $|1\rangle$ located a few MHz below. Consequently, we should notice that the effective Rabi frequency $\tilde{\Omega}$ is, in our case, small compared to the typical effective interaction energy $\hbar^2/(ma^2) \geq 10$ MHz with $|a|$ in $[0, 100]\, a_B$.

The problem of low-energy elastic scattering of a pair in state $|--\rangle$ is more complex than a single channel scattering problem. Indeed, the effective Rabi frequency introduces a new intermediate length-scale $l_{\tilde{\Omega}} = \sqrt{\hbar/m\tilde{\Omega}}$ with $b_{vdW} \ll l_{\tilde{\Omega}} \ll 1/k$. We will follow here the method introduced by D. Petrov in a private communication and already available in J. Sanz Sanchez thesis [25].

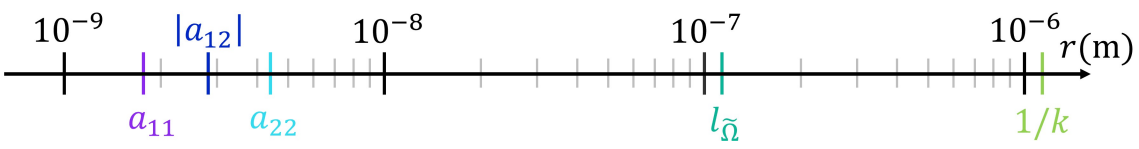

Figure 1.19: Order of magnitude for the length-scales in the dressed-state collision problem. Note the intermediate location of $l_{\tilde{\Omega}}$ around the geometric average between the parameters describing two-body quantum collision a_{ij} and the parameter describing macroscopic dynamics $1/k \sim \hbar/\sqrt{m\mu}$. The value of the scattering length are taken at a magnetic field of 56.76 G and chemical potential μ is estimated to 100 Hz.

Mathematical form of the scattering solution

As in subsection 1.1.2, we start by introducing the s-wave radial wave-function ϕ_E of the pair, in the center of mass frame, with kinetic energy $E = \hbar^2 k^2/m$ and with asymptotic behavior (arbitrary but convenient normalisation):

$$\phi_E \underset{r\to\infty}{\sim} \frac{\sin(kr+\delta)}{kr}|--\rangle \tag{1.42}$$

In the limit of low energy, $k \to 0$, we shall recover the effective two-body elastic scattering length a_{--} by taking the limit $\tan(\delta)/k \underset{k\to 0}{=} -a_{--}$.

In the interaction zone, $r \leq b_{vdW}$, the Rabi Hamiltonian and the energy E can both be neglected with respect to the interaction potentials $V_{ij}(r)$ between two atoms in the symmetric state (i,j), which are defined as in subsection 1.2.1 by:

$$(i,j) = \begin{cases} |i,j\rangle & \text{if } i = j \\ (|i,j\rangle + |j,i\rangle)/\sqrt{2} & \text{if } i \neq j \end{cases} \tag{1.43}$$

Therefore, the form of ϕ_E with respect to r is, in a sense, universal at the edge of the interaction zone $r \simeq b_{vdW}$. In the zero range limit $b_{vdW} \to 0$ and thanks to the linearity of quantum mechanics, we recover a behavior conform to Bethe-Peierls conditions in terms of the three scattering lengths a_{ij} with three unknown coefficients c_{ij}:

$$\phi_E \underset{r\to 0}{\sim} c_{11}\left(1-\frac{a_{11}}{r}\right)(1,1) + c_{22}\left(1-\frac{a_{22}}{r}\right)(2,2) + c_{12}\left(1-\frac{a_{12}}{r}\right)(1,2) \tag{1.44}$$

Still in the zero-range limit, the radial wave-function ϕ_E obeys a free Schrödinger equation everywhere except at the origin because of the Dirac distribution. Consequently, we may expect asymptotic expression 1.42, which is a free wave solution, to be valid at any radius $r > 0$. However, this would be incompatible with asymptotic behavior 1.44. The error comes from states $(++)$ and $(+-)$ that need to exist at the edge of the interaction zone to ensure continuity of ϕ_E and its derivative. The radial Schrödinger equation shows that these states, energetically forbidden at infinity, are exponentially decaying with r. The two attenuation lengths are given by the energy balance with imaginary wave-vectors:

$$\begin{array}{ccc} \frac{\hbar^2k^2}{m} = 2\hbar\tilde{\Omega} + \frac{\hbar^2(i\kappa_{++})^2}{m} & \longrightarrow & \kappa_{++} = \sqrt{2/l_{\tilde{\Omega}}^2 - k^2} \\ \frac{\hbar^2k^2}{m} = \hbar\tilde{\Omega} + \frac{\hbar^2(i\kappa_{+-})^2}{m} & \longrightarrow & \kappa_{+-} = \sqrt{1/l_{\tilde{\Omega}}^2 - k^2} \end{array} \tag{1.45}$$

And ϕ_E has to be of the following form, with two new unknown coefficients e_{++}, e_{+-}:

$$\phi_E \underset{r>0}{=} \frac{\sin(kr+\delta)}{kr}(--) + e_{++}\left(\frac{e^{-\kappa_{++}r}}{\kappa_{++}r}\right)(++) + e_{+-}\left(\frac{e^{-\kappa_{+-}r}}{\kappa_{+-}r}\right)(+-) \tag{1.46}$$

Around the origin and in the limit $k \to 0$, it has asymptotic behavior :

$$\phi_E \underset{r\to 0}{\sim} \left(1-\frac{a_{--}}{r}\right)(--) + e_{++}\left(1-\frac{l_{\tilde{\Omega}}}{\sqrt{2}r}\right)(++) + e_{+-}\left(1-\frac{l_{\tilde{\Omega}}}{r}\right)(+-) \tag{1.47}$$

We can now match equations 1.44 and 1.47 by projecting them on the three states $(--)$, $(++)$ and $(+-)$ then identifying coefficients by pairs in front of either r^{-1} or r^0 terms. This gives a linear system of six equations for the six unknowns $(c_{11}, c_{22}, c_{12}, e_{++}, e_{+-}, a_{--})$. However, another perfectly equivalent system can be derived by rather projecting on the

three states (11), (22) and (12). As we shall see, it is better to project on states $(--)$, $(++)$, $(+-)$ to identify the r^{-1} coefficients, and project on states (11), (22) and (12) to identify the r^0 coefficients. We get the following system after intentionally reordering the equations.

$$\begin{cases} e_{++}l_{\tilde{\Omega}} &= c_{11}\sqrt{2}\mathfrak{c}^2a_{11} &+ c_{22}\sqrt{2}\mathfrak{s}^2a_{22} &- c_{12}2\mathfrak{s}\mathfrak{c}a_{12} \\ e_{+-}l_{\tilde{\Omega}} &= -c_{11}\sqrt{2}\mathfrak{s}\mathfrak{c}a_{11} &+ c_{22}\sqrt{2}\mathfrak{s}\mathfrak{c}a_{22} &+ c_{12}(\mathfrak{s}^2-\mathfrak{c}^2)a_{12} \\ c_{11} &= \mathfrak{s}^2 &+ e_{++}\mathfrak{c}^2 &- e_{+-}\sqrt{2}\mathfrak{s}\mathfrak{c} \\ c_{22} &= \mathfrak{c}^2 &+ e_{++}\mathfrak{s}^2 &+ e_{+-}\sqrt{2}\mathfrak{s}\mathfrak{c} \\ c_{12} &= \sqrt{2}\mathfrak{s}\mathfrak{c} &- e_{++}\sqrt{2}\mathfrak{s}\mathfrak{c} &+ e_{+-}(\mathfrak{s}^2-\mathfrak{c}^2) \\ a_{--} &= c_{11}\mathfrak{s}^2a_{11} &+ c_{22}\mathfrak{c}^2a_{22} &+ c_{12}\sqrt{2}\mathfrak{s}\mathfrak{c}a_{12} \end{cases} \tag{1.48}$$

With $\mathfrak{s} = \sin\left(\frac{\theta_d}{2}\right)$ and $\mathfrak{c} = \cos\left(\frac{\theta_d}{2}\right)$, introduced before to define the $|\pm\rangle$ states in function of the driving parameters δ and Ω.

Zeroth order solution to the scattering problem

Thanks to this optimized system 1.48, the scattering length a_{--} and all other unknowns coefficients can be found without any matrix inversion by noticing that the typical value of the ratio $a_{ij}/l_{\tilde{\Omega}}$ is, for our experimental parameters, less than 0.05, thus allowing a power expansion converging with certainty to the exact solution of the system. By iterating the equations in the order they are now arranged, we shall find the power expansion at zeroth and first orders, which will be enough to get the physically relevant solution. We still need some initial values to start the iteration. Hopefully, at zeroth order, the first two lines imply that coefficients e_{++} and e_{+-} must vanish as $l_{\tilde{\Omega}} \to \infty$. We can then inject apply lines L_3, L_4, L_5 to get the values of the three coefficients $c_{ij}^{(0)}$ at zeroth order, and finally line L_6 for $a_{--}^{(0)}$:

$$\begin{cases} e_{++}^{(0)} &= 0 \\ e_{+-}^{(0)} &= 0 \\ c_{11}^{(0)} &= \mathfrak{s}^2 \\ c_{22}^{(0)} &= \mathfrak{c}^2 \\ c_{12}^{(0)} &= \sqrt{2}\mathfrak{s}\mathfrak{c} \\ a_{--}^{(0)} &= \mathfrak{s}^4a_{11} + \mathfrak{c}^4a_{22} + 2\mathfrak{s}^2\mathfrak{c}^2a_{12} \end{cases} \quad \text{with} \quad \begin{cases} \mathfrak{s} &= \sin\left(\frac{\theta_d}{2}\right) \\ \mathfrak{c} &= \cos\left(\frac{\theta_d}{2}\right) \end{cases} \tag{1.49}$$

Interestingly, even if the zeroth order correspond to the limit of small effective Rabi frequency $\tilde{\Omega}$ and large domain of existence $l_{\tilde{\Omega}}$ of states $(++)$ and $(+-)$, they still completely disappear of the scattering problem because e_{++} and e_{+-} are null. This counter intuitive fact can be interpreted as a consequence of the normalisation of these quasi-bound states over a volume that tends to infinity. The scattering length at zeroth order could have been found by assuming equation 1.42 was valid everywhere and using Bethe-Peierls conditions recklessly without looking at the incoherence of the asymptotic behavior near the origin for projections on $(++)$ or $(+-)$.

First order correction

We shall discuss the behavior and tunability of the scattering length $a_{--}^{(0)}$ with respect to the internal state in subsection 1.4.3. To conclude this discussion, we also give the first order correction for the scattering length. It is given by a second iteration of system 1.48.

$$a_{--}^{(1)} = \frac{\sqrt{2}\mathfrak{s}^4\mathfrak{c}^4}{l_{\tilde{\Omega}}}\left(a_{11}+a_{22}-2a_{12}\right)^2 + \frac{2\mathfrak{s}^2\mathfrak{c}^2}{l_{\tilde{\Omega}}}\left(\mathfrak{s}^2(a_{12}-a_{11})+\mathfrak{c}^2(a_{22}-a_{12})\right)^2 \tag{1.50}$$

This formula will be used again in chapter 3 and 6 although we can already say that this correction is always positive, proportional to $\sqrt{\tilde{\Omega}}$ and disappears for large detunings $\sin\theta_d \to 0$. In our experimental conditions it will be at most equal to $2\,a_0$ for a Rabi frequency of 40 kHz.

1.4.2 Inelastic two-body collisions and second quantisation formalism

The origin of two-body inelastic collisions between atoms in RF-dressed states is similar to the subsection 1.2.1. Any collision involving at least one atom in internal state $|+\rangle$ is going to be inelastic because it is energetically favorable and caused by the introduction of a phase shift, by the potentials $V_{ij},(r)$, between the two coefficients describing the internal state of the atom in the $\{|1\rangle,|2\rangle\}$ basis. Conservation of energy fixes the value of outgoing kinetic energy $\hbar^2k_{out}^2/m$ in each channel according to :

$$\begin{array}{ll}(++)\to(--): & k_{in}^2+2(l_{\tilde{\Omega}})^{-2}=k_{out}^2\\ (++)\to(+-): & k_{in}^2+(l_{\tilde{\Omega}})^{-2}=k_{out}^2\\ (+-)\to(--): & k_{in}^2+(l_{\tilde{\Omega}})^{-2}=k_{out}^2\end{array} \tag{1.51}$$

The incoming kinetic energy $\hbar^2k_{in}/m$ of the pair is usually negligible compared to the Rabi energy $\hbar^2(l_{\tilde{\Omega}})^{-2}/m$. Furthermore, we saw in the previous subsection that, at the edge of the interaction zone $r\simeq b_{vdW}$, the three internal symmetric states $(--),(++),(+-)$ are present. We could solve exactly the inelastic scattering problem with the same methodology. For example with an incoming state $(+-)$, we introduce the wave-function ϕ_E with incoming energy $E=\hbar^2k^2/m$ and behavior:

$$\phi_E \underset{r\geq 0}{\sim} \frac{e^{-ikr}-d_{+-}e^{ikr+2i\delta}}{r}(+-)+d_{--}\frac{e^{ir/l_{\tilde{\Omega}}}}{r}(--)+d_{++}\left(\frac{e^{-r/l_{\tilde{\Omega}}}}{r}\right)(++) \tag{1.52}$$

The seven unknowns can then be computed as power series of $1/l_{\tilde{\Omega}}$ with the help of the Bethe-Peierls conditions and the equation of conservation of probability at the origin.

However, it is more interesting to derive the elastic and inelastic interaction strengths in the second quantization formalism. As a consequence, we will obtain an expression of the many-body interaction Hamiltonian in the $\{|+\rangle,|-\rangle\}$ basis. We start by writing the two-body contact interaction Hamiltonian in the momentum basis :

$$\hat{H}_{2b}=\frac{1}{2V}\sum_{\vec{p}_1+\vec{p}_2=\vec{p}_3+\vec{p}_4}\left[\sum_{i,j}g_{ij}\hat{a}_{i,\vec{p}_1}^\dagger\hat{a}_{j,\vec{p}_2}^\dagger\hat{a}_{i,\vec{p}_3}\hat{a}_{j,\vec{p}_4}\right] \tag{1.53}$$

Where the operator $\hat{a}_{i,\vec{p}}^\dagger$ creates a particle in internal state $|i\rangle$ and momentum $\vec{p}$. Thanks to the linearity of quantum mechanics, we can also write :

$$\begin{cases}\hat{a}_1^\dagger(\vec{p}) = \mathfrak{s}\ \hat{a}_-^\dagger(\vec{p}) - \mathfrak{c}\ \hat{a}_+^\dagger(\vec{p})\\ \hat{a}_2^\dagger(\vec{p}) = \mathfrak{c}\ \hat{a}_-^\dagger(\vec{p}) + \mathfrak{s}\ \hat{a}_+^\dagger(\vec{p})\end{cases} \quad \text{with} \quad \begin{array}{l}\mathfrak{s}=\sin\left(\frac{\theta_d}{2}\right)\\ \mathfrak{c}=\cos\left(\frac{\theta_d}{2}\right)\end{array} \tag{1.54}$$

With basic algebra, we get the two-body Hamiltonian in the $\{|+\rangle, |-\rangle\}$ basis:

$$\begin{aligned}\hat{H}_{2b} = \frac{1}{V} \sum_{\vec{p}_1+\vec{p}_2=\vec{p}_3+\vec{p}_4} \Bigg[& \frac{1}{2} \sum_{\sigma,\tau} g_{\sigma\tau}^{\sigma\tau}\, \hat{a}^\dagger_{\sigma,\vec{p}_1} \hat{a}^\dagger_{\tau,\vec{p}_2} \hat{a}_{\sigma,\vec{p}_3} \hat{a}_{\tau,\vec{p}_4} \\ & + \frac{1}{2} \sum_{\sigma\neq\tau} g_{\sigma\sigma}^{\tau\tau}\, \hat{a}^\dagger_{\tau,\vec{p}_1} \hat{a}^\dagger_{\tau,\vec{p}_2} \hat{a}_{\sigma,\vec{p}_3} \hat{a}_{\sigma,\vec{p}_4} \\ & + \sum_{\sigma\neq\tau} g_{\sigma\sigma}^{\sigma\tau}\, \hat{a}^\dagger_{\sigma,\vec{p}_1} \hat{a}^\dagger_{\tau,\vec{p}_2} \hat{a}_{\sigma,\vec{p}_3} \hat{a}_{\sigma,\vec{p}_4} + g_{\sigma\tau}^{\sigma\sigma}\, \hat{a}^\dagger_{\sigma,\vec{p}_1} \hat{a}^\dagger_{\sigma,\vec{p}_2} \hat{a}_{\sigma,\vec{p}_3} \hat{a}_{\tau,\vec{p}_4} \Bigg] \end{aligned} \tag{1.55}$$

Where indices σ and τ refer to either $+$ or $-$. Each coefficient $g_{\mu\nu}^{\sigma\tau}$ gives the probability of a process where two atoms in state $|\mu\rangle$ and $|\nu\rangle$ collide and get out of the scattering zone in states $|\sigma\rangle$ and $|\tau\rangle$ with conservation of total momentum.This should be understood in the sense of the S-matrix of quantum field theory[4].

• The first sum with $\sigma\tau$ in $\{--, +-, -+, ++\}$ describes the three possible elastic processes : $(--) \longrightarrow (--)$, $(+-) \longrightarrow (+-)$ and $(++) \longrightarrow (++)$. The $1/2$ factor before the sum disappears for distinguishable atoms in state $(+-)$ since the index pair appears twice. On the contrary, if the two particles are in the same internal state $(--)$ or $(++)$, it is physically impossible to know if they have been exchanged or not during the contact interaction (see figure 1.20). Consequently, the physically measured transition probability will be doubled which cancels the $1/2$ factor and proves that in both cases $g_{\sigma\tau}^{\sigma\tau}$ is the physically measurable quantity.

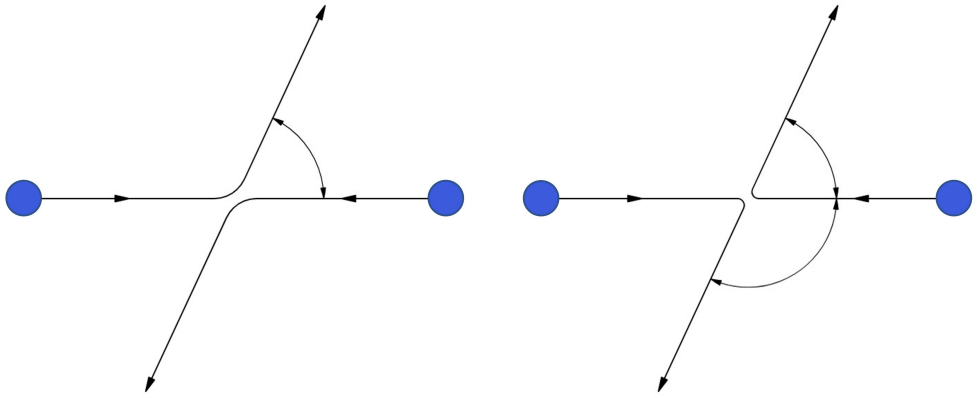

Figure 1.20: Schematic view of a point like collision. In the scattering of two identical particles, the two processes are indistinguishable [26].

• The second sum with $\sigma\tau$ in $\{+-, -+\}$ describes the two following inelastic processes: $(--) \longrightarrow (++)$ and $(++) \longrightarrow (--)$. The $1/2$ factor accounts for the equivalence of the two processes where the particles get exchanged during the point like collision (figure 1.20).

• The third sum with $\sigma\tau$ in $\{+-, -+\}$ describes the other four inelastic processes: $(--) \longrightarrow (+-)$, $(++) \longrightarrow (+-)$, $(-+) \longrightarrow (--)$ and $(-+) \longrightarrow (++)$. The particles are distinguishable in either the initial or final state so the physically measurable quantity will be directly the $g_{\sigma\sigma}^{\sigma\tau}$ coefficient.

[4] *"So if you see a theoretical physicist pacing the floor and saying, "All I have to do is calculate the S-matrix," you will know what he is worried about"* Feynman courses, volume III chapter 8.4 [26]

Because of the reversibility of quantum mechanics, encased in the hermitian nature of the Hamiltonian, interaction strengths have the following symmetries:

- $g_{\mu\nu}^{\sigma\tau} = g_{\nu\mu}^{\sigma\tau} = g_{\mu\nu}^{\tau\sigma}$
- $g_{\mu\nu}^{\sigma\tau} = g_{\sigma\tau}^{\nu\mu}$

$$\begin{cases} g_{--}^{--} &= \mathfrak{s}^4 & g_{11} & + & \mathfrak{c}^4 & g_{22} & + & 2\mathfrak{s}^2\mathfrak{c}^2 & g_{12} \\ g_{++}^{++} &= \mathfrak{c}^4 & g_{11} & + & \mathfrak{s}^4 & g_{22} & - & 2\mathfrak{s}^2\mathfrak{c}^2 & g_{12} \\ g_{+-}^{+-} &= 2\mathfrak{s}^2\mathfrak{c}^2 & g_{11} & + & 2\mathfrak{s}^2\mathfrak{c}^2 & g_{22} & + & \left(\mathfrak{s}^2 - \mathfrak{c}^2\right)^2 & g_{12} \\ g_{--}^{++} &= \mathfrak{s}^2\mathfrak{c}^2 & g_{11} & + & \mathfrak{s}^2\mathfrak{c}^2 & g_{22} & - & 2\mathfrak{s}^2\mathfrak{c}^2 & g_{12} \\ g_{--}^{+-} &= -\mathfrak{s}^3\mathfrak{c} & g_{11} & + & \mathfrak{s}\mathfrak{c}^3 & g_{22} & + & \mathfrak{s}\mathfrak{c}\left(\mathfrak{s}^2 - \mathfrak{c}^2\right) & g_{12} \\ g_{++}^{+-} &= -\mathfrak{s}\mathfrak{c}^3 & g_{11} & + & \mathfrak{s}^3\mathfrak{c} & g_{22} & - & \mathfrak{s}\mathfrak{c}\left(\mathfrak{s}^2 - \mathfrak{c}^2\right) & g_{12} \end{cases} \tag{1.56}$$

The first line gives back the scattering length a_{--} that we computed in the previous subsection, with the prescription $g_{--}^{--} = 4\pi\hbar^2 a_{--}/m$, but only if we stop our computation of $a_{--}^{(0)}$ at zeroth order ! This is predictable because, the exact resolution of the two-body problem takes into account the Rabi Hamiltonian which is absent in the above computation. The other terms of the total Hamiltonian of the gas are single particles operators, they are easily expressed in the $|\pm\rangle$ basis:

$$\hat{H}_{1b} = \sum_{\vec{p}} \left(\frac{p^2}{2m}\right) \hat{a}_{-,\vec{p}}^{\dagger} \hat{a}_{-,\vec{p}} + \sum_{\vec{p}} \left(\frac{p^2}{2m} + \hbar\tilde{\Omega}\right) \hat{a}_{+,\vec{p}}^{\dagger} \hat{a}_{+,\vec{p}} \tag{1.57}$$

Non-conservation of energy and virtual particles

Finally, we should note that the conservation of energy is not anymore imposed by the Hamiltonian 1.55. This is because the volume of the interaction zone is assumed to be zero, while in reality the two atoms are strongly accelerated during the penetration in the interaction zone (deep potential well), bounce on the coulomb repulsive core and finally get decelerated while exiting the interaction zone. If the outgoing internal state of the pair has a lower Rabi energy than the incoming one, the net balance is an acceleration to a velocity of either $\hbar/(ml_{\tilde{\Omega}})$ or $\sqrt{2}\hbar/(ml_{\tilde{\Omega}})$, for both atom and on two opposite directions. Although this classical picture is clarifying, in the end we must accept that the local two-body Hamiltonian 1.55 allows transfer to some quantum states with a negative kinetic energy ! We already encountered them in the solving of the exact two-body $(--)$ problem, since the $(++)$ and $(+-)$ parts of the scattered wave-function ϕ_E had imaginary wave-vectors. This is a well-known effect in quantum field theory, refered to as "*virtual particles*".

1.4.3 Tunability of two-body interaction strength in RF-dressed BEC

To finish this first chapter, we are left with study of the dependence of scattering length $a_{--}^{(0)}$, with respect to the external parameters of our experiment. There are three of them, the magnetic field B, the Rabi frequency Ω and the detuning δ. The magnetic fields controls the bare interaction strength g_{ij} through Feshbach resonances. And the last two parameters control the internal state $|-\rangle$ through the value of their ratio $\delta/\Omega = \cot(\theta_d)$

since:

$$|-\rangle = \sin\left(\frac{\theta_d}{2}\right)|1\rangle + \cos\left(\frac{\theta_d}{2}\right)|2\rangle$$

In order to study this double tunability and fully grasp the universality of dressed-state two-body interactions, we begin by introducing three parameters:

$$\overline{g} = \frac{g_{11} + g_{22} - 2g_{12}}{4} \qquad g_\infty = \frac{g_{11}g_{22} - g_{12}^2}{4\overline{g}} \qquad \kappa = \frac{g_{11} - g_{22}}{4\overline{g}} \tag{1.58}$$

We will call g_∞ **interaction offset**, $\overline{g}$ **interaction flexibility** and κ **interaction asymmetry**. The previous formulas can be inverted to get back the three initial interaction strength :

$$g_{12} = g_\infty + \overline{g}\left(\kappa^2 - 1\right) \qquad g_{11} = g_\infty + \overline{g}\,(1+\kappa)^2 \qquad g_{22} = g_\infty + \overline{g}\,(1-\kappa)^2 \tag{1.59}$$

From these formulas, we see that κ quantifies how different are the two intra-species interaction strength g_{11} and g_{22}. They are equal if and only if κ is zero. In addition, if the interaction flexibility $\overline{g}$ is zero, then the three interaction strengths g_{ij} are equal to the offset g_∞. Interactions are state insensitive.

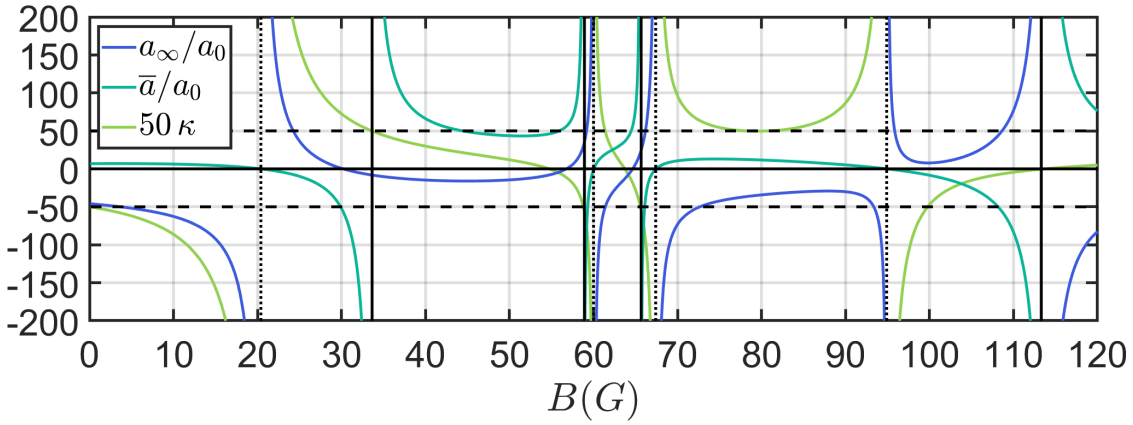

Figure 1.21: scattering length offset a_∞, scattering length flexibility $\overline{a}$ and scattering length asymmetry κ for states $|1\rangle$ and $|2\rangle$ of potassium^{39}K in function of external magnetic field. Feshbach resonances happen only on black plain curves.

The peculiar case $\overline{g} = 0$: For several magnetic fields, we see that $\overline{g}$ tends to 0 while both $|\kappa|$ and $|g_\infty|$ tend to infinity. This happens when the equality $g_{11} + g_{22} = 2g_{12}$ is verified. In this case, formulas 1.5 and 1.59 should simply be replaced by :

$$\overline{g} = 0 \qquad g_+ = \frac{g_{11} + g_{22}}{2} \qquad g_- = \frac{g_{11} - g_{22}}{2} \tag{1.60}$$

$$g_{12} = g_+ \qquad g_{11} = g_+ + g_- \qquad g_{22} = g_+ - g_- \tag{1.61}$$

These fake divergences for $\overline{a} = 0$, visible on figure 1.21 at 20.4 G, 60.0 G, 67.4 G and 94.9 G (*dotted*) have nothing physical and should not be confused with true Feshbach resonances, where on the contrary $\overline{a} \to \pm\infty$, at 33.6 G, 58.9 G, 65.7 G and 113.3 G (*plain*). This scenario is not physically interesting for potassium but we still mention it for objectivity and for clarity of figure 1.21.

Double tunability of g_{--}^{--}

From now on, we will assume equations 1.58 and 1.59 are well defined because $\overline{g} \neq 0$. We can then go back to the expression of the effective two-body interaction strength for atoms in a $|-\rangle$ dressed state. Inserting the expressions from equation 1.59 into the analytic formula for g_{--}^{--} 1.56 , we get :

$$g_{--}^{--} = g_\infty + \overline{g}\,(\cos\theta_d - \kappa)^2 \tag{1.62}$$

This formula implies that the bigger $|\overline{g}|$ is, the more we can externally change the strength of two-body interactions in the RF-dressed BEC by changing internal state through the relative detuning δ/Ω. When the detuning δ is large compared to the Rabi frequency Ω, the $|-\rangle$ state coincide with state $|2\rangle$ and the effective interaction strength g_{--}^{--} tends to g_{22}. Inversely, at a very negative detuning, it tends to g_{11}. In between these two asymptotic values, and only if $|\kappa| \leq 1$, there is one extremum of $g_{--}^{--}(\delta/\omega)$, equal to g_∞, which is certainly a desirable feature. According to figure 1.21, it will be the case for us since we will work between 33.6 G (resonance of a_{11}) and 58.8 G (resonance of a_{22}). As can be seen

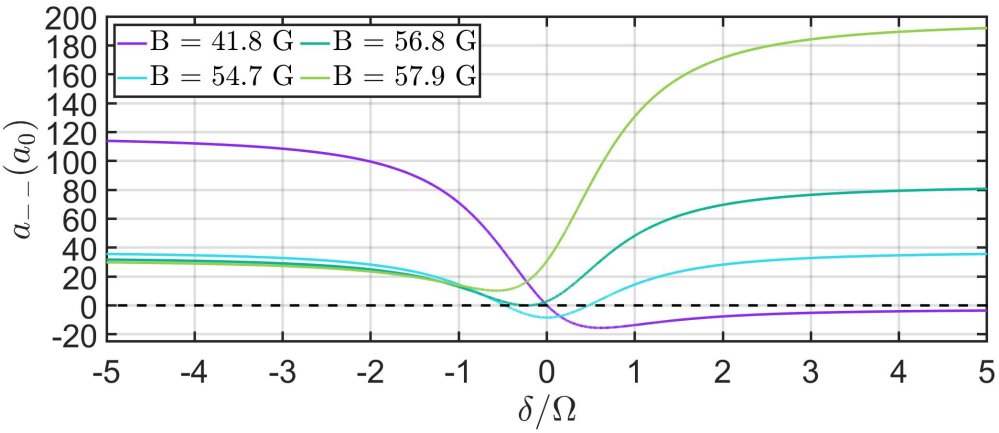

Figure 1.22: Behavior of the $a_{--}^{(0)}$ scattering length as a function of relative detuning at different relevant magnetic fields used in this thesis.

on figure 1.21, $\overline{a}$ is always positive ($\overline{a} \geq 43a_0$) in this region so the extremum will be a minimum. The mixture angle θ_∞ at which the minimum happen is given by:

$$\cos(\theta_\infty) = \kappa \qquad \text{with} \qquad \theta_\infty \in [0, \pi] \tag{1.63}$$

In this thesis, we decided to work, in order to understand step by step the collective effects in a RF-dressed BEC, at a few specific magnetic fields for which the curve $a_{--}(\delta/\Omega)$ has some good properties, visible on figure 1.22:

- At $B = 41.8\,\text{G}$, a_{--} has a zero crossing for the 50/50 mixture, namely for $|-\rangle = (|1\rangle + |2\rangle)/\sqrt{2}$.
- At $B = 54.7\,\text{G}$, the curve $a_{--}(\delta/\Omega)$ is symmetric because $a_{11} = a_{22} = 33\,a_0$.
- At $B = 56.8\,\text{G}$, the minimum of $a_{--}(\delta/\Omega)$ is zero because $a_{11}a_{22} = a_{12}^2$.
- At $B = 57.5\,\text{G}$, the minimum of $a_{--}(\delta/\Omega)$ is $5.6\,a_0$, a non negligible value, and a_{11} is large but not too close to its Feshbach resonance at $B = 58.8\,\text{G}$.

In chapter 4, we shall study the conditions of thermodynamic stability of a RF-dressed BEC. They will be different than stability conditions for a incoherent mixture. The main difference is that for RF-dressed BEC, the mixture proportion is imposed externally. As a first guess, let's say that the stability condition should simply be $a_{--}(\theta_d) > 0$. We are therefore allowed to explore the dynamics of a RF-dressed BEC at any externally imposed polarisation $\cos(\theta_d)$ as long as it gives a positive interaction strength g_{--}^{--}. If the minimum g_∞ is negative, then the polarisation $\cos(\theta_d)$ should not go too close to $\cos(\theta_\infty)$ as can be seen on figure 1.22.

On the contrary, the stability condition for the incoherent mixture are much stricter because they require stability for any mixture polarisation. Interestingly, they are equivalent to:

$$\begin{cases} g_{11} > 0 \\ g_{22} > 0 \\ g_{11}g_{22} > g_{12}^2 \end{cases} \Leftrightarrow \begin{cases} \overline{g} > 0 \\ g_\infty > 0 \end{cases} \tag{1.64}$$

To end this section, We give the simple expressions of all elastic and inelastic interaction strengths in the dressed-states basis in function of g_∞, $\overline{g}$ and θ_∞.

$$\begin{cases} g_{--}^{--} &= g_\infty &+ \overline{g} & (\cos\theta_d - \cos\theta_\infty)^2 \\ g_{++}^{++} &= g_\infty &+ \overline{g} & (\cos\theta_d + \cos\theta_\infty)^2 \\ g_{+-}^{+-} &= g_\infty &+ \overline{g} & (\sin^2\theta_d + \cos^2\theta_\infty - \cos^2\theta_d) \\ g_{--}^{++} &= &\overline{g} & \sin^2\theta_d \\ g_{--}^{+-} &= &\overline{g} & \sin\theta_d\,(\cos\theta_d - \cos\theta_\infty) \\ g_{++}^{+-} &= &\overline{g} & \sin\theta_d\,(\cos\theta_d + \cos\theta_\infty) \end{cases} \tag{1.65}$$

Interestingly, the state-changing transitions (inelastic), have interaction strengths independent of the interaction offset g_∞. We shall come back in further chapters to the physical appearance of these inelastic interaction strengths in our experiments.

1.5 chapter conclusion

In this chapter, we gave an overview of some few-body properties of dilute quantum gases. Starting from the definition of two-body scattering length, we justified the use of effective contact potentials to study the macroscopic dynamics. We then presented the dependence of the scattering lengths with magnetic field for potassium ^{39}K given by Feshbach resonances, and allowing us to tune, to some extent, the strengths of the two-body interactions g_{ij}

Secondly, we discussed the stability of a BEC of potassium ^{39}K both on the microscopic scale and macroscopic scale, by considering two-body inelastic collisions, three body-recombinations and also the compressibility self-equilibrium of the gas. This imposes severe restrictions on the available internal state for the BEC and on the value of magnetic field we apply on the gas. For a binary mixture, the window of stability is even narrower. In summary, we will work only with the $|1\rangle$ and $|2\rangle$ states, and between 33.6 G and 58.8 G.

In a third part, we came back on the effect of magnetic fields on the lowest internal states : the non-linear Zeeman effect caused by a constant magnetic field and the coherent coupling induced by a resonant RF-magnetic field. This leads to an effective two-level Rabi Hamiltonian with a detuning δ and non diagonal constant coupling $-\Omega$. Rather than Rabi oscillations, we are more interested in adiabatic sweep because they allow us to maintain the atoms in a state of minimal energy, the $|-\rangle$ dressed state. This state is a quantum superposition of $|1\rangle$ and $|2\rangle$.

Lastly, we started to study theoretically the RF-dressed BEC at the two-body level. Collision between two atoms in $|-\rangle$ state are elastic and short-range, we gave the full mathematical solution of the two-body scattering problem to compute the scattering length and the effective range. Then, we took the perspective of second quantization to write the two-body contact Hamiltonian on the dressed states basis. On this basis, the elastic and inelastic interaction strength are more elegantly expressed in terms of the three parameters $\overline{g}$, g_∞ and θ_∞. We concluded on the double tunability of the interaction strength g^{--}_{--} with the magnetic field and the ratio δ/Ω. It has a minimum for $\theta_d = \theta_\infty$ equal to g_∞ and can go up to roughly $\overline{g} \gg |g_\infty|$. The tunability with respect to the internal state, which is externally chosen, is large.

Chapter 2

2. The ^{39}K experiment : maintenance and improvements

In this chapter, we present the experimental works of the ^{39}K team apart from the data-taking covered by our publications. The overall "cooling to quantum degeneracy" sequence was working quite well even before 2020, but day to day adjustments certainly changed a few steps and their performances. Therefore, we start with a quick summary of the current state of the experiment. Then, we present the troubles encountered with RF adiabatic sweeps on thermal gases during the cooling sequence. We pursue with the installation and characterisation of a box-trapping device or flat potential. Finally, we present the recent addition of an absorption imaging setup, the chosen optical transitions and a first evaluation of its performances after optimization.

2.1 Current cooling sequence

2.1.1 Magneto optical traps (MOT) and optical molasses

In the resting state of the potassium experiment, atoms are continuously pushed out of a 2D MOT located above the potassium oven into the 3D MOT located in the glass cell of the science chamber. Both MOTs work on the D_2 optical transition ($^2S_{1/2} \leftrightarrow {}^2P_{3/2}$) with principal and repumping beams[1]. Only three seconds are needed for the 3D MOT to load to saturation with a total number of atom of 2×10^9 and a temperature of 3 mK. The cooling sequence, computer controlled, starts with 12 ms of compressed hybrid MOT with increased magnetic gradients, the D_2 repump beams and the D_1 ($^2S_{1/2} \leftrightarrow {}^2P_{1/2}$) principal beams. It is followed by a gray molasses lasting 6.7 ms and working with the principal and repump of the D_1 optical transition. The temperature is then around $6\mu K$ and the rms size of 1 mm.

fig/2/molasses.png

Figure 2.1: Optical molasses seen from above after 0.3 ms time of flight

[1]The frequency detunings are already summarised in Lucas Lavoine PhD manuscript[27].

2.1.2 Transfer with a magnetic quadrupolar trap

After the gray molasses cooling, atoms are optically pumped into the state $|8\rangle = |F = 2, m_F = 2\rangle$ with a σ^+ polarised beam coming from below the science chamber with resonant principal and repumping of the D_1. The duration of the transfer is $200\mu s$. Atoms in state $|F = 2, m_F = 2\rangle$ can be trapped at a minimum of magnetic field (low-field seeker) and are stable with respect to two-body collisions (stretched state). The quadrupole magnetic trap centered on the cloud is then turned on in 35 μs. It contains approximately 6×10^8 atoms with a temperature of $300\mu K$ explained by the heating caused by the transfers and loading.

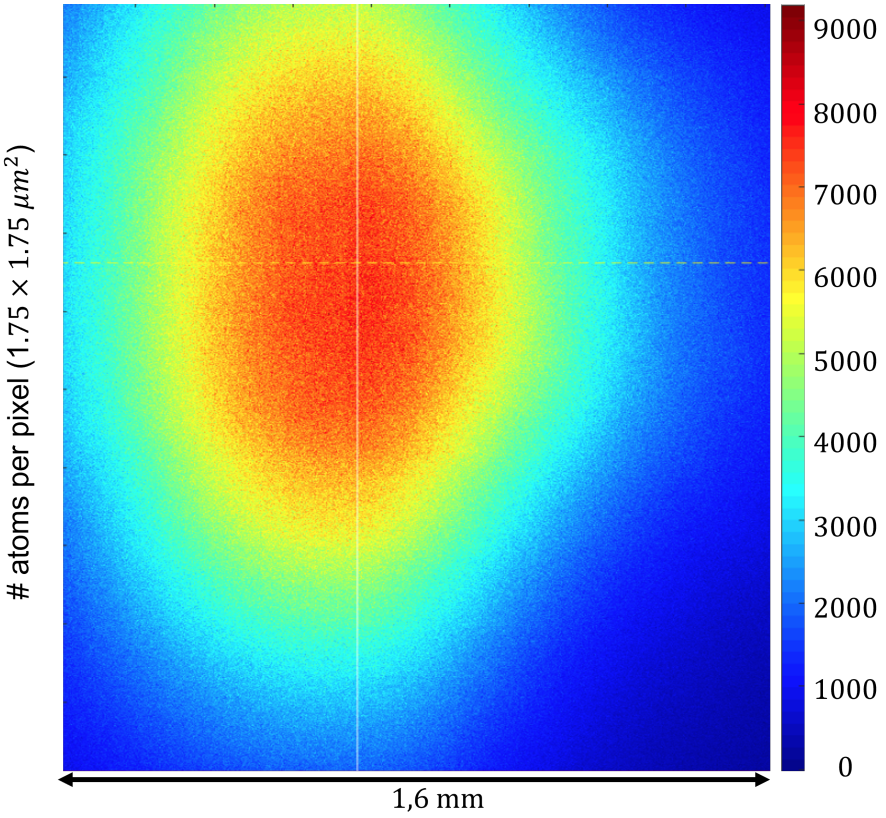

Figure 2.2: Atoms trapped in the quadrupole seen from the side after a time of flight of 0.3 ms

The quadrupole is then compressed and moved of a few hundreds of micrometers to enable a good loading of atoms into the first optical dipole trap. This trap consist in a 1550 nm laser beam which is called FORT1 (far-off-resonance trap). It comes from a fiber IPG (ELR-30-1550- LP) with an output power of 30 W. The power arriving on atoms in the science chamber is up to 19 W and the beam waist is such that we have the following parameters at max power:

- Depth $U \simeq k_B \times 3\text{mK}$
- Radial trapping frequency $\omega_r \simeq 14$ kHz
- Axial trapping frequency $\omega_r \simeq 300$ Hz

2.1.3 Evaporation in Far-off-resonance optical traps (FORT)

After the loading of atoms into the FORT1 beam (see figure 2.3), they are transferred to the internal state $|2\rangle$ to ultimately get a condensate in this state. The transfer happen in three consecutive adiabatic sweep. However, a first evaporative cooling is performed before because it is important to reduce quickly the density to limit three-body losses. This first evaporation lasts 100 ms and the power of the beam is decreased exponentially to 6 % with a characteristic time of 35 ms. We get a cloud of 5×10^6 atoms at a temperature of about $20\mu K$. We then apply the three consecutive RF adiabatic sweeps.

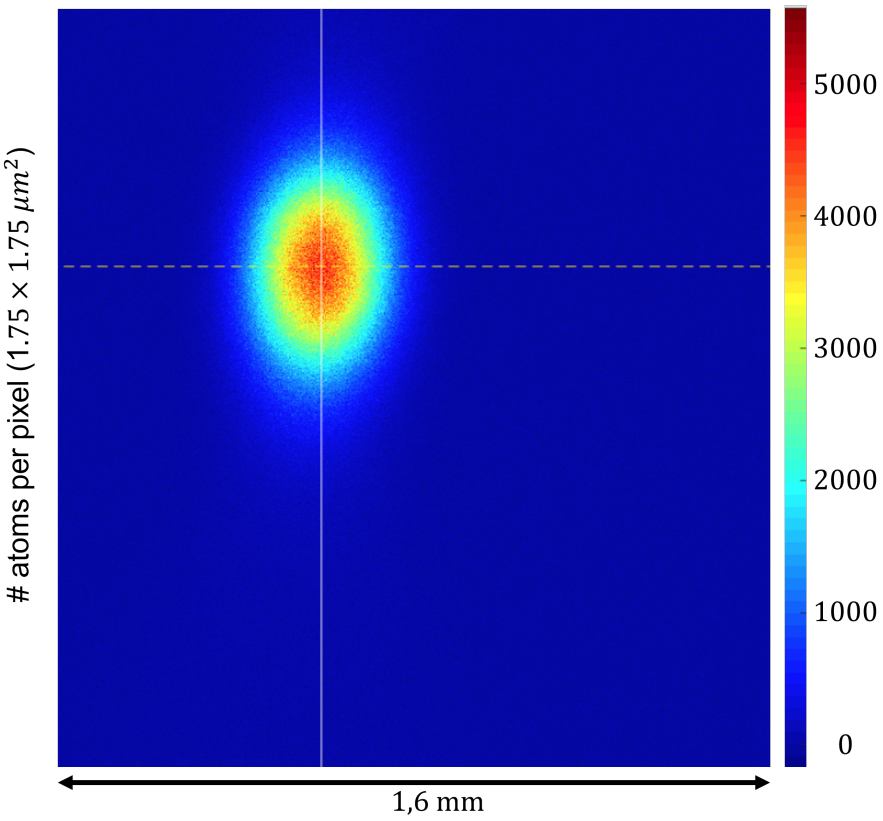

Figure 2.3: Freshly loaded far-off-resonance trap 1 (FORT1) seen from the side after a time of flight of 0.3 ms

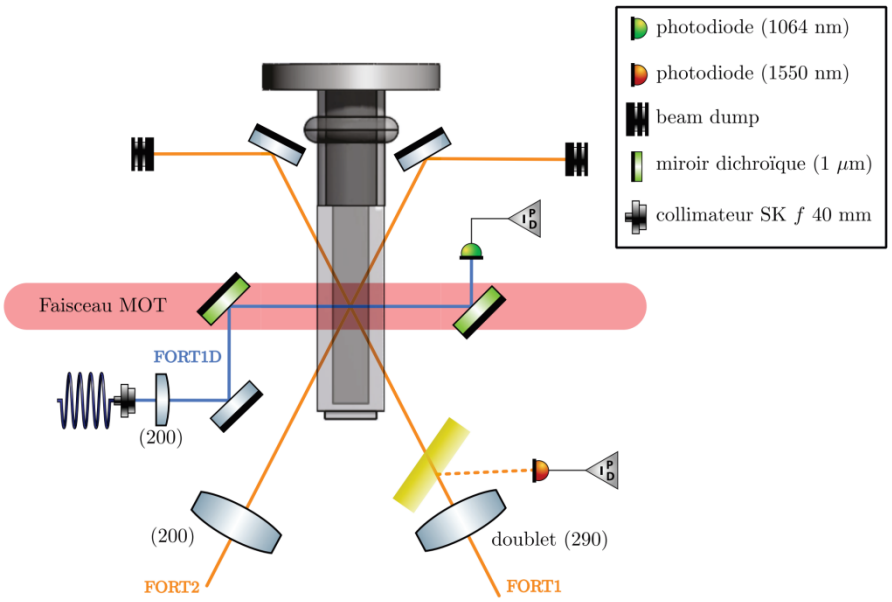

Figure 2.4: Optical setup of the three dipole traps: FORT1, FORT2 and FORT1D

The condensation is achieved after several evaporative coolings and transfers to two other infrared beams crossing the cloud from other angles. The three beams are horizontal and approximately at angles $\pi/3$ of each others (figure 2.4). The FORT2 which also comes from the 1550 nm laser has a larger waist than the FORT1. Its role is at first to ensure a longitudinal trapping when the FORT1 beam is decreased during evaporation. After 500 ms of evaporation in these two beams, the FORT1D beam is turned on. It comes from a 1064 nm fibre laser of max power 0.5 W. The final evaporation towards condensation lasts 2000 ms. It happens in the crossing of FORT2 and FORT1D. After condensation, the frequencies of the traps can be changed slowly. the radial frequency is fixed by the FORT1D and is chosen between 100 Hz and 500 Hz, the axial frequency is fixed by the FORT2 and is between 7 Hz and 100 Hz. Condensates have a typical number of atoms of 1.5×10^5 and a temperature around 100 nK.

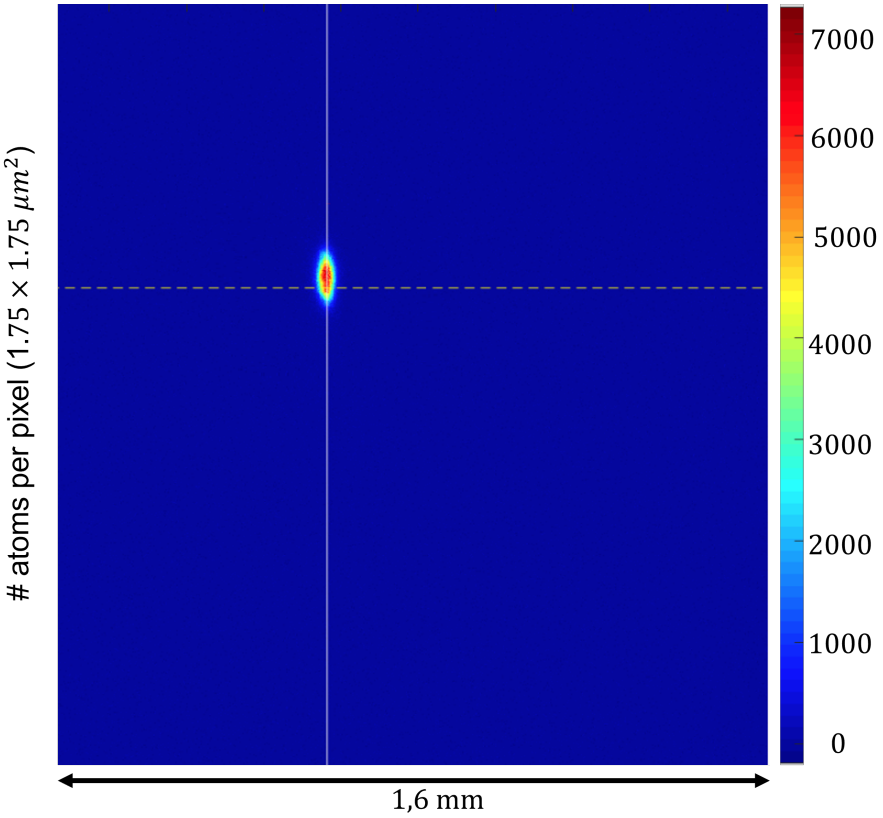

Figure 2.5: Cloud at the beginning of the last 2000 ms evaporative cooling leading to condensation, seen from the side after a time of flight of 0.3 ms. At this stage the FORT1 beam is off and atoms are trapped in the crossing of the FORT2 and the FORT1D. The number of atom is 0.8×10^6.

2.2 Non-adiabatic sweeps on trapped thermal gases

2.2.1 Observation of the phenomenon

After the first evaporation, the atoms are transferred from state $|8\rangle = |F = 2, m_F = 2\rangle$ to state $|2\rangle$. This change of internal state happen with three consecutive RF sweeps around different resonant transitions. The time sequence is summarized below:

- 5ms sweep around 473 MHz with a slope of 1 MHz/ms to transfer atoms from state $|8\rangle$ to state $|0\rangle$.
- 2ms sweep around 30.3 MHz with a slope of 0.7 MHz/ms to transfer atoms from state $|0\rangle$ to state $|1\rangle$.
- 2ms sweep around 37.0 MHz with a slope of 0.7 MHz/ms to transfer atoms from state $|1\rangle$ to state $|2\rangle$.

Remember that at low magnetic field, the state are asymptotically equal to:

- $|0\rangle \to |F = 1, m_F = 1\rangle$
- $|1\rangle \to |F = 1, m_F = 0\rangle$
- $|2\rangle \to |F = 1, m_F = -1\rangle$

The magnetic field during the first transfer is 5 Gauss to have a well define quantization axis but an experimentally reachable resonance frequency ($\leq$ 500 MHz). For the last two sweep, the magnetic field is 52 Gauss to clearly separate the two transitions (see 1.3.1) and to be already close to the magnetic field at which condensation will be achieved ($B = 40G$). At any time of the experiment, we are able to measure the internal state of atoms with a Stern-Gerlach experiment (5ms Magnetic field gradient followed by a few ms of time of flight). It was then observed that only the last transfer from $|1\rangle$ to state $|2\rangle$ was imperfect, with at least 5 % of atoms remaining in the initial internal state at the end of the sweep.

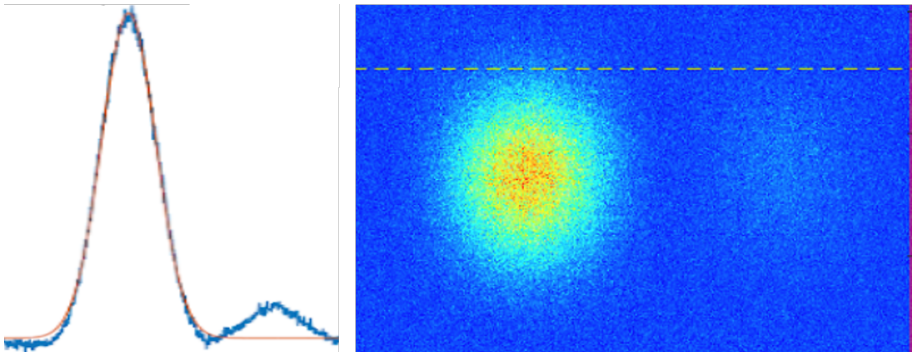

Figure 2.6: Typical result of a Stern-Gerlach experiment performed after the third sweep on the thermal cloud. The left cloud consists in atoms in state $|2\rangle$ while the right cloud gives the unwanted population in $|1\rangle$.

2.2.2 Possible physical origins

Standard non-adiabadicity : speed of the frequency scan

For the last transfer, we use our RF generator at maximum power. The Rabi frequency is then around 40 kHz. For a linear sweep, the adiabatic criterion is most restrictive around resonance and writes (see 1.3.1) $\left|\frac{d\delta}{dt}\right| \ll \Omega^2$. The criterion is well verified with the 40 kHz Rabi frequency and the linear slope of 0.7 MHz/ms with a small dimensionless parameter (ratio of the sweep slope with Ω^2) of 0.07. Therefore, the explanation likely lies elsewhere.

Detuning wobbling induced by oscillations in the dipolar trap

Another possible phenomenon is a wobbling of the detuning felt by an atom as it moves in the optical dipolar potential. Indeed, because the atomic structure is more complex than a two-level system, the trapping potential slightly depends on the projection of total angular momentum m_F. At low magnetic field and for a far-detuned laser, the potential felt by an atom in a state $|F, m_F\rangle$ reads [28]:

$$U_{\text{dip}}(r) = \frac{3\pi c^2 \Gamma}{2\omega_0^3(\omega - \omega_0)} \left(1 + \frac{1}{3}\mathcal{P} m_F g_F \frac{\Delta_{FS}}{\omega - \omega_0}\right) I(r) \tag{2.1}$$

Where $\Delta_{HF} \simeq 1.7 \times 10^{12}$ Hz is the difference in energy between the centers of the $^2P_{1/2}$ and $^2P_{3/2}$ manifolds, $\mathcal{P} \in [-1, 1]$ is the helicity of the FORT1 beam around the vertical axis and should be almost zero because the laser is linearly polarised horizontally. Note however that the magnetic field during the third transfer is 52 G which implies that internal

states $|i\rangle_{0\leq i\leq 8}$ have ill-defined quantum F number (Breit Rabi regime) but well-defined m_F. We expect formula 2.1 to be slightly modified by the replacement of Landé factor g_F by a number depending on internal state but close in order of magnitude.

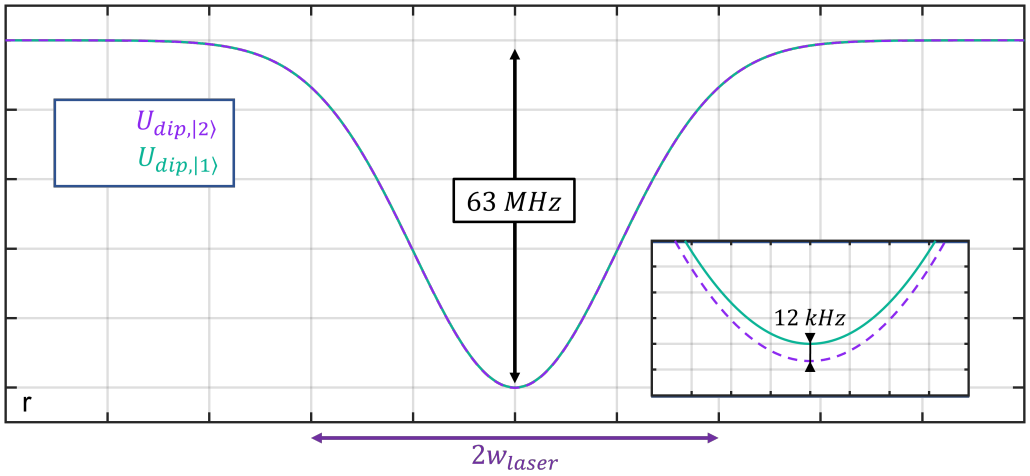

Figure 2.7: Radial dipolar potential felt by atoms depending on their internal state. *Inset:* $\times 1000$ zoom at the center of the trap.

On the right-hand side of equation 2.1, the zeroth order term (independent of m_F) simply gives the same negative Gaussian potential for all 8 hyperfine states of the $^2S_{1/2}$ manifold, with a total depth of 3 mK (63 MHz) for a FORT1 at max power. The first order term gives a relative correction in trapping potential of the order of 2×10^{-4} between two states with $\Delta m_F = 1$ (with an unfavorable estimation of $|\mathcal{P}|$ equal to 0.1). This gives an additional detuning of 12 kHz at the center of the trap.

In addition, the detuning felt by an atom as it moves in the trap changes at the double of the trap frequency, 28 kHz at maximum power. This frequency is close to the Rabi frequency so, even a low amplitude, this detuning wobbling may lead to resonant transfer from state $|-\rangle$ to $|+\rangle$. We can check numerically the non-adiabadicity caused by a sinusoidal fluctuation of the detuning $\delta_{dip}(t) = A\sin(2\pi f t)$ with $f = 28$ kHz and $A = 3$ kHz.

Although we accepted at first this detuning wobbling as the most probable cause of non adiabadicity, it fails to describe experimental observations:

- Only the third transfer is difficult, the second transfer works well in the experiment. Meanwhile the detuning wobbling model predicts the same non-adiabadicity for both.
- A resonance between the Rabi frequency and twice the frequency of the optical dipole trap is not observed experimentally.
- The sweeps are performed after a first evaporative cooling so the power in the FORT1 is not its maximum value but rather at 1/20 of it. With a trap frequency multiplied by $\sqrt{0.05}$, the numbers don't match anymore and the numerical simulation suggest that the sweep should be adiabatic
- There is no physical explanation on why the laser helicity $\mathcal{P}$ is not zero in the model. The polarisation of the beam was precisely adjusted as linear horizontal by former phD student Guillaume Berthet (as detailled in his manuscript [29]).

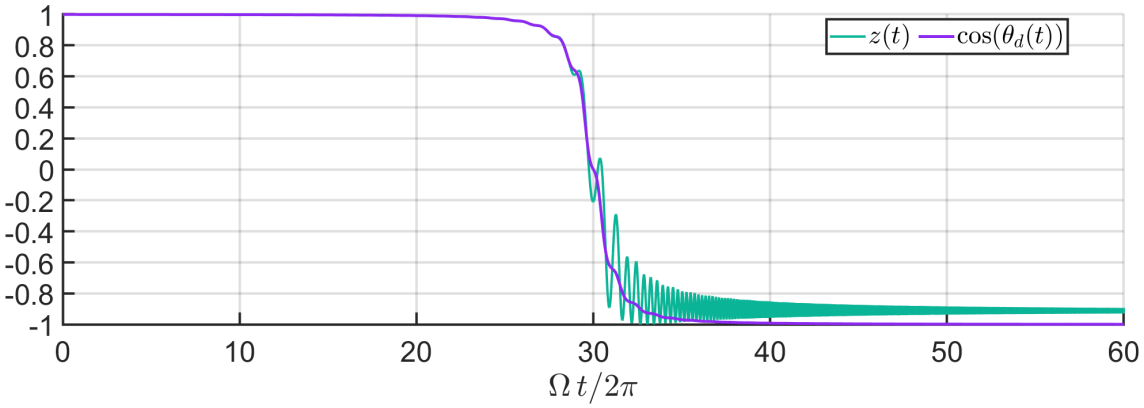

Figure 2.8: Numerical simulation of internal polarisation $z(t)$ of an atom for a linear sweep with an additional sinusoidal fluctuation of detuning. The effect of the wobbling is slightly visible on the targeted mixture polarisation $\cos(\theta_d(t))$ but the non adiabadicity it causes is even more striking. At the end of the sweep, a tenth of atoms are in the incorrect internal state ($|1\rangle$ instead of $|2\rangle$). For the simulation, the parameters are those of the third sweep in the experiment (2 ms duration and 0.7 MHz/ms slope), the Rabi frequency is taken to 30 kHz.

Two-body inelastic collisions

A more convincing physical origin is given by two body inelastic collisions where two atoms in a dressed state $|-\rangle$ collide and exit the interaction zone in a more energetic internal state, the final internal state of the pair is either $(+-)$ or $(++)$. The conservation of energy requires that the initial relative kinetic energy of the two atoms was at least $\hbar\tilde{\Omega}$ or $2\hbar\tilde{\Omega}$. This is of course possible in a thermal gas if the thermal energy k_BT is bigger than the Rabi energy $\hbar\tilde{\Omega}$. If we integrate out the spatial degrees of freedom of an atom, position and velocity, given by Boltzmann factors for a thermal gas, we should get an effective transfer rate from state $|-\rangle$ to state $|+\rangle$ due to two-body inelastic collision. Note that the two particles are not lost because their kinetic energy actually diminishes. The reversibility of the processes is irrelevant if the population in state $|+\rangle$ remains small which we assume here.

$$\frac{dn_-}{dt} = -\Gamma^{+-}_{--}n_- - 2\Gamma^{++}_{--}n_- \tag{2.2}$$

The temperature of the gas in the FORT1 during the sweep, is around 20 μK which is still in the limit for s-wave collision $k_BT \ll 2\hbar^2/(mb^2_{vdW}) = 500\mu K$. Therefore, two-body collisions mostly happen at zero angular momentum. The total cross sections, of both inelastic processes at relative wave-vector $\vec{k}$, are in good approximation independent of k and expressed in term of the s-wave scattering lengths (see 1.4.2 and [24]):

$$\begin{cases} \sigma^{+-}_{--} &= 4\pi\left(\overline{a}\sin(\theta_d)\left(\cos(\theta_d)-\cos(\theta_\infty)\right)\right)^2 \\ \sigma^{++}_{--} &= 8\pi\left(\overline{a}\sin(\theta_d)^2\right)^2 \end{cases} \tag{2.3}$$

With a rule of thumb, we can guess the following scaling for the inelastic processe rates:

$$\Gamma_i = 2\sigma_i\overline{v}n_-f \tag{2.4}$$

Where σ_i is the scattering cross section of the process and $\overline{v}$ the typical relative velocity of the pair of atoms. f is the fraction of pair of atoms which have an initial relative kinetic

energy above the threshold $\hbar\tilde{\Omega}$ or $2\hbar\tilde{\Omega}$. It may be taken to 1 for a thermal gas with kinetic energy $k_BT \gg \hbar\tilde{\Omega}$. The relatively high value of $\overline{a}$ for the two states $|1\rangle$ and $|2\rangle$ around 40 to 60 Gauss ($\overline{a} \simeq 40a_0$) are likely explain why two-body inelastic collisions are only observed during the third adiabatic sweep.

Finally, we may summarize that the total decay rate $\Gamma_{tot} = \Gamma^{+-}_{--} + 2\Gamma^{++}_{--}$ due to inelastic processes is proportional to the density of atoms n_-, to the square of the scattering length $\overline{a}$ and to the square root of the temperature $\overline{v} \propto \sqrt{T}$. We estimate the density by a Boltzmann distribution and get a peak density of $n \simeq 2.4 \times 10^{19}\,\mathrm{m}^{-3}$. This gives a typical inelastic collision rate of $\Gamma_{tot} = 10^3\,\mathrm{s}^{-1}$ which explains a 10% non-adiabadicity of a 2 ms sweep (remember that the inelastic process happen only around the resonance which represent a tenth of the duration of the full sweep). Finally, we conclude that these inelastic two-body collisions may be the dominant cause of non-adiabadicity of the third sweep. The experimental scan below confirms this hypothesis through the dependence of the adjustable parameters.

2.2.3 Experimental scan

The two parameters we can adjust to reduce the non-adiabadicity of the third sweep are the power in the FORT1 beam at the end of the first evaporation and the duration of the sweep (thus also changing the slope in MHz/ms).

- Firstly, a decrease of the optical dipole trap power mainly decreases the density of atoms during the sweep, which in turn decreases the inelastic collision rate. However the FORT1 power should not be decreased too much otherwise too many atoms are lost during the first 100 ms evaporation without any gain in the phase space density. Based on recent experimental scans, we decided to change the power of the FORT1 beam at the end of the first evaporation from 10% to 6%.
- Secondly, a decrease of the duration of the sweep is favorable because in the limit of very fast sweep, inelastic two-body collisions do not have time to occur. We can only reduce the duration of the sweep up to the point where it becomes naturally non adiabatic because of a too high frequency slope.

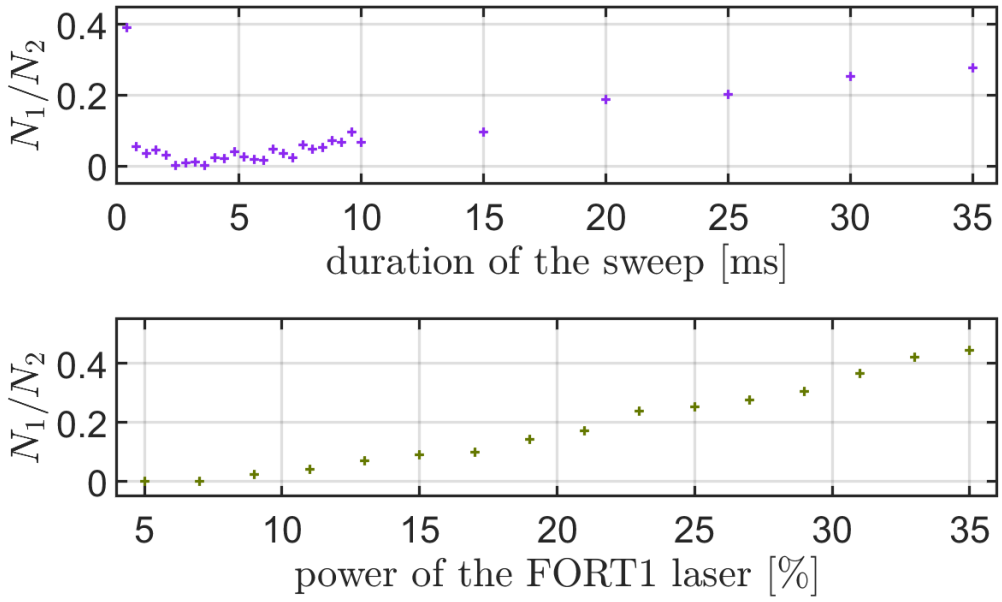

Figure 2.9: *(Top)* Fraction of atoms in the incorrect state ($|1\rangle$) at the end of the third RF sweep in function of the duration of the sweep. Below 2.4 ms, the non-adiabadicity is simply due to a too high frequency slope. Above 3.6 ms, the frequency slope is small but the inelastic collisions, $(--) \rightarrow (++), (+-)$, starts to be visible. For this scan, the power in the FORT1 trap was set to 10%. *(Bottom)* Fraction of atoms in the incorrect state ($|1\rangle$) at the end of the third RF sweep in function of the power in the FORT1 laser beam. Two-body inelastic collisions are more visible at high powers because it increases the density and the temperature. For this scan, the duration of the sweep was 10 ms.

2.3 Box trapping with digital micro-mirror device (DMD)

2.3.1 Optical setup

A digital micro-mirror device (DMD) consist in an array of mirrors with two possible inclinations electronically controlled by computer. In our case, the array contains 1920 × 1080 square mirrors of size $7.56\,\mu m$. The two inclinations of each mirror are $\pm 12.5\,^\circ$ and should correspond, in an appropriate optical setup, respectively to an on-state and an off-state (see figure 2.10). We shine a collimated laser beam on the mirror plane. The laser is a Verdi 532 nm (green) one with maximal output power of 15W. The waist of the laser, initially of 1.56 mm, is firstly multiplied by 20 with an a-focal telescope with two lenses of focal lengths $f_1' = -12.5\,mm$ and $f_2' = 250\,mm$. The beam then arrives on the DMD with an angle, adjusted experimentally, so that the specular reflection from mirrors in the on-state almost coincides with a maximum of intensity for the grating diffraction by adjacent mirrors. More importantly, the beam reflected by on-state mirrors is orthogonal to the DMD plane which allows a conjugation of the DMD plane with the atom plane. This is done by adjusting the height of an objective (chromatic triplet) above the science chamber. Because the optical access is also used by the top camera, we use a dichroic mirror to engage the green beam into the vertical axis (see figure 2.11).

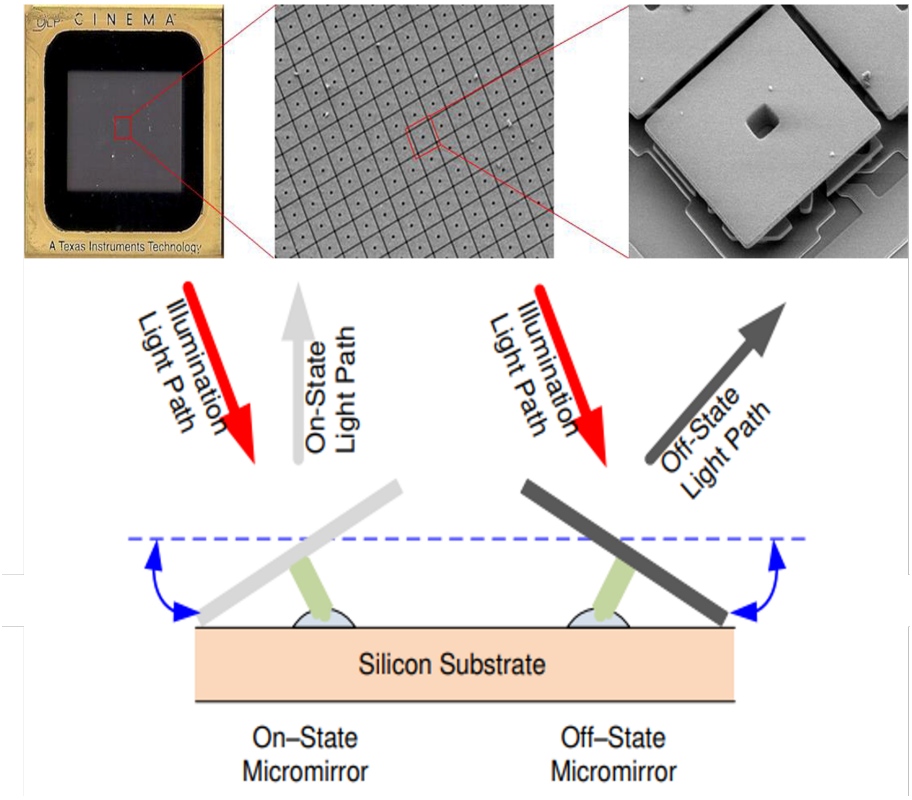

Figure 2.10: Picture of a digital micro-mirror device and its working principle

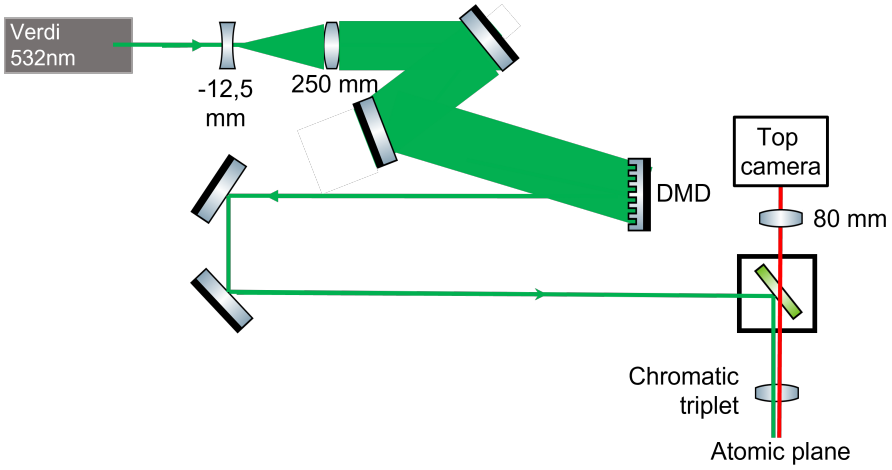

Figure 2.11: Optical setup used with the DMD and the green laser to produce box potentials on atoms.

2.3.2 Focusing protocol

The DMD setup allow to print a repulsive 2D potential in the atom plane. The formula is given by the far-off-resonance dipole potential:

$$U_{Verdi}(x,y) = \frac{3\pi c^2 \Gamma}{2\omega_0^3(\omega - \omega_0)} I(x,y) \tag{2.5}$$

The laser frequency ω is blue detuned with respect to the atomic D transition line at ω_0. Therefore the applied potential is repulsive. When the DMD plane is correctly conjugated optically with the atomic plane, the intensity profile is almost given by the binary map of on/off DMD pixels. Only the diffraction by the chromatic triplet lens perturbs this result of classical optics. We will come again to this in the next subsection. On the contrary, when the image of the DMD is not in the atomic plane, the target intensity profile appears grossly blurred in the atomic plane. The intensity of on-state pixels is spread-out and the height of the potential hill at the pixel location is decreased. This observation is the basis of the focusing protocol.

Firstly, we draw a centered cross of on-state pixels on the DMD. Using the green laser at low power (typically 0.1 mW for security), we get a collimated beam with a cross intensity profile and we align this beam on the vertical optical axis passing through the science chamber. The cross then becomes visible on the top camera thanks to two partial reflections on the glass-cell walls. With this camera in live-recording mode, we precisely align the center of these two crosses on the location of the condensate (which we simply get from a single shot of the experiment). At this stage, the DMD optical setup is already able to print a 2D potential on atoms. We turn on the verdi laser at its 15W max output power (an AOM serves as an off-switch for the rest-state of the experiment). However, only a fraction of the power arrives on the reflective part of the DMD because the beam is voluntarily enlarged. In addition, the grating diffraction limits the power reflected in the direction of the atomic plane. We estimate the order of magnitude of maximum repulsive potential to 10^4 Hz (0.5μK) for a DMD optically conjugated with the atomic plane.

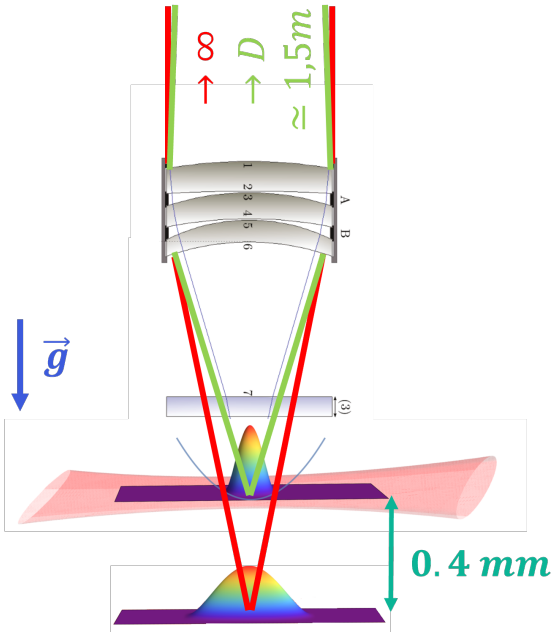

Figure 2.12: Setting at focus for the DMD and location of the plane conjugated with the camera sensor for red light (770 nm) and location of the plane conjugated with the DMD (atomic plane) for green light (532 nm). The location of the atomic plane is imposed by the final optical dipole trap (FORT1D) schematised in red. A free fall of 9ms moves the atoms from the atomic plane to the plane at focus for red light.

The vertical position of the objective is, at first, such that the fluorescence image of the cloud is at focus on the top camera. However, the focal length of the objective is 42.7 mm at 770 nm while it is 41.2 mm at 532 nm. In addition, the DMD is not at infinity but approximately 1.5m before the objective. According to geometrical optics, the DMD image is, in this initial setting, formed in the plane 0.4 mm above the atomic plane. To correct this, we lower the objective so that the camera is at focus with the plane 0.4mm below the atomic plane. This plane is given by a free fall of 9ms ($gt^2/2 \simeq 0.4$ mm) of an ultra-cold cloud (See figure 2.12). The above protocol is based on estimations of the parameters (for example distance D) and it is preferable to finish the focusing protocol with a fully experimental optimization detailled below.

We start with a thermal cloud of 10^6 atoms at temperature below $1\mu K$ in a harmonic trap with frequencies $\omega_r = 300$ Hz and $\omega_z = 20$ Hz. The radial frequency is given by the FORT1D beam and the axial frequency is given by the FORT2 beam. We apply a box potential in the axial direction with the DMD then we release the trapping in this direction by ramping down the FORT2 trap to zero. After 40 ms of expansion in the axial direction, we image the cloud to see if the box potential was strong enough to trap all atoms. The axial size of the box is 400 DMD pixels and the width of the wall of potential is 2 DMD pixels. Classical optics tell us that the magnification factor between the DMD plane and the atomic plane should be around $\gamma = -1/37$ so that each DMD pixel is equivalent to a square of 0.2 μm side in the atomic plane. Diffraction by the objective spreads out the intensity of the wall barrier according to a pattern close to sinc function (cardinal sinus) with first cancellation at $\simeq 1\,\mu$m. We get an effective wall of potential much wider and smaller (see figure 2.13). In addition, we decrease the power of the green laser to be just below the threshold for atom trapping (typically $k_BT/2$). We then move the vertical position of the objective of $\pm 20\,\mu$m and check if the trapping has improved or

not. By iterating this process, we are able to find the objective vertical position at which the potential walls are the least smeared , the precision of this protocol is $\pm 10\,\mu$m.

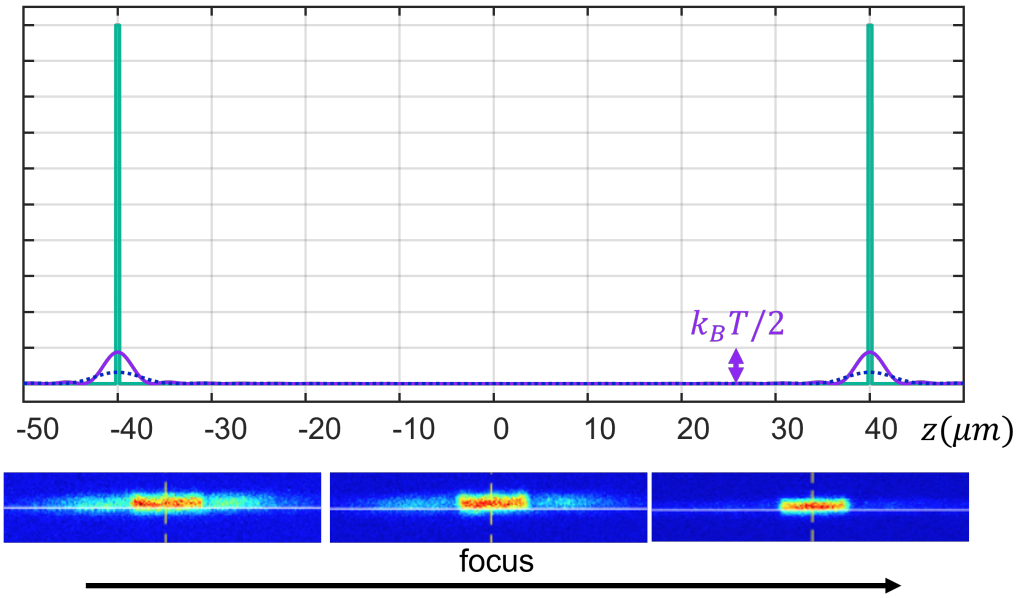

Figure 2.13: *Top:* Box potential applied on atoms, the indigo curve is the step potential predicted by geometrical optics. The purple curve is the potential in the atomic plane if it is at focus and taking into account the smearing by diffraction. The blue dotted curve is the potential in the atomic plane when out of focus: the smearing is wider than in the diffraction limit, the potential walls are smaller in height. *Bottom:* Typical density profiles observed during the focusing protocol

2.3.3 Calibration and performances

To calibrate the DMD setup, we investigated experimentally these three physical quantities:

- the magnifying factor
- the smearing due to the diffraction by the objective

Firstly, the magnifying factor was measured by applying a periodic binary potential with a period of 100 DMD pixels ($\simeq 20\,\mu$m in the atomic plane) on an elongated thermal cloud. After 20 ms of wait-time, the one-dimensional density profile has become periodic. This gives us a precise measurement of the magnifying factor: $\gamma = -1/38.2$ (figure 2.14).

Secondly, the smearing due to diffraction can be estimated given the numerical aperture of the objective $N.A. = 0.27$. The one-dimensional point-spread function for electric field E should be close to $PSF(x) = \frac{1}{\pi x}\sin\left(\frac{\pi x}{\sigma}\right)$ with $\sigma = \lambda/(2\,N.A.) \simeq 1\,\mu$m. The space coherence of the incident light in the DMD plane is total since it is laser light. In consequence, the electromagnetic fields reflected by adjacent DMD pixels and arriving at a given point of the atomic plane sum up coherently. The intensity at this point is proportional to the square of the total electric field amplitude. $I(x) = I_0\left|\int t(u)\,PSF(x-u)du\right|^2$ with $t(u = z/\gamma) \in \{0, 1\}$ the transmission factor of the DMD array at z.

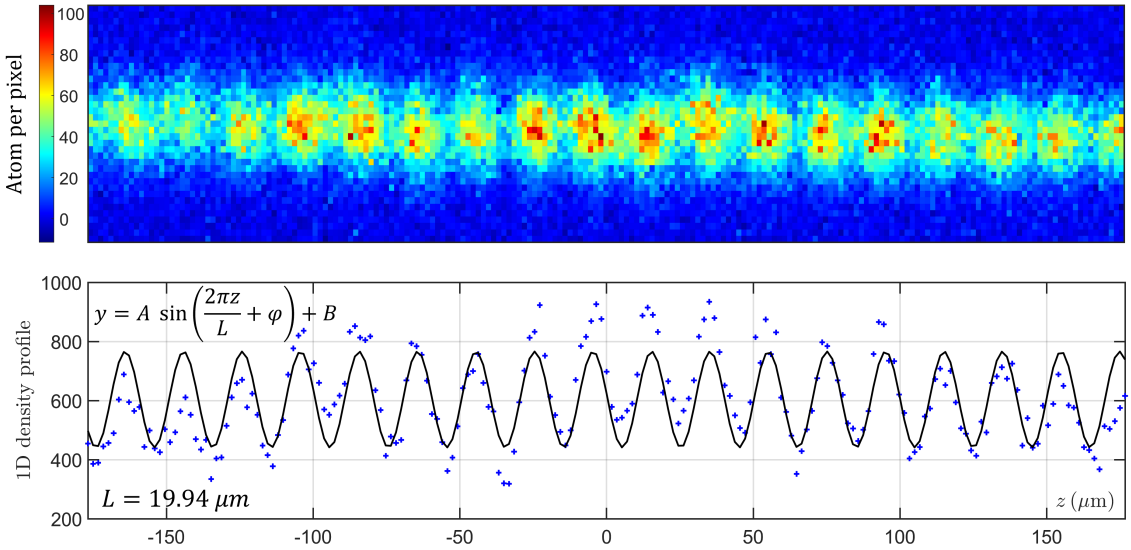

Figure 2.14: Experimental measurement of the magnifying factor for the DMD setup at focus with the help of a periodic potential.

The characteristic size σ of the point spread function can be measured through the transmission coefficient of a condensate launched on a set of two potential barriers of two pixels and separated by p pixels. This set of experiments was done by phD student Roy Eid during his master internship. The two potential barriers have a negative impact on each other when the maximum of the PSF of one is at the same location than the first negative minimum of the PSF of the other. In other words, the interference is destructive. This happen for a distance between the two barriers of 10 ± 1 pixels (see figure 2.15). According to the sinc function, this distance is theoretically equal to $1.43 \times \sigma$. The measure therefore yields the estimation $\sigma = 1.3 \pm 0.1\,\mu$m, 30% larger than the ideal diffraction limit $\lambda/2N.A$.

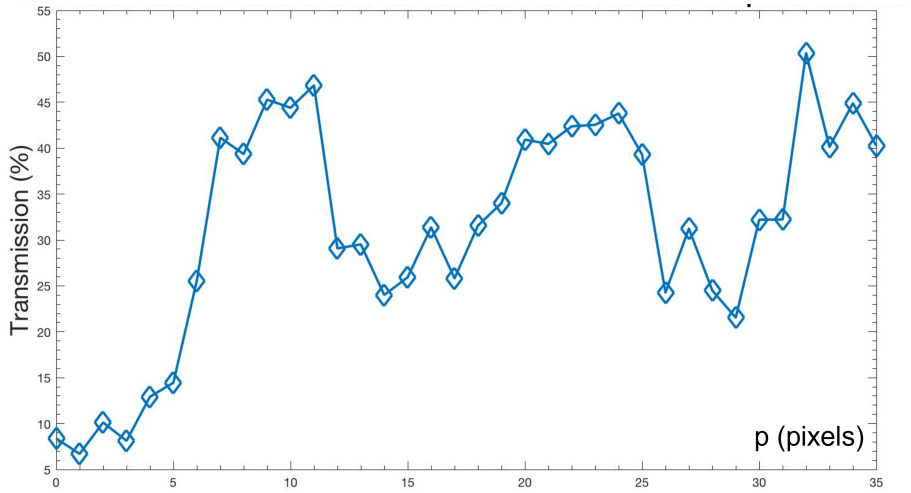

Figure 2.15: transmission coefficient of a condensate through a double barrier with p pixels between the two. The height of a single barrier is adjusted so that the quantum transmission on the barrier is close to 50% which in turn will increase the effect of interference between the two barriers.

2.4 Absorption imaging

2.4.1 Optical setup and cycling transition

In March 2022, we started the implementation of an absorption imaging setup on the vertical axis with the top camera. Geometrically, there was already a beam which could be directed on the atoms from below: the optical pumping beam, used between the optical molasses and the quadrupole, which contains both the principal and the repumping of the D_1 transition. In a first non-optimal setup, we did the absorption imaging with a hybrid combination of D_1 coming from below (absorbed) and D_2 in the MOT beams (repump).

To get a better cycling transition with only D_2 light, we modified the optical table. The principal of the D_2 can now be collected and injected into the optical fiber arriving below the science chamber. This beam has a σ_+ polarisation and replaces the D_1 optical pumping beam (now unused during absorption imaging). The MOT beams contain only the repump of the D_2 transition to depopulate states non-resonant with the absorbed beam ($^2S_{1/2}$ with $F = 1$). The frequency detunings and the intensities are adjusted experimentally:

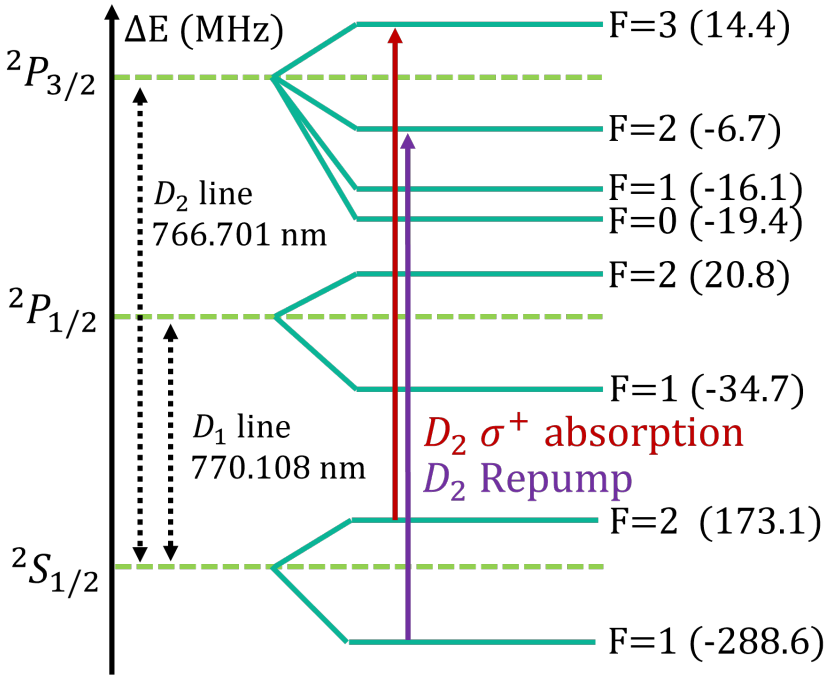

Figure 2.16: Optical transitions used for the absorption imaging. The absorbed light comes from below the science chambes, it has a σ^+ polarisation. The repump light come from the six 3D MOT beams, their sum allow all transitions with $\Delta m_F \in \{-1, 0, 1\}$.

2.4.2 Optimisation and performance

To compute the density of atoms with absorption imaging, we take three images on the camera with 30 μs of exposure time:

- the first image is the intensity profile I_{atoms} collected by the camera when the atoms are present. The absorbed beam, the repump beams and the ambient light are on.
- the second image is the intensity profile I_{no_atoms} collected by the camera after the 15 ms reading time of the first image. Atoms are not present. The absorbed beam, the repump beams and the ambient light are on.
- the third image is the intensity profile $I_{background}$ with only the ambient light of the room.

In good approximation, the absorption of the red resonant light by atoms is given by the formula:

$$\frac{dI}{dx} = -\sigma n(x) I \tag{2.6}$$

where $\sigma = \frac{3\lambda^2}{2\pi}$ is the absorption resonant cross section at small intensity compared to the saturation intensity and for the addressed two-level transition: $^2S_{1/2}, F = 2, m_F = 2 \longrightarrow {}^2P_{3/2}, F = 3, m_F = 3$. This equation is easily integrated and gives, after subtracting the ambient background light:

$$(I_{atoms} - I_{background}) = (I_{no\_atoms} - I_{background}) \exp\left\{-\sigma \int n dx\right\} \tag{2.7}$$

The number of atom in the volume covered by a pixel is given by integration over its area:

$$N = -C \log\left(\frac{I_{atoms} - I_{background}}{I_{no\_atoms} - I_{background}}\right) \tag{2.8}$$

The constant C should be equal to the ratio of the pixel area with the scattering cross section σ: $C_{theory} = 43$. However, the comparison between absorption and fluorescence imaging rather gives $C \simeq 230$. This suggests that the scattering cross section is not as big as expected. We believed that this is mostly due to the large spectral width of the red laser light, thus being only partly at resonance. We recently measured a laser width of 7 MHz with a two-lasers beats method. This is in agreement with the observed crossed section frequency width of 13 MHz for the absorbed beam, indeed the natural width of the D_2 transition is 6 MHz [7]. However, it is not enough to explain the discrepancy between C and C_{theory}, suggesting the existence of other limiting effects. Finally, in the near future, we aim at a better detectivity with the use of a recently bought 1560 nm laser with a frequency width of 2.3 kHz.

2.5 Chapter conclusion

In this chapter, we gave a quick reminder of the cooling sequence. It can be divided in three: the cooling and trapping with resonant red light, the magnetic trapping for the in-between and finally the evaporative cooling in far-off-resonance traps.
In a second part, we reported on the non-adiabadicity of sweeps between state $|1\rangle$ and $|2\rangle$ at 45 G and on thermal clouds. Different explanation were considered but only the inelastic two-body collisions model seemed relevant.
The third part focused on the installation and characterisation of a box-trapping device with a DMD and green laser light. This will for sure be useful in further experiments of the team.
Finally, we presented the beginning of the implementation of an absorption imaging setup. The performances and the atom detectivity can still be improved, therefore it is still a work in progress.

Chapter 3

3. Beyond-mean-field energy in ideal RF-dressed ^{39}K BEC

In this chapter, we will start to really study collective effects in RF-dressed quantum gases, with the theoretical tools given in chapter one. There, we focused on two-body physics of quantum gases, on the macroscopic stability of mixtures of BEC and finally, on the case of two-body collision in RF-dressed BEC. The specific aspects of potassium ^{39}K were mildly highlighted, in order to justify requirements for experimental stability of the gas. Notably, the two-body scattering lengths a_{ij} of ^{39}K are negative at most magnetic fields, causing effective attractive interactions for the macroscopic BEC. This dangerous phenomenon actually becomes a feature when working on BEC in states $|1\rangle$ or $|2\rangle$ between 33.6 G and 58.8 G. Indeed, with some care, it allows us to cancel perfectly the mean-field interaction energy.

After explaining in more details the underlying mechanism, we will talk about beyond-mean-field effects in quantum gases and our first attempt at measuring the so-called beyond-mean-field energy. After some surprising experimental results, we will present the theoretical understanding provided by D. Petrov and A. Recati: the analytic expression for the BMF energy of RF-dressed BEC will be given and compared to the case of incoherent mixtures of BEC. This will drive us to a discussion on analytic development for the ground state energy of quantum gases. We will then present the exact methodology and the experimental results of the first publication measuring BMF energy in RF-dressed BEC [2]. The article is attached at the end of this manuscript. Finally, we will report on experimental asymmetric losses, due to three-body recombination, observed during the measurement of BMF energy either in Rabi-driven or classical mixtures.

3.1 Mixtures of BEC with vanishing MF energy, deviation from ideal gases

3.1.1 Cancelation of mean-field energy of coherent and incoherent mixtures

The idea to study potassium ^{39}K BEC mixtures in state $|1\rangle$ and $|2\rangle$ around 56.8 G sprouted from D. Petrov article "Quantum mechanical stabilization of a collapsing Bose-Bose mixture" [30]. At the magnetic field of 56.8 G, pure BEC in state $|1\rangle$ and $|2\rangle$ are stable because $a_{11} \simeq 84.4a_0$ and $a_{22} \simeq 33.4a_0$. In other words, the intra-species interactions are repulsive. On the other hand, $a_{12} \simeq -53.2a_0 \simeq -\sqrt{a_{11}a_{22}}$[1]: the inter-species interactions are attractive and, in accordance with 1.24, they place any incoherent binary mixture of $|1\rangle$ and $|2\rangle$ at the edge between the homogeneous stability and the partial collapse. On the other hand, the interaction strength g_{--}^{--} for the coherent mixture, or RF-dressed BEC, has a minimum of $g_\infty = 0$ at a polarisation $\cos\theta_\infty = -0.218$ (see figure 1.22). By making either coherent or incoherent mixture with this polarisation, we can cancel exactly the mean-field interaction energy in the thermodynamic limit.

Mean-field states for homogeneous mixtures

We take an homogeneous binary mixture of condensates in a large box of volume V. Under the mean-field approximation (Hartree-Fock ansatz), all particles are in a state of zero-momentum. The normalized space wave-function is $\phi(r) = 1/\sqrt{V}$ so we shall rather focus on internal states. Moreover, the kinetic and trapping energies of the gas will vanish so the the total energy will simply be the expectation value of the two-body interaction Hamiltonian[2]:

$$E_{int} = \left\langle \hat{H}_{2b} \right\rangle = \frac{1}{2V} \left\langle \sum_{i,j} g_{ij} \hat{N}_i \hat{N}_j \right\rangle \tag{3.1}$$

Where operators $\hat{N}_i$ count the number of atoms in state $|i\rangle$ in the system.

The state of the system for an incoherent mixture of a BEC with N_1 particles in state $|1\rangle$ and a BEC with N_2 particles in state $|2\rangle$ reads:

$$|\Psi_{incoh.}\rangle = \frac{\left(a_1^\dagger\right)^{N_1}}{\sqrt{N_1!}} \frac{\left(a_2^\dagger\right)^{N_2}}{\sqrt{N_2!}} |vac\rangle \tag{3.2}$$

Meanwhile, the coherent mixture corresponds to a BEC with $N = N_1 + N_2$ particles in internal state $|-\rangle = \sin(\theta_d/2)|1\rangle + \cos(\theta_d/2)|2\rangle$. This system has the same polarisation than the incoherent one under the condition $N\cos(\theta_d) = N_2 - N_1$, and the state of the system reads:

$$|\Psi_{coh.}\rangle = \frac{\left(a_-^\dagger\right)^{N}}{\sqrt{N!}} |vac\rangle \tag{3.3}$$

[1] the equality shall be achieved exactly experimentally by scanning the magnetic field
[2] we also forget the constant Rabi energies of the $|-\rangle$ particles in the RF-dressed case

Mean-field energies in the thermodynamic limit

Let's assume the mixtures were made with the polarisation that minimize the interaction energy of the incoherent mixture, given by equations 1.25. A further simplification can be made thanks to the equality $a_{12} = -\sqrt{a_{11}a_{22}}$:

$$\frac{N_1}{N_2} = \frac{a_{22} - a_{12}}{a_{11} - a_{12}} = \frac{\sqrt{a_{22}}}{\sqrt{a_{11}}} \tag{3.4}$$

Of course, we can also verify with the second equation of 1.25 that the mixture polarisation $\cos\theta_d$ coincides with the polarisation $\cos\theta_\infty$ which minimizes g_{--}^{--}:

$$\cos\theta_d = \frac{N_1 - N_2}{N_1 + N_2} = \frac{a_{22} - a_{11}}{a_{11} + a_{22} - a_{12}} = \cos\theta_\infty \tag{3.5}$$

Under the thermodynamic limit, we can now compute the mean-field energies:

$$\begin{aligned} E_{incoh.}^{MF} &= \frac{1}{2V}\left(g_{11}N_1(N_1-1) + g_{22}N_2(N_2-1) + 2g_{12}N_1N_2\right) \\ &= \frac{1}{2V}\left(g_{11}N_1^2 + g_{22}N_2^2 + 2g_{12}N_1N_2\right) + o(\frac{N^2}{V}) \\ &\simeq \frac{1}{2V}\left(\sqrt{g_{11}}N_1 - \sqrt{g_{22}}N_2\right)^2 \\ &\simeq 0 \end{aligned} \tag{3.6}$$

For the coherent mixture, we use the two-body Hamiltonian written in the $|\pm\rangle$ basis (equation 1.55):

$$\begin{aligned} E_{coh.}^{MF} &= \frac{1}{2V} g_{--}^{--} \left\langle \Psi_{coh.} | \hat{N}_-^2 | \Psi_{coh.} \right\rangle \\ &= \frac{1}{2V} g_{--}^{--} N(N-1) \\ &= \frac{1}{2V}\left(g_\infty + \overline{g}\left(\cos\theta_d - \cos\theta_\infty\right)^2\right) N^2 + o(\frac{N^2}{V}) \\ &\simeq 0 \end{aligned} \tag{3.7}$$

Finally, we proved that the interaction energies for both homogeneous mixtures, coherent and incoherent, cancel out in the thermodynamic and mean-field limits. It actually takes very little effort to prove the two mixtures always have equal mean-field energies provided they have the same number of atoms $N = N_1 + N_2$ and the same polarisation $N\cos\theta_d = N_2 - N_1$, but only in the thermodynamic limit.

$$\begin{aligned} N^2 g_{--}^{--} &= N^2\left(\mathfrak{s}^4 g_{11} + \mathfrak{c}^4 g_{22} + 2\mathfrak{s}^2\mathfrak{c}^2 g_{12}\right) \\ &= N_1^2 g_{11} + N_2^2 4 g_{22} + 2N_1N_2 g_{12} \end{aligned} \tag{3.8}$$

3.1.2 Uprising of the beyond-mean-field energy

The equation of states of the two gases are $E = 0$, which is the equation of state of an ideal gas at zero temperature. It is however pathological, because there are always some excitation present in a physical system. Their effect cannot be neglected with respect to 0. At finite temperature, thermally excited particles should exist and no physical

system can be made exactly at a zero temperature. In some other cases, more relevant for us, the dominant correction to $E = 0$ comes from quantum depletion rather than thermal depletion. Even for temperatures tending to zero, it is theoretically known and experimentally measured here at Laboratoire Charles Fabry [31] that not all atoms of a dilute quantum gas can be in the condensate. The two-body interactions modify the ground-state of the system away from the mean-field ansatz 3.3 and 3.2. As a consequence, the ground-state energy of the system is modified and the first correction is called the beyond-mean-field energy E^{BMF}. Note that we continue here to neglect effects that disappear in the thermodynamic limit (the $o(N)$ of equations 3.6 and 3.7).

For a pure homogeneous dilute quantum gas with interaction strength $g = 4\pi\hbar^2 a/m$, the energy has a universal form when the mean-field and beyond-mean-field terms are taken into account [4][5]:

$$\frac{E}{V} = g\frac{n^2}{2}\left(1 + \frac{128}{15\sqrt{\pi}}\sqrt{na^3}\right) \tag{3.9}$$

The first term is the mean-field energy, it has the same form than in equation 3.7 with $n = N/V$. It is directly linked to the number of pair of atoms in the condensate $(N(N-1)/2)$ because interactions are pairwise. The second term, proportional to $n^{5/2}$ is the beyond-mean field energy. It is, for a pure condensate, negligible compared to the mean-field energy because the dilute criteria is $na^3 \ll 1$. As a tends to zero, both the mean-field energy and the beyond-mean-field energy cancel out. However, D. Petrov proved in 2015[30], that for an incoherent mixture, the mean-field energy can be canceled out while the beyond-mean-field energy remains constant. It therefore becomes the only contribution to the energy of the system.

3.1.3 An attempt at measuring the beyond-mean-field energy of incoherent mixtures

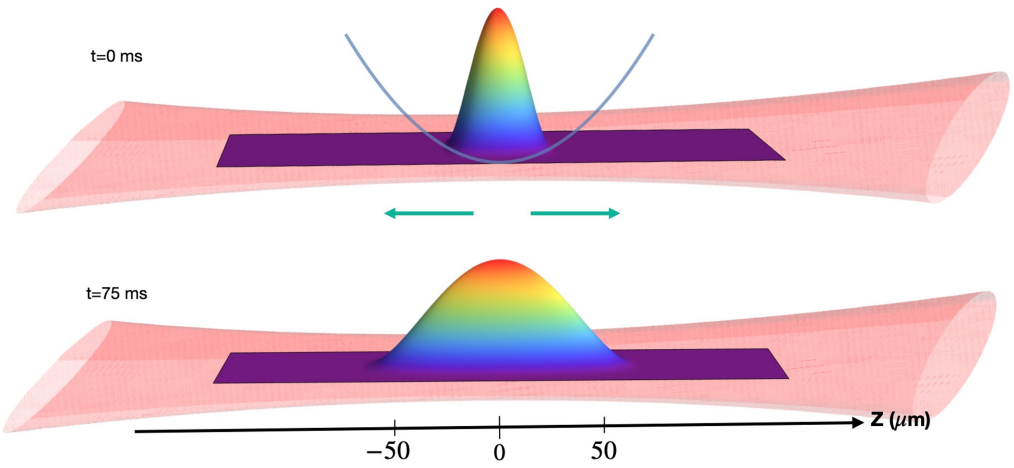

Figure 3.1: Qualitative picture of the protocol used to measure the release of beyond-mean-field energy of mixture, coherent or incoherent, into kinetic energy in the axial (Oz) direction. Note the very low order of magnitude in the released energy as the 1D time of flight lasts for 75ms

Our first goal, at the end of 2020, was to measure directly this beyond-mean-field energy for a Bose-Bose mixture, which was never quantitatively achieved. The idea was to

trap a quantum mixture of potassium ^{39}K in optical dipole traps. Then turn off the axial trap (FORT2) and let the gas expand in the direction of the FORT-1D beam. The energy released in this direction would, after a substantial time of flight, be purely kinetic and its measurement would give us, by the conservation of energy the initial beyond-mean-field energy.

However, a quantum pressure or zero-point energy would also be present initially because of the harmonic trapping in the axial direction. For an initial density profile of the gas $n(r)$ and no permanent currents, it reads:

$$E_{k,zp} = \int \sqrt{n(r)} \frac{-\hbar^2}{2m} \nabla^2 \left(\sqrt{n(r)} \right) d^3r \tag{3.10}$$

Therefore, we intended to subtract the released energy for the coherent mixture (RF-dressed BEC) to the one for the incoherent mixture. This was implicitly assuming that the beyond-mean-field energy of the coherent mixture was cancelling out, as it would for a pure condensate with $a_{--} = 0$. Indeed, the RF-dressed BEC does look like a pure BEC when we look at equation 3.3. We expected a positive difference of energies equal to the beyond-mean-field energy of the incoherent mixture.

The experimental results were in complete disagreement ! There was more energy in the RF-dressed BEC than in the incoherent mixture ; even though both had zero mean-field interaction energies thanks to the process described above.

3.2 Beyond-mean-field (BMF) energy of the RF-dressed gas

It is always a good thing to have clear negative results in an experiment because no theoretical truth may be taken for granted but experimental wrongs give unquestionable answers : "the theoretical model is incorrect". The good thing is that we are allowed to look for the errors we made. And indeed, our experimental results of Winter 2020 needed some kind of explanation on why RF-dressed BEC do not behave like pure BEC. The physical arguments came with an elegant derivation by D. Petrov and A. Recati based on a paper they had resigned to publish. We shall now give the key elements, although they are present, in more condensed and theoretical form, in the supplementary materials of the finally co-written paper [2].

3.2.1 Bogoliubov prescription and quantum depletion

The beyond-mean-field energy is in essence linked to the quantum depletion. Due to two-body interactions, in the true ground state of the gas at zero temperature, some pair of atoms should have left the condensate to go to states with small opposed momenta $\vec{k}, -\vec{k}$. By doing so, they may have decreased the total energy of the system. In the Bogoliubov approximation, the condensate is considered as a reservoir of particles and the excited pairs are only allowed to interact with it and not with other pairs. This is an approximation justified by the macroscopic number of atoms in the condensate. This simplifies the quantum problem and the approximated ground state of the system can usually be computed. The expectation value of the many-body Hamiltonian then gives

the mean-field plus beyond mean-field energy. However, finding this ground state for an RF-dressed BEC at arbitrary values of δ and Ω is quite tedious.[3].

Hopefully, the beyond-mean-field energy can also be computed without knowing the exact ground state. We only need the excitation spectrum of the homogeneous system under the Bogoliubov approximation. In other words, after having linearized the dynamical equations or kept only quadratic terms in the Hamiltonian, we find uncoupled excitations modes of energies $\hbar\omega(k)$. Then, we simply sum the zero-point energies of all these quantum modes. The sum over $\vec{k}$ usually diverges but the cutoff $k \leq \Lambda$ should not be forgotten. Any term diverging when Λ goes to infinity has a counter term hidden somewhere in the mean-field energy. The reason is because it is not really legitimate to replace the contact pseudo-potentials by Dirac potentials. One may proves we get the same non-diverging result with the more legitimate but tedious use of a contact pseudo-potentials. In the end, the beyond-mean-field energy is the sum of the zero-point energies of excitation modes minus all its UV-divergent terms.

3.2.2 Bologiubov modes of the RF-dressed BEC with vanishing MF energy

In an homogeneous RF-dressed condensate with total density n and effective Rabi frequency $\tilde{\Omega}$, there are two Bogoliubov excitation branches: the density modes and the spin modes. From now on, for simplicity, we shall talk only in the case where $a_{12} = -\sqrt{a_{11}a_{22}}$ and $N_1\sqrt{a_{11}} = N_2\sqrt{a_{22}}$. In this case, the nature of the two modes is tremendously simplified... so much that we can actually explicit their exact nature[4]. A density excitation corresponds to a particle of momentum k in state $|-\rangle$. Meanwhile, a spin excitation corresponds to a particle in state $|+\rangle$ with momentum $\vec{k}$. Their excitation spectra are given by:

$$\left\{ \begin{array}{rcl} \varepsilon_n(\vec{k}) & = & \frac{\hbar^2k^2}{2m} \\ \varepsilon_s(\vec{k}) & = & \sqrt{\left(\frac{\hbar^2k^2}{2m} + \hbar\tilde{\Omega}\right)\left(\frac{\hbar^2k^2}{2m} + \hbar\tilde{\Omega} + 2\tilde{g}n\right)} \end{array} \right. \tag{3.11}$$

Where $\tilde{g} = \sqrt{g_{11}g_{22}} = -g_{12}$. If on top of the RF-dressed condensate, we add two density excitations at $\vec{k}, -\vec{k}$, we get a stationary wave for which the two components 1 and 2 have oscillations in the same ratio than in the condensate $\delta n_1\sqrt{a_{11}} = \delta n_2\sqrt{a_{22}}$. On the contrary, if two spin excitations at $\vec{k}, -\vec{k}$ are added, the oscillations of densities of components 1 and 2 are in orthogonal ratio than the one of the condensate $\delta n_1\sqrt{a_{22}} = -\delta n_2\sqrt{a_{11}}$(see figure 3.3).

The fact that the density mode is quadratic in k is a direct consequence of the cancelling of interaction strength g_{--}^{--}. On the other hand, the spin mode is gaped at small momenta with also a quadratic behavior in k. Experimentally we are in the limit $\hbar\tilde{\Omega} \gg \tilde{g}n$, therefore $\varepsilon_s(k) \underset{k\to 0}{\sim} \hbar\tilde{\Omega} + \tilde{g}n + \frac{\hbar^2k^2}{2m}\left(1 + \frac{\tilde{g}n}{\hbar\tilde{\Omega}}\right)$

[3]The main reason is because the simple approach in terms of pairs $\vec{k}, -\vec{k}$ fails for RF-dressed BEC.

[4]One may have a look at the supplementary materials of [2] to see the scary exact form of excitation spectra in the general case. The nature of the excitation modes were not derived.

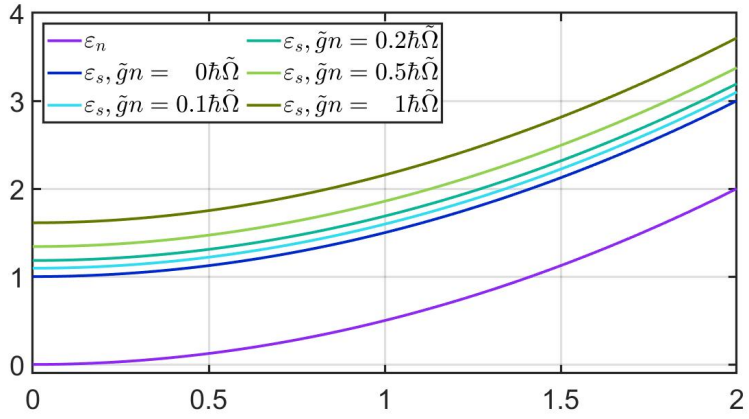

Figure 3.2: Dispersion relation for the two Bogoliubov excitation branches. The case of a free $|+\rangle$ particle of momentum $\vec{k}$ has been included for comparison.

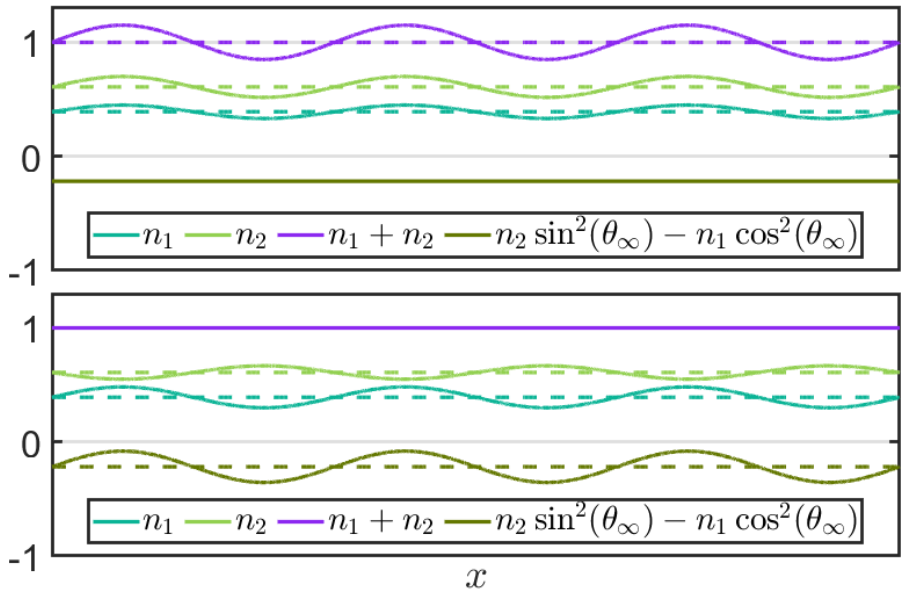

Figure 3.3: Qualitative picture of density and spin stationary waves corresponding to the sum of two excitations at $\vec{k}, -\vec{k}$

3.2.3 Theoretical computation of the BMF energy of RF-dressed BEC

With the previous analytic expressions, we get the following beyond-mean-field energy:

$$\begin{aligned}\frac{E^{BMF}}{V} &= \frac{1}{2}\int\left(E_n(k) + E_s(k) - \frac{\hbar^2k^2}{m} - \hbar\tilde{\Omega} - \tilde{g}n + \frac{\tilde{g}^2n^2m}{\hbar^2k^2}\right)\frac{d^3k}{(2\pi)^3} \\ &= \tilde{g}\frac{n^2}{2}\frac{128}{15\sqrt{\pi}}\sqrt{n\tilde{a}^3} \times I\left(\frac{\hbar\tilde{\Omega}}{2\tilde{g}n}\right)\end{aligned} \tag{3.12}$$

$$\text{with} \qquad I(y) = \frac{15}{4}\int_0^1 \sqrt{x(1-x)(x+y)}dx \tag{3.13}$$

Where $\tilde{g} = \sqrt{g_{11}g_{22}} = -g_{12}$. The beyond mean field energy has a form analog to equation 3.9 for a pure condensate, except for the multiplicative factor $I(y)$. This factor, $I(y)$, is

always larger than one. It implies, as it was observed experimentally, that the beyond-mean-field energy of the RF-dressed BEC is always bigger than the one of an incoherent mixture. As $\tilde{\Omega}$ tends to 0, the integral tends to 1 and we recover the result computed by D. Petrov in 2015: the beyond-mean-field energy of the incoherent mixture is equal to the one of a pure BEC with interaction strength $\tilde{g}$. Note also that in the integral 3.12, only spin modes actually contributes because the energy ε_d of density modes is a purely UV-divergent term.

3.3 Analytic development of the BMF energy

3.3.1 Breaking of non-analiticity

In the experiment, we have large Rabi energies $\hbar\tilde{\Omega} \geq 10\,\mathrm{kHz}$ compared to the interaction energy of spin modes $\tilde{g}n \leq 100\,\mathrm{Hz}$, it is thus relevant to express the integral $I(y)$ with its asymptotic behavior for large arguments:

$$I(y) \simeq \frac{15\pi}{128}\left(4\sqrt{y} + \frac{1}{\sqrt{y}}\right) \tag{3.14}$$

As a consequence, we get the following form for the beyond-mean-field energy:

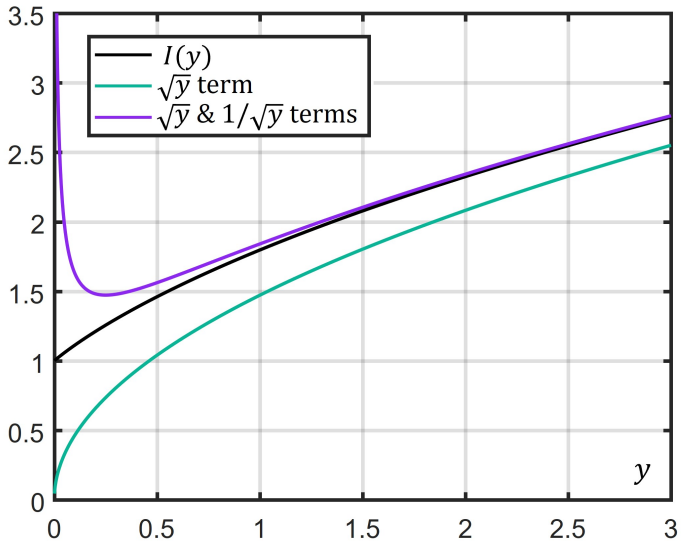

Figure 3.4: Multiplicative factor $I(y)$ between the beyond-mean-field energy of a RF-dressed BEC and an incoherent mixture at the same polarisation.

$$\frac{E^{BMF}}{V} = \frac{n^2}{2}\left(\frac{4\pi\hbar^2\tilde{a}}{m}\frac{\tilde{a}\sqrt{2}}{l_{\tilde{\Omega}}}\right) + \frac{n^3}{3}\left(\frac{4\pi\hbar^2\tilde{a}}{m}\,3\pi\frac{\tilde{a}^2 l_{\tilde{\Omega}}}{\sqrt{2}}\right) \tag{3.15}$$

At this point, we should insist that the beyond-mean-field energy is usually, for a pure BEC, non-analytic: $\propto n^{5/2}$ (see 3.9). In other words, it is not possible to express it with integer powers of the density n. It has its importance because physicists like to develop everything in power series. For example, the mean-field energy is proportional to $n^2/2$

which we directly interpret as a consequence of the short range and two-body nature of interactions in the gas. The non-analyticity of the beyond mean-field energy of the pure condensate comes from the phonic nature of bogoliubov modes at low momenta and the impossibility to see such excitations as free-particles slightly perturbed by interactions with the condensate. In the incoherent mixture, as $\tilde{\Omega} \to 0$, the spin excitation branch recovers a phonic nature at low energies which explains why the beyond-mean-field energy is again non-analytic.

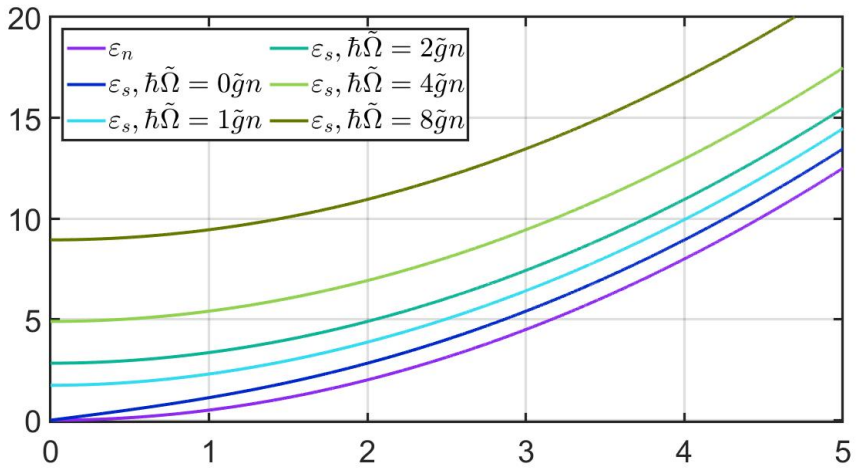

Figure 3.5: Excitation branches of the RF-dressed BEC at different effective Rabi frequencies $\tilde{\Omega}$

Formula 3.15 can be interpreted as the sum of a repulsive two-body energy and a repulsive three-body energy. We shall now physically interpret this result.

3.3.2 Renormalization of two-body interactions

In the context of quantum field theory, it is common to talk about renormalization of interactions. It happens for quantum-fields coupled with each others only by local interactions to ensure causality. The bare/local interaction strengths are not the physically observable ones mainly because of virtual excitations. However, the physical relevant quantities may be expressed in terms of the bare ones. It relies on the use of power series in terms of a small parameter. For example, the famous electron spin g-factor g_S, can be computed in a power-series of the fine structure α.

In our case, we study the macroscopic behavior of RF-dressed condensates, the true potentials have been replaced by contact ones to get an effective Hamiltonian. On the other hand, we already encountered the small parameters at stake in the exact solving of the two-body problem (see 1.2.1): $a_{ij}/l_{\tilde{\Omega}} \ll 1$. The mean-field ansatz takes a two-body interaction strength $g^{--}_{--} = 4\pi\hbar^2 a^{(0)}_{--}/m$. We can now check that the first correction to this interaction strength, the so-called first order renormalization of two-body interactions between particles in state $|-\rangle$, is given by the $a^{(1)}_{--}$ computation of the 2-body scattering problem or equivalently by the beyond-mean-field computation.

We found in chapter 1 the following expression (equation 1.50) :

$$a_{--}^{(1)} = \frac{\sqrt{2}\mathfrak{s}^4\mathfrak{c}^4}{l_{\tilde{\Omega}}}(a_{11}+a_{22}-2a_{12})^2 + \frac{2\mathfrak{s}^2\mathfrak{c}^2}{l_{\tilde{\Omega}}}\left(\mathfrak{s}^2(a_{12}-a_{11})+\mathfrak{c}^2(a_{22}-a_{12})\right)^2$$

The second term on the right hand side is, in the current situation, zero because the polarisation $\cos\theta_d$ was chosen to minimize the interaction energy of the mixture (equation 1.25):

$$\frac{\mathfrak{s}^2}{\mathfrak{c}^2} = \frac{\sin^2(\theta_d/2)}{\cos^2(\theta_d/2)} = \frac{N_1}{N_2} = \frac{g_{22}-g_{12}}{g_{11}-g_{12}} \tag{3.16}$$

To express the first term in term of $\tilde{a} = -a_{12}$, we use the previously defined $\overline{g}$, g_∞, $\cos\theta_\infty$ (see 1.58 and 1.59) which verify in the current case $g_\infty = 0$ and $\cos\theta_\infty = \cos\theta_d$.

$$\tilde{a}^2 = (a_{12})^2 = \overline{a}^2(1-\cos^2\theta_\infty)^2 = (a_{11}+a_{22}-2a_{12})^2\sin^4\frac{\theta_d}{2}\cos^4\frac{\theta_d}{2} \tag{3.17}$$

Consequently, the two-body term of the beyond-mean-field energy is exactly equal to:

$$E_{2b}^{BMF} = \frac{n^2}{2}\frac{4\pi\hbar^2 a_{--}^{(1)}}{m} \tag{3.18}$$

It seems natural to find this first order renormalization of two-body interactions in the beyond-mean-field energy since it could in no way be present in the mean-field energy. The mean-field ansatz assume that the wave-function of the condensate is macroscopically smooth and replace the zero-range pseudo-potentials by dirac potentials. Then, it assumes that all particles are in the same internal state $|-\rangle$. With these prescriptions, any virtual state, $(++)$ or $(+-)$, present only during a collision completely disappears.

By extrapolation, we can guess that at other mixture proportions $\cos\theta_d \neq \cos\theta_\infty$, the beyond-mean-field energy will also be analytic. Without solving the Bogoliubov problem, we known the two body term should be given by $a_{--}^{(1)}$. At last, we plot this renormalisation of interaction strength ($\propto \sqrt{\tilde{\Omega}}$) at our biggest Rabi frequency: 40 kHz. The correction is at most of $3.6\,a_0$ but the value decreases to $2.3\,a_0$ around the minimum of $a_{--}^{(0)}$

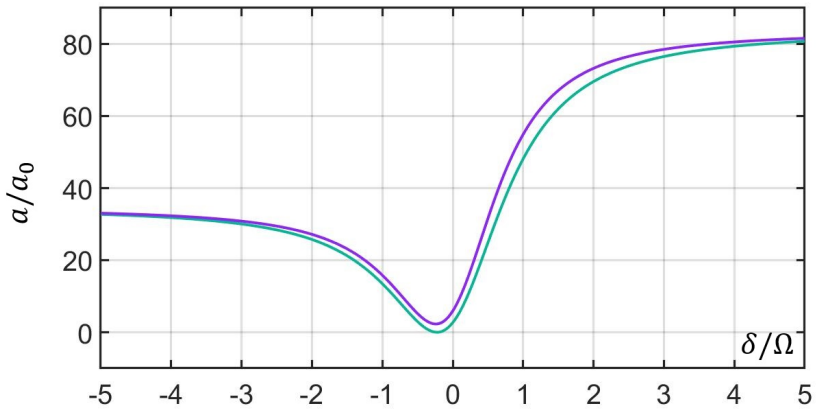

Figure 3.6: Two body scattering length for RF-dressed atoms. The indigo curve is $a_{--}^{(0)}/a_0$ and the beyond-mean-field correction $a_{--}^{(1)}/a_0$ is added to get the purple curve.

3.3.3 Effective BMF three-body

$$E_{3b}^{BMF} = \frac{n^3}{3}\left(\frac{4\pi\hbar^2\tilde{a}}{m}\,3\pi\frac{\tilde{a}^2 l_{\tilde{\Omega}}}{\sqrt{2}}\right)$$

The three body effect computed by the beyond-mean-field method is, according to D. Petrov, consistent with the exact solution of the three-body scattering problem [32], although the latter is rather difficult to pose and solve. The beyond-mean-field method is in comparison a much simpler computation. The appearance of the very small volume $\tilde{a}^2 l_{\tilde{\Omega}}$ suggests that this three body effect will be difficult to see.

Finally, we note that the two-body and three-body terms in the beyond-mean-field energy have different scaling with $\tilde{\Omega}$: - the two-body term is proportional to $\sqrt{\tilde{\Omega}}$ while the three-body term is proportional to $1/\sqrt{\tilde{\Omega}}$. This behaviors may be verified experimentally by measuring the beyond-mean-field energy at different Rabi frequencies $\tilde{\Omega}$.

3.4 Experimental measurement of BMF energy of RF-dressed BEC

In this chapter, we review the different aspects of the experimental measuring of the beyond-mean-field energy of the RF-dressed condensate: from the method to ensure the cancellation of mean-field energy to the data analysis. We also discuss the effects of undesirable magnetic field fluctuations.

3.4.1 Experimental protocol: adiabatic sweep and one-dimensional dynamics

The goal of the experiment is to measure the beyond-mean-field energy for RF-dressed condensates by the mean of one dimensional expansions. This process allows for a very long time of flight ($\sim 75\,\mathrm{ms}$) during which the beyond-mean-field energy governs the dynamics until the ballistic regime is reached. A special care is taken to cancel the mean-field energy. We start by calibrating the magnetic field with the resonance of RF pulses at 41.076 MHz on a condensate in state $|2\rangle$. This allows to apply precisely 56.830(1) G on the atoms. In this conditions the scattering lengths are $a_{11} = 83.4\,a_0$, $a_{22} = 33.4\,a_0$ and $a_{12} = -53.2\,a_0$. giving a minimum of $a_{--}^{(0)}$ of $-0.2\,a_0$ which is sufficiently close to 0 to have a dominance of beyond-mean-field effects.

To make the RF-dressed BEC, we start with a quasi-pure condensate of 1.2×10^5 atoms in state $|2\rangle$. They are optically trapped in an elongated harmonic potential with frequencies $(\omega_x, \omega_y, \omega_z) = (137, 137, 25.4)\,\mathrm{Hz}$. The coherent mixture in $|-\rangle$ is prepared in an adiabatic passage, in which the radio-frequency (RF) detuning is swept from $\delta = 7.5\,\Omega$ to its final value $\delta \approx 0.22\,\Omega$, for which $\cos\theta_d \simeq \cos\theta_\infty$. During the RF sweep, $a_{--}^{(0)}$ decreases from $33.3\,a_0$ to a value close to 0. Its shape and duration of 9 ms are chosen in order to be adiabatic not only with respect to the internal-state dynamics but also with respect to the radial evolution of the wave function, which progressively shrinks and approaches the ground state of the radial harmonic confinement. We have checked that we cannot detect any residual oscillations of the radial size after the RF sweep. In addition, the axial trap frequency is progressively turned off during the sweep and adjusted such that the gas is neither axially expanding nor shrinking in a three-dimensional expansion after the sweep. The radially confined condensate is then free to expand in the axial direction for a time

of 75 ms. During the very final stage of the expansion, we sweep back the RF frequency to its initial value to map the dressed states $|-\rangle$ and $|+\rangle$ back onto $|1\rangle$ and $|2\rangle$, which we independently detect by fluorescent imaging after a short Stern-Gerlach separation.

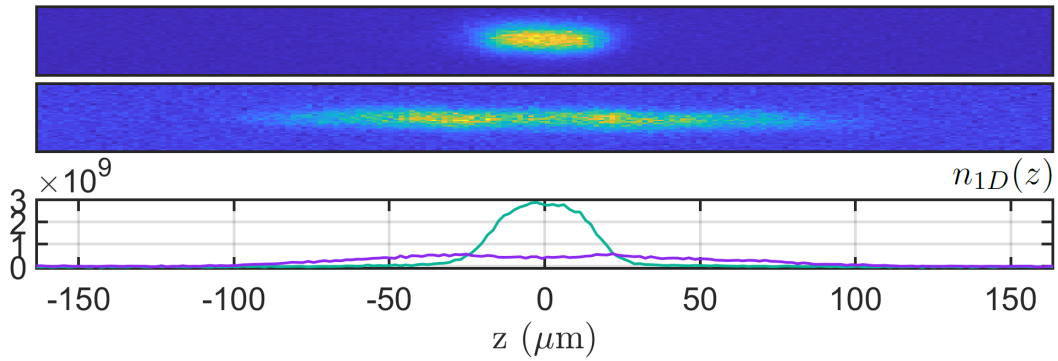

Figure 3.7: Typical experimental density profile before and after the 1D time of flight of 75 ms.

During the sweep, the cloud begin to compress axially because the interaction strength is gradually reduced and also because the sweep is not infinitely fast compared to the axial trapping frequency ω_z. To cancel any unwanted flow energy present at the beginning of the 1D time of flight, the axial trap is turned-off at a chosen time during the 9 ms adiabatic sweep. The moment of turn-off was experimentally found with another protocol : we adjust this time to minimize the axial motion in a 3D time of flight starting right after the adiabatic sweep. By doing so, the cloud is quickly diluted in the radial direction and the dynamics in the axial direction is only given by the initial velocity field.

3.4.2 Minimization of mean-field energy with respect to final detuning

After the expansion, we first measure the condensate density profile and extract the condensate sizes from fits with 1D Thomas-Fermi density profiles $n_{1D}(z) \propto (1 - (z/R_{\mathrm{TF}})^2)$ which were better minimizing the fits error compared to Gaussian or 3D Thomas-Fermi density profiles. As a function of the detuning δ, a clear minimum in size appears at $\delta/\Omega \approx 0.22$, i.e., a position where we expect $a_{--}^{(0)}$, and thus also the mean-field energy to be minimized.

We checked theoretically (see figure 3.6) that this minimization of total energy gives in very approximation the mixture polarisation that cancels the mean-field energy because the beyond-mean-field energy is weakly dependent on mixture polarisation $\cos\theta_d$. However, note that far from the minimum of $a_{--}^{(0)}$, we found out that the internal state minimizing the mean-field energy is not only given by θ_d but also depends on density n (see chapter 4).

Thanks to this scan and minimization, we are able to cancel the mean-field interactions. The method can be applied for several Rabi frequencies.

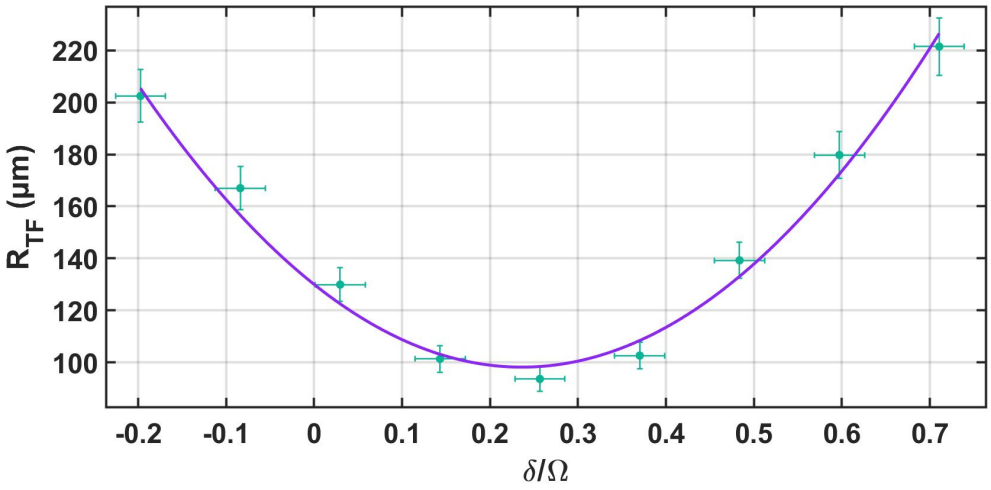

Figure 3.8: Experimental 1D Thomas-Fermi radius of the condensate after 75 ms of expansion as a function of δ/Ω, for a Rabi frequency $\Omega/2\pi = 12.29\,\mathrm{kHz}$. The curve is a parabolic guide to the eye

3.4.3 Scan of Rabi frequency and main experimental results

By changing the Rabi frequency Ω in $2\pi \times [3, 40]$ kHz, we change the magnitude and ratio of coefficients in front of the two-body and three-body terms of the beyond-mean-field energy. Equivalently, we also decrease the multiplicative factor $I(y)$, so the beyond mean field energy should globally decrease with Ω. For Rabi frequencies $\Omega/2\pi$ between 38 kHz and 6 kHz , we observe a slow decrease of the measured size as a function of Ω, which corresponds to a decrease of the BMF energy as predicted. More precisely, the size after a long time of flight is expected to scale with $\sqrt{E_{\mathrm{LHY}}} \propto \Omega^{1/4}$ for a dominant two-body term at large Ω, in qualitative agreement with our observed behavior.

As the Rabi frequency is decreased, the three-body beyond-mean-field term becomes non-negligible. As an example, for a value $\Omega/2\pi = 10\,\mathrm{kHz}$, $\hbar\tilde{\Omega}/(\tilde{g}n) \approx 1$ and the initial two-body and three-body energies per particle are calculated to be 20 Hz and 3.2 Hz, respectively. This encouraged us to perform a more precise fitting process relying on extended Gross-Pitaevski 1D simulation with a non-linearity given the beyond-mean-field energy. The initial density profile was the radially integrated Thomas Fermi profile of the BEC in state $|2\rangle$, then we proceeded with the numerical dynamics during the time of flight of 75 ms. Both the experimental profile and the numerical solution were finally fitted with a 1D Thomas-Fermi profile.

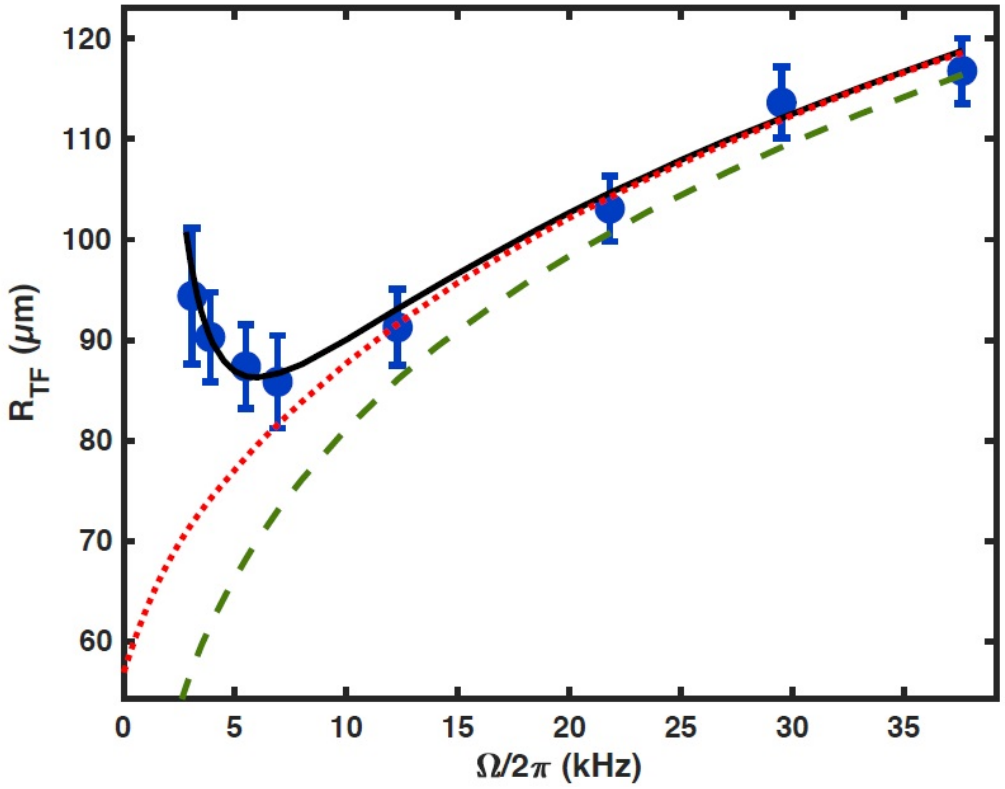

Figure 3.9: Thomas Fermi sizes of the cloud at $\delta = 0.23\Omega$ and after 75 ms 1D expansion time. Each point is obtained by averaging over 15 images at a given Rabi frequancy Ω and the error bars correspond to the standard deviation of the set of data. The different curves correspond to different simulation of the 1D Gross Pitaevski dynamics. The green dashed curve takes into account only the two-body term of the BMF energy. The red dotted curve is obtained with the exact expression of the BMF energy. The black plain curve has the exact expression of the BMF energy and takes into account the effect of magnetic field fluctuation on the mean-field energy at low Rabi-frequencies (see next subsection).

In the numerical simulations, the BMF energy was at first, expressed as a sum of its two-body plus three-body asymptotic behavior. This allowed a good fit of experimental data above 7 kHz. However, at smaller Rabi frequencies, the power expansion started to give unreliable results. Mainly because the BMF energy was approaching back its non analytical behavior $\propto n^{5/2}$ and the power expansion was past its radius of convergence (diverging serie). We thus had to rely on the exact analytical expression of the BMF energy (red dotted curve) with a numerical computation of integral $I(y)$. Note that above 7 kHz, the red dotted curve is equivalent to the result with the two-body and three-body expansion.

Nevertheless, the experimental increase of Thomas-Fermi sizes as the Rabi-frequency was decreased below 7 kHz could not be explained in any way with the BMF energy because it is a function strictly decreasing with Ω. We rather understood this increase as a consequence of magnetic field fluctuation on the mean-field energy.

3.4.4 Effect of magnetic field fluctuations

At small Rabi frequencies, typically under 7 kHz, the relative detuning δ/Ω may be ill defined during the 75 ms one-dimensional expansion of the condensate. Indeed, fluctuations of the magnetic field, inherent to the 50 Hz inherent noise and to the limit of stability of the feedback loop on magnetic field were both visible with a magnetic field sensor on timescales of a few ms. The rms noise on ω_0, propagating to the detuning δ, was estimated experimentally to 700 Hz. The effect of this fast-change of detuning, compared to the typical dynamical time of expansion, is to add an offset of two-body interaction given by the exploration of the $a_{--}^{(0)}(\theta_d)$ around its minima at θ_∞. This exploration effect is schematized on the figure below.

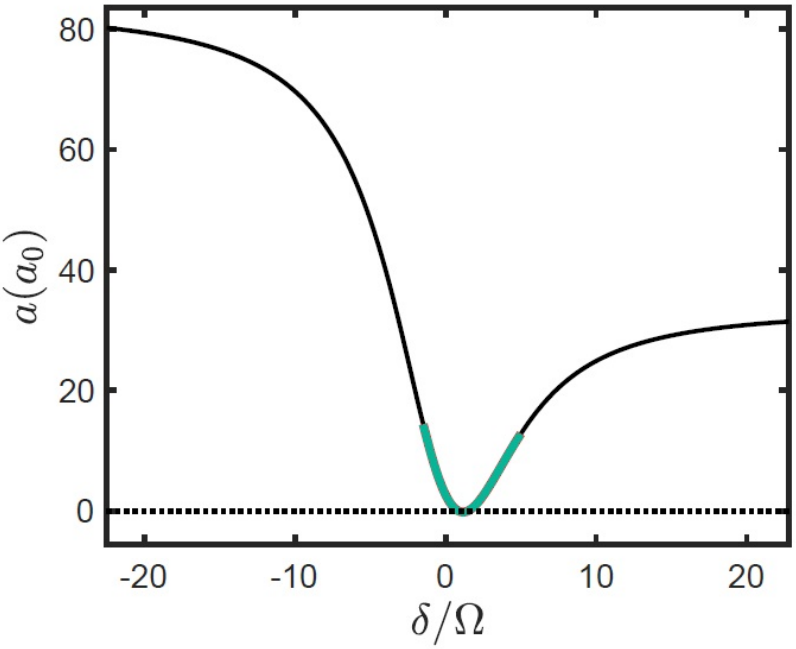

Figure 3.10: Qualitative picture on the effect of detuning fluctuations, symbolized by the indigo area, on the average two-body interaction strength. This phenomenon is dominant at Rabi frequencies Ω below 5 KHz.

3.5 Role of asymmetric three-body recombinations

3.5.1 The case of incoherent mixture

Interestingly, if we come back to the initial goal which was measuring the beyond mean-field energy of the incoherent mixture, we are faced with a serious problem : the asymmetry of losses. Indeed, three-body recombination happen dominantly for atoms in state $|2\rangle$ because the magnetic field is close to the Feshbach resonance of this state (at 58.9 G). During the 75 ms one-dimensional expansion time for the incoherent mixture, the mixture polarisation between the two states changes because of the disappearance of atoms in state $|2\rangle$. The density profile we finally obtain, present a double structure. An excess of atoms in state $|2\rangle$ expand fastly because of mean-field effects. In the middle, a peak in a ratio

close to the one minimizing the mean-field energy, $\frac{n_2}{n_1} = \sqrt{\frac{g_{11}}{g_{22}}} = 2.47$, expands at a much smaller speed (figure 3.11).

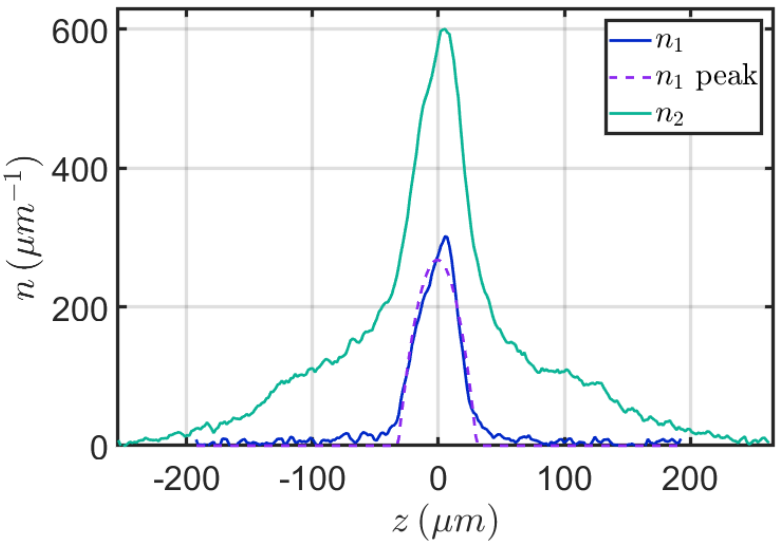

Figure 3.11: Measured one-dimensional density profiles in the two internal states thanks to a Stern Gerlach process.

3.5.2 Coherent mixtures

In presence of RF, we still observed losses of atoms during the expansion. Yet, the Rabi coupling compels the mixture to be in the correct polarisation $\cos\theta_\infty$. We never observed any double structure. The phenomenon can be also be interpreted as a symetrisation of losses by the Rabi coupling, happening mostly in state $|1\rangle$. A mathematical analysis was given in L. Lavoine phD thesis [27]. The main idea is that when a three-body recombination happen, it has no effect on the internal state of the rest of the atoms, remaining in $|-\rangle$.

This ability to maintain the condensate in a state where the mean-field energy is minimized and close to zero is a very interesting feature. In particular, this is crucial in the phenomenon of quantum droplets, that will be discussed briefly in chapter 5.

3.6 Chapter conclusion

In this chapter, we investigated the beyond-mean-field energy of the RF-dressed condensate. Firstly, we explained how the cancellation of mean-field interaction energy of binary mixture follows from an appropriate choice of magnetic field, giving $g_\infty = 0$, and a specific choice of detuning such that $\theta_d = \theta_\infty$. This method works for both coherent and incoherent binary mixtures of condensates. Consequently, the next order energy term, *e.g.* the beyond-mean-field energy, becomes the leading contribution in the equation of state of the condensate and governs the dynamics. Our first experimental idea was to measure the beyond-mean-field energy of the incoherent mixture by means of one-dimensional expansions. To understand experimental results, we had to focus on the theoretical expression of the beyond-mean-field energy in RF-driven mixtures (coherent).

After quickly recalling the standard interpretation of beyond-mean-field energy in terms of zero-point energies of excitation modes (Bogoliubov), we presented the theoretical derivation written for the paper by D. Petrov and A. Ricatti. The nature of excitation modes and their dispersion relation are simple in the very specific case we were studying (linked to the cancellation of mean-field energy). The formula for the beyond-mean-field energy of the RF-driven condensate was then easily obtained.

We then studied the surprising breaking of non-analyticity of beyond-mean-field energy compared to the standard $\propto n^{5/2}$ scaling for the one of a pure condensate. We found-out that the power expansion gives a renormalisation of two-body interaction strength $a_{--}^{(1)}$ in agreement with the theoretical solution of the two-body $|-\rangle$ scattering problem. For the experiment, we only needed the two-body and three-body term of the BMF energy.

In a fourth part, we detailed the experimental protocol to measure the BMF energy with one-dimensional expansion. A few sensitive points were discussed : method to ensure the cancellation of mean-field energy, minimization of the initial flow energy, Thomas-Fermi fits after the 75 ms expansion. At Rabi frequencies below 7 kHz, we found out that we were limited by the magnetic field noise.

Finally, we presented the results of the same protocol on an incoherent mixture. Asymmetric losses were observed, they undermined any viable measurement of beyond-mean-field energy. On the contrary, the use of RF-dressed condensate has two advantages on the context of quantum droplets: the 3-body losses are symetrized by the Rabi coupling and the beyond-mean-field energy is also increased.

Chapter 4

4. Mean-field three-body interactions in RF-dressed ^{39}K BEC

While establishing the experimental protocol to measure the BMF energy of the RF-dressed condensate, it became patent that the internal state of atoms is not uniquely fixed by the dimensionless driving parameter δ/Ω because of mean-field energy shifts. We will begin by justifying this statement with Gross Pitaevski equations on the RF-dressed condensate. Then, we will show that the internal state of the condensate verifies a self consistent equation involving the local density n. At low densities, the correction to internal state will simply become proportional to the density n, at the origin of an effective three body term in the equation of state. After proving that this three-body energy may still dominate the dynamics of the condensate, we will present a first method to measure its scaling : frequency measurements in the radial breathing of a cigar-shaped RF-dressed condensate. We then observed experimentally that the three body effect may also, in some specific conditions, lead to radial collapses of the cigar-shaped condensate. The experimental scan at different Rabi frequencies Ω gave clear data on the threshold $\pm\delta_c(\Omega)$ at which the cloud becomes unstable. These experiments proved that the three-body effect can strongly modify the dynamics.

4.1 Mean-field model and adiabatic elimination of internal dynamics

4.1.1 internal state of the RF-dressed condensate

To derive the mean-field dynamical equations on the RF-dressed BEC, we have to compute the expectation value of the many-body Hamiltonian written here in the $(|1\rangle, |2\rangle)$ basis:

$$\hat{H} = \int \sum_i \hat{\Psi}_i^\dagger \left(-\frac{\hbar^2 \nabla^2}{2m} + V_{ext}(r) \right) \hat{\Psi}_i + \sum_{i,j} \frac{g_{ij}}{2} \hat{\Psi}_i^\dagger \hat{\Psi}_j^\dagger \hat{\Psi}_i \hat{\Psi}_j \, d^3r + \int \frac{\hbar\delta}{2} \left(\hat{\Psi}_1^\dagger \hat{\Psi}_1 - \hat{\Psi}_2^\dagger \hat{\Psi}_2 \right) - \frac{\hbar\Omega}{2} \left(\hat{\Psi}_1^\dagger \hat{\Psi}_2 + \hat{\Psi}_2^\dagger \hat{\Psi}_1 \right) d^3r \quad (4.1)$$

For a general wave-function of the condensate of the form $\psi = \psi_1 |1\rangle + \psi_2 |2\rangle$, the mean-field energy is obtained by replacing operators $\hat{\Psi}_i$ by complex wave-functions ψ_i, and the Gross-Pitaevski equation reads:

$$i\hbar\partial_t \begin{pmatrix} \psi_1 \\ \psi_2 \end{pmatrix} = \left[\frac{-\hbar^2\nabla^2}{2m} + V_{ext} + \frac{\hbar}{2} \begin{pmatrix} \delta & -\Omega \\ -\Omega & -\delta \end{pmatrix} + \begin{pmatrix} g_{11}|\psi_1|^2 + g_{12}|\psi_2|^2 & 0 \\ 0 & g_{22}|\psi_2|^2 + g_{12}|\psi_1|^2 \end{pmatrix} \right] \begin{pmatrix} \psi_1 \\ \psi_2 \end{pmatrix} \quad (4.2)$$

In the above equation, the the Rabi frequency Ω is the only parameter that enables and forces the mixture to be coherent, which ultimately justifies the use of a single wave-function for the system. For large Rabi-frequency, the internal dynamics of the condensate will also happen on much shorter timescale than the space dynamics. This key point implies that **the interaction energy per particle $g_{--}n/2$ has to be small compared to $\hbar\Omega$**. By starting from a configuration without any spin currents or spin excitations, we may assume that the internal state of the condensate on the Bloch sphere will adiabatically follow the changes in the total density profile $n(r,t)$. For now, we will also suppose that the gas is in a large box with homogeneous density $n(t)$ which could vary on long timescales compare to $2\pi/\Omega$. The polarisation of the internal state of the gas, described on the Bloch sphere, will not be considered as externally imposed anymore ($\cos\theta \neq \cos\theta_d$) but rather determined by the minimization of mean-field energy. Moreover, the presence of the Rabi coherent coupling continue to forces the two components of the condensate wave-function to be in phase so the azimuth angle φ will be zero. We may therefore take the mean-field wave-function of the homogeneous RF-dressed condensate as:

$$\psi = \sqrt{n} e^{-i\mu t/\hbar} \left(\sin\left(\frac{\theta}{2}\right) |1\rangle + \cos\left(\frac{\theta}{2}\right) |2\rangle \right) \quad (4.3)$$

The internal state will be labeled $|-\rangle_\theta$ to account for the change of polarisation angle from θ_d to θ. With this ansatz, the kinetic and external potential energies vanish and the mean-field energy is only given by the two-body interactions and the Rabi-Hamiltonian:

$$\frac{E^{MF}}{N} = \frac{n}{2} \left(g_{11} \sin^4\left(\frac{\theta}{2}\right) + g_{22} \cos^4\left(\frac{\theta}{2}\right) + 2g_{12} \sin^2\left(\frac{\theta}{2}\right) \cos^2\left(\frac{\theta}{2}\right) \right) + \frac{\hbar\delta}{2} \left(\cos^2\left(\frac{\theta}{2}\right) - \sin^2\left(\frac{\theta}{2}\right) \right) - \frac{\hbar\Omega}{2} \left(2\sin\left(\frac{\theta}{2}\right) \cos\left(\frac{\theta}{2}\right) \right) \quad (4.4)$$

Or more elegantly, with the use of $\cot\theta_d = \delta/\Omega$, $\tilde{\Omega} = \sqrt{\delta^2+\Omega^2}$, $\overline{g}$, g_∞, θ_∞ (see 1.4.3):

$$\frac{E^{MF}}{N} = \frac{n}{2}\left(g_\infty + \overline{g}\left(\cos\theta - \cos\theta_\infty\right)^2\right) - \frac{\hbar\tilde{\Omega}}{2}\cos\left(\theta - \theta_d\right) \tag{4.5}$$

We recognize the form of $g^{--}_{--}(\theta)$ the interaction strength between two particles in state $|-\rangle_\theta$, and the Rabi energy of the $|-\rangle_{\theta_d}$ internal state $\varepsilon_- = -\hbar\tilde{\Omega}/2$. Finally, the condition of minimal mean-field energy will simply be:

$$\frac{\partial E^{MF}}{\partial\theta} = 0 = -n\overline{g}\sin\theta\left(\cos\theta - \cos\theta_\infty\right) + \frac{\hbar\tilde{\Omega}}{2}\sin\left(\theta - \theta_d\right) \tag{4.6}$$

This equation self-consistently defines the polarisation angle θ of the RF-dressed condensate with respect to its density n. The unique solution in $[0,\pi]$ giving the mixture angle θ in function of the density can be found numerically. It is plotted on the following figure.

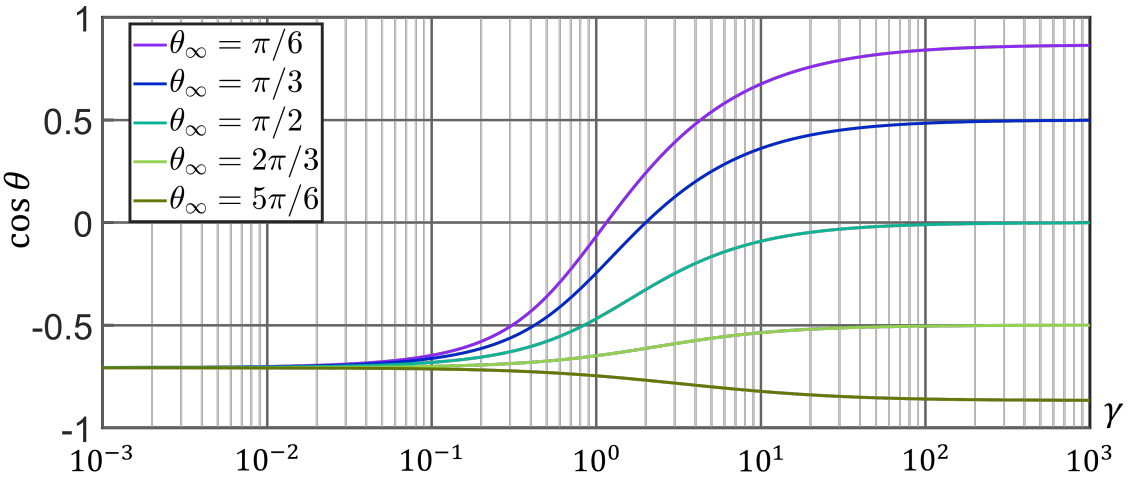

Figure 4.1: polarisation of the condensate in function of the dimensionless density $\gamma = 2\overline{g}n/(\hbar\Omega)$. The driving mixture angle θ_d is taken here to $3\pi/4$. In this chapter we focus on effects valid at $\gamma \ll 1$.

4.1.2 Physical interpretation with mean-field energy shifts

The use of polarisation angle θ heavily simplifies the mathematical solving of the above problem but it partly hides the physical processes at play in the determination of the internal state of the condensate. To get a physical interpretation, we go back to the Gross-Pitaevski equation 4.2.

If we add an atom in state $|1\rangle$ in the box, it will interact both with the condensate and with the RF-magnetic field. Its internal energy will be shifted from a quantity equal to the $(1,1)$ diagonal element of equation 4.2: $\hbar\delta/2 + g_{11}n_1 + g_{12}n_2$. Equivalently, the energy of an added atom in state $|2\rangle$ will be shifted from a quantity $-\hbar\delta/2 + g_{22}n_2 + g_{12}n_1$. The two processes lead to a modified detuning equal to δ' as can be verified on figure 4.2:

$$\delta' = \delta + \frac{g_{11}n_1 + g_{12}n_2 - g_{22}n_2 - g_{12}n_1}{\hbar} \tag{4.7}$$

If we now add an atom with a given internal state on the Bloch sphere and require it to be a stationary state of minimal energy - consistently with the adiabatic elimination of

internal dynamics - we find that it must be written: $|-\rangle_\theta = \sin\left(\frac{\theta}{2}\right)|1\rangle + \cos\left(\frac{\theta}{2}\right)|2\rangle$ with $\cot\theta = \delta'/\Omega$. This is exactly equivalent to equation 4.6 and gives us another useful form:

$$\begin{aligned}\cot\theta &= \frac{\delta}{\Omega} + \frac{n}{\hbar\Omega}\sin^2\left(\frac{\theta}{2}\right)(g_{22}-g_{12}) - \frac{n}{\hbar\Omega}\cos^2\left(\frac{\theta}{2}\right)(g_{11}-g_{12}) \\ &= \cot\theta_d + \frac{2\overline{g}n}{\hbar\Omega}\left[\sin^2\left(\frac{\theta}{2}\right)(1+\cos\theta_\infty) - \cos^2\left(\frac{\theta}{2}\right)(1-\cos\theta_\infty)\right] \\ &= \cot\theta_d - \frac{2\overline{g}n}{\hbar\Omega}(\cos\theta - \cos\theta_\infty)\end{aligned} \tag{4.8}$$

Equation 4.6 directly follows by remarking $\tilde{\Omega} = \sqrt{\delta^2+\Omega^2} = \Omega/\sin\theta_d$. In the end, for

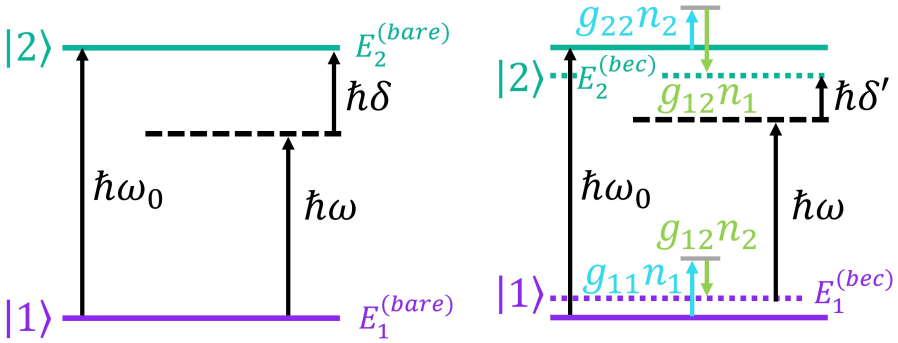

Figure 4.2: Mean-field induced energy shifts and reduction of effective detuning in the case depicted here.

the internal dynamics, the presence of the condensate is equivalent to the addition of a magnetic field on the z-axis. This picture is consistent with the works of M. Oberthaler on the two-level internal dynamics rubidium condensates in presence of coherent coupling [33], and also with recent works from G. Ferrari's team on effective ferromagnetic effects in RF-dressed condensates of sodium [34]. Indeed, the effective magnetic field is created by a magnetization of the system $M_z \propto -2\overline{g}n(\cos\theta - \cos\theta_\infty)/\hbar$ which does not necessarily responds linearly to the external driving parameter δ/Ω.

4.1.3 A competition between Rabi energy and two-body interaction energy

To physically predict the internal state of the condensate, solution of the self-consistent equations 4.6 and 4.8, it is convenient to compare the two competing terms in the mean-field energy per particle 4.5: the interaction energy $g_{--}^{--}(\theta)n/2$ and an effective Rabi energy $-\hbar\tilde{\Omega}\cos(\theta-\theta_d)/2$. The sum of the two must be minimized by the internal state. We plotted both of them on figure 4.3

In the case of potassium, the interaction rigidity $\overline{g}$ is positive so the interaction energy is minimized at $\theta = \theta_\infty$. On the other hand, the Rabi energy is minimized at $\theta = \theta_d$. The interplay between these two energy terms is given by the dimensionless density γ:

$$\gamma = \frac{2\overline{g}n}{\hbar\Omega} \tag{4.9}$$

As can be seen on figure 4.1, at any density γ the polarisation angle is uniquely determined and between θ_d and θ_∞.

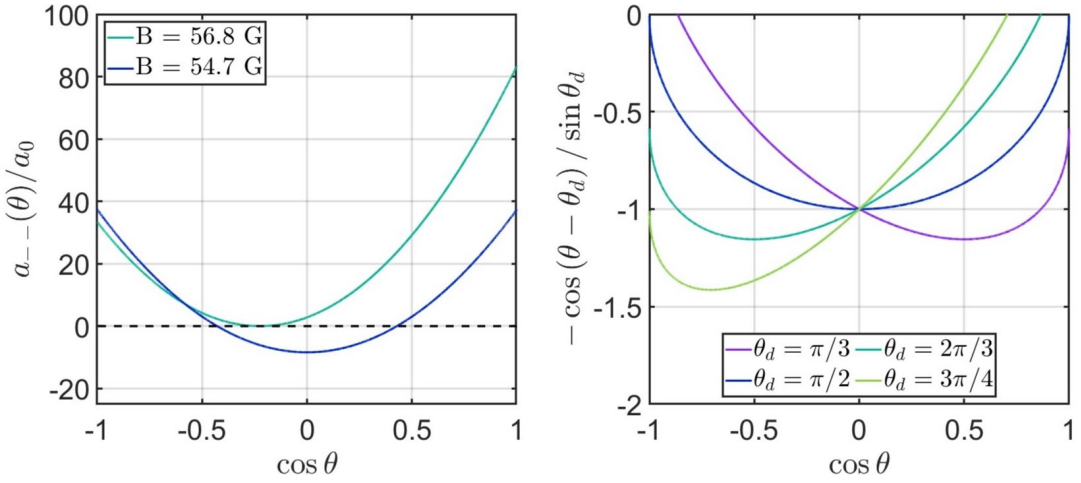

Figure 4.3: The two competing energy terms: (*left*) two-body interaction strength, (*right*) Rabi energy

As a side note, for other alkali gases, it is possible to use Feshbach resonances to have a negative value of $\overline{g}$, for example in sodium. The interaction energy is then maximized at $\theta = \theta_\infty$ and minimized at $\theta = 0$ and $\theta = \pi$. At high densities $|\gamma| \gg 1$, these two polarisation angle will be local minima of the mean-field energy because the Rabi energy can be neglected. The system will thus display a form of ferromagnetism [34].

4.2 Low density behavior : attractive tunable three-body interactions

4.2.1 Linear correction to internal state

In the experiment, the Rabi frequency is typically above 5 kHz and the density of the order of $2 \cdot 10^{20}\,\mathrm{m}^{-3}$. this places us in the low density regime, $\gamma \ll 1$. At vanishing density, the internal state is fixed by the minimization of Rabi energy only, $-\hbar\tilde{\Omega}\cos(\theta-\theta_d)/2$. The solution is obviously $\theta = \theta_d$ which is the result for an isolated particle in the $|-\rangle_{\theta_d}$ state. As the density is increased, or the Rabi frequency decreased at constant δ/Ω, collective interaction effects between a particle and the rest of the condensate starts to play a role. The mixture polarisation is slightly modified with a correction linear in γ. It is straightforwardly derived from equation 4.6:

$$\begin{aligned}\theta - \theta_d &\simeq \frac{2\overline{g}n}{\hbar\tilde{\Omega}}\sin\theta_d\left(\cos\theta_d - \cos\theta_\infty\right)\\ &\simeq \gamma\sin^2\theta_d\left(\cos\theta_d - \cos\theta_\infty\right)\end{aligned} \tag{4.10}$$

Because γ is positive and the two mixture angles θ_d and θ_∞ in $[0,\pi]$, this linear correction always brings the mixture angle θ away of θ_d and closer to θ_∞. Note that the sinus squared factor is close to 1 around the resonance.

In the case of symmetric interaction $a_{11} = a_{22}$ - happening at 54.7 G for states $|1\rangle|2\rangle$ of potassium - we know that θ_∞ is equal to $\pi/2$. In other words, the interaction strength g_{--}^{--} is minimized for an equal mixture. In this case, the correction to internal state simply becomes:

$$\theta - \theta_d \simeq \gamma\sin^2\theta_d\cos\theta_d \tag{4.11}$$

4.2.2 Correction to the mean-field energy: tunable three-body interactions

The linear correction to the mixture angle θ also modifies the mean-field energy per particle away from the infinitely diluted result given at θ_d. Still at smallest order in γ, we find a corrective effect in n^2. The interaction energy per particle reads:

$$\frac{n}{2}\left(g_\infty + \overline{g}\left(\cos\theta - \cos\theta_\infty\right)^2\right) \simeq \frac{n}{2} g_{--}^{--}(\theta_d) - 2\frac{\overline{g}^2 n^2}{\hbar\Omega}\sin^3\theta_d\left(\cos\theta_d - \cos\theta_\infty\right)^2 \tag{4.12}$$

The Rabi energy also get a correction at the same order in γ ($\propto n^2$):

$$-\frac{\hbar\tilde{\Omega}}{2}\cos\left(\theta - \theta_d\right) \simeq -\frac{\hbar\tilde{\Omega}}{2} + \frac{\overline{g}^2 n^2}{\hbar\Omega}\sin^3\theta_d\left(\cos\theta_d - \cos\theta_\infty\right)^2 \tag{4.13}$$

The sum of these two energies gives a negative correction to the mean-field energy. Note however that the effect is decreased by half because of the positive Rabi contribution:

$$\frac{E^{MF}}{N} = -\frac{\hbar\tilde{\Omega}}{2} + \frac{n}{2} g_{--}^{--}(\theta_d) - \frac{\overline{g}^2 n^2}{\hbar\Omega}\sin^3\theta_d\left(\cos\theta_d - \cos\theta_\infty\right)^2 \tag{4.14}$$

The first term is the constant Rabi-energy of the $|-\rangle_{\theta_d}$ internal state, the second term is the standard two body interaction controlled by δ/Ω.

Three-body interaction:

The last term is interpreted as an effective attractive three-body interaction. The density of three body interactions is $g_3 n^3/3$, with :

$$g_3 = -\frac{3\overline{g}^2}{\hbar\Omega}\sin^3\theta_d\left(\cos\theta_d - \cos\theta_\infty\right)^2 < 0 \tag{4.15}$$

With this definition, and noting $g_2 = g_{--}^{--}(\theta_d)$, the local chemical potential of the condensate is correctly given by:

$$\mu = \frac{\partial\left(E^{MF}/V\right)}{\partial n} \simeq -\frac{\hbar\tilde{\Omega}}{2} + g_2 n + g_3 n^2 \tag{4.16}$$

A notable result is that **the three-body interaction strength can be tuned independently of the two-body interaction strength** $g_2 = g_{--}^{--}(\theta_d)$. Indeed, the latter depends only on δ/Ω while g_3 can be, at fixed θ_d, adjusted with an increase or decrease of Rabi frequency Ω.

However, the three-body interaction strength is zero regardless of the Rabi frequency for three values of θ_d (see figure 4.4) corresponding to the following situations:

- a coherent mixture already minimizing the interaction energy at $\theta_d = \theta_\infty$
- a pure condensate in state $|1\rangle$ given for $\theta_d \to 0$ or equivalently $\delta \ll \Omega$
- a pure condensate in state $|2\rangle$ given for $\theta_d \to \pi$ or equivalently $\delta \gg \Omega$

The first case was met in the beyond-mean-field study of chapter 3, we were indeed able to cancel perfectly the mean-field interaction energy at all orders in n because it only contained a two-body interaction term $g_2 n^2/2$.

Except in those three peculiar cases, we may be able to make the three-body term dominant for the dynamics by decreasing the two-body mean-field interaction strength.

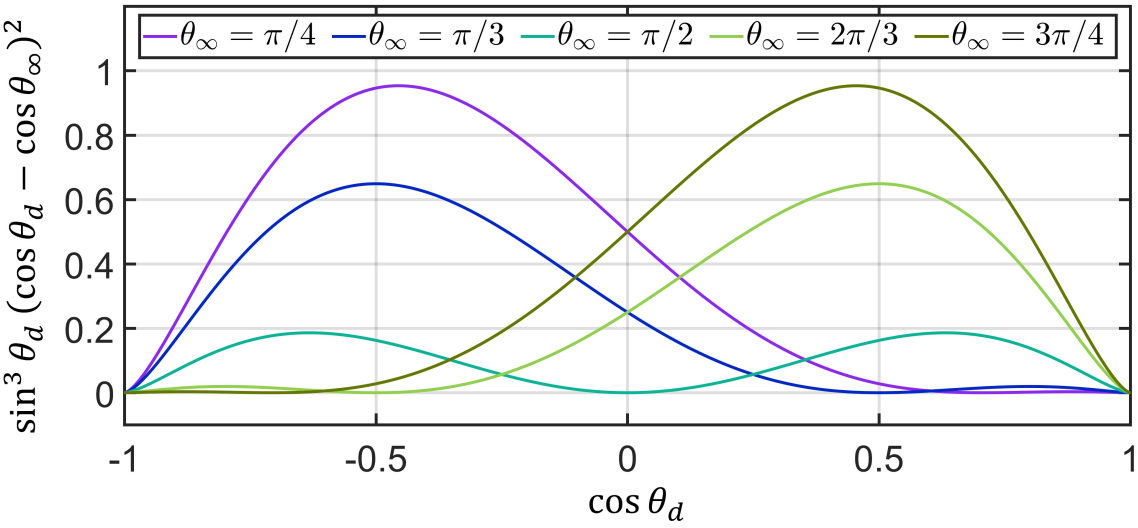

Figure 4.4: Amplitude of the three-body interaction in function of the driving polarisation $\cos(\theta_d) = \delta/\sqrt{\delta^2 + \Omega^2}$. The $1/\Omega$ dependence is not visible on the graph.

For example, at 54.7 G (symmetric case), the two cancellations of $g_{--}^{--}(\theta = \theta_d)$ (see figure 4.3) happen at $\cos\theta_d = \pm\sqrt{-g_\infty/\overline{g}} = \pm 0.429$, or equivalently for a mixture with proportions 71%/29% or 29%/71%. In the experimental part of this chapter we shall focus on the symmetric case because it allows simpler protocols and easier understanding of the observed phenomena. Note however, that it does not give a maximal three body strength (at a given interaction rigidity $\overline{g}$). The three-body strength can be made larger for more asymmetric interactions and around $\theta_d \simeq -\theta_\infty$ as can be seen on figure 4.4.

4.2.3 The case of harmonically trapped gas

A question remains on the extrapolation of above results in the case of an harmonically trapped condensate. We should check if it is allowed to use a local density approximation to get the mixture angle θ of the condensate. The problem comes from the kinetic term $-\hbar^2\nabla^2/2m$ which is not minimized by the solution $\theta(n)$ given by the local density approximation

To compute the density of kinetic energy, we take a wave-function of the form:

$$\psi = \sqrt{n(r)}e^{-i\varphi(r)}\left(\sin\left(\frac{\theta(r)}{2}\right)|1\rangle + \cos\left(\frac{\theta(r)}{2}\right)|2\rangle\right)$$

Where the space dependence of θ is implicitly assumed through its density dependence $\theta(r) = \theta(\delta/\Omega, n(r))$. We get the following results:

$$-\psi^*\frac{\hbar^2\nabla^2}{2m}\psi = -\sqrt{n}\frac{\hbar^2\nabla^2\sqrt{n}}{2m} + n\frac{m}{2}\left(\frac{\hbar\vec{\nabla}\varphi}{m}\right)^2 + n\frac{\hbar^2\left(\vec{\nabla}\theta\right)^2}{8m} - i\hbar\vec{\nabla}\cdot\left(n\frac{\hbar\vec{\nabla}\varphi}{m}\right) \quad (4.17)$$

On the right hand side, the first term is the quantum pressure. The second one the classical kinetic energy with the velocity field of the gas $\vec{v} = \frac{\hbar\nabla\varphi}{m}$. The third term is the one we want to neglect, it gives a cost to any in-homogeneity of the polarisation angle θ. The last term (pure imaginary number) ensures the conservation of probability $\partial_t n = -\vec{\nabla}\cdot(n\vec{v})$.

The correction of θ is given by equation 4.10, which yields the in-homogeneity energy:

$$\begin{aligned}\int n\frac{\hbar^2}{8m}\left(\vec{\nabla}\theta\right)^2 d^3r &= \int n\frac{\hbar^2}{8m}\left(\vec{\nabla}n\right)^2\left(\frac{2\overline{g}}{\hbar\Omega}\sin^2\theta_d\left(\cos\theta_d-\cos\theta_\infty\right)\right)^2 d^3r \\ &= \int l_{\tilde{\Omega}}^2\frac{|g_3|}{6}n\left(\vec{\nabla}n\right)^2 d^3r\end{aligned} \tag{4.18}$$

It should be compared to the gain in energy obtained by the local-density-approximation, *e.g.* the three body interaction energy:

$$E_{3b}^{MF} = \int \frac{g_3}{3}n^3 d^3r \tag{4.19}$$

For a condensate in an harmonic trap of frequency $\overline{\omega}$, the gradient of density $\vec{\nabla}n$ will be of the order of $n/a_{h.o}$ (or even smaller for a Thomas-Fermi profile), where the harmonic oscillator length is simply $a_{h.o.} = \sqrt{\frac{\hbar}{m\overline{\omega}}}$. The ratio of the θ in-homogeneity energy to the mean-field three-body energy is bounded from above by $\overline{\omega}/\tilde{\Omega}$ which is typically less than $1/20$. The local density approximation for mixture angle $\theta(n)$ is therefore valid. This is easily understood physically because the energy cost of θ in-homogeneity gives a moderation law to an already first order correction of mixture angle $\theta(n)$. Therefore, it is a second order correction in $\overline{\omega}/\Omega \ll 1$.

4.3 Measure of three-body interactions with radial breathing

For a cigar-shaped pure condensate in an harmonic trap with radial frequency ω_r and axial frequency $\omega_z \ll \omega_r$, The frequency of isotropic radial breathing oscillations is expected to be independent of the strength of two-body interactions g_2. This invariance relies on a hidden symmetry of Gross-Pitaevski equation under scale transformation and with the assumption of a reasonable ansatz for the time dependent radial density profile[35][36][37]. This constant breathing frequency is equal to $2\omega_r$, as it would be for an ideal gas, but also for a strongly interacting Thomas Fermi configuration. In this section we study experimentally the modification of radial breathing frequency by the three-body interaction appearing in an RF-dressed condensate.

4.3.1 Experimental observation

The experiment starts with a pure condensate of 1.4×10^5 atoms in state $|2\rangle$. The frequencies of the elongated trap are: $(\omega_r,\omega_z)/2\pi = (300, 16.4)$ Hz. The RF-dressed condensate is then created with a 0.4 ms frequency sweep from a detuning $\delta = 7.5\,\Omega$ to a chosen final value. Its duration guarantees that the internal dynamics is an adiabatic transfer but the space dynamics is a quench of interaction. Indeed, inequality $\Omega/2\pi \gg 1/0.4\,\text{kHz} \gg \omega_r/2\pi$ implies that the radial density profile is almost frozen during the sweep meanwhile the internal state has enough time to adiabatically follow the change of $|-\rangle$ state. The change of internal state induce a change of the interaction strengths (two-body and three-body) in the RF-dressed condensate. The two-body strength, initially equal to g_{22}, is reduced to $g_{--}^{--}(\theta_d)$ as the mixture angle comes closer to $\theta_\infty = \pi/2$. On the contrary, the three-body strength, initially zero, is increased (in norm) to a negative value depending on the final mixture angle θ_d (see figure 4.4 in the symmetric case). These two effects lead to a decrease

of interaction energy in the final configuration. The equilibrium size, for the final detuning, is therefore smaller than the initial Thomas-Fermi radius. Radial breathing oscillations start right after the end of the sweep. We limit our experimental study on the first 15 ms in order to neglect any axial dynamics, happening on larger timescales ($\omega_z = 16.4$ Hz). Our analysis focus on the radial dynamics of the condensate, in particular, at the center of the axial trap where the cigar-shaped Thomas-Fermi profile initially gives an almost constant one-dimensional density n_{1D}.

The Rabi-frequency is fixed at $\Omega/2\pi = 25.4\,\mathrm{kHz}$ and the final detuning δ_f in $[0.8, 1.4]\,\Omega$. They are maintained constant for a waiting time in $[0, 15]$ ms, which allows the radial density profile to oscillate freely. Because the radial size of the condensate is of the order of $1\,\mu$m, we had to observe breathing oscillations in momentum space. At the end of the chosen waiting time, the two dipole traps are suddenly turned-off and the adiabatic sweep is reversed in 0.4 ms to transfer back the condensate in state $|2\rangle$. This greatly increases the interaction energy and allow for a better resolution after a 9.7 ms time of flight. The measured radial size after time of flight clearly oscillates with respect to the waiting time (see inset of figure 4.5). The frequency of breathing oscillations is found by a sinusoïdal fit and then plotted with respect to δ_f/Ω. Contrary to the invariant $2\omega_r$ found in the case of purely two-body interactions, we get a clear decrease of the frequency up to 8 %.

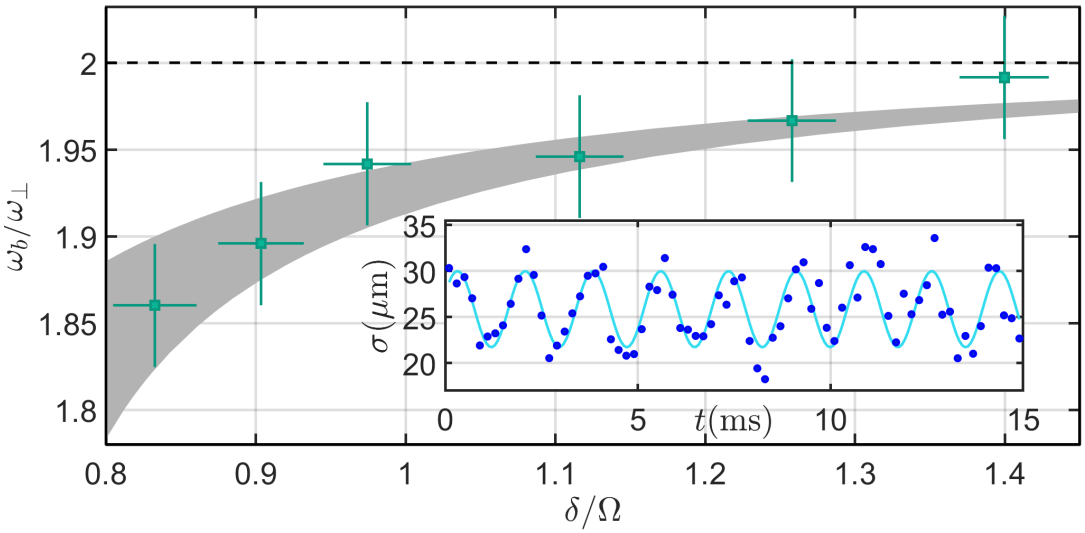

Figure 4.5: Frequency of radial breathing oscillations in function of the finale detuning δ_f/Ω at $\Omega/2\pi = 25.4\,\mathrm{kHz}$. Dots correspond to experimental data, vertical bars to an uncertainty of 1.5 % on the measured frequency, horizontal bars are linked to the dominant noise on δ_f: the magnetic fluctuation of around 0.8 mG. The shaded area is the theoretically allowed frequencies for an estimated one-dimensional density $2.3 \times 10^9\,\mathrm{m}^{-1} \leq n_{1d} \leq 2.65 \times 10^9\,\mathrm{m}^{-1}$ given by experimental fluctuations and uncertain detectivity. The inset is the time dependence of the radial size of the condensate for $\delta/\Omega = 0.9$ and after the reverse sweep and the 9.7 ms time of flight.

4.3.2 Variational ansatz and Virial theorem

In order to compare the experimental results to a theoretical prediction, we use a variational ansatz for the condensate wave-function, in analogy with [5] and [38]:

$$|\psi\rangle(r,t) = \sqrt{\frac{n_{1D}}{2\pi}}\frac{1}{R(t)} f\left(\frac{r}{R(t)}\right) e^{i\varphi(r,R,t)} \; |-\rangle_{\theta(n)} \tag{4.20}$$

Where $\varphi(r,R,t)$ is a phase and the function $f(u)$ is real, positive and normalised to 1:

$$\int u\, f^2(u)\, du = 1 \tag{4.21}$$

The radius $R(t)$ gives the radial size of the condensate at time t and the only allowed transformations are dilations because the shape of the radial density profile remains given by $f(r/R)$ at all times. The wave-function of the condensate verifies the Gross-Pitaevski equation so the phase φ is in fact entirely fixed by the conservation of probability. By writing this phase in function of the super-fluid velocity field $\vec{v}$ with $\varphi = -m\vec{v}\cdot\vec{r}/\hbar$, one can check that the velocity field must be:

$$\vec{v} = \frac{\vec{r}\dot{R}}{R} \tag{4.22}$$

And the conservation of probability follows from the following equalities, with $u = r/R$:

$$\begin{aligned}
\frac{\partial n}{\partial t} = \frac{\partial}{\partial t}\left(f^2\left(\frac{r}{R}\right)\frac{1}{R^2}\right) &= \frac{1}{r^2}\frac{\partial}{\partial t}\left(f^2(u)\,u^2\right) \\
&= -\frac{\dot{R}}{rR^2}\frac{\partial}{\partial u}\left(f^2(u)\,u^2\right) \\
&= -\frac{1}{r}\frac{\dot{R}}{R}\frac{\partial}{\partial r}\left(f^2(u)\,u^2\right) \\
&= -\frac{1}{r}\frac{\partial}{\partial r}\left(r\times\frac{r\dot{R}}{R}\times f^2\left(\frac{r}{R}\right)\frac{1}{R^2}\right) = -\vec{\nabla}\cdot(n\vec{v})
\end{aligned} \tag{4.23}$$

Inserting the ansatz 4.20 for the wave-function into the mean-field energy functional, with harmonic trapping and two-body and three-body interaction strengths, we get the energy of the condensate with respect to its radial size $R(t)$:

$$E(R,\dot{R}) = E_{\text{flow}} + E_{\text{pot}} + E_{\text{zp}} + E_{2b} + E_{3b} + N\varepsilon_- \tag{4.24}$$

The classical kinetic energy (or flow energy) is:

$$E_{\text{flow}} = N\left(\int u^3 f^2(u)\, du\right)\frac{m}{2}\dot{R}^2 \tag{4.25}$$

The harmonic radial potential energy is:

$$E_{\text{pot}} = N\left(\int u^3 f^2(u)\, du\right)\frac{m\omega_r^2}{2}R^2 \tag{4.26}$$

The zero-point motion (or quantum kinetic) energy is:

$$E_{\text{zp}} = N\left(-\int f(u)\frac{\partial}{\partial u}\left(u\frac{\partial f(u)}{\partial u}\right)\, du\right)\frac{\hbar^2}{2m}\frac{1}{R^2} \tag{4.27}$$

The two-body energy is:

$$E_{2b} = N\left(\int uf^4(u)\,du\right)\frac{n_{1D}g_{--}^{--}(\theta_d)}{4\pi}\frac{1}{R^2} \tag{4.28}$$

And the effective three-body energy is:

$$E_{3b} = N\left(\int uf^6(u)\,du\right)\frac{n_{1D}^2 g_3(\theta_d,\Omega)}{12\pi^2}\frac{1}{R^4} \tag{4.29}$$

The θ in-homogeneity energy was neglected as justified in 4.2.3. In the same spirit, the ansatz 4.20 for the wave-function of the condensate, didn't allow different phases for the two components $\langle 1|\psi\rangle$ and $\langle 2|\psi\rangle$. In other words, spin-currents are forbidden by the form of the ansatz. This is justified by the slow space dynamics compared to the fast internal dynamics at Rabi frequency Ω. We now consider only small oscillations of radial size R and develop the effective potential $V_{\text{eff}} = E_{\text{pot}} + E_{\text{zp}} + E_{2b} + E_{3b}$ around the equilibrium size R_0 given by the competition between repulsive energy terms (zero-point motion, two-body interactions) and attractive energy terms (harmonic trap, three-body interactions). The equilibrium size is fixed by the following equality, also called Virial theorem:

$$R_0\left.\frac{dV_{\text{eff}}}{dR}\right|_{R_0} = 0 = 2E_{\text{pot}} - 2E_{\text{zp}} - 2E_{2b} - 4E_{3b} \tag{4.30}$$

Derivating once again, gives the equalities:

$$\begin{aligned} R_0^2\left.\frac{d^2V_{\text{eff}}}{dR^2}\right|_{R_0} &= 2E_{\text{pot}} + 6E_{\text{zp}} + 6E_{2b} + 20E_{3b} \\ &= 8E_{\text{pot}} + 8E_{3b} \\ &= 8N\left(\int u^3f^2(u)\,du\right)\frac{m\omega_r^2}{2}R_0^2\left(1+\frac{E_{3b}}{E_{\text{pot}}}\right) \end{aligned} \tag{4.31}$$

Where we used the Virial equation 4.30 between the first and second lines. This allows us to write the parabolic expansion of the potential around R_0 then derive the semi-classical equation of motion from $\frac{dE(R)}{dt} = 0$. The numerical factors $\left(\int u^3f^2(u)\,du\right)$ appearing in E_{flow} and E_{pot} cancel out, as do the total mass Nm:

$$\ddot{R} + 4\omega_r^2\left(1+\frac{E_{3b}}{E_{\text{pot}}}\right)(R-R_0) = 0 \tag{4.32}$$

Finally, the frequency of the low-amplitude breathing oscillation is:

$$\omega_b = 2\omega_r\sqrt{1+\frac{E_{3b}}{E_{\text{pot}}}} \tag{4.33}$$

As expected, the frequency would be exactly $2\omega_r$ in the absence of three-body interactions. The magic is hidden in the Virial equality although we can understand it as a direct consequence of the same scaling of two-body interactions and zero-point energy ($\propto R^{-2}$) for two-dimensional dynamics.

For the RF-dressed condensate, we expect a decrease of frequency because the three-body interaction is attractive ($g_3 < 0$). Finally, we computed numerically the two-dimensional ground-state of the condensate in order to evaluate the energies E_{3b} and E_{pot}.

The external parameters were the following: the two-body interaction strength $g_{--}^{--}(\theta_d)$ and three-body interaction strength g_3 were precisely estimated thanks to a precise knowledge of Rabi frequency Ω and detuning δ. The trap frequency ω_r was also fixed according to the experimental measure of dipole oscillations $\omega_r/2\pi = 16.4\,\mathrm{Hz}$. The experimental one-dimensional density was known with a 10 % precision so we had to do the numerical computation for $2.3 \times 10^9\,\mathrm{m}^{-1} \leq n_{1d} \leq 2.65 \times 10^9\,\mathrm{m}^{-1}$. This uncertainty leads to the estimation of breathing frequency in the shaded area of figure 4.5.

4.3.3 Negligible influence of three-body recombinations and conclusion on breathing

During the 15 ms of evolution, a progressive loss of atoms of around 20 % was observed. It is attributed to three-body recombinations. However, the amplitude of oscillation displayed no visible decrease (see inset of figure 4.5). The effective quality factor Q of the radial breathing oscillator is large compared to 1 and three-body recombination have negligible impact on the measured frequency of the few (8 to 12) breathing oscillations happening in 15 ms. Physically, to estimate the quality factor we have to think about causes of energy loss during the oscillations. When a three-body recombination happen, the three atoms are lost and the decrease in energy for the rest of the condensate is on the two-body and three-body real interaction energies. If the losses are small compared to these interaction energies, no damping is observed $Q \gg 1$.

We therefore checked that the characteristic energy of real three-body interactions $g_3\frac{n^3}{3}$ dominates the effective imaginary term linked to three-body recombination $-i\hbar K_3\frac{n^3}{3}$. At the Rabi frequency $\Omega/2\pi = 25.4\,\mathrm{kHz}$ and detuning $\delta/\Omega \simeq 0.8$ the $g_3/\hbar$ coefficient is of the order of $10^{-38}\,\mathrm{m}^{-6}\mathrm{s}^{-1}$ which is a factor 100 larger than the typical K_3 coefficient. Therefore, the measured decrease of breathing frequency ω_b is entirely given by the elastic three-body interactions with strength g_3 and have no link with any damping of oscillations. Moreover, the variational ansatz 4.20 gives a satisfying fit of experimental data. It proves that the dependence of the three-body interaction strength with respect to internal state has been correctly derived and measured. The scaling of g_3 in $1/\Omega$ remains to be verified in the next experiment.

4.4 Three-body induced radial collapses

In the previous experiment, we worked with relative detunings δ/Ω in $[0.8, 1.4]$. Compared to the pure condensate in state $|2\rangle$ at $\delta/\Omega \gg 1$, this allowed a decrease of two-body interactions and an increase, in norm, of the three-body attractive interactions. Before going further, three specific values of detuning should be highlighted. Firstly, still in the symmetric case at $\mathrm{B} = 54.8\,\mathrm{G}$, the three body interaction strength is maximal at $\cos\theta_d = \sqrt{2/5}$, *i.e.* $\delta/\Omega = 0.8165$. For smaller detuning, g_3 decreases until it cancels out at $\delta = 0$ (see figure 4.4). Secondly, the two-body interaction strength is minimal and negative at $\delta = 0$, it is then equal to $g_\infty = 4\pi\hbar^2 a_\infty/m$ with $a_\infty = -8.4\,a_0$. The cancellation of two-body interaction strength g_{--}^{--} happen at $\delta/\Omega = \pm 0.4739$.

For detunings $|\delta|/\Omega$ below 0.4739 we expect the RF-dressed condensate to be unstable because of attractive two-body interactions. But between 0.4739 and the 0.8 lower bound of the previous experiment, the two-body interaction strength remains positive.

By approaching 0.4739 from above, the space dynamics of the condensate is increasingly dominated by three-body attractive interactions. Experiments at these detuning no longer display radial breathing with modified frequency but instead radial collapses. As a first guess, this phenomenon may be linked to the apparition of imaginary breathing frequencies in equation 4.33. We will develop a more complete theoretical prediction after presenting this second experiment and its results.

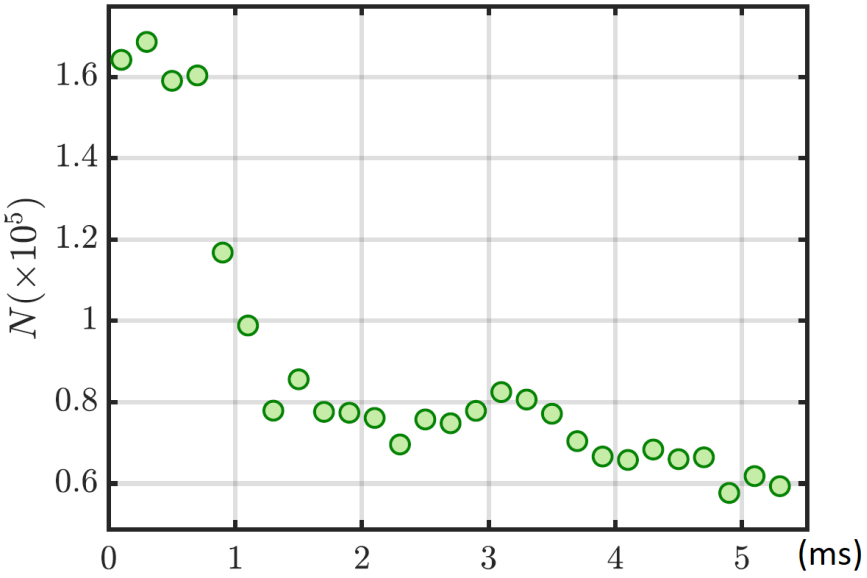

Figure 4.6: Total number of atom in the gas with respect to time at a detuning of $\delta/\Omega = 0.6$ and Rabi frequency of $\Omega/2\pi = 10.5$kHz.

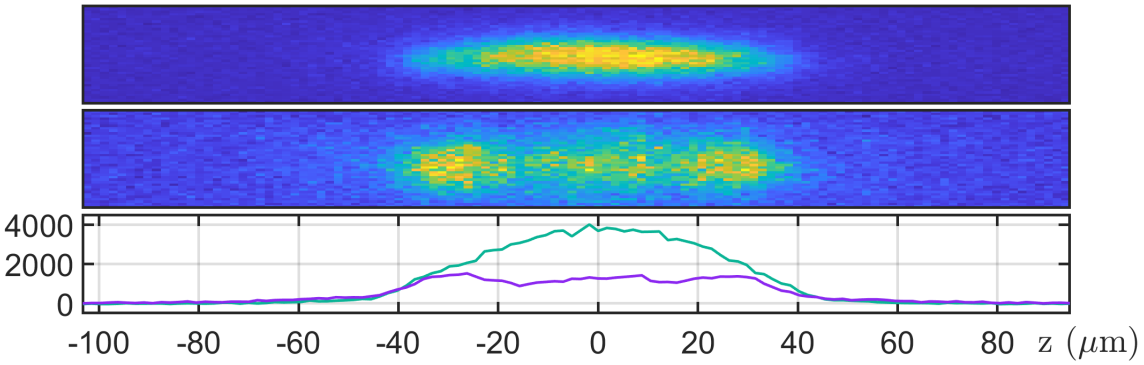

Figure 4.7: Density profiles at $\Omega/2\pi = 20.3\,$kHz when observed after a 3 ms wait-time in the traps followed by 4.3 ms of time-of-flight. *(up)* At a detuning of $\delta/\Omega = 2$, no radial collapse happen. *(middle)* At a detuning of $\delta/\Omega = 0.5$, the losses caused by radial collapse happen mostly in the central axial region ($z \sim 0$). *(bottom)* Radially integrated density profiles at the two above detunings, the y-axis is the number of atoms detected per unit axial cell of width $1.75\,\mu$m.

4.4.1 Experimental observation: detuning thresholds for collapses

For relative detunings δ/Ω below 0.8, the previous protocol yields almost no breathing oscillations. Instead the number of atoms in the middle axial area - in an axial length of $12\,\mu$m where the one-dimensional density is initially almost constant - is divided by 3 in less than 2 ms (see figure 4.6). In comparison, the typical frequency of breathing oscillations would be around $\pi/\omega_r = 3\,$ms. We interpret this as a collapse of the condensate due to a prevail of attractive effects on repulsive effects. After the sweep, we wait 3 ms then do a fast reverse sweep followed by time of flight. We measured the remaining atoms in the middle area as a function of the relative detuning δ/Ω and observed a clear threshold effect (see figure...). There are no atom losses for detunings $|\delta|$ above $\delta_c > 0$, while two third of atoms are lost under δ_c independently of the exact value of the detuning. This allows a precise measurement of δ_c with step function fits. The scan of detuning is now on $[-1.5, 1.5]\,\Omega$ to take advantage of the symmetry of interaction and discard the uncertainty on the exact location of the resonance $\delta = 0$. The observed variable is the remaining one-dimensional density in the central axial zone of width $\Delta z = 12\,\mu$m (7 pixels in the z direction, see figure 4.7 for justification).

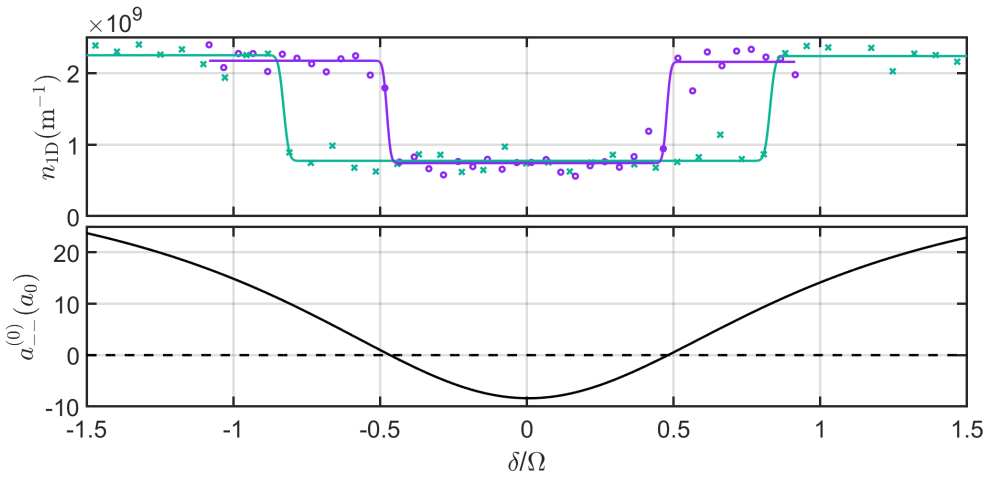

Figure 4.8: Scan of the detuning at two different values of Rabi frequencies and remaining one-dimensional density of atom in the central $12\,\mu$m axial region.

The experiment can be iterated at different Rabi frequencies, we find relative detuning thresholds δ_c/Ω smaller for smaller Ω. The only effect depending on Ω, and not only on δ/Ω is the three-body attractive interaction. This experiment thus investigates the scaling $g_3 \propto 1/\Omega$. We plot relative detuning thresholds δ_c/Ω with respect to Ω on figure 4.10.

4.4.2 Gaussian radial model

Because we work, in this experiment, close to a cancellation point of mean-field interactions $g_{--}^{--}(\theta(n)) \simeq 0$, we decided to take a radial Gaussian model for the wave-function of the condensate in the variational ansatz 4.20. Such assumption is exact for an ideal gas in the harmonic trap. In our case, the radial size of the condensate will be different from the harmonic oscillator length $a_{ho} = \sqrt{\hbar/(m\omega_r)}$. We work with the dimensionless size $\sigma(t)$

such that the radial density profile is:

$$n(r) = \frac{n_{1D}}{\pi a_{ho}^2 \sigma^2} \exp\left(-\frac{r^2}{a_{ho}^2 \sigma^2}\right) \tag{4.34}$$

Equivalently, the function $f(u = r/R)$ of ansatz 4.20 is given by $R = a_{ho}\sigma$ and :

$$f(u) = \sqrt{2} \exp\left(-\frac{u^2}{2}\right) \tag{4.35}$$

With such Gaussian ansatz, and contrary to a Thomas-Fermi profile with diverging zero-point energy, we are able to compute exactly all energy terms in equation 4.24:

$$\begin{aligned} \frac{E(\sigma)}{N\hbar\omega_r} &= \frac{\dot{\sigma}^2}{2\omega_r^2} + \frac{\sigma^2}{2} + \frac{1}{2\sigma^2} + \frac{n_{1D} a_{--}^{(0)}(\theta_d)}{\sigma^2} - \frac{16\omega_r}{3\Omega} \frac{n_{1D}^2 \bar{a}^2}{\sigma^4} \sin^3\theta_d \cos^2\theta_d \\ &= \frac{\dot{\sigma}^2}{2\omega_r^2} + V_{eff}^{(3b\,approx)}(\sigma) \end{aligned} \tag{4.36}$$

Where the terms are ordered in the first line as : flow energy, trapping energy E_{pot}, zero-point energy E_{zp}, two-body energy E_{2b}^{MF}, three-body energy E_{3b}. We omitted the constant $N\varepsilon_-$ internal Rabi energy. The effective potential $V_{eff}(\sigma)$ is calculable for all sizes σ. At a given Ω and δ/Ω, we can plot its profile (4.9). For very small condensate sizes $\sigma \ll 1$ the three-body attractive energy dominates. For large sizes, $\sigma \gg 1$, the attractive trapping energy dominates. At intermediate sizes, $\sigma \sim 1$ the repulsive two-body and zero-point energy play a role and may enable the presence of a local potential barrier. Its height depends on the relative detuning $|\delta|/\Omega$ and decreases when the two-body term approaches the zero crossing ($a_{--} = 0$) from above at 0.4739. However, as can be seen on figure 4.9, the three-body approximation slightly overestimate the attractive effect. A more accurate estimation, detailed in 4.4.4 replaces E_{3b} by V_{corr}. We also explain in 4.4.3 the adding of E_{2b}^{BMF}. Finally, the exact effective potential is $V_{eff}^{(exact)} = E_{pot} + E_{zp} + E_{2b}^{MF} + V_{corr} + E_{2b}^{BMF}$.

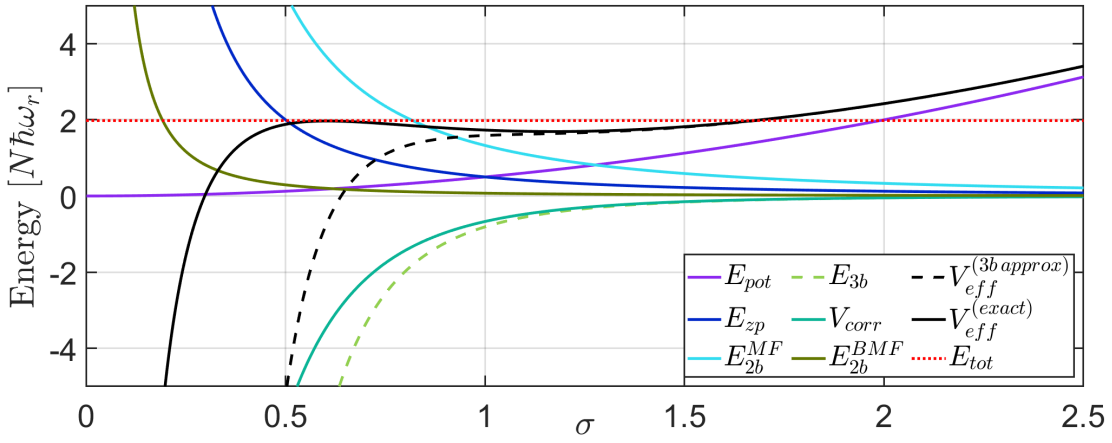

Figure 4.9: Effective potential and the different energy terms it contains for parameters : $\Omega = 10\,\mathrm{kHz}$, $\delta/\Omega = 0.88$, $n_{1D} = 2.3 \times 10^9\,\mathrm{m}^{-1}$. The dotted curve is the conserved total energy of the condensate. The dashed curves are valid only under the three-body approximation and were not used for the analysis. All five colored plain curves add up to form $V_{eff}^{(exact)}$, which is our most precise model.

Before the sweep, the pure condensate in state $|2\rangle$ has a tri-dimensional Thomas-Fermi profile. Since the sweep is short compared to the time periods of the traps, the initial size is found by matching the radial rms size of the two-dimensional Thomas-Fermi profile with the radial rms size of the Gaussian ansatz. We find numerically $\sigma(0) = 1.7$. The initial velocity is simply zero ($\dot{\sigma}(0) = 0$). With these initial conditions, the dynamics is given by a one-dimensional classical conservative motion. If the height of the potential hill, around $\sigma = 0.5$, is higher than the total energy, then the size σ will remain in the potential well. On the contrary, if the height of the potential hill is smaller than the energy, the size will decrease rapidly to zero, until a collapse occurs.

By changing either the relative detuning δ/Ω or the Rabi frequency Ω, we increase or decrease the height of the potential barrier. Choosing a given Rabi frequency Ω sets the strength of the three-body interactions g_3. The scan of relative detuning δ/Ω then enable us to find experimentally the critical value δ_c at which the height of the potential barrier is equal to the energy. Both the two-body and the three-body interaction strengths depends on this scan, so we numerically find it by dichotomy. We start with an arbitrary value of $\delta/\Omega = 1$. The height of the potential hill is then computed with the expression of exact effective potential. If this height is smaller (resp. higher) than the initial energy of the condensate, we add a small negative (resp. positive) correction to δ/Ω equal to $\pm 2^{-n}$ at the n-th iteration. The serie quickly converges to the critical value for threshold δ_c/Ω at which the height of the potential hill is exactly equal to the energy of the condensate. We can then perform this numerical computation at a different Rabi frequencies and we get theoretical prediction to the edge between collapse and stability.

Experimental data (figure 4.10) shows that for smaller Rabi frequencies, the two-body interaction strength is, at collapse threshold, further above its zero crossing ($a_{--}^{(0)} = 0$) because it needs to compensate for stronger mean-field attractive effects. To better fit experimental data points, we improved the three-body mean-field model by including BMF energy and more accurately estimating the mean-field energy at $\gamma \sim 1$ (see next two subsections).

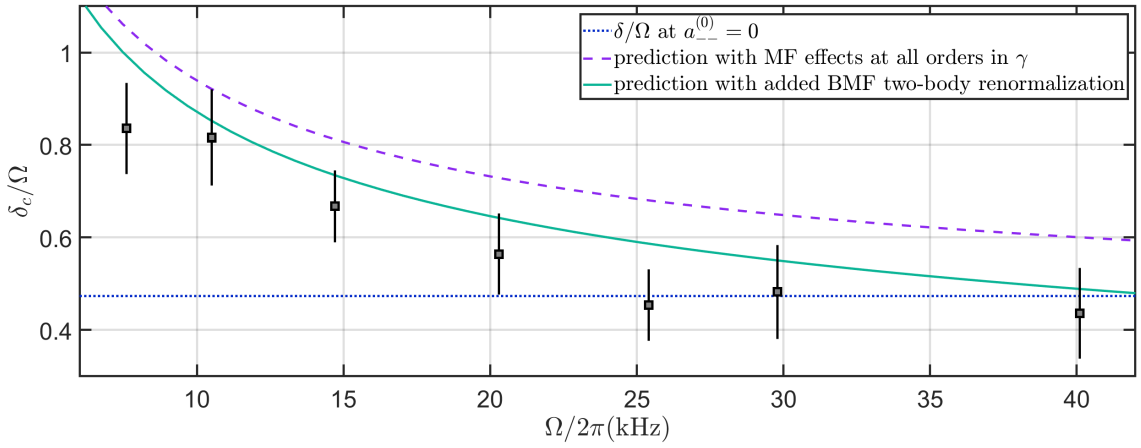

Figure 4.10: Experimental data on detuning thresholds as a function of the Rabi frequency and theoretical predictions. For the purple dashed curve, the mean-field energy is computed self-consistently ($E_{3b} \to V_{corr}$) and not only in the three-body approximation valid only at small γ (see 4.4.4). The plain indigo curve is the final prediction also including the BMF two-body renormalization (see 4.4.3), it is calculated with $V_{eff}^{(exact)}$.

4.4.3 Discussion on beyond-mean-field effects

In the second experiment on radial collapse, we worked near a cancellation point of mean-field interaction energy. It is natural that beyond-mean-field effects should start to play a role in the dynamics. Moreover, the beyond-mean-field energy is a repulsive effect, or positive energy, so it should bring down the prediction curve.

We don't have an analytical expression of the beyond-mean-field energy except in the very specific conditions where $g_\infty = 0$ and $\theta_d = \theta_\infty$ (see chapter 3). However, in our experiment, the Rabi frequency is large compared to the typical chemical potential of the condensate. We can again assume that the beyond-mean-field energy is analytical and express it in a power serie of the density. The first term is the two-body renormalization calculated in chapter 1 (equation 1.50). It scales as $\sqrt{\Omega}$. We didn't take into account further terms in the beyond-mean-field energy by lack of analytical expressions for their coefficients.

$$E_{2b}^{BMF} = \frac{n_{1\mathrm{D}} a_{--}^{(1)}(\theta_d)}{\sigma^2} \tag{4.37}$$

Note that in the first experiment on radial breathing frequencies, the renormalization of two-body interaction strength by beyond-mean-field effects had negligible influence. Firstly, because the two-body interaction strength was not small. Secondly, because of the hidden scale invariance, the protocol worked regardless of the value of total two-body interaction term and allowed us to measure only the three-body term of the total energy.

4.4.4 Validity of three-body approximation and beyond

Another possible source of disagreement between theory and experiment is an overestimation of attractive effects. Indeed, the tree-body effect is only a low density approximation.

The small dimensionless parameter for the power expansion of the mean-field energy is $\gamma = 2\bar{g}n/\hbar\Omega$. Initially, the Thomas-Fermi radius of the condensate are $R_z = 50\,\mu$m and $R_r = 2.7\,\mu$m. The peak density of the Thomas-Fermi profile is $2 \times 10^{20}\,\mathrm{m}^{-3}$. This gives an initial value of γ of 0.07 for $\Omega/2\pi = 40.1\,$kHz to 0.4 for $\Omega/2\pi = 7.6\,$kHz. However, as the cloud radially contracts, the radial size σ decreases and the peak density $n_{1\mathrm{D}}/(\pi a_{ho}^2\sigma^2)$ increases. The barrier of potential is typically at $\sigma \simeq 0.5$ which means that values of γ around 1.4 to 7 are reached during the compression (depending on the value of Ω). The three-body approximation should no longer be valid.

We will study in more detail the behavior of the mean-field energy at large γ in the next chapter. However, for our prediction on radial collapse, we blindly used integration tricks on the mean-field energy functional to get an exact, yet obscure, replacement of E_{3b} by V_{corr}. It is explained below.

In the local density approximation for mixture angle θ and with the ansatz 4.34, the two terms depending on internal state read:

$$\begin{aligned} E_{int+Rabi}^{MF} &= \int \left[\frac{n^2}{2} g_{--}^{--}(\theta) - \frac{n\hbar\Omega}{2\sin\theta_d} \cos(\theta - \theta_d) \right] 2\pi r dr dz \\ &= \frac{N\pi a_{ho}^2 \sigma^2}{n_{1\mathrm{D}}} \int \left[\frac{n}{2} g_{--}^{--}(\theta) - \frac{\hbar\Omega}{2\sin\theta_d} \cos(\theta - \theta_d) \right] dn \end{aligned} \tag{4.38}$$

Where we used the differential of the density $dn = -n2r\,dr/(a_{ho}^2\sigma^2)$.
We can then integrate exactly by changing the integration variable to θ since equation 4.6 can be rewritten $n = \frac{\hbar\Omega}{2\overline{g}}\left(\frac{\cot\theta_d}{\cos\theta} - \frac{1}{\sin\theta}\right)$.Finally we find :

$$\frac{E_{int+Rabi}^{MF}}{N\hbar\omega_r} = -\frac{\varepsilon_-}{\hbar\omega_r} + \frac{n_{1D}a_{--}^{(0)}(\theta_d)}{\sigma^2} + V_{corr}(\sigma) \tag{4.39}$$

$$V_{corr}(\sigma) = \frac{n_{1D}\overline{a}}{\sigma^2}\left(\cos^2\theta_0 - \cos^2\theta_d\right) - \frac{\tilde{\Omega}}{2\omega_r}\left(\cos\left(\theta_0 - \theta_d\right) - 1\right) - \frac{\tilde{\Omega}}{4\omega_r\gamma_0}\left[\log|\sin\theta| - \cot^2\theta_d\log|\cos\theta| - 2\theta\cot\theta_d\right]_{\theta_d}^{\theta_0} \tag{4.40}$$

Where the polarisation angle θ_0 at the center of the condensate is then given by the numerical solution of $\sin\left(\theta_0 - \theta_d\right) = \gamma_0\sin\theta_d\sin\theta_0\cos\theta_c$.
For low central densities $\gamma_0 \ll 1$, one may check that the corrective potential V_{corr} is equal to the three-body energy term E_{3b}. However, at higher densities $\gamma_c \geq 1$, we can check on figure 4.9 that the three-body energy overestimate the attractive effect compared to the exact mean-field results.

Finallly, the theoretical prediction, with all added effects, is only partially able to explain the experimental results (4.10) because it is slightly biased towards higher threshold detunings δ_c. We believe this is due to the imperfect assumption of a Gaussian radial profile and also because the dynamics may partially starts during the sweep. Nevertheless, the collapse experiment clearly proved that the collective mean-field effect (three-body or beyond) increases as the Rabi frequency Ω is decreased.

4.5 Chapter conclusion

In this chapter we derived and experimentally investigated the collective mean-field effect on the energy. The remarkable feature is the apparition of a non-linearity more complex than a standard two-body energy term in n^2. The physical origin is the dependence of internal state of the condensate on its local density. At low densities, the additional non-linearity is given by a three-body attractive interaction term. Its strength can be doubly tuned with δ/Ω and Ω. The first dependence was experimentally verified with the measure of breathing frequencies. The second dependence was experimentally investigated with detuning threshold for radial collapses. The experiment clearly proved the increase of attractive mean-field effects as the Rabi frequency Ω is decreased. High densities were however reached suggesting that the three-body approximation was no longer valid.

Chapter 5

5. Behavior of the RF-dressed BEC at small Rabi coupling

In the two previous chapters, we saw that the Rabi energy $\hbar\Omega/2$ may be compared to the typical interaction energy of spin excitations $\overline{g}n$. When the ratio of the two $\gamma = 2\overline{g}n/\hbar\Omega$ is small, the BMF energy becomes analytic, and a three-body interaction term appears in the MF energy. In this theoretical chapter, we want to investigate the physics for value of γ typically going to 10, that we could reach with Rabi frequencies of the order of 1 kHz. Interactions will be strong compared to the coherent Rabi coupling. Therefore, the first source of concern is the coherent nature of the condensate. In other words, is it valid to assume the mean-field internal state is a coherent state ?

We start by introducing the numerical solving of the exact internal ground state of N condensed atoms in presence of Rabi-coupling at any value of γ. The form of the solution motivates us to introduce, in the second section, a synthetic dimension on which the state of the condensate can be found analytically with an effective Schrödinger equation. The model is able to predict the limit of incoherent mixtures is at $\gamma \simeq N$ which is far beyond our experimental conditions and legitimates the use of a mean-field coherent internal state. In the third part, with this coherent ansatz, we study the behavior of mean-field internal state and mean-field energy in function of γ. We also present experimental measurements at $\gamma \simeq 1$.
Finally, the behavior of beyond-mean-field energy at non-small γ is studied numerically. This allows a discussion on the existence and properties of RF-dressed quantum droplets.

5.1 Numerical solution for the internal state of an RF-dressed BEC of N particles

5.1.1 Zero-dimensional model

In order to study the validity of the mean-field coherent-state ansatz used in previous chapter, we want to compute exactly the internal state of a condensate of N particles in a zero-dimensional model. We assume all particles are in the same normalised space wave-function $\phi_0(\vec{r})$. The quantum state will belong to the vector space with N atoms either in state $|1\rangle$ or $|2\rangle$. This space is engendered by the $N+1$ states, with $0 \leq i \leq N$:

$$|i, N-i\rangle = \frac{\left(\hat{a_1}^\dagger\right)^i}{\sqrt{i!}} \frac{\left(\hat{a_2}^\dagger\right)^{N-i}}{\sqrt{(N-i)!}} |vac\rangle \tag{5.1}$$

We now have to compute the matrix element H_{ij} of the many-body Hamiltonian on this basis. The external trapping potential and kinetic Hamiltonian give a constant energy contribution independent of internal state since the wave-function $\phi_0(\vec{r})$ is fixed. We therefore forget them and we consider only the Rabi Hamiltonian and the two-body interaction Hamiltonian. The only non-diagonal elements H_{ij} come from the Rabi coupling operator $-\hbar\Omega/2\left(\hat{a_1}^\dagger\hat{a_2} + \hat{a_2}^\dagger\hat{a_1}\right)$. It couples the states with a ± 1 difference in number of atoms in state $|1\rangle$, so $i = j \pm 1$. The coupling is easily computed:

$$H^{(Rabi)}_{i,i+1} = H^{(Rabi)}_{i+1,i} = -\frac{\hbar\Omega}{2} \langle i+1, N-i-1| \hat{a_1}^\dagger\hat{a_2} |i, N-i\rangle = -\frac{\hbar\Omega}{2}\sqrt{(i+1)(N-i)} \tag{5.2}$$

We also compute the diagonal contribution due to detuning operator $\hbar\delta/2\left(\hat{a_1}^\dagger\hat{a_1} - \hat{a_2}^\dagger\hat{a_2}\right)$:

$$H^{(Rabi)}_{i,i} = \frac{\hbar\delta}{2} \langle i, N-i| \hat{a_1}^\dagger\hat{a_1} - \hat{a_2}^\dagger\hat{a_2} |i, N-i\rangle = \frac{\hbar\delta}{2}(2i - N) \tag{5.3}$$

Finally, we compute the contribution from the two-body contact interaction operator:

$$\hat{H}^{(int)} = \left(\int |\phi_0(\vec{r})|^4 d^3r\right)\left(g_{11}\frac{(\hat{a_1}^\dagger)^2(\hat{a_1})^2}{2} + g_{22}\frac{(\hat{a_2}^\dagger)^2(\hat{a_2})^2}{2} + g_{12}(\hat{a_2}^\dagger\hat{a_1}^\dagger\hat{a_2}\hat{a_1})\right) \tag{5.4}$$

We note the first integral $\tilde{n}_0 = \int |\phi_0(\vec{r})|^4 d^3r$.

$$H^{(int)}_{i,i} = g_{11}\tilde{n}_0\frac{i(i-1)}{2} + g_{22}\tilde{n}_0\frac{(N-i)(N-i-1)}{2} + g_{12}\tilde{n}_0\,(i(N-i)) \tag{5.5}$$

We can further simplify this expression by expressing the interaction strengths g_{ij} in terms of $\overline{g}$, g_∞ and $\cos\theta_\infty$. This yields:

$$H^{(int)}_{i,i} = g_\infty\tilde{n}_0\frac{N(N-1)}{2} + \frac{\overline{g}\tilde{n}_0}{2}\left[(N - 2i - N\cos\theta_\infty)^2 - \left(N\sin^2\theta_\infty + 4i\cos\theta_\infty\right)\right] \tag{5.6}$$

The first term on the right hand side is a constant contribution independent of i so we can forget it. The second term gives a contribution proportional to $N^2/2$ and is the mean-field contribution to the interaction energy. The third term is proportional to N and accounts for the incorrect counting of number of pairs in each state in the second term

$N^2/2 \longrightarrow N(N-1)/2$. Finally, we divide the Hamiltonian by $N\hbar\Omega/2$ to get dimensionless equations. The dimensionless detuning and dimensionless density are defined by:

$$\left\{ \begin{array}{rcccl} D & = & \delta/\Omega & = & \cot\theta_d \\ \gamma & = & 2\overline{g}\tilde{n}_0 N/(\hbar\Omega) & & \end{array} \right. \tag{5.7}$$

The matrix elements $\tilde{H}_{ij}$ of the dimensionless Hamiltonian (in unit of $N\hbar\Omega/2$) read:

$$\left\{ \begin{array}{l} \tilde{H}_{i,i+1} = \tilde{H}_{i+1,i} = -\frac{1}{N}\sqrt{(i+1)(N-i)} \\ \tilde{H}_{i,i} = -\frac{D}{N}(2i-N) + \frac{\gamma}{2N^2}\left[(N-2i-N\cos\theta_\infty)^2 - (N\sin^2\theta_\infty + 4i\cos\theta_\infty)\right] \end{array} \right. \tag{5.8}$$

5.1.2 Numerical computation

With these matrix elements, the diagonalization can be performed numerically after choosing the values of the four parameters θ_d, θ_∞, N and γ. The state of the condensate $|\Psi_{BEC}\rangle$ is the eigen-vector with the smallest energy. It is entirely defined by the $N+1$ complex coefficients $c_i = \langle\Psi_{BEC}|i, N-i\rangle$. The results are plotted on figure 5.1 for $\theta_\infty = \pi/2$, $\theta_d = \pi/3$, $N = 800$ and different values of γ in logarithmic units.

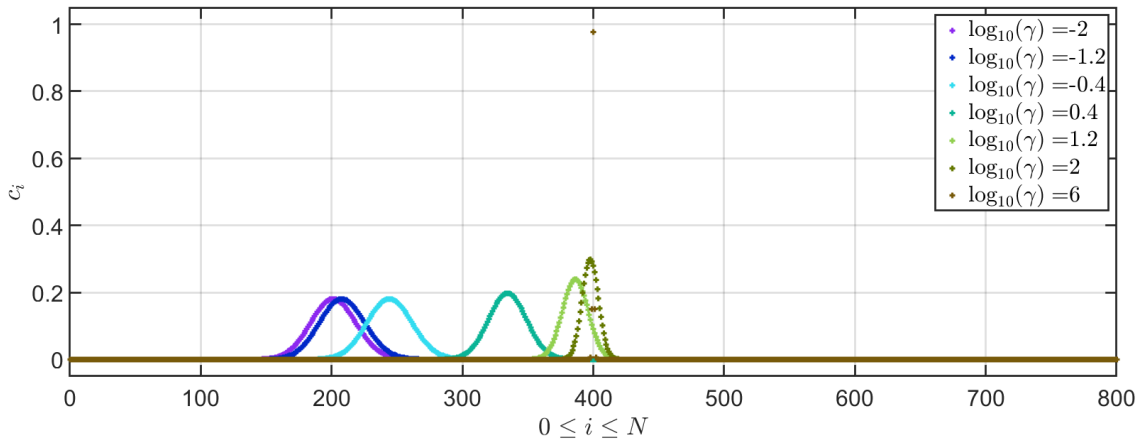

Figure 5.1: Results of the numerical diagonalization and coefficients c_i defining the internal state of the condensate at different dimensionless densities γ. The fixed parameters are $\theta_\infty = \pi/2$, $\theta_d = \pi/3$ and $N = 800$

The limit of vanishing density ($\gamma \to 0$):

In the limit of vanishing density γ, the internal state of each particle of the condensate is simply $|-\rangle_{\theta_d}$. The probability to find a given particle in state $|1\rangle$ is $\sin^2(\theta_d/2)$. The independence of particles together with the central limit theorem asserts that the probability $|c_i|^2$ to find i particles in state $|1\rangle$ should be, for large N, asymptotically equal to:

$$|c_i|^2 \underset{N\to\infty}{\longrightarrow} \frac{1}{\sigma\sqrt{2\pi}} \exp\left\{-\frac{(i-N_{1,coh})^2}{2\sigma^2}\right\} \tag{5.9}$$

Where $N_{1,coh} = N\sin^2(\theta_d/2)$ and $\sigma = \sqrt{N}\sin(\theta_d)/2$. For the value of the parameters chosen in the computation, we get $N_{1,coh} = 200$ and $\sigma = 12.2$. Note however that we

plot coefficients c_i and not their squares. This multiplies the width of the peak around $N_{1,coh}$ by $\sqrt{2}$. The fact that coefficients c_i are all positive real numbers comes from the phase locking induced by the Rabi coupling. Only this off-diagonal contribution depends on the relative phase of coefficients and the energy is definitely minimised if they have the same phase. Finally, one can check that the values $N_{1,coh} = 200$ and $\sqrt{2}\sigma = 17.3$ are in agreement with the purple low density curve ($\gamma = 10^{-2}$) on figure 5.1.

The limit of vanishing Rabi coupling($\gamma \to \infty$)

At very large values of γ, the interaction energy dominates and it is minimised if and only if the mixture polarisation is exactly $\cos\theta_\infty$. This implies that all coefficients c_i should be almost zero except the one at $N_{1,inco}$ given by $N - 2N_{1,inco} = N\cos\theta_\infty$. In other words, the mixture polarisation is optimal for interactions and it has no quantum fluctuation. This scenario of almost infinite density is visible on figure 5.1 with the brown curve ($\gamma = 10^6$). However it is completely unreachable experimentally, at least for our potassium gas system.

Crossover with γ

Finally, in between the two limit cases for the density γ, we may have an interesting behavior of the internal state of the condensate. The shape of the c_i coefficients looks like a Gaussian with displaced peak and reduced size. Indeed, we expect the polarisation to smoothly go from $\cos\theta_d$ to $\cos\theta_\infty$ as the density is increased. Meanwhile, the peak size (or standard deviation) should decrease from $\sqrt{N}\sin(\theta_d)/2$ to 1. In the next paragraph, we show that the internal state of the N particles can also be derived analytically. The above numerical calculation will be a comparison reference.

5.2 Effective Schrödinger equation and polarisation squeezing

5.2.1 Synthetic dimension and effective Schrödinger equation

The goal of this paragraph is simply to get analytic formulas for the position and the size of the Gaussian peak of coefficients (c_i). We will mostly inspire on the 2012 article "Dynamic generation of spin-squeezed states in bosonic Josephson junctions" [39]. The idea is to consider the coefficients c_i as continuous with respect to i. We then introduce the continuous wave-function $\tilde{\varphi}(x_i = i/N) = \sqrt{N}c_i$ and transforms the eigen-energy matrix equations, $E\,c_i = \sum H_{ij}c_j$, into into a continuous sum on $x \in [0,1]$ depending on $\tilde{\varphi}$ and its derivatives. For example, $\tilde{\varphi}(x_{i+1})$ is approximated by $\tilde{\varphi}(x_i) + h\partial_x\tilde{\varphi} + h^2/2\partial_x^2\tilde{\varphi}$ with $h = 1/N \ll 1$. With a change of variable, $\cos\theta = 1 - 2x$, the final wave-function $\varphi(\theta)$ depends on the synthetic dimension θ. It is normalized by $\int |\varphi(\theta)|^2 \sin\theta\, d\theta = 1$.

The energy of the condensate $\tilde{E}$, expressed in unit of $N\hbar\Omega/2$ is at order two in $h = 1/N$:

$$\tilde{E} = \int_0^\pi |\varphi(\theta)|^2 \left[-\frac{\cos(\theta - \theta_d)}{\sin(\theta_d)} + \frac{\gamma}{2}(\cos\theta - \cos\theta_\infty)^2 + \delta\mathcal{V}(\theta) \right] \sin\theta \, d\theta \\ - 2h^2 \int_0^\pi \varphi^*(\theta)\varphi''(\theta) \sin\theta \, d\theta \quad (5.10)$$

With $\delta\mathcal{V} = h\frac{1}{\sin\theta} - h^2\frac{(1+\cos^2\theta)}{2\sin^3\theta} + h\frac{\gamma}{2}\left[\sin^2\theta + (\cos\theta - \cos\theta_\infty)^2\right]$ and $\varphi(0) = 0 = \varphi(\pi)$

The first line gives an effective potential energy $\mathcal{V}(\theta) + \delta\mathcal{V}(\theta)$. The term $\delta\mathcal{V}$ can be neglected as it is a factor h smaller than $\mathcal{V}$. The second line gives an effective kinetic energy in the synthetic dimension θ with an effective mass $\tilde{m} = 1/4$. The internal state of the condensate is the normalised function $\varphi(\theta)$ minimizing the energy $\tilde{E}$:

$$\varphi(\theta) = \left(\frac{1}{\sin^2(\theta_{MF})\pi b^2} \right)^{\frac{1}{4}} \exp\left(-\frac{(\theta - \theta_{MF})^2}{4b^2} \right) \quad (5.11)$$

This form is justified by the parabolic approximation of the potential $\mathcal{V}(\theta)$ around its minimum at θ_{MF} such that $\frac{\partial}{\partial\theta}\mathcal{V}(\theta_{MF}) = 0$.

$$\mathcal{V}(\theta) \simeq \mathcal{V}(\theta_{MF}) + \tilde{m}\omega^2 \frac{(\theta - \theta_{MF})^2}{2} \quad (5.12)$$

$$\omega^2 = 4\left[\frac{\cos(\theta_{MF} - \theta_d)}{\sin\theta_d} + \gamma(\sin^2\theta_{MF} + \cos\theta_{MF}\cos\theta_d - \cos^2\theta_{MF}) \right] \quad (5.13)$$

By analogy with the quantum harmonic oscillator, the rms-size is:

$$b = \sqrt{\frac{h}{2\tilde{m}\omega}} \quad (5.14)$$

5.2.2 Mean-field polarisation

By minimizing the potential $\mathcal{V}(\theta)$, we recover the self-consistent equation defining the polarisation $\cos\theta_{MF}$ of the coherent internal state in chapter 4:

$$\cot\theta_{MF} = \cot\theta_d - \gamma(\cos\theta_{MF} - \cos\theta_\infty)$$

We can now compare it with the numerical solution computed previously. The average polarisation is $P_{avg} = \sum_i |c_i|^2(1 - 2i/N)$. As can be seen on figure 5.2, the analytical solution matches the numerical one at any density γ in $[10^{-2}, 10^2]$.

This perfect agreement is not surprising since we found in chapter 3 that the coherent and incoherent mixtures have the same interaction energy if they have equal average polarisation. To go further and be able to conclude on the level of coherence, we need to study the behavior of the rms-size b with γ.

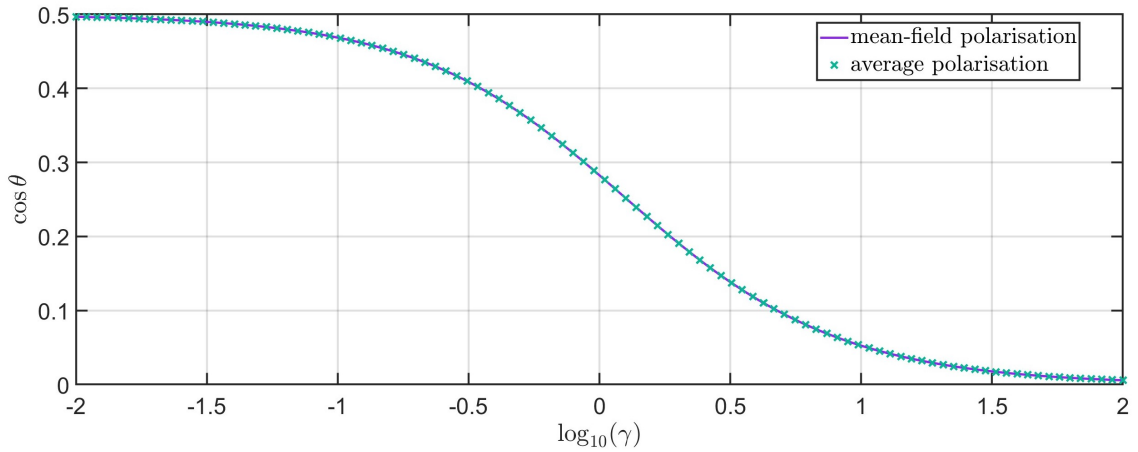

Figure 5.2: Comparison of the numerically computed condensate polarisation with the mean-field prediction as a function of the density γ. The fixed parameters are $\theta_\infty = \pi/2$, $\theta_d = \pi/3$ and $N = 800$

5.2.3 Level of coherence and squeezing of polarisation

In the the specific case where $\theta_d = \theta_\infty$ the position of the Gaussian peak is independent of γ. The effect of interactions is then only an increase of the curvature $\tilde{m}\omega^2$ of the parabolic potential at large γ, which causes a decrease of the Gaussian rms-size b:

$$\left\{ \begin{array}{rcl} h\omega & = & \frac{2}{N}\sqrt{\frac{1}{\sin\theta_\infty} + \gamma \sin^2\theta_\infty} \\ b & = & \sqrt{\frac{1}{N}}\left(\frac{1}{\sin\theta_\infty} + \gamma\sin^2\theta_\infty\right)^{-1/2} \end{array} \right. \tag{5.15}$$

From coherent to incoherent mixture

Firstly we can study the variance of the polarisation operator.

$$\int_0^\pi |\varphi(\theta)|^2(\cos\theta - \cos\theta_{MF})^2 \sin\theta\, d\theta \underset{b\ll 1}{\simeq} b^2 \sin^2\theta_\infty = \frac{\sin^2\theta_\infty}{N(1/\sin\theta_\infty + \gamma\sin^2\theta_\infty)} \tag{5.16}$$

When γ approaches N, the variance tends to $1/N^2$ which means that the quantum fluctuations of the polarisation are negligible. The mixture can be considered incoherent above this limit (and the continuous model fails). It behaves as two distinct condensates, one in state $|1\rangle$ and the other in state $|2\rangle$, each with its own phase and number of atoms. In real experiments, we are not in this incoherent limit since γ is at most equal to 10.

Squeezing of polarisation

On the other hand, at low densities, $\gamma \ll 1$, the decrease of b by interactions is equivalent to a slight squeezing of the mixture polarisation. there is a weak depletion of the $|-\rangle$ internal state through a creation of pairs of atoms in state $|+\rangle$ (see figure 5.3 and 5.4). If the RF-dressed condensate is made with an adiabatic sweep, the internal state of the condensate is intrinsically and permanently squeezed in polarisation (b decreases with γ). On the other hand, the quantum operator conjugated with the global polarisation is the relative phase between the two components of the condensate (states $|1\rangle$ and $|2\rangle$). According to Heisenberg principle, the quantum fluctuations on this relative phase are increased. The mixture is less coherent than in the absence of interactions.

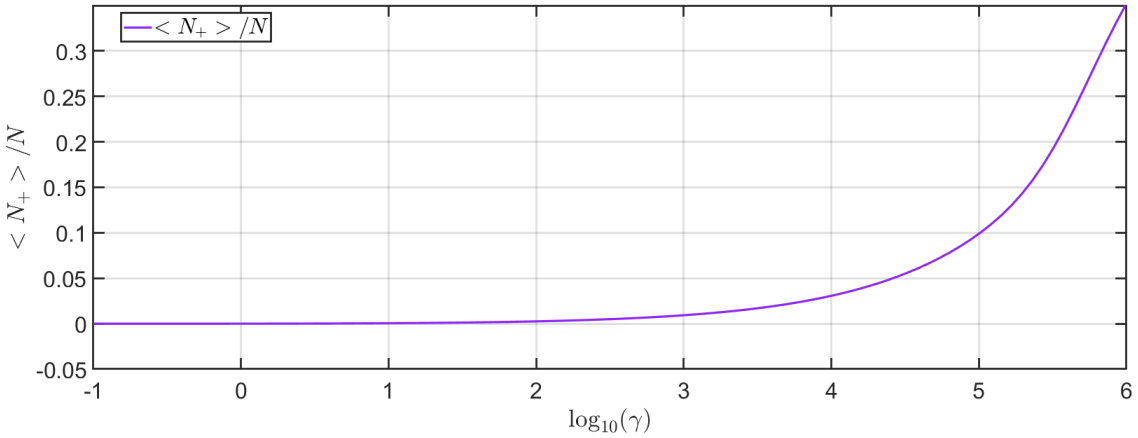

Figure 5.3: Mean number of particles of the condensate in the internal state $|+\rangle$. The fixed parameters are $\theta_\infty = \theta_d = \pi/2$ and $N = 800$. At $\gamma = 10$ the population is $N_+/N = 0.0005$.

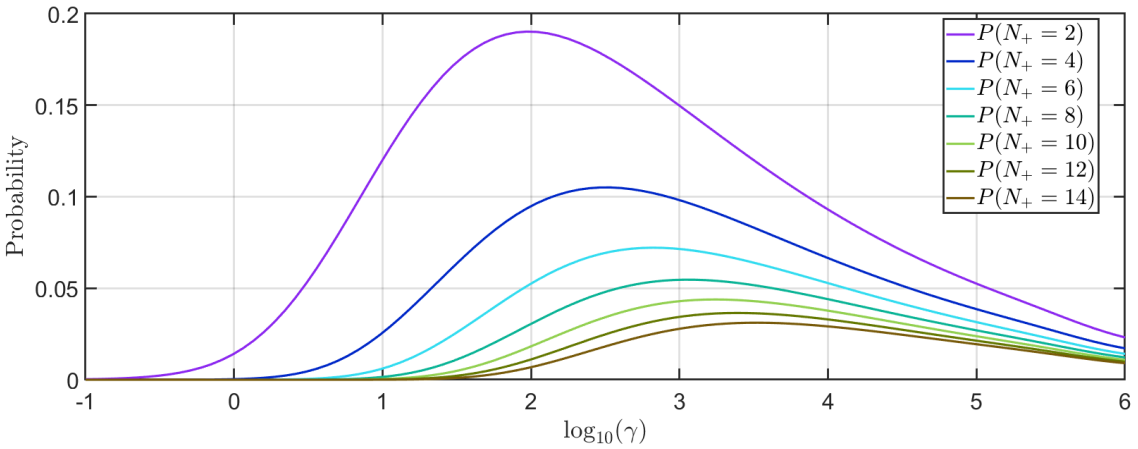

Figure 5.4: Probability of even numbers of particles in internal state $|+\rangle$. All odd numbers probabilities are numerically zero. The fixed parameters are $\theta_\infty = \theta_d = \pi/2$ and $N = 800$.

A measurable effect ?

Even though this time independent squeezing seems interesting, there are two reasons why it may not be possible to experimentally observe it in our system:

- Firstly, according to formula 5.16, quantum fluctuations of the polarisation are imperceptible if the number of atom is $N = 10^5$. We would need a much smaller number of atoms of the order of 100 to 1000. In addition, the counting of atoms by the camera must have a precision of the order of the unit.
- Secondly, we expect most of the fluctuations of polarisation to be classical. The Feshbach magnetic field has small fluctuations over time which in turns creates an rms imprecision on the detuning of $\Delta\delta = 2\pi \times 400\,\text{Hz}$. Incidentally, we usually use statistical fluctuations of the populations, at a small Rabi frequency, to measurement the in-situ magnetic noise on the atoms.

5.3 Behavior of mean-field effects in function of γ

Because the previous section concluded that the quantum squeezing of polarisation is imperceptible at $\gamma \leq 10$, it is fully legitimate to use of a coherent-state ansatz for the mean-field description of the condensate. In this section, we measure and analyse the behavior of mean-field polarisation and mean-field energy with γ.

5.3.1 Measurement of mean-field polarisation

In order to experimentally reach higher values of γ, while maintaining a clear mean-field stability, we worked at a magnetic field of $B = 57.5\,\mathrm{G}$ (see figure 1.22) where $a_{11}/a_0 = 133.7$, $a_{22}/a_0 = 32.2$, $a_{12}/a_0 = -52.8$. Equivalently, $a_\infty = 5.6\,a_0$ is now positive, $\bar{a} = 67.9\,a_0$ is larger than for previous experiments and $\cos\theta_\infty = 0.37$.

The condensate is initially in a harmonic cigar trap with frequencies $\omega_z = 2\pi \times 72\,\mathrm{Hz}$ and $\omega_r = 2\pi \times 268\,\mathrm{Hz}$. The number of atom is on average $N = 1.5 \times 10^5$. The RF adiabatic sweep lasts 0.6ms, starts at $\delta = 9\,\Omega$ and ends at a chosen δ in $[-4, 2]$. We then cut the RF-source. This freezes the two populations N_1 and N_2. We let the cloud expand for a 3 ms time-of-flight still at 57.5 G and separate the two populations by 3 ms in a strong gradient of magnetic field (Stern-Gerlach) followed by 5 ms of another time of flight. The density profiles of the two clouds are fitted with 1D Gaussians in the axial direction after being integrated on the other direction, along which they have been separated by the Stern Gerlach process.

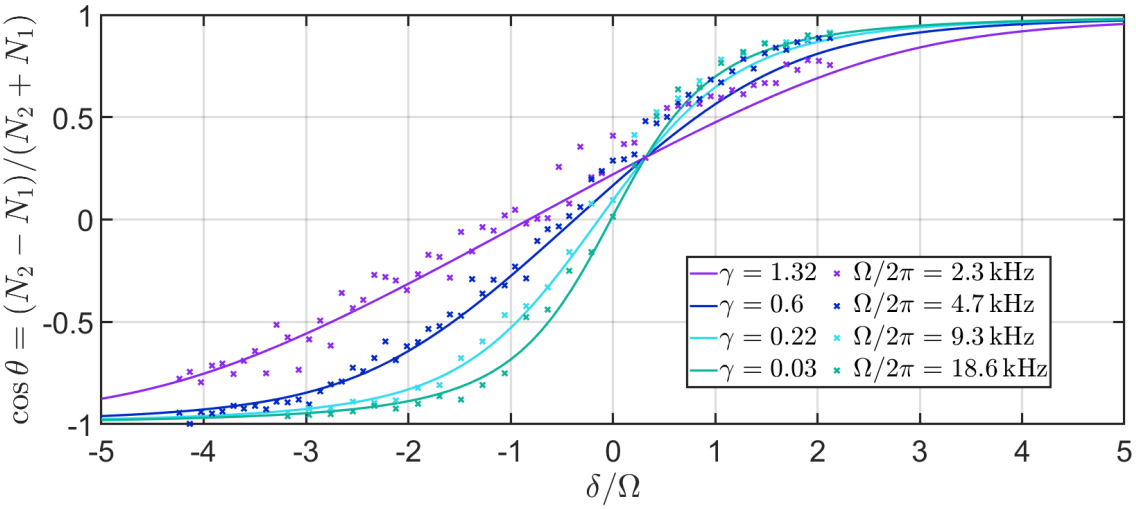

Figure 5.5: Polarisation of the condensate against relative detuning δ/Ω and at $B = 57.5\,\mathrm{G}$.The curves are fitted with the numerically computed $\cos(\theta_{MF}(\gamma))$ depending on a single parameter γ.

The protocol is iterated at different values of $\Omega/2\pi$ in a geometric progression with a ratio of 2: $\Omega \in \{2.3, 4.6, 9.3, 18.6\}$ kHz. We fit the curves of polarisation against relative detuning δ/Ω with the numerical solutions $\cos(\theta_{MF}(\gamma))$ and γ the adjustable parameter. The curves are not symmetric with respect to $\delta/\Omega = 0$ because of the substantial difference in scattering lengths: $a_{11} = 133.7\,a_0$ and $a_{22} = 32.1\,a_0$. As a consequence, the effect of interactions is stronger at negative detunings, for which the atoms would be, in absence

of interactions, more in state $|2\rangle$ than in state $|1\rangle$. The fitting curves all intersect at $y = \cos\theta_\infty = 0.37$ and $x = \delta/\Omega = \cot\theta_\infty = 0.4$ because the internal state is independent of the density when the polarisation is already minimizing the interaction energy.

The list of fit parameters $\gamma = \{1.32, 0.6, 0.22, 0.03\}$ is, within the fitting precision estimated to $\Delta\gamma = 0.1$, a geometric progression of ratio of $1/2$. This is in agreement with the idea of a constant density profile for all shots (initial Thomas-Fermi profile frozen during the fast RF sweep) thus giving a variation of γ only due to the change of Ω.

5.3.2 Mean-field energy

In this paragraph, we investigate the validity of a power serie in n for the mean-field energy. We will work on the mean-field chemical potential because it is an intensive quantity. At small γ, we already have an approximate expression with a two-body and a three-body terms: $\mu \simeq g_2 n + g_3 n^2$. It would be possible to refine this approximation by calculating higher order corrections, like $g_4 n^3$, from a serie expansion of the mean-field equations:

$$\cot\theta_{MF} = \cot\theta_d - \gamma\,(\cos\theta_{MF} - \cos\theta_\infty) \tag{5.17}$$

$$\mu_{MF} = (g_\infty + \overline{g}(\cos\theta_{MF} - \cos\theta_\infty)^2)n - \frac{\hbar\Omega}{2\sin\theta_d}\cos(\theta_{MF} - \theta_d) \tag{5.18}$$

On the other hand, it is possible to express θ_{MF} in terms of γ and get an expression of the chemical potential in terms of only n and constants like Ω, g_∞... In the general case with arbitrary θ_d and θ_∞, this elimination is possible but laborious and disgraceful. We prefer analysing numerically the behavior of the chemical potential (figure 5.6) and comparing it to asymptotic limits.

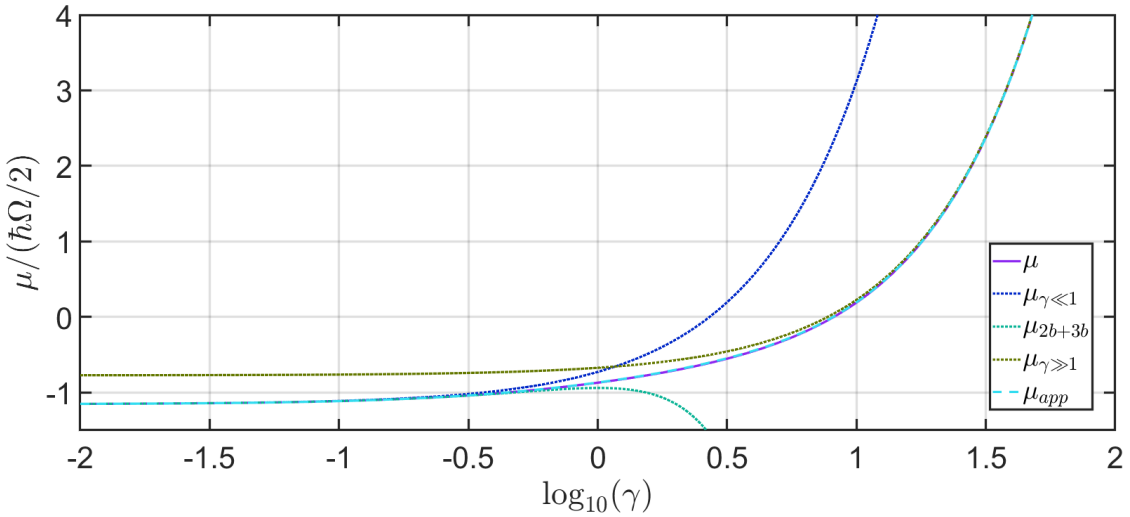

Figure 5.6: Mean-field chemical potential of the RF-dressed BEC as a function of γ. External parameters are $\theta_d = 0.33 \times \pi$, $\theta_\infty = 0.6 \times \pi$, $g_\infty = 0.1 \times \overline{g}$

The behavior of the chemical potential changes in the logarithmic window given by $\gamma \in [10^{-1}, 10^{1}]$. At negligible γ, the polarisation is approximately $\cos\theta_d$ and the chemical potential:

$$\mu_{\gamma\ll1} = (g_\infty + \overline{g}(\cos\theta_d - \cos\theta_\infty)^2)n - \frac{\hbar\Omega}{2\sin\theta_d} \tag{5.19}$$

At very large γ, the polarisation is approximately $\cos\theta_\infty$ and the chemical potential:

$$\mu_{\gamma\gg1} = (g_\infty)n - \frac{\hbar\Omega}{2\sin\theta_d}\cos\left(\theta_\infty - \theta_d\right) \tag{5.20}$$

In realistic experiments, we study weakly asymmetric mixtures (contrary to the physics of impurities). All angles θ_d, θ_∞ and θ_{MF} are far from 0 or π. This allows an approximate solving of the mean-field equation. The idea is to find a formula of $\cos\theta_{MF}$ compatible with the computed graphical behavior on figure 5.7. Let's assume that:

$$\cos\theta_{MF} \simeq \frac{A + B\gamma}{1 + C\gamma} \equiv (\cos\theta_{MF})_{(app)} \tag{5.21}$$

Coefficients A, B, C are fixed by the two asymptotic limits for the mixture angle and by the linear correction at small density. We find the very simple but approximate formula:

$$(\cos\theta_{MF})_{(app)} = \frac{\cos\theta_d + \gamma\sin^3\theta_d\cos\theta_\infty}{1 + \gamma\sin^3\theta_d} \tag{5.22}$$

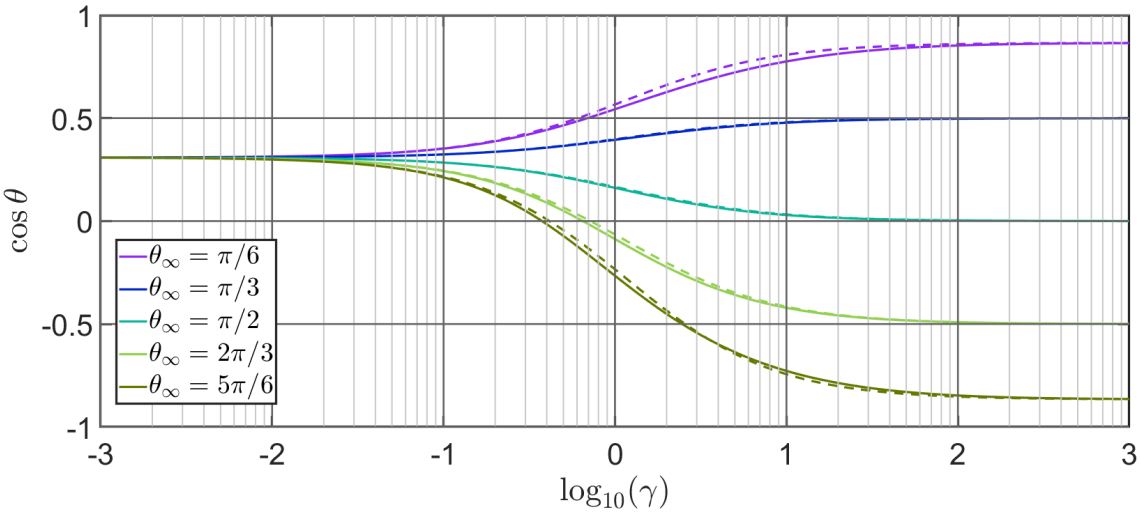

Figure 5.7: Mean-field polarisations $\cos\theta_{MF}$ (plain) and comparison with the approximate formula 5.22 (dotted). The drive mixture angle is $\theta_d = 0.4 \times \pi$. The approximation is relatively imperfect if θ_∞ or θ_d are far from $\pi/2$ (very asymmetric mixtures). This is not the case in our experiment.

Finally, the approximate formula for the mean-field chemical potential, represented in dashed blue on figure 5.6, is:

$$\mu_{app} = \left(g_\infty + \overline{g}\frac{(\cos\theta_d - \cos\theta_\infty)^2}{(1 + \gamma\sin^3\theta_d)^2}\right)n - \frac{\hbar\Omega}{2\sin\theta_d}(\cos(\theta_{MF} - \theta_\infty))_{(app)} \tag{5.23}$$

Where the last term is calculated with trigonometry by expressing it in terms of $(\cos\theta_{MF})_{(app)}$. This formula and the exact computed chemical potential brings up several remarks:

- For small Rabi frequencies (as soon as $\gamma\sin^3\theta_d \geq 1$), the chemical potential cannot anymore be expressed with an analytical expansion in powers of n.

- The approximate formula is a simple prediction of the chemical potential in the regime where there is no analytic formula $1 \leq \gamma \leq 10$ (see figure 5.6). In particular, this is beyond the three-body approximation which is highly incorrect at these γ. This regime is experimentally reachable.
- We can discard all speculations on the existence of first order phase transitions (liquid/gas) due to an hypothetical competition between attractive and repulsive terms with different scaling in n, in the mean-field energy. Such behavior would happen if and only if $\mu_{MF}(\gamma)$ had a local minima (figure 5.6).
- The RF-dressing allows a smooth change of the local slope $\frac{d\mu}{dn}$ from its asymptotic values $g_{--}^{--}(\theta_d)$ to the other g_∞ (figure 5.8 with $g_\infty < 0$). For positive g_∞, this may be interesting experimentally as it allows Thomas-Fermi profiles with a non parabolic shape if the center density gives $\gamma_0 \simeq 10$.

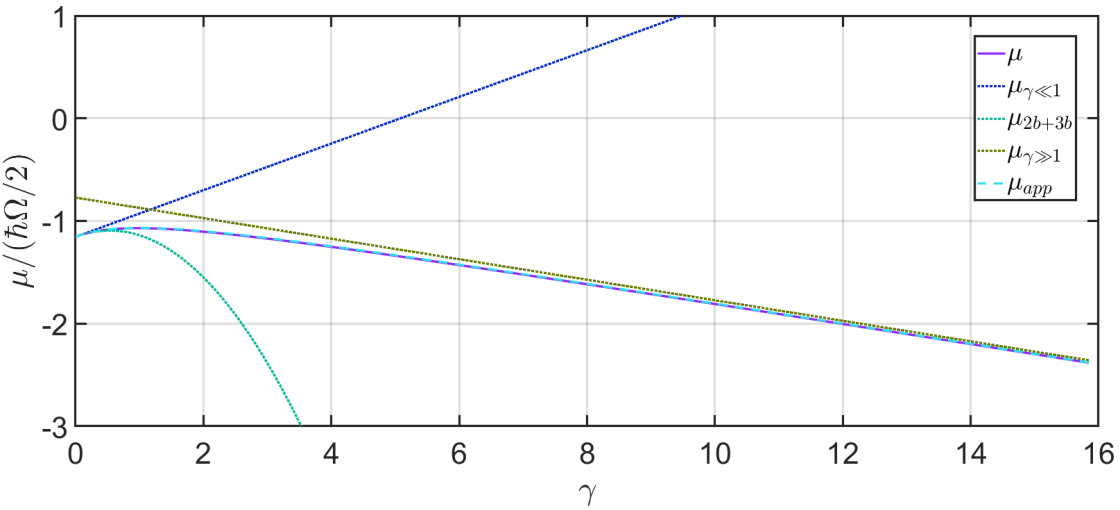

Figure 5.8: Mean-field chemical potential in the case of negative minimal interaction strength g_∞. Note the linear scale of the x-axis. External parameters are $\theta_d = 0.33 \times \pi$, $\theta_\infty = 0.6 \times \pi$, $g_\infty = -0.1 \times \overline{g}$.

Measuring MF-energy with radial expansion

We also tried to measure the MF-energy at non-small values of γ with the same setup as for the polarisation. After the adiabatic sweep on the cigar-shaped condensate, the RF coupling at a constant δ/Ω was maintained during the time-of-flight. The cloud expanded radially and the measurement of the radial size after 7 ms of time-of-flight gave an indirect measure of the initial energy of the gas. Sadly, the measured sizes depended weakly in Ω (and so in γ).
A possible explanation may lie in the non-vanishing offset of energy $g_\infty n^2/2$ conjugated to the square-root dependence between size and energy. In addition, the shot-to-shot fluctuations of the Feshbach field give an rms of δ of typically 500 Hz, non negligible at small Rabi frequencies.

5.4 Behavior of the BMF energy in function of γ

5.4.1 Change of the density scaling of the BMF energy

We start with formula 3.12 of the BMF energy, valid in the limit of a bulk condensate where all spin excitation waves at $\vec{k} \neq 0$ are taken into account. The density modes do not contribute because $g_{--}^{--} = g_\infty$ is assumed small. We rewrite this formula in terms of more convenient variables: $\overline{g}$ and $\gamma = 2\overline{g}n/(\hbar\Omega)$, with n the local density of the condensate.

$$\frac{\delta E^{BMF}}{\delta V} = \overline{g}\frac{n^2}{2}\frac{128}{15\sqrt{\pi}}\sqrt{n\overline{a}^3}(\sin\theta_\infty)^{5/2} \times I\left(\frac{1}{\gamma\sin^2\theta_\infty}\right) \tag{5.24}$$

The form of chapter 3 is recovered with $\tilde{\Omega}\sin\theta_\infty = \Omega$ and $\overline{a}\sin\theta_\infty = \tilde{a} = \sqrt{a_{11}a_{22}} = -a_{12}$.

For $\gamma \ll 1$, this density of BMF energy is in good approximation the sum of a two-body term and a three-body term (see 3.3). On the contrary, for $\gamma \gg 1$ the integral I is 1 and we get a 2.5 body term. The BMF chemical potential is $\mu^{BMF} = \frac{\partial}{\partial n}\left(\frac{\delta E^{BMF}}{\delta V}\right)$.

$$\mu^{BMF} = \frac{\hbar\Omega}{2} \times A \times \frac{\partial}{\partial\gamma}\left(\gamma^{5/2}\, I\left(\frac{1}{\gamma\sin^2\theta_\infty}\right)\right) \tag{5.25}$$

With $A = \frac{32}{15\pi}(\sin\theta_\infty)^{5/2}\frac{\overline{a}}{\sqrt{2}l_\Omega}$. The following asymptotic behaviors are compared to the numerical solution of figure 5.9.

$$\begin{cases} \mu^{BMF}_{\gamma\ll1} &= \frac{\hbar\Omega}{2} \times A \times \frac{15\pi}{16\sin\theta_\infty}\left(\gamma + \frac{3}{8}\gamma^2\sin^2\theta_\infty\right) \\ \mu^{BMF}_{\gamma\gg1} &= \frac{\hbar\Omega}{2} \times A \times \frac{5}{2}\gamma^{3/2} \end{cases} \tag{5.26}$$

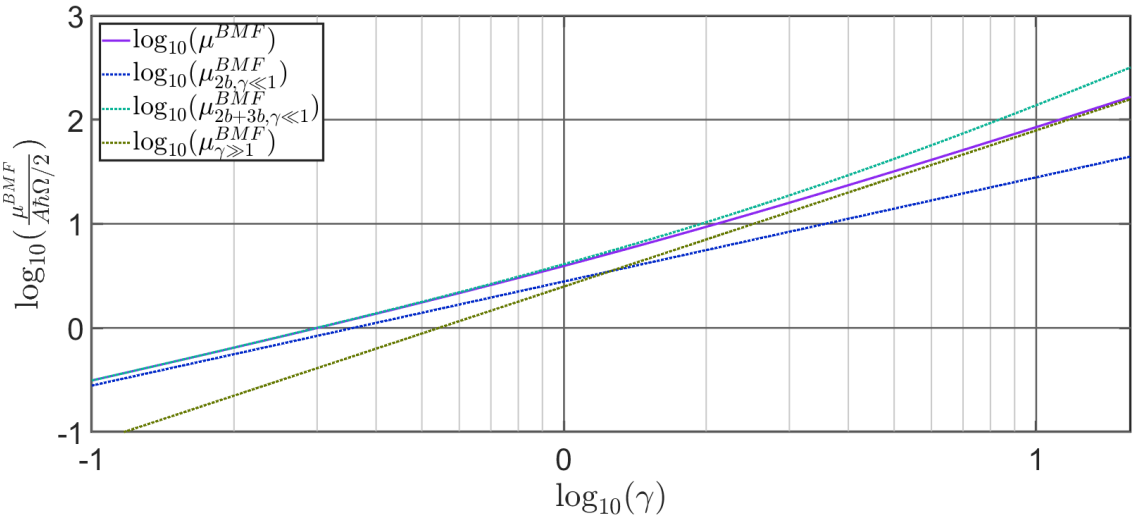

Figure 5.9: Beyond-mean-field chemical potential as a function of γ in log/log scale. External parameters are $\theta_d = \theta_\infty = 0.57 \times \pi$. The change in scaling happen for γ in $[0.1, 10]$ from γ to $\gamma^{1.5}$.

5.4.2 RF-dressed quantum droplets

The physics of quantum droplets is the competition between a repulsive BMF density of energy with an attractive MF density of energy. This leads to the possible existence

of a stable self-bound state with a constant density n_d fixed by the minimization of the total density of energy. In other words, the sum $\mu^{MF} + \mu^{BMF}$ has a local minimum at $\gamma_d = 2\overline{g}n_d/\hbar\Omega$. At this density, the slope $\frac{\partial\mu}{\partial\gamma}$ is zero. This competition was studied and observed experimentally in incoherent mixtures with the correct polarisation [30][40]. Sadly, the size of the droplet and the number of atom were too small to observe a flat top density profile.

We now want to consider the case of the mixture in presence of RF coupling and in particular the possible existence and density of the droplet with respect of Ω. We assume the magnetic field is like in chapter 3, $B = 56.7\,\mathrm{G}$, so that g_∞ is slightly negative. The detuning should be fixed so that the polarisation is $\cos\theta_\infty$ because we don't have any practical expression of the BMF energy except at this polarisation. Firstly, note the typical order of magnitude of constant A of formula 5.25: $A = 8 \times 10^{-3}$ for $\Omega = 10\mathrm{kHz}$ and with a scaling in $\sqrt{\Omega}$.

The case $\gamma_d \gg 1$

This case is equivalent to a standard droplet in the absence of RF coupling (incoherent mixture). The total chemical potential is:

$$\frac{2\mu(\gamma)}{\hbar\Omega} = \frac{g_\infty}{\overline{g}}\gamma + A \times \frac{5}{2}(\gamma)^{3/2} \tag{5.27}$$

And the dimensionless density of the droplet is:

$$\gamma_d = \left(\left|\frac{g_\infty}{\overline{g}}\right|\frac{4}{15A}\right)^2 \tag{5.28}$$

The true density $n_d^{incoh} = \gamma_d \times \frac{\hbar\Omega}{2\overline{g}}$ is independent of Ω and equal to $2 \times 10^{20}\mathrm{m}^{-3}$ for $a_\infty = -1 \times a_0$.

The case $\gamma_d \ll 1$

In this case, the total chemical potential takes the form:

$$\frac{2\mu(\gamma)}{\hbar\Omega} = \frac{g_\infty}{\overline{g}}\gamma + A \times \frac{15\pi}{16\sin\theta_\infty}\left(\gamma + \frac{3}{8}\gamma^2\sin^2\theta_\infty\right) \tag{5.29}$$

Equalizing the slope of total chemical potential to zero gives us the dimensionless density of the droplet:

$$\gamma_d^{(3b)} = \left|\frac{g_\infty}{\overline{g}}\right|\frac{64}{45\pi}\frac{1}{A\sin\theta_\infty} - \frac{4}{3\sin^2\theta_\infty} \tag{5.30}$$

This solution is acceptable only if $1 \ll \gamma_d^{(3b)} > 0$. Thus only if A, or equivalently Ω, are slightly below a critical value analysed in the next paragraph. In this condition, the droplet exist and is called a three-body droplet because it is stabilized by the three-body BMF term.

Critical value of Ω for a RF-dressed droplet

The idea of a critical value for Ω can be understood from the following picture. Let's substract from the BMF chemical potential its two-body contribution at low γ. According

to figure 5.9, we are left with a repulsive BMF energy term because $\mu^{BMF} \geq \mu^{BMF}_{2b,\gamma\ll 1}$. Now we add this subtracted two-body BMF term to the mean-field chemical potential $g_\infty n < 0$. A droplet state exist only if the total two-body term is attractive, so that it can compete with the remaining repulsive part of the BMF chemical potential. Therefore, the critical value Ω_c is fixed by equalizing to zero the exact two-body scattering length for a $(--)$ collision. It was calculated in the two-body problem of chapter 1 (1.4.1):

$$0 = a_\infty + \overline{a}^2\sqrt{\frac{2m\Omega_c \sin^3\theta_\infty}{\hbar}} \tag{5.31}$$

$$\Omega_c = \frac{2\hbar}{m\overline{a}^2 \sin^3\theta_\infty}\left(\frac{a_\infty}{\overline{a}}\right)^2 \tag{5.32}$$

For a typical $a_\infty = -1 \times a_0$, the critical value is $\Omega_c = 20\text{kHz}$.

Density of the RF-dressed droplet for Ω between 0 and Ω_c

For Ω under the critical value, the RF-dressed droplet state always exists, regardless of the value of γ. Its density in the crossover ($\gamma \sim 1$) can be calculated numerically by once again equalizing to zero the slope of total chemical potential. The behavior for realistic parameters looks like a linear dependence of the real density n_d with Ω. It naturally tends to n_d^{incoh} at vanishing Ω and to zero at Ω equal to Ω_c.

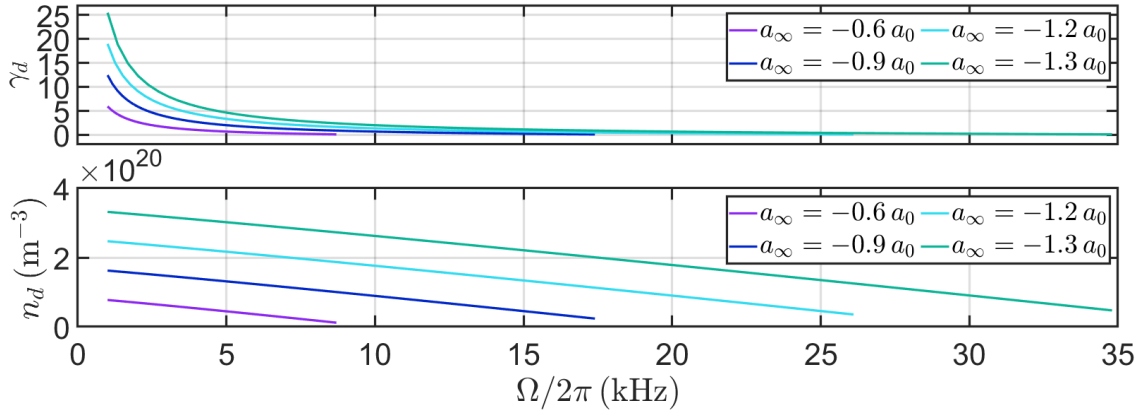

Figure 5.10: Density of the RF-dressed droplet as a function of the Rabi frequency Ω. Only the crossover is numerically studied, in other words Ω/Ω_c is taken not too close to 0 or 1.

RF-dressed droplets with reduced density

The density of the RF-dressed droplet is decreased compared to its high γ limit ($\Omega \to 0$) which is a favorable effect. It is interpreted as a consequence of the increased energy of spin waves with Ω.

Lastly, a confinement in two of the three space dimensions may help to observe a flat top density profile in the remaining direction. The BMF energy is even increased in the crossover between one and three dimensions [41], which decreases the flat-top density n_d of the droplet.

5.5 Chapter conclusion

In this theoretical chapter, we studied the behavior of the condensate at non-small γ.
A first concern was the validity of taking a coherent internal state for the mean-field ansatz. The exact numerical solution of the internal state of N condensed particles proved that the mixture is incoherent only for $\gamma \simeq N$. At realistic values of $\gamma \leq 10 \ll N$, there is only a very slight squeezing of the collective polarisation and the mean-field internal state is indeed a coherent state. With this ansatz, we found out that the mean-field energy is non-analytic for γ typically above 1. However, the behavior of the mean-field chemical potential is relatively simple since its slope with n varies significantly only for γ between 0.1 and 10 from its low-γ value g_{--}^{--} to its high-γ value $g_\infty \leq g_{--}^{--}$.
In the last part, we studied the effect of Ω on the beyond-mean-field energy, specifically in the context of quantum droplets. It was found that the RF-dressed quantum droplets exists only for values of Ω in $[0, \Omega_c]$, with $\Omega_c \propto g_\infty^2$. The flat-top density of the droplet decreases linearly with Ω from its value in incoherent mixture (at $\Omega = 0$) to a vanishing density at the critical value $\Omega = \Omega_c$. Future experiments could aim at making more dilute droplets, thereby increasing their lifetime and possibly leading to the first observation of a flat-top density.

Chapter 6

6. One-dimensional dynamics and density excitations

In this chapter, we present prospective work on one-dimensional dynamics. We start with a thought experiment on the effective nature of the three-body mean-field interaction. Assuming low γ, we use quantum perturbation theory to answer the question by proving that the three-body attractive interaction (MF) really involves three particles and that it coexists with the two-body renormalization (BMF).
In the second part, we use the above result to write a simple one-dimensional hydrodynamic equation for the RF-dressed condensate. The conditions are chosen to have vanishing two-body interactions and attractive three-body contact interactions. We predict the birth of a modulation instability with peculiar properties due to a scale invariance of the equations of motion.

6.1 Effective or real three-body interaction ?

6.1.1 Thought experiment for a system of only two particles

In Autumn 2022, Jean Dalibard proposed a convincing thought experiment suggesting that the three-body mean-field interaction is an effective process without truly involving three particles.

We consider a system of only two atoms of ^{39}K at zero temperature in presence of the RF coupling and in a periodic box. Because of interactions and supposing $\theta_d \neq \theta_\infty$, the internal state of the pair is slightly different from $(--)$. The correction of internal state leads to a small decrease of the total energy of the system. This suggests that the mean-field three-body effect, derived by the same method, is also present for a system of two particles. Therefore, it appears as not a real three-body interaction.

However, the existence of virtual $(++), (+-)$ excitations in the interaction zone between the two atoms is also changing the state of the pair from $(--)$. Thus it appears, that we cannot conclude so simply on the effectiveness question. In the next paragraph, we show that quantum perturbation theory gives a complete answer. But firstly, we have to justify it is a valid approach.

6.1.2 The answer of quantum perturbation theory at second order

The standard way to compute mean-field and beyond-mean-field energies is to apply the Bogoliubov prescription: replacing operators $\hat{a}_{\vec{k}=0}, \hat{a}^\dagger_{\vec{k}=0}$ by complex numbers and performing a quadratic approximation on the remaining Hamiltonian with operators $\hat{a}_{\vec{k}\neq 0}, \hat{a}^\dagger_{\vec{k}\neq 0}$. The quadratic Hamiltonian $\hat{H}_{Bog.}$ can then be diagonalized. In a single component condensate, this exact diagonalization is very important to get the phonic branch.

The situation is a bit different for an RF-dressed condensate, **if** $\hbar\Omega \gg \overline{g}n$ **and** $g^{--}_{--} = 0$. Density waves are free particles and spin waves have an energy gap $\hbar\tilde{\Omega}$. Because of this gap, quantum perturbation theory will converge quickly and an exact diagonalization is not needed. We may even consider the whole two-body Hamiltonian as the perturbation. This means that the unperturbed ground state is N particles in the free-particle state $|-\rangle_{\theta_d}, \vec{k} = 0$:

$$|\psi_0\rangle = \frac{1}{\sqrt{N!}} \left(\hat{a}^\dagger_{-_{at}\,\theta_d, \vec{k}=0} \right)^N \tag{6.1}$$

The total Hamiltonian is then written in second quantization on the free-particle $\{|\pm\rangle_{\theta_d}, \vec{k}\}$ basis with formulas of subsection 1.4.2: $\hat{H} = \hat{H}_{1b} + \hat{H}_{2b}$.
At zeroth order, the ground state energy is $E_0 = \langle\psi_0|\,\hat{H}_{1b}\,|\psi_0\rangle = 0$.
At first order, the energy correction is:

$$E^{(1)} = \langle\psi_0|\,\hat{H}_{2b}\,|\psi_0\rangle = g^{--}_{--}\frac{N(N-1)}{2V} = 0 \tag{6.2}$$

At second order in the perturbation, we have to consider the states $|\psi_e\rangle$, of the N free-

particles basis, directly coupled with $|\psi_0\rangle$ by $\hat{H}_{2b}$. The energy correction is then:

$$E^{(2)} = -\sum_e \frac{\left|\langle\psi_0|\,\hat{H}_{2b}\,|\psi_e\rangle\right|^2}{E_e - E_0} \tag{6.3}$$

The excited states $|\psi_e\rangle$ that contributes to this sum are:

- $N-2$ particles in the condensate plus a pair in state $|+\rangle_{\theta_d}, \vec{k}$ and $|+\rangle_{\theta_d}, -\vec{k}$.
- $N-2$ particles in the condensate plus a pair in state $|-\rangle_{\theta_d}, \vec{k}$ and $|+\rangle_{\theta_d}, -\vec{k}$ with $\vec{k} \neq 0$
- $N-1$ particles in the condensate plus an atom in state $|+\rangle_{\theta_d}, \vec{k} = 0$
- $N-2$ particles in the condensate plus a pair in state $|-\rangle_{\theta_d}, \vec{k}$ and $|-\rangle_{\theta_d}, -\vec{k}$ with $\vec{k} \neq 0$. However, this contribution is zero because $g^{--}_{--} = 0$.

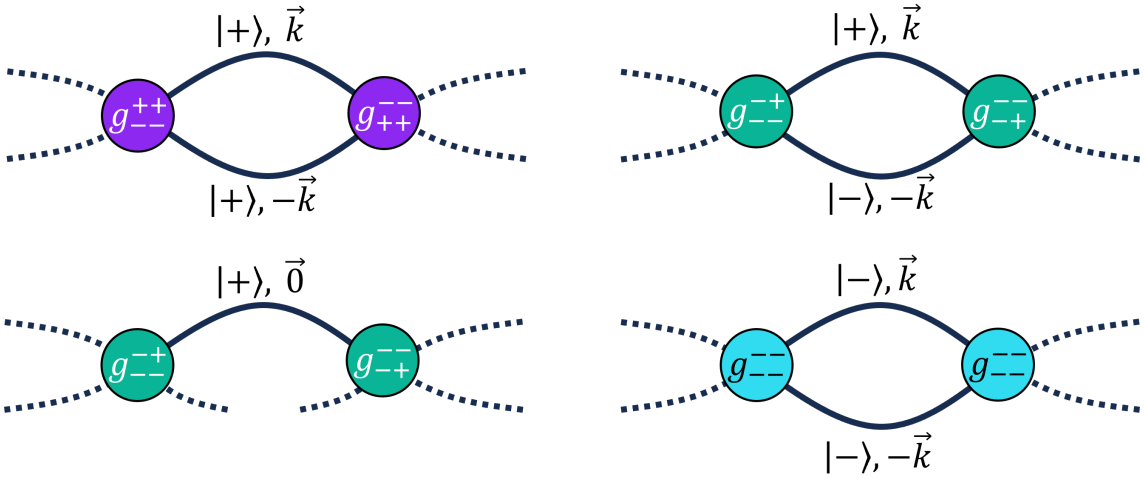

Figure 6.1: The four processes involved in the modification of energy at second order in interactions. Dotted lines represent particles from the condensate and plain lines represent excitations.

This four processes are summed-up with the diagrams of figure 6.1. Their contributions are respectively (with $\varepsilon_k = \frac{\hbar^2 k^2}{2m}$)

$$E^{(2)} = -\frac{1}{2}\sum_{\vec{k}} \left(\frac{g^{++}_{--}}{V}\right)^2 \frac{N(N-1)}{2\varepsilon_k + 2\hbar\tilde{\Omega}} - \sum_{\vec{k}\neq 0} \left(\frac{g^{+-}_{--}}{V}\right)^2 \frac{N(N-1)}{2\varepsilon_k + \hbar\tilde{\Omega}} - \left(\frac{g^{+-}_{--}}{V}\right)^2 \frac{N(N-1)^2}{\hbar\tilde{\Omega}} \tag{6.4}$$

Where the $1/2$ factor in front of the first sum corrects the double counting of $(\vec{k}, -\vec{k})$ pairs by indexing with $\vec{k}$. The occurrence of $N(N-1)^2$ in the last term is due to the triple appearance of creation/annihilation operators of a condensed particle in the third process. Following the method of [42], we write $N(N-1)^2 = N(N-1)(N-2) + N(N-1)$. We get a three-body effect in $N(N-1)(N-2)$. Comparing it to equation 4.14, we see that it has the exact expression of the mean-field three-body energy in the limit $N \gg 1$. The remaining $N(N-1)$ contribution can be injected in the second sum so that $\vec{k} = 0$ now belongs to it.

In the continuous limit for $\vec{k}$, we get:

$$E^{(2)} = -\frac{N(N-1)}{V 2\pi^2}\int_0^\infty \left(\frac{\left|g_{--}^{++}\right|^2}{2(2\varepsilon_k + 2\hbar\tilde{\Omega})} + \frac{\left|g_{--}^{-+}\right|^2}{2\varepsilon_k + \hbar\tilde{\Omega}}\right) k^2 dk \\ - \left(\frac{g_{--}^{+-}}{V}\right)^2 \frac{N(N-1)(N-2)}{\hbar\tilde{\Omega}} \quad (6.5)$$

The integral is UV divergent because of the use of contact potentials. We admit it becomes regular with a counter-term hidden in $E^{(1)}$ (Born approximation at second order). After removing this UV divergence, we find the two-body renormalization $a_{--}^{(1)}$, scaling as $\bar{a}^2\sqrt{\tilde{\Omega}}$, and calculated in the two-body problem of chapter 1.

$$E^{(2)} = \frac{N(N-1)}{2V}\frac{4\pi\hbar^2 a_{--}^{(1)}}{m} + \frac{N(N-1)(N-2)}{V^2}\frac{g_3}{3} \quad (6.6)$$

Finally, the use of quantum perturbation theory shows that, at second order, two effects happen at the same time: - the appearance of an attractive three-body interaction and the renormalization of two-body interaction strength. Both terms have an energy contribution scaling in $\bar{a}^2$ which is a signature of a second order perturbation.

In conclusion, for a system of only two particles, the factor $N(N-1)(N-2)$ vanishes and there is no three-body effect, only the renormalization of two-body interactions is observed. At third order in perturbation theory, we expect the appearance of a four body interaction and the renormalization of two-body and three body interaction strength. However, according to D. Petrov some of these third order effects are not grasped by the approaches of previous chapters in terms of mean-field and beyond-mean-field.

6.2 One-dimensional dynamics : modulation instabilities and quasi-solitons

In this section, we consider an RF-dressed condensate, with two-body interactions g_2 and three-body interactions g_3, trapped radially in a Gaussian beam (harmonic trapping ω_r). The axial confinement will be a flat box potential created by the DMD setup. The size of the box can be tuned between 100 μm to 300 μm. The interaction strengths g_2 and g_3 will be assumed small, so that the radial part of the wave-function will be the ground state of the radial harmonic oscillator. In addition, the condition of validity of mean-field equations will be strongly verified [4]: $n_{1D}a_{ho}^2 \gg a_2$ (with typical values of one-dimensional density $n_{1D} = 10^9\,\mathrm{m}^{-3}$, harmonic oscillator length $a_{ho} = 1\,\mu$m and two body scattering length $a_2 = 2\times10^{-10}\,\mathrm{m}$)

6.2.1 One-dimensional equation of motion

The dynamical equation of one-dimensional motion is the Gross-Pitaevskii equation integrated radially with the following tri-dimensional wave-function of the condensate:

$$\psi(r,z,t) = \frac{1}{\sqrt{\pi a_{ho}^2}}\exp\left\{-\frac{r^2}{2a_{ho}^2} - i\omega_\perp t\right\}\times\varphi(z,t) \quad (6.7)$$

The integration is straightforward and it yields:

$$i\hbar\partial_t\varphi = \left(-\frac{\hbar^2\partial_z^2}{2m} + g_2^{1D}|\varphi|^2 + g_3^{1D}|\varphi|^4\right)\varphi \tag{6.8}$$

Where $g_2^{1D} = \frac{g_2}{2\pi a_{ho}^2}$ and $g_3^{1D} = \frac{g_3}{3\pi^2 a_{ho}^4}$.
If we take the expressions of g_2 and g_3 valid up to second order in perturbation theory, we get:

$$\begin{cases} g_2^{1D} &= 2\hbar\omega_r \times (a_{--}^{(0)} + a_{--}^{(1)}) \\ g_3^{1D} &= -\frac{\hbar^2}{2m} \times \left(32\sin^3\theta_d(\cos\theta_d - \cos\theta_\infty)^2 \frac{\bar{a}^2}{a_{ho}^2}\frac{l_\Omega^2}{a_{ho}^2}\right) = -\frac{\hbar^2}{2m}\alpha \end{cases} \tag{6.9}$$

Under this form, it is clear that the three-body interaction strength in one-dimensional motion is characterised by a pure number α. In our experiment, it is typically of the order of 10^{-7}. The validity criterion for a mean-field treatment of one dimensional dynamics in presence of the three-body interactions is $\alpha \ll 1$.

Lastly, the equations of fluid dynamics are obtained by taking the real and imaginary part of equation 6.8 with $\varphi = \sqrt{n_{1D}}e^{i\phi}$. The first one is the conservation of particle, the second one is the local balance of momentum, the third one simply express the potential nature of the velocity flow.

$$\begin{cases} \partial_t n_{1D} + \partial_z\left(n_{1D}v\right) = 0 \\ m\partial_t v = -\partial_z\left(-\frac{\hbar^2}{2m\sqrt{n_{1D}}}\partial_z^2(\sqrt{n_{1D}}) + g_2^{1D}n_{1D} + g_3^{1D}n_{1D}^2 + m\frac{v^2}{2}\right) \\ v = \frac{\hbar}{m}\partial_z\phi \end{cases} \tag{6.10}$$

6.2.2 Modulation instabilities at vanishing two-body interactions

Starting from an approximately flat one-dimensional density profile in the box potential, and if there is an attractive net sum of interactions ($\mu_{int} = g_2^{1D}n_{1D} + g_3^{1D}n_{1D}^2 < 0$), we can show that the density profile is unstable. In a characteristic time of $\tau = \hbar/\mu_{int}$, the condensate splits into several clouds. The phenomenon is called a modulation instability, it can be understood roughly through linearised hydrodynamics. At short times, some density excitation modes above the flat density profile have an imaginary frequency. They will grow exponentially fast until the density profile is strongly modulated, thus forming a row of smaller clouds.

In condensates with only two-body interactions, modulation instability have been thoroughly studied [43], both theoretically and experimentally. One advantage of our system is that we can in principle, cancel exactly the two-body interaction strength and let the attractive three-body interaction drive the instability. At a magnetic field of 41.8 G, and at $\delta/\Omega = 0$ the bare two-body scattering length $a_{--}^{(0)}$ cancels out as can be seen on figure 1.22. With a very small adjustment of δ/ω around 0 we can cancel the renormalization part $a_{--}^{(1)}$. Meanwhile, the three-body interaction strength is large because the mixture polarisation $\cos\theta_d \simeq 0$ is far from either $-1, 1$ and $\cos\theta_\infty = 0.52$.

Like in previous experiment, we should start with a condensate in state $|1\rangle$ and perform an adiabatic sweep to a final detuning $\delta \simeq 0$ canceling g_2. The sweep should be slow with respect to internal dynamics at $\tilde{\Omega}$ and radial dynamics at ω_r. On the contrary, it should be fast compared to the characteristic timescale of the instability. A possible way to verify

these three conditions is to perform the sweep at a large Rabi frequency $\Omega \simeq 30\,\mathrm{kHz}$, and once the detuning is at $\delta/\Omega = 0$, we quench the value of Ω to a smaller value. This is equivalent to promptly switching-on attractive three-body interactions at an (almost-constant) vanishing two-body interactions.

Right after the quench of three-body interactions, the linearised hydrodynamic equation for the fluctuation of density $\rho(z,t)$ above the constant n_{1D} is:

$$-\hbar^2\partial_t^2\rho = -\frac{\hbar^2}{m}\partial_z^2\left(-\frac{\hbar^2}{4m}\partial_z^2 - \frac{\hbar^2}{2m}\alpha n_{1D}^2\right)\rho \tag{6.11}$$

The dispersion relation is then easily derived by looking for solution of the form $\rho(z,t) = Ae^{i(kz-\omega t)}$, noting $\varepsilon = \hbar\omega$, $\varepsilon_k = \frac{\hbar^2k^2}{2m}$ and $k_{MI} = \sqrt{\alpha}n_{1D}$

$$\varepsilon^2 = \varepsilon_k\left(\varepsilon_k - 2\varepsilon_{k_{MI}}\right) \tag{6.12}$$

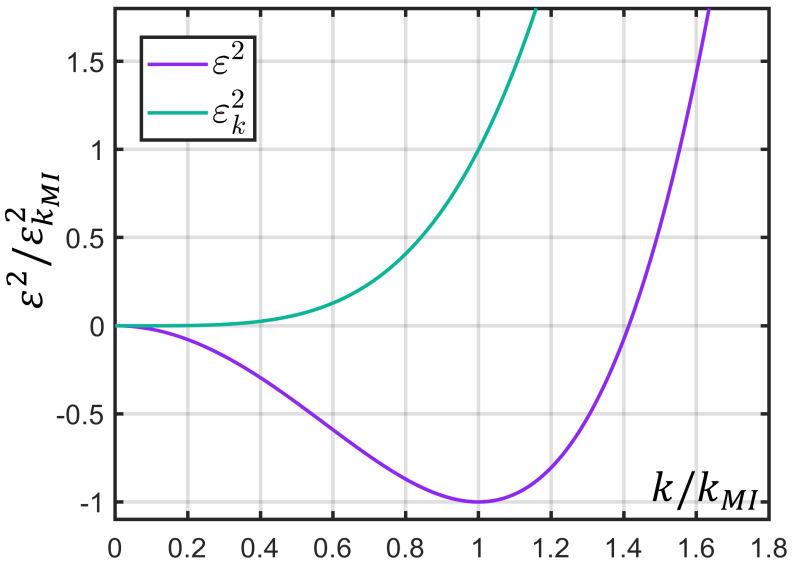

Figure 6.2: Dispersion relation for the density modes above the condensate

Modes with wave-vectors $k \in \left[0, \sqrt{2}\,k_{MI}\right]$ have an imaginary frequency and are therefore unstable. Among them, the most unstable one is at $k = k_{MI}$ and its instability timescale is $\tau = 1/|\omega| = \frac{2m}{\hbar k_{MI}^2} = \frac{2m}{\hbar\alpha\, n_{1D}^2}$, which vary of a factor 10 when the size L of the box is changed from 100 μm to 300 μm. Taking a typical value of $\alpha = 10^{-7}$, the timescale τ is between 10 ms and 100 ms for $N = 10^5$.

The most striking property of a modulation instability driven by three-body interactions is its scale invariance. The wavelength of the instability is around $\lambda_{MI} = \frac{2\pi}{\sqrt{\alpha}\,n_{1D}} = \frac{2\pi L}{\sqrt{\alpha}\,N}$, where N is the total number of atoms. When the size of the box is multiplied by a given factor, the wavelength is multiplied by the same factor. In other words, the modulation instability splits the condensate in a number M, independent of L, of smaller clouds. It can be estimated by $M = L/\lambda_{MI} = \frac{\sqrt{\alpha}\,N}{2\pi}$ which is typically between 5 and 10 depending on the value of α (itself depending on $1/\Omega$). This number may fluctuate shot

to shot depending on the initial fluctuations of the density profile n_{1D} since many modes with different wave-vectors k are unstable. Lastly, the number of atom in each smaller cloud is estimated to $N_{cloud} = N/M = \frac{2\pi}{\sqrt{\alpha}}$ of the order of 10^4.

6.2.3 Three-body quasi-solitons and fate of the modulation instability

After the modulation instability has divided the condensate into several clouds. We may investigate their time evolution and their possible stability. To do so, it is convenient to start by studying the stationary solutions of the one-dimensional Gross-Pitaevski equation with only three-body attraction:

$$i\hbar\partial_t\varphi = \mu\varphi = \left(-\frac{\hbar^2\partial_z^2}{2m} - \frac{\hbar^2}{2m}\alpha|\varphi|^4\right)\varphi \tag{6.13}$$

The relevant solutions should be bound states ($\mu < 0$), spatially localized $\left(\varphi, \partial_z\varphi \underset{|z|\to\infty}{\longrightarrow} 0\right)$. In addition, one-dimensional stationary state can always be expressed with a real wave-function [14]. By analogy with standard solitons, we expect the stationary solution to be the result of a competition between attractive three-body interactions and the repulsive quantum kinetic energy. However it is not possible to define any length-scale from the right-hand side of the above equation since α is a pure number. This consequence of scale invariance is in perfect analogy with the Townes quasi-soliton solution (attractive two-body interactions in a two-dimensional geometry) [44]. The equation can be integrated with a method similar to a classical conservative one-dimensional motion. We find a class of solution with an arbitrary length-scale ℓ also used to define the chemical potential $\ell = \sqrt{\frac{\hbar^2}{-2m\mu}}$:

$$\varphi_\ell(z) = \left(\frac{3}{\alpha}\right)^{1/4} \frac{1}{\sqrt{\ell\cosh\left(\frac{2(z-z_0)}{\ell}\right)}} \tag{6.14}$$

Where z_0 is the location of the peak of density. The multiplicative factor $\left(\frac{3}{\alpha}\right)^{1/4}$ in front of the wave-function is imposed by the equation of stationarity. As a consequence, the number of atom in the solution φ_ℓ is fixed and independent of ℓ:

$$N_s = \int_{-\infty}^{\infty} |\varphi_\ell|^2\, dz = \frac{\pi}{2}\sqrt{\frac{3}{\alpha}} \tag{6.15}$$

Stationary solutions $\{\varphi_\ell\}$ are only quasi-solitons since, contrary to true solitons [45], they lack the property of strong stability against perturbations. In other words, a small fluctuation of their number of atoms, of their density profile or of the external (flat) potential will lead to an instability. It will manifest in a collapse, a never-ending dilution or both at the same time.

Regarding the fate of the modulation instability, we note that the number of atom N_{cloud} in each cloud is $4/\sqrt{3}$ larger than N_s, the required number to have a stationary solution. After the exponential growth of unstable mode, the dynamics becomes more complex and can only be predicted with an effective Gross-pitaevskii simulations including losses. We may focus on the Fourier spectrum of the density profile at short times and look

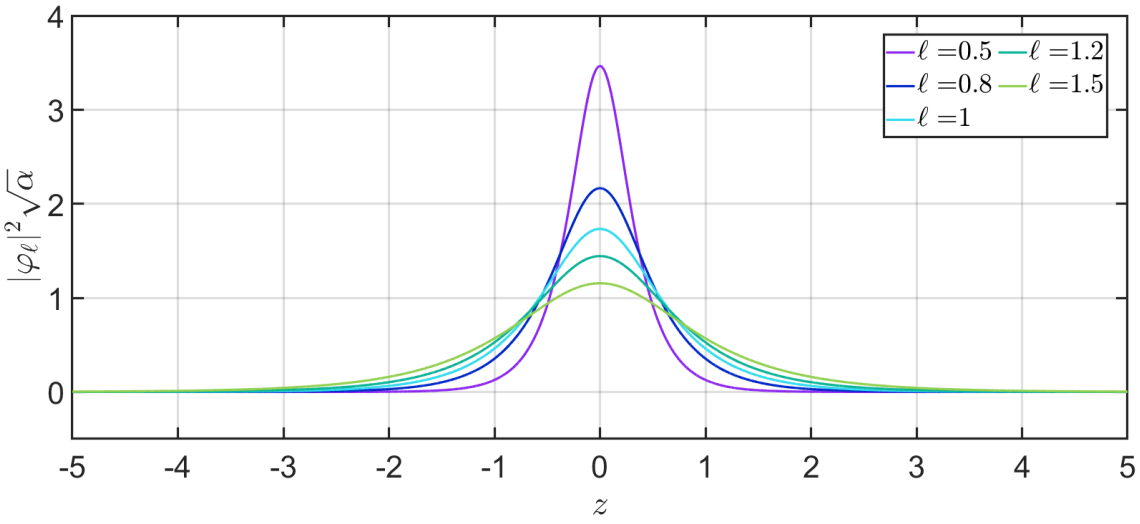

Figure 6.3: Density profiles $|\varphi_\ell|^2$ of quasi-solitons with attractive three-body interactions.

for the signature of scale invariance. It may also be an experimental challenge to precisely cancel the two-body interaction strength for a duration τ of tens of ms. Indeed, the slope of $a_{--}^{(0)}$ with δ/Ω is large ($\simeq 20a_0$)and classical fluctuations of δ happen at frequencies up to a few kHz with an rms of 500 Hz.

6.3 Chapter conclusion

In this chapter, we pinpointed at the legitimate use of standard quantum perturbation theory for low values of $\gamma = 2\overline{g}n/\hbar\Omega$. This allowed us to conciliate the effects observed in chapter 3 and 4 under different conditions. In RF-dressed condensate, the three-body attractive interaction involving three real particles coexists with a two-body renormalization of interactions. The first one scales as $\left(g_{--}^{-+}\right)^2/\Omega$ and the later scales as $\overline{g}^2\sqrt{\Omega}$
In the second part, we focused on the one-dimensional space dynamics of a condensate with vanishing two-body interactions and attractive three-body contact interactions. The equation of motion displayed a form of scale invariance. Consequently, we predict a three-body induced modulation instability that splits the elongated condensate in a number of clouds independent of the box size. This experiment could be realised in the near future on our apparatus, thanks to the box trapping setup (DMD) taking advantage of the upcoming optimization of the absorption imaging setup.

Conclusion

This thesis aimed at understanding RF-dressed condensates close to the cancellation of two-body interactions strength. This cancellation is realised by taking advantage of Feshbach resonances to get repulsive intra-species interactions $g_{ii} > 0$ and attractive inter-species interactions $g_{ij} < 0$. In addition, the radio-frequency coherent drive enable us to control the internal state $|-\rangle$ of atoms of the condensate with the ratio δ/Ω and thereby tune precisely the interaction strength between two RF-dressed atoms.

In these almost ideal RF-dressed condensates, uncommon interaction processes become visible. We observed two of them: one grasped by a mean-field description, and the other appearing with a beyond-mean-field treatment. They are both intimately linked to the possibility of spin excitations ($|-\rangle \rightarrow |+\rangle$) at a reasonable energy cost $\hbar\tilde{\Omega}$. This was formally anticipated by the introduction of inelastic two-body interaction strengths at the end of chapter 1, such as g_{--}^{++} and g_{--}^{-+}. The latter are best expressed in terms of the three parameters g_∞, $\overline{g}$ and $\cos\theta_\infty$ highlighting the universality of all binary spin mixtures of condensates.

In chapter 3, we worked at a specific value of δ/Ω so that only the beyond-mean-field effect would be visible in the system. The beyond-mean-field energy, calculated as the sum of the zero-point energies of spin waves ($|+\rangle$ at $\pm\vec{k}$) give rise to a renormalization of two-body interactions in $\overline{g}^2\sqrt{\tilde{\Omega}}$ and a three-body interaction in $\overline{g}^3/\sqrt{\tilde{\Omega}}$, both repulsive. This energy was measured experimentally with one-dimensional cloud expansions, at several Rabi frequencies Ω. The results quantitatively agreed with the BMF formula. As a collateral result, we found out that RF dressing is a viable protection against asymmetric three-body recombinations happening mostly in state $|1\rangle$ and thus it allows to properly cancel the mean-field energy. In comparison, incoherent mixtures displayed a density double structure with an excess of atoms in state $|2\rangle$ after losses of atoms in state $|1\rangle$.

In chapter 4, we investigated the mean-field effect corresponding at small $\gamma = 2\overline{g}n/\hbar\Omega$ to a three-body attractive interaction strength g_3 scaling as $-\left|g_{--}^{-+}\right|^2/\tilde{\Omega}$. The strength g_3 can be tuned independently of the two-body g_{--}^{--} by changing Ω at constant δ/Ω. In a first set of experiments, we measured the frequency of radial breathing oscillations to verify the δ/Ω dependence of g_3. The second set of experiments, closer to the zero crossing of g_{--}^{--} showed a clear threshold on δ/Ω for radial collapses. This was explained by the competition between attractive effects and repulsive ones. At smaller Rabi frequency, the three-body attractive interaction is stronger and the collapse range larger. Finally, the mean-field effect was able to strongly change the dynamics of the system by inducing radial collapses.

The last two chapters were devoted to theoretical work and perspectives.

Chapter 5 focused on the modification of the two effects for non-small values of γ.
A first concern was the validity of taking a coherent internal state for the mean-field ansatz. The exact numerical solution of the internal state of N condensed particles proved that the mixture is incoherent only for $\gamma \simeq N$. At realistic values of $\gamma \leq 10 \ll N$, there is only a very slight squeezing of the collective polarisation and the mean-field internal state is indeed a coherent state. With this ansatz, we found out that the mean-field energy is non-analytic for γ typically above 1. However, the behavior of the mean-field chemical potential is relatively simple since its slope with n varies significantly only for γ between 0.1 and 10 from its low-γ value g_{--}^{--} to its high-γ value $g_\infty \leq g_{--}^{--}$. As a possible application, it could lead to more peaked Thomas-Fermi profiles.
We also studied the behavior of the beyond-mean-field energy at potentially high γ, specifically in the context of quantum droplets. It was found that the RF-dressed quantum droplets exists only for values of Ω in $[0, \Omega_c]$, with $\Omega_c \propto g_\infty^2$. The flat-top density of the droplet decreases linearly with Ω from its value in incoherent mixture (at $\Omega = 0$) to a vanishing density at the critical value $\Omega = \Omega_c$. Future experiments could aim at making more dilute droplets, thereby increasing their lifetime and possibly leading to the first observation of a flat-top density.

In chapter 6, we properly justified with second order quantum perturbation theory that the two effects coexists at low γ. The MF three-body interactions describes a real process where three particles of the condensate are at play. The BMF two-body renormalization is a process where two particles of the condensate collide and one or two virtual $|+\rangle$ excitations are created in the interaction zone.
With this unified description, we moved on to the study of one-dimensional dynamics of the RF-dressed condensates. An interesting scenario is at the exact cancellation of the total two-body strength. The hydrodynamics equations, with only three-body attractive interactions, are scale invariant. Starting from a homogeneous gas in a one-dimensional box, a modulation instability should split the condensate in several clouds. Because of scale invariance, the number of clouds will be independent of the size of the box.

Finally, in future experiments, the new box-potential setup (DMD) and the absorption imaging setup (chapter 2) should be of great interest to observe this modulation instability. They also open a way to measure the two excitation branches, spin and density, with Bragg spectroscopy and compare it with the dispersion relation of Bogoliubov modes. Carrying out these experiment at different values of Ω is interesting since, above $\gamma \simeq 1$, the MF and BMF effects become non-analytic.

List of Figures

Bibliography

[1] C Cohen-Tannoudji and Serge Haroche. Absorption et diffusion de photons optiques par un atome en interaction avec des photons de radiofréquence. *Journal de Physique*, 30(2-3):153–168, 1969.

[2] L Lavoine, A Hammond, A Recati, DS Petrov, and Thomas Bourdel. Beyond-mean-field effects in rabi-coupled two-component bose-einstein condensate. *Physical Review Letters*, 127(20):203402, 2021.

[3] A Hammond, L Lavoine, and Thomas Bourdel. Tunable three-body interactions in driven two-component bose-einstein condensates. *Physical Review Letters*, 128(8):083401, 2022.

[4] Lev Pitaevskii and Sandro Stringari. *Bose-Einstein condensation and superfluidity*, volume 164. Oxford University Press, 2016.

[5] Christopher J Pethick and Henrik Smith. *Bose–Einstein condensation in dilute gases*. Cambridge university press, 2008.

[6] C. Cohen-Tannoudji, B. Diu, and F. Laloe. *Mécanique Quantique - Tome 2: Nouvelle édition*. EDP sciences, 2018.

[7] TG Tiecke. Properties of potassium. *University of Amsterdam, The Netherlands, Thesis*, pages 12–14, 2010.

[8] J.C. Slater. *Quantum Theory of Matter*. International series in pure and applied physics. McGraw-Hill, 1968.

[9] W. Demtröder. *Atoms, Molecules and Photons: An Introduction to Atomic-, Molecular- and Quantum Physics*. Graduate Texts in Physics. Springer Berlin Heidelberg, 2019.

[10] Chiara d'Errico, Matteo Zaccanti, Marco Fattori, Giacomo Roati, Massimo Inguscio, Giovanni Modugno, and Andrea Simoni. Feshbach resonances in ultracold 39k. *New Journal of physics*, 9(7):223, 2007.

[11] Stephan Falke, Horst Knöckel, Jan Friebe, Matthias Riedmann, Eberhard Tiemann, and Christian Lisdat. Potassium ground-state scattering parameters and born-oppenheimer potentials from molecular spectroscopy. *Physical Review A*, 78(1):012503, 2008.

[12] J.P. Pérez. *Mécanique: Fondements et applications, avec 320 exercices et problèmes résolus*. Fondements et applications. Dunod, 2014.

[13] A. Messiah. *Quantum Mechanics*. Dover Books on Physics. Dover Publications, 2014.

[14] L.D. Landau and E.M. Lifshitz. *Quantum Mechanics: Non-Relativistic Theory*. Course of theoretical physics. Elsevier Science, 2013.

[15] Bo Gao. Quantum-defect theory of atomic collisions and molecular vibration spectra. *Physical Review A*, 58(5):4222, 1998.

[16] Jean Dalibard. Les interactions entre atomes dans les gaz quantiques. *cours du collège de France, chaire Atomes et rayonnement*, 2020-2021.

[17] Noam Gross, Zav Shotan, Servaas Kokkelmans, and Lev Khaykovich. Observation of universality in ultracold li 7 three-body recombination. *Physical review letters*, 103(16):163202, 2009.

[18] PO Fedichev, MW Reynolds, and GV Shlyapnikov. Three-body recombination of ultracold atoms to a weakly bound s level. *Physical review letters*, 77(14):2921, 1996.

[19] Eric Braaten and H-W Hammer. Three-body recombination into deep bound states in a bose gas with large scattering length. *Physical review letters*, 87(16):160407, 2001.

[20] C Cohen-Tannoudji. Atomes "habillés" par des photons optiques ou de radiofréquence. *Le Journal de Physique Colloques*, 32(C5):C5a–11, 1971.

[21] Serge Haroche. L'atome habillé: une étude théorique et expérimentale des propriétés physiques d'atomes en interaction avec des photons de radiofréquence-première partie. In *Annales de Physique*, volume 14, pages 189–326. EDP Sciences, 1971.

[22] Serge Haroche and J-M Raimond. *Exploring the quantum: atoms, cavities, and photons*. Oxford university press, 2006.

[23] C. Cohen-Tannoudji, B. Diu, and F. Laloe. *Mécanique Quantique - Tome 1: Nouvelle édition*. EDP Sciences, 2018.

[24] J Sanz, A Frölian, CS Chisholm, CR Cabrera, and L Tarruell. Interaction control and bright solitons in coherently coupled bose-einstein condensates. *Physical Review Letters*, 128(1):013201, 2022.

[25] Julio Sanz Sánchez. Two-component bose-einstein condensates with competing interactions. 2020.

[26] R.P. Feynman, R.B. Leighton, and M. Sands. *The Feynman Lectures on Physics, Vol. III: The New Millennium Edition: Quantum Mechanics*. Basic Books, 2015.

[27] Lucas Lavoine. *Mélange de spin dans un condensat de Bose-Einstein: Gouttelette quantique et couplage cohérent*. PhD thesis, université Paris-Saclay, 2022.

[28] Rudolf Grimm, Matthias Weidemüller, and Yurii B Ovchinnikov. Optical dipole traps for neutral atoms. In *Advances in atomic, molecular, and optical physics*, volume 42, pages 95–170. Elsevier, 2000.

[29] Guillaume Berthet. *Désordre et interactions dans les gaz quantiques bosoniques*. PhD thesis, Université Paris-Saclay (ComUE), 2019.

[30] DS Petrov. Quantum mechanical stabilization of a collapsing bose-bose mixture. *Physical review letters*, 115(15):155302, 2015.

[31] Hugo Cayla, Salvatore Butera, Cécile Carcy, Antoine Tenart, Gaétan Hercé, Marco Mancini, Alain Aspect, Iacopo Carusotto, and David Clément. Hanbury brown and twiss bunching of phonons and of the quantum depletion in an interacting bose gas. *Physical Review Letters*, 125(16):165301, 2020.

[32] DS Petrov. Three-body interacting bosons in free space. *Physical Review Letters*, 112(10):103201, 2014.

[33] Tilman Zibold, Eike Nicklas, Christian Gross, and Markus K Oberthaler. Classical bifurcation at the transition from rabi to josephson dynamics. *Physical review letters*, 105(20):204101, 2010.

[34] Riccardo Cominotti, Anna Berti, Clement Dulin, Chiara Rogora, Giacomo Lamporesi, Iacopo Carusotto, Alessio Recati, Alessandro Zenesini, and Gabriele Ferrari. Ferromagnetism in an extended coherently-coupled atomic superfluid, 2023.

[35] Yu Kagan, EL Surkov, and GV Shlyapnikov. Evolution of a bose-condensed gas under variations of the confining potential. *Physical Review A*, 54(3):R1753, 1996.

[36] LP Pitaevskii and A Rosch. Breathing modes and hidden symmetry of trapped atoms in two dimensions. *Physical Review A*, 55(2):R853, 1997.

[37] Frédéric Chevy, Vincent Bretin, Peter Rosenbusch, KW Madison, and Jean Dalibard. Transverse breathing mode of an elongated bose-einstein condensate. *Physical review letters*, 88(25):250402, 2002.

[38] Nils B Jørgensen, Georg M Bruun, and Jan J Arlt. Dilute fluid governed by quantum fluctuations. *Physical review letters*, 121(17):173403, 2018.

[39] B Juliá-Díaz, T Zibold, MK Oberthaler, M Melé-Messeguer, J Martorell, and A Polls. Dynamic generation of spin-squeezed states in bosonic josephson junctions. *Physical Review A*, 86(2):023615, 2012.

[40] CR Cabrera, L Tanzi, J Sanz, B Naylor, P Thomas, P Cheiney, and L Tarruell. Quantum liquid droplets in a mixture of bose-einstein condensates. *Science*, 359(6373):301–304, 2018.

[41] L Lavoine and T Bourdel. 1d to 3d beyond-mean-field dimensional crossover in mixture quantum droplets. *arXiv preprint arXiv:2011.12394*, 2020.

[42] PR Johnson, Eite Tiesinga, James V Porto, and Carl J Williams. Effective three-body interactions of neutral bosons in optical lattices. *New Journal of Physics*, 11(9):093022, 2009.

[43] Cheng-An Chen and Chen-Lung Hung. Observation of universal quench dynamics and townes soliton formation from modulational instability in two-dimensional bose gases. *Physical Review Letters*, 125(25):250401, 2020.

[44] B Bakkali-Hassani, C Maury, Y-Q Zou, É Le Cerf, R Saint-Jalm, Patricia Christina Marques Castilho, Sylvain Nascimbene, Jean Dalibard, and Jérôme Beugnon. Realization of a townes soliton in a two-component planar bose gas. *Physical Review Letters*, 127(2):023603, 2021.

[45] Michel Peyrard and Thierry Dauxois. *Physique des solitons*. Number BOOK. EDP sciences Paris, 2004.

université PARIS-SACLAY

ÉCOLE DOCTORALE
Ondes et Matière (EDOM)

Titre: Effets collectifs dans les gaz ultra-froids de potassium ^{39}K habillé par radio-fréquence

Mots clés: BEC, atome habillé, gaz quantique, mélange cohérent, N corps

Résumé: Tout comme les gaz de Van der Waals, les gaz quantiques ont des propriétés thermodynamiques universelles et proches de celles du gaz parfait. Un fluide quantique dilué de particules neutres a une équation d'état faisant intervenir peu de paramètres intrinsèques. L'utilisation d'un mélange de deux condensats de Bose-Einstein permet de diminuer voire d'annuler complètement certains termes de l'équation dynamique du fluide. Dans ce contexte, il a été observé expérimentalement que la physique d'un gaz atomique habillé par un champ radio-fréquence (mélange quantique) est beaucoup plus riche qu'en l'absence du champ. D'une part, des effets collectifs habituellement négligeables - interactions élastiques à trois corps - apparaissent et deviennent prépondérant dans les propriétés de champ moyen du fluide. D'autre part, des effets au-delà du champ moyen - renormalisation des interactions et énergie quantique de point zéro - sont modifiés et exaltés. En conséquence, nous avons pu observer des propriétés dynamiques nouvelles dans des gaz quantiques de potassium 39 habillé par radio-fréquence.

Title: Collective effects in RF-dressed ^{39}K ultra-cold gases

Keywords: BEC, dressed-states, quantum gas, coherent mixture, many-body

Abstract: Just like Van der Waals gases, quantum gases have some universal thermodynamic properties in deviation to the ideal gas. A dilute quantum fluid of neutral particles has an equation of state involving very few intrinsic parameters. The use of mixtures of two Bose-Einstein condensate allow for the diminution or even cancellation of some terms in the dynamical equation of the fluid. In this context, it was experimentally observed that the physics of an ultra-cold RF-dressed atomic gas (quantum coherent mixture) is much richer than in absence of RF coupling. On the one hand, collective effects usually insignificant – three body elastic interactions – rise and dominate the mean-field properties of the fluid. On the other hand, some beyond-mean field effects - interaction renormalization and quantum vacuum energy - are modified and enhanced. Consequently, We observed novel dynamical properties in potassium 39 RF dressed quantum gases.

Université Paris-Saclay
Espace Technologique / Immeuble Discovery
Route de l'Orme aux Merisiers RD 128 / 91190 Saint-Aubin, France